UNIVERSITY OF READING

Department of Meteorology

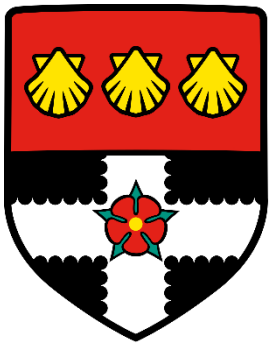

A Statistical Approach to Evaluate the Parametrisation of Turbulence in Convection-Permitting Models using Radar-Retrieved Eddy Dissipation Rates

Matthew Feist

A thesis submitted for the degree of Doctor of Philosophy

September, 2018

Declaration

I confirm that this is my own work and the use of all material from other sources has been properly and fully acknowledged.

Matthew Feist

Abstract

The effects of turbulence on the evolution of convective clouds remains uncertain both in observations and in numerical weather prediction (NWP) models. Turbulent processes remain parametrised in convection-permitting models (CPMs), and simulated clouds remain highly sensitive to the configuration of sub-filter turbulence schemes. It remains unclear whether assumptions implicit in these schemes are valid for CPMs, indicating the need for thorough evaluation of their performance using observations; the primary aim of this thesis.

Eddy dissipation rates ε, are retrieved in radar data by applying a comprehensive method to infer the turbulent component of the Doppler spectrum variance. Hydrometeor fall-speed variances are shown to be negligible when sampling at elevations lower than 11.5°. Shear is calculated directly by applying a linear velocity model to Doppler velocities. New equations are presented to account for variance from azimuthal shear – an unseen dimension in range-height scans. Resulting values of ε are insensitive to the scale over which shear is calculated.

A thorough statistical analysis of ε in observed clouds suitable for model evaluation is presented for the first time. Retrievals of ε were analysed for two contrasting case studies; shallow "shower" clouds and more vigorous "deep" clouds. Values of ε range from $10^{-3} - 10^{-1}\ \mathrm{m^2\ s^{-3}}$ in shower clouds and from $10^{-3} - 1\ \mathrm{m^2\ s^{-3}}$ in deep clouds. Turbulent intensity increases with height in deep clouds while remaining constant in shower clouds. In both cases, significant positive correlations are demonstrated between ε and many cloud characteristics. The strongest correlations are found between the velocity and horizontal shear in updrafts. Coherent features of ε are found to have typical spatial scales of 0.5 – 1 km.

Results are compared with equivalent statistics derived in 100-m and 55-m grid-length Met Office Unified Model simulations of the observed cases to evaluate the Smagorinsky-Lilly sub-grid mixing scheme. Simulated turbulence is characterised by small, intense regions of ε more strongly co-located with shear around updrafts than observed. The 95th

and 99th percentiles of model ε are one and two orders of magnitude larger than observations, respectively, with similar median values. Values of ε increase consistently with the mixing length and appear insensitive to grid-length suggesting 100-m was sufficient to resolve an inertial sub-range.

Acknowledgements

I would like to thank my supervisors **Chris Westbrook**, **Peter Clark**, **Thorwald Stein**, **Humphrey Lean** and **Alison Stirling** for their extremely useful insight and guidance throughout this project. I would also like to thank my monitoring committee **Steve Woolnough** and **Bob Plant** for their guidance and very constructive feedback on my progress.

I would like to express my gratitude to the staff at STFC for their help operating CAMRa and processing the data, in particular, **Chris Walden** and **Darcy Ladd**.

I am especially thankful to my parents **Bridget** and **Stephen** whose support and unwavering confidence in me was invaluable throughout. I would finally like to thank my family and friends for their support, in particular **Kaitlyn**, who was always there for a (4-hour) chat.

Contents

Chapter 1

Introduction

The effects of turbulence on the structure and evolution of convective clouds remain unclear in observations and numerical weather prediction (NWP) models. The turbulent entrainment of dry environmental air into cumulus clouds has long been known to play an important role in their growth and decay (Blyth, 1993). The specific location of entrained air can have a varied and substantial impact on resulting air motions within the cloud (Blyth *et al*., 1988). Turbulent mixing within clouds significantly impacts the microphysical processes governing the initiation of convective precipitation; turbulence can accelerate cloud drop growth through increased rates of collision and coalescence (Vohl *et al*., 1999). Although there is much evidence for the effects of turbulence on cloud processes, there remains uncertainty in their precise nature, and the implications for cloud evolution. This is compounded by difficulty collecting observations of turbulence over the range of scales that impact complex cloud processes.

In recent years, regional numerical weather prediction (NWP) has improved to sufficient resolution that it is worthwhile abandoning the parametrisation of deep convective clouds, and, instead, allowing the unstable growth of explicit convective clouds. However, it is not feasible to forecast using resolutions sufficient to properly resolve all of the important features of the flow. Hence such models are known as 'convection-permitting' models (CPMs; Clark *et al*. 2016). The formal treatment of turbulent flow in numerical simulation remains an unsolved problem. Therefore, physical processes occurring on scales below those resolved in CPMs, such as turbulence, remain parametrised. Model simulations show that assumptions made regarding parametrised turbulence in clouds have a profound effect on the characteristics of simulated clouds (e.g. Hanley *et al*., 2015). To test the assumptions

made in these parametrisations, the characteristics of turbulence in simulated clouds must be evaluated using corresponding observations in real clouds. Until understanding of the effects of turbulence in observed clouds is advanced, justifiable attempts to improve turbulence parametrisations are difficult to make.

To improve both understanding of turbulence in observed clouds and guide the development of turbulence parametrisation in NWP, high-resolution observations of convective cloud turbulence are required. By scanning clouds with high-resolution Doppler weather radar, near-instantaneous observations of turbulence can be made across large swathes of atmosphere. This has clear benefits over using methods such as aircraft or radiosonde ascent measurements which can only collect time-series information from single points in space. Doppler-capable radars measure the variability in the component of the wind along the line-of-sight; which is increased by turbulence. Previous studies have estimated turbulence, expressed in terms of the dissipation rate of turbulent kinetic energy, ε, from the width of the Doppler velocity spectrum (Frisch and Clifford, 1974; Istok and Doviak, 1986; Chapman and Browning, 2001; Meischner *et al*., 2001).

Although the general theoretical approach to retrieving ε from the Doppler spectrum width is well established, past turbulence retrieval studies generally focus only on single storm cases. Often, the contributions to the Doppler velocity spectrum from processes aside from turbulence are either purely assumed to be negligible or are shown to be negligible only for the purpose of the application. As a result, a comprehensive method to retrieve ε from radar fields under a wide range of conditions has not been presented. By developing such a method, consistent retrievals of turbulence can be made across many cloud cases allowing for a statistical assessment of turbulence in convective clouds; which has also not been presented. This approach allows for more reliable relationships to be determined between turbulence and cloud processes than those which can be identified in individual case studies, providing the robust framework of turbulence statistics required for the evaluation of turbulence parametrisation methods in NWP.

In this thesis, a comprehensive method to retrieve ε using high-resolution Doppler weather radar is presented and compared to the more limited approaches that have appeared in the literature. This retrieval algorithm is applied to radar data collected with the Chilbolton Advanced Meteorological Radar (CAMRa); the highest resolution weather radar in the world. A large dataset of radar observations collected on two contrasting case days is used to conduct a detailed statistical assessment of turbulence in convective clouds. These statistics are then used to evaluate the parametrisation of turbulence in Met Office Unified Model (MetUM) simulations that have been performed for the corresponding case days.

1.1 Turbulence

1.1.1 What is turbulence?

If the kinetic energy in a fluid flow is large enough to locally exceed the damping effects of the viscosity of the fluid, the flow can become turbulent, resulting in chaotic fluctuations in flow velocity. In this sense, turbulence describes the resulting irregularities in the flow, and is easier to induce in flows with low kinematic viscosity, ν. Turbulent flows are complex and unpredictable; the precise impact of turbulence on the evolution of clouds remains unclear, and the formal treatment of turbulent flow in numerical simulation remains an unsolved problem.

Described by Reynolds (1883), the potential for turbulence in a fluid can be predicted using the dimensionless Reynolds number, Re. This is the ratio of the inertial and viscous force terms in the incompressible Navier-Stokes equation. For a non-rotating (omitting Coriolis acceleration), incompressible fluid, the acceleration of a fluid parcel is given by:

$$\frac{\partial \mathrm{u}}{\partial \mathrm{t}} + (\mathrm{u} \cdot \nabla)\mathrm{u} + \frac{1}{\rho}\nabla p + g\mathbf{k} = \nu \nabla^2 \mathrm{u} \tag{1.1}$$

Where u is the flow velocity, ρ is the fluid density, p is the pressure and g is the gravitational acceleration. From left to right, the terms in (1.1) describe the acceleration of a fluid parcel due to: the local time derivative of u; advection (inertial forces); pressure gradients; gravity (where **k** is a unit vector parallel to the gravitational acceleration); and fluid viscosity. The ratio of $(\mathrm{u}\cdot\nabla)\mathrm{u}$ and $\nu\nabla^2\mathrm{u}$ therefore provides Re, which can then be simplified using dimensional analysis:

$$\mathrm{Re} = \frac{\text{inertial forces}}{\text{viscous forces}} = \frac{(\mathrm{u}\cdot\nabla)\mathrm{u}}{\nu\nabla^2\mathrm{u}} \sim \frac{\left(U\cdot\frac{1}{L}\right)\cdot U}{\nu\cdot\frac{1}{L^2}\cdot U} \sim \frac{UL}{\nu} \tag{1.2}$$

Where U and L are the characteristic velocity and length scales of a fluid, respectively. If the Reynolds number of a fluid flow exceeds a critical value $\mathrm{Re_c}$, then the flow can become turbulent. Although the value of $\mathrm{Re_c}$ depends on the geometry of the flow (Potter *et al.*, 2012), values of $\mathrm{Re_c} > 5\times10^3$ generally correspond to fully turbulent flow, e.g. for air flow in a pipe, $\mathrm{Re_c} \sim 4\times10^3$ Holman (2002)). In the atmospheric boundary layer, $U \sim 10$ m s^{-1}, $L \sim 10^3$ m (boundary layer depth) and $\nu \sim 10^{-5}$ m^2 s^{-1}, so (1.2) can be used to find $\mathrm{Re} \sim 10^9 > \mathrm{Re_c}$, far exceeding the typical values of $\mathrm{Re_c}$. Values of Re in convective clouds (as is appropriate for this project) can be even larger than for the boundary layer. In deep, convective clouds, U and L can range from $10-50$ m s^{-1} and 5 – 15 km, respectively. If $\nu \sim 10^{-5}$ m^2 s^{-1}, values of Re can range from 10^9-10^{11} which, again, far exceeds typical threshold values for fully turbulent flow.

Once turbulence can be initiated, flows are characterised by instabilities called *eddies*, which are roughly defined as coherent, swirling structures in the flow velocity. A turbulent flow may contain eddies on a spectrum of spatial scales (or wavelengths). Figure 1.1 illustrates the change in transverse velocity v, during the passage of a turbulent eddy, where Δt represents the timescale of eddy advection. The length scale (or wavelength) of the eddy is given by $v\Delta t$. Fluctuations in velocity such as this can be seen in time series of turbulent

wind flows, indicating the presence of turbulent eddies of varying scale embedded in the mean flow.

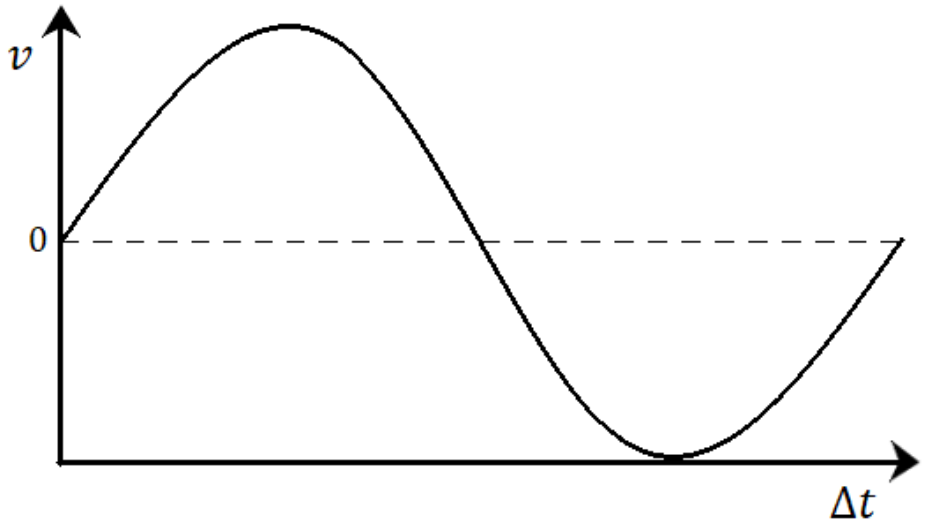

Figure 1.1: Illustration of the variation in velocity perpendicular to the flow v, during the complete passage of an eddy over a fixed location.

1.1.2 Turbulent kinetic energy

The separation of turbulent velocity fluctuations from the mean velocity allows closer examination of the properties of turbulence in a flow; this is achieved using the Reynolds decomposition technique. For a given point in a flow with a velocity of u at time t, the velocity can be decomposed into a mean and fluctuating component:

$$u(t) = \overline{u(t)} + u'(t) \tag{1.3}$$

Where $\overline{u(t)}$ is the mean velocity obtained by sampling $u(t)$ over a time period, T,

$$\overline{u(t)} = \frac{1}{T}\int_{t-T}^{t} u(t')\, dt' \tag{1.4}$$

and $u'(t)$ is the deviation from $\overline{u(t)}$ owing to turbulence in the flow. The turbulent properties of a flow can be found by analysing the statistics of $u'(t)$.

The kinetic energy associated with the flow can too be decomposed into mean and turbulent components. Expressed per unit mass, the total kinetic energy e_T, associated with a 3-dimensional flow is given by:

$$e_T = \frac{1}{2}(\bar{u}^2 + \bar{v}^2 + \bar{w}^2) + \frac{1}{2}\left(u'^2 + v'^2 + w'^2\right) + (\bar{u}u' + \bar{v}v' + \bar{w}w') \tag{1.5}$$

The right-hand terms describe (from left to right) the kinetic energy in the mean flow, the kinetic energy in the turbulent flow, and so-called "cross terms". Averaging (1.5) leaves the kinetic energy in the mean flow the same $\left(\bar{\bar{X}} = \bar{X}\right)$, the "cross terms" equal to zero $(\overline{X'} = 0)$ and turbulent kinetic energy (TKE) e, is given by:

$$e = \frac{1}{2}\left(\overline{u'^2} + \overline{v'^2} + \overline{w'^2}\right) \tag{1.6}$$

Where the factor $\frac{1}{2}$ in (1.6) is often omitted.

Under the assumption of horizontal homogeneity, the change in e in a fluid flow is governed by the TKE equation (1.7), which can be obtained by multiplying the incompressible Navier-Stokes equations by u and using Reynolds-averaging.

$$\frac{De}{Dt} = -\overline{u'w'}\frac{\partial \bar{u}}{\partial z} - \overline{v'w'}\frac{\partial \bar{v}}{\partial z} + \frac{g}{\theta_0}\overline{w'\theta'} - \frac{1}{\rho}\frac{\partial}{\partial z}\overline{w'p'} - \frac{\partial}{\partial z}\overline{w'e'} - \nu\overline{\left(\frac{\partial w'}{\partial z}\right)^2} \tag{1.7}$$

Where θ is the potential temperature and g is the gravitational acceleration. The rate of viscous TKE dissipation (referred to as the eddy dissipation rate, ε) is given by the final term on the RHS of (1.7):

$$\varepsilon = \nu\overline{\left(\frac{\partial w'}{\partial z}\right)^2}$$

The expanded form of the LHS of (1.7) is given by:

$$\frac{De}{Dt} = \frac{\partial e}{\partial t} + \bar{u}\frac{\partial e}{\partial x} + \bar{v}\frac{\partial e}{\partial y} + \bar{w}\frac{\partial e}{\partial z} \tag{1.8}$$

The $\frac{\partial}{\partial x}$ and $\frac{\partial}{\partial y}$ terms on the RHS of (1.8) are zero under the assumption of horizontal homogeneity and the vertical advection term is generally ignored; it is small when averaged over a large area. The first four terms on the RHS of (1.7) describe the sources of TKE from shear, buoyancy and pressure perturbations. This is followed by a turbulent transport term which accounts for the movement of TKE by turbulent eddies. This process alters the magnitude of TKE at fixed locations but has no net effect on total TKE. Under the assumption of homogenous, steady-state turbulence in a co-ordinate system aligned with the flow (the $\overline{v'w'}$ term is removed), the production of TKE by shear and buoyancy is balanced by viscous dissipation:

$$\varepsilon = -\overline{u'w'}\frac{\partial \bar{u}}{\partial z} + \frac{g}{\theta_0}\overline{w'\theta'} \tag{1.9}$$

1.1.3 Turbulence spectra

The largest (integral) length scale Λ_L, of eddies in a fluid flow is determined by the spatial constraints of the system. For example, the largest eddy scale in a flow through a pipe is equal to the pipe diameter, whereas for convective circulations in the atmosphere, this scale can be 10 km. Eddies on this input scale degrade into smaller and smaller eddy circulations in the Richardson energy cascade – the downscale transfer of TKE from the integral length scale to dissipation scales, where eddy energy is converted to heat by viscous forces.

Kolmogorov (1941) proposed, through dimensional analysis, that the dissipation of turbulent eddies began at a length scale Λ_D (the Kolmogorov microscale), that was a function only of the fluid viscosity ν, and the rate of eddy energy dissipation, ε ($m^2\ s^{-3}$):

$$\Lambda_D = \left(\frac{\nu^3}{\varepsilon}\right)^{\frac{1}{4}} \tag{1.10}$$

Kolmogorov further proposed that for a fluid with very high Re, the anisotropy of large scale eddies was lost in the Richardson energy cascade. This leads to a range of isotropic eddy scales called the "inertial sub-range", the largest scale of which (the outer scale, Λ_0), exists between Λ_L and Λ_D (see Figure 1.2). Within this range, there are no mechanisms generating new eddy energy, nor is eddy energy dissipated, it is merely transferred downscale at a rate equal to ε. As a result, the energy spectrum of the inertial sub-range could be characterised through dimensional analysis of ε and the wavenumber k, where $k = \frac{2\pi}{\Lambda_0}$. To achieve this, the energy associated with eddies of a given wavenumber $E(k)$, which has units of $m^3\ s^{-2}$, is expressed as:

$$E(k) = A\varepsilon^a k^b \tag{1.11}$$

Where A is a constant, and a and b can be determined. In dimensional terms, $E(k) = \frac{L^3}{T^2}$, $\varepsilon = \frac{L^2}{T^3}$, and $k = \frac{1}{L}$. Substituting these into (1.11) provides:

$$\frac{L^3}{T^2} = A\left(\frac{L^{2a}}{T^{3a}}\right)\left(\frac{1}{L^b}\right) \tag{1.12}$$

Solving for a and b provides values of $a = \frac{2}{3}$, and $b = -\frac{5}{3}$, which leaves the final form of the energy spectrum of the inertial sub-range as:

$$E(k) = A\varepsilon^{2/3}k^{-5/3} \tag{1.13}$$

Where A is the universal constant of isotropic turbulence with values ranging from 1.53 to 1.68 (Gossard and Strauch, 1983).

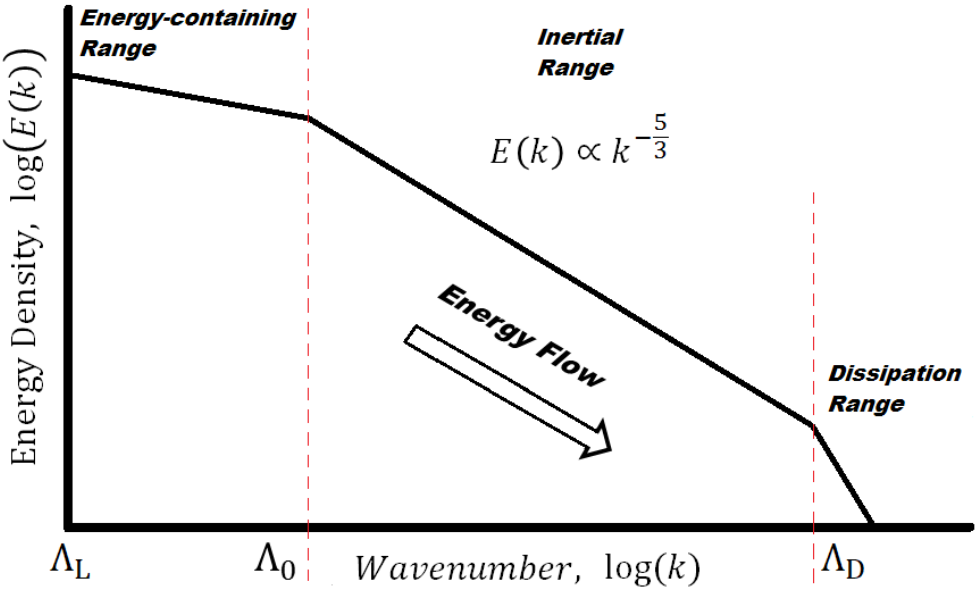

Figure 1.2: Under the assumptions of Kolmogorov (1941), the energy spectrum of turbulence includes an "inertial sub-range" between wavenumbers Λ_0 and Λ_D which has an energy spectrum proportional to $k^{-5/3}$ given by (1.13).

The value of Λ_0 is not fixed but can depend on the characteristic scales of the system. For a convective cloud, the largest eddies are mainly produced by buoyant updraft circulations. These so-called *energy-containing* eddies can have wavelengths of $\Lambda_L = 5 - 10$ km and are anisotropic. Isotropy is attained at scales smaller than Λ_L during the down-scale Richardson cascade. Values of Λ_0 can therefore vary significantly depending on the scales of cloud processes. In cumulus clouds of 1 – 4.5 km depth, MacPherson and Isaac (1977) found values of Λ_0 up to 400 m. In severe convective storms, Sinclair (1974) reported the inertial sub-range extending to $\Lambda_0 = 1$ km, Rhyne and Steiner (1964) reported $\Lambda_0 = 1.2$ km, Battan (1975) observed turbulence on scales up to 2 km, Brewster and Zrnic (1986) reported values from $\Lambda_0 = 2.4 - 3$ km and Foote and Fankhauser (1973) found Λ_0 to be as large as 4 km in a Colorado hailstorm. In addition, Λ_0 can vary spatially within clouds; Sinclair (1974) found that Λ_0 was largest in the upper half of the cloud where updraft velocity and turbulence was most intense. The degree to which precise measurements of Λ_0 are required when attempting to estimate ε from clouds sampled with Doppler radar is discussed in Chapter 3.

1.2 Turbulence and cloud processes

Clouds in the atmosphere are characterised by a Reynolds number ($\mathrm{Re} \sim 10^9$; see Section 1.1.1) that exceeds the critical value of $\mathrm{Re_c} \sim 3 \times 10^3$ for associated fluid flows to become turbulent. Turbulence is important in the formation of clouds and precipitation, however, its precise role in small-scale cloud processes remains unclear (a detailed summary is given by Devenish *et al.*, 2012). Turbulence remains just one of many physical processes (such as dry air entrainment and microphysical processes) that affect the evolution of clouds and precipitation. The effects of turbulence occur on a wide range of spatial scales within clouds making an assessment of its importance relative to other cloud processes a significant challenge. This is compounded by difficulty in collecting precise observations of turbulence simultaneously with other cloud processes, and across a wide range of scales. This section summarises the importance and uncertainty associated with turbulence in cloud and precipitation processes.

1.2.1 Turbulent entrainment

The density of air within clouds is different to that of the surrounding environmental air. The process by which environmental air mixes into the cloud is called entrainment; a process which can significantly influence cloud evolution, first described by Stommel (1947). The entrainment of dry unsaturated air locally reduces cloud liquid water content through evaporation of cloud droplets. In cumulus clouds, this effect has been shown to occur through the full cloud depth (Warner, 1955; Blyth and Latham, 1990; Blyth, 1993) and is independent of cloud width except in very small clouds (Warner, 1955). Among the conclusions of Blyth (1993) was that vertical mixing, i.e. the downward mixing of environmental air into the tops of cumulus updrafts, leading to penetrative downdrafts, were more responsible for diluting cumulus clouds than mixing through horizontal entrainment. However, Heus *et al.*, (2008) used large-eddy simulations to demonstrate that almost all

entrainment occurs laterally in shallow cumulus cloud. Characteristics of entrainment have previously depended on whether updrafts are considered as either "plume-type" and "thermal-type". Thermal-type and plume-type updrafts are described in Blyth (1993) as "instantaneous" and "maintained" regions of vertical velocity, respectively. In thermal-type updrafts, Blyth *et al.* (1988) proposed that entrained parcels enter near the cloud top and descend around the updraft producing a turbulent wake region; a process which is far less applicable to plume-type updrafts. The exact processes by which environmental air is entrained into (and mixes with) convective clouds remains unclear.

1.2.2 Turbulence and cloud microphysics

The growth of water droplets in clouds depends on the supersaturation and small-scale dynamics of the cloud environment, which can be modulated by turbulence. As a result, turbulence has long been considered to impact the growth of raindrops and the initiation of precipitation in convective clouds. The interaction of turbulence on cloud droplets takes place on the smallest scales within the cloud. More specifically, the fluid motions that affect droplet collisions, coalescence and collection efficiency occur on spatial scales below 1 mm (Shaw, 2003). This indicates that turbulent motion on dissipative scales is more important for cloud droplets, rather than turbulence on inertial sub-range scales which is more important for entrainment processes (Devenish *et al.*, 2012).

Turbulence of the scale of individual cloud droplets can impact the rate of droplet growth via condensation. In modelling experiments, Khvorostyanov and Curry (1999) identified that small-scale turbulence can lead to fluctuations in supersaturation that increase cloud droplet growth independent of drop radius; this process has also been shown to broaden the drop-size distribution (Pinksy *et al.,* 1999; Sidin *et al.,* 2009). Further complexity associated with this process is identified by Shaw *et al.* (1998) who propose that the fluctuations in droplet

concentration from small-scale turbulence alter the supersaturation such that droplet growth rates vary considerably over small distances.

Droplet collision and coalescence is a key process by which cloud droplets grow. Although the collection efficiency of droplets remains dependent on multiple factors (such as relative droplet sizes), the presence of turbulence can accelerate cloud drop growth through increased rates of collision and coalescence (Grover and Pruppacher, 1985; Khain and Pinsky, 1995; Vohl *et al*., 1999). Turbulent motion in clouds has also been shown to increase the rate of large droplet formation in shallow cumulus (Pinksy and Khain, 2002; Falkovich *et al*., 2002); a key step in the initiation of precipitation. Through numerical simulation of mixed-phase deep clouds, Benmoshe *et al*. (2012) identified that the initial rain-drops developed in regions of the strongest turbulence near the tops of updrafts, and that these developed earlier and at a lower altitude in turbulent conditions. Research into the effects of turbulence into ice nucleation and ice particle growth is less extensive than for liquid water droplets. However, similar impacts of turbulence on ice particles were identified by Benmoshe *et al.* (2014) who showed (for mixed-phase deep clouds simulated in a 50-m grid-scale numerical model) that turbulence increases the collision rates of ice-ice and ice-water particles and accelerates the growth of ice aggregates and graupel by riming.

1.2.3 Summary and discussion

It is clear from this brief section that turbulence has a complex and profound impact on the evolution of convective clouds over a range of scales. The entrainment of dry environmental air by inertial sub-range scale turbulent eddies dilutes cumulus clouds, evaporating cloud droplets and affecting vertical motion within the cloud. Cloud microphysical processes are modulated by turbulence on dissipative scales, with impacts on the condensational growth of cloud droplets, growth by collision and coalescence, the drop-size distribution, the formation of large droplets and the timing and location of rain-drop

development. Although the research in this area of cloud physics is extensive, significant uncertainty remains in the precise role of turbulence in clouds processes. Perhaps the most significant challenge is to reconcile the many theoretical, observational and numerical approaches used to investigate turbulence in clouds. Owing to the difficulty observing characteristics of turbulence simultaneously with the thermodynamic and microphysical properties of clouds, many of the developments included in this section have been made using numerical models, often through Direct Numerical Simulation (DNS). However, the development of these models, and more importantly, those that approximate the effects of turbulence through parametrisation, must be guided by precise observations of turbulence in clouds.

1.3 Turbulence in NWP models

1.3.1 Characteristics of convection-permitting models (CPMs)

Precise forecasts of convective precipitation remain an ongoing challenge for numerical weather prediction (NWP) models. The increasing frequency of extreme precipitation events predicted with climate change (Meehl *et al*., 2000) emphasises the need for short-range, high-resolution forecasts of precipitation. Until only recently, operational NWP models have used horizontal grid-lengths larger than 10 km. Such grid-lengths are insufficient to resolve details of convection so these processes must be approximated using parametrisations. In recent years, improvements to computing power has enabled operational models to forecast with horizontal grid-lengths well below 5 km. For example, the Met Office operational forecast model (UKV) is a variable-resolution configuration of the Unified Model (MetUM) which uses a horizontal grid-length of 1.5 km (see Section 2.3). With models using grid-lengths lower than ~ 4 km it is possible to switch off the parametrisation for convection, allowing the processes to occur explicitly (e.g. Tang *et al*., 2013). Numerical models in

which convective parametrisations are turned off to allow the unstable growth of convective clouds are referred to as convection-permitting models (CPMs; Clark *et al*., 2016).

Although CPMs are often referred to as cloud-resolving models (CRMs), there is uncertainty in the precise distinction between models that allow for explicit convective processes (CPMs) and those that can *resolve* the convective processes (CRMs). Depending on the spatial scales of convection and degree of organisation, a number of grid points will be required to resolve the basic structure of a convective cloud feature in a CPM. More generally in CPMs, a 3-D convective process may require at least 5-8 grid points in each direction to be considered resolved. This can be considered synonymous with the 'effective' model resolution described by Skamarock (2004), which was shown to be modified by sub-grid mixing and diffusion processes. It is not clear for which grid-length simulated convective processes can be considered well resolved. A grid-length of 1 km may be sufficient to resolve the general structure a deep convective cloud with width and height scales of 10 km, while a 4-km grid-length may only be sufficient to resolve some features of large-scale, organised convection (such as squall lines; Weisman *et al*., 1997; Weisman *et al*., 2008). Lean *et al*. (2008) found that explicit clouds simulated in the MetUM using a 4-km grid-length were "seriously" under-resolved compared to those using a 1-km grid-length. CPMs that forecast with grid-lengths that can only resolve some scales of convective processes are often referred to as performing simulations in the "grey zone" of convection; a significant challenge for current CPMs. It seems intuitive to assume that forecasts of convection improve as the model grid-length is decreased, as more scales of convective motion are resolved. However, researchers have widely reported a high degree of sensitivity of simulated convection to changes in grid-length, ranging from scales of 4 km down to 100 m (Weisman *et al*., 1997; Petch and Gray, 2001; Petch *et al*., 2002; Adlerman and Droegemeier, 2002; Stein *et al*., 2015). As demonstrated by Hanley *et al*. (2015), the characteristics of explicit convection using grid-lengths below 1 km remain highly sensitive

to the configuration of parametrisations used to approximate the effects of sub-grid turbulent mixing.

1.3.2 Turbulence in CPMs

As summarised by Bryan *et al.* (2003), the current computing power available to CPMs is not sufficient to simulate all scales of motion governed by the Navier-Stokes equation (1.1). To resolve all scales of motion down to the dissipative length scale of turbulent eddies (~ 1 mm) would require grid-lengths close to 0.1 mm. As a result, spatial filtering is applied to (1.1) (Lilly, 1967) such that physical processes occurring below those which can be resolved by the model are not included in the solution. This introduces a distinction between processes that are resolved by the model grid and those that occur below resolved scales, which require a form of parametrisation.

Terms in the filtered Navier-Stokes equation governing the effects of turbulence are often parametrised using the Smagorinsky-Lille sub-grid mixing scheme (Smagorinsky, 1963; Lilly, 1967) (See Section 2.3.2). Schemes such as this are required to approximate the effects of sub-grid mixing processes on the resolved components of the flow. Therefore, 'sub-filter' is more appropriate than 'sub-grid' when referring to such schemes, though 'sub-grid' remains widely used to imply 'sub-filter'. As noted by Bryan *et al*. (2003) and Mason and Brown (1999), the Smagorinsky-Lille scheme is employed by most conventional large-eddy simulation (LES) models (as well as in the MetUM). LES aims to resolve the large-scale, energy-containing eddies (hence large-eddy simulation) while parametrising the downscale transfer of TKE to sub-grid scales. Correct implementation of a sub-grid turbulence parametrisation for LES therefore requires that the grid-length is much larger than the dissipative length scales of eddies but is considerably smaller than the scale of energy-containing eddies, i.e. the grid-length is well within the inertial sub-range.

Sub-grid turbulence schemes from LES are often adopted for use in CPMs. For example, the Smagorinsky-Lilly scheme is used in the operational UKV model and in higher-resolution MetUM models used for research purposes. However, to be consistent with the assumptions required for their use in LES, CPMs must forecast with grid-lengths that are well within the inertial sub-range. As noted in Section 1.1.3, the largest scale of the inertial sub-range Λ_0, is not clearly defined in deep clouds. Observed values can range from 0.4 – 4 km and vary throughout individual clouds. Most operational forecast models use grid-lengths larger than 1 km so it is unlikely that the inertial sub-range requirement is met for such models (as highlighted by Klemp and Wilhelmson (1978)). In CPM simulations of deep convective clouds, the mere existence of an inertial sub-range is not always demonstrated. In simulations of supercell thunderstorms using grid-lengths as low as 250 m, Droegemeier *et al*. (1994, 1997) found no clear evidence of an inertial sub-range, suggesting that even higher resolutions need to be investigated. Bryan *et al*. (2003) demonstrated that 250-m and 125 m grid-length models resolve an inertial sub-range but conclude that CPMs used to simulate deep convection require grid-lengths of 100 m or smaller to satisfy the assumptions of turbulence schemes taken from LES models.

Smagorinsky-type sub-grid turbulence schemes are characterised by a length scale λ_0, referred to as the 'mixing length', which controls the degree of turbulent mixing. For a given model, this length scale can be prescribed by changing the mixing length constant C_s – the ratio of the mixing length and the model grid-length (see Section 2.3.2). The value for C_s is selected to change λ_0 (and therefore the eddy viscosity – see (2.14)) so that the effects of sub-grid mixing occur close to the grid-scale. A C_s of 0.2 (Lilly, 1967) is widely used as a suitable value for this; Mason (1994) concluded that simulated eddies were well resolved when using a C_s of 0.2. However, Canuto and Cheng (1997) have shown the value of C_s is a function of physical processes that differ depending on the characteristics of the flow, suggesting that C_s should be treated as a dynamical variable. Mason and Brown (1999)

conclude that the value of C_s (and therefore λ_0) is more important than the grid-length in determining the scales that are resolved by the model.

Given the uncertainty associated with the correct implementation and suitability of using LES-based sub-grid schemes in CPMs, combined with the impact they have on the resolved scales of the model, it is perhaps unsurprising that the characteristics of convection in CPMs are found to be highly sensitive to the configuration of sub-grid turbulence schemes. Verrelle *et al*. (2014) applied 1-D (vertical) and 3-D configurations of a mixing-length-based, TKE closure scheme to a simulation of a deep convective cell. The 3-D configuration provided more mixing than the 1-D scheme, enhancing microphysical processes and leading to larger amounts of precipitation. Using the Smagorinsky-Lilly scheme in LES, Mason and Callen (1986) demonstrated that, when the grid-length is held constant, larger values of C_s provided smooth flow features while using smaller values of C_s resulted in simulations with noise at the grid-scale. Similar results were produced by Takemi and Rotunno (2003) in a 1-km grid-length CPM simulation of a squall line. They found overly smoothed cloud features when C_s was large and grid-scale noise when C_s was small, concluding that a value of $C_s = 0.25 - 0.3$ was suitable for their simulation.

Hanley *et al*. (2015) tested the sensitivity of convective clouds simulated in 1500-m, 500-m and 200-m grid-length configurations of the MetUM to λ_0. They found that as λ_0 is decreased, the number of small clouds with intense precipitation increased and convective initiation occurred earlier in each model. By changing the mixing length in the 200-m model, it was possible to produce similar cloud features to those in the 500-m model. This appears to reflect the effects of sub-grid turbulence schemes on model resolution noted earlier in this section. Further to this, Hanley *et al*. noted that when changes to the mixing length were made consistently across each model, some models were improved and others were worsened. For example, reducing the mixing length improved the timing of convective initiation in the UKV, but worsened the timing (relative to observations) in the 200-m model.

This suggested that there is no single value of C_s that provided the most accurate simulation for each model.

Stein *et al*. (2015) used cloud characteristics observed with the Chilbolton Advanced Meteorological Radar (CAMRa) (see Section 2.1) to evaluate the morphology and evolution of convective clouds simulated in MetUM. This study used the modelling suites from Hanley *et al*. (2015) to run simulations using grid-lengths of 1500 m, 500 m, 200 m and 100 m for the same case studies. They concluded that the 200-m model using $\lambda_0 = 40$ m (C_s of 0.2) provided simulations that were most consistent with observations. The 100-m model produced convective clouds and updrafts that were too short-lived and narrow compared with observations. They found that shallower clouds were better represented using smaller values of λ_0, whereas deeper clouds were better represented when λ_0 values were large. This suggests that no fixed value of λ_0 is suitable to accurately represent all scales of convective clouds in a simulation, providing further evidence that λ_0 (or C_s) should be treated as a dynamical variable.

1.3.3 Summary and discussion

This section has outlined the current limitations of CPMs and the ongoing requirement to parametrise the effects of sub-grid turbulent mixing. In LES, these parametrisations conventionally take the form of mixing-length-based TKE closure schemes – such as the Smagorinsky-Lilly scheme – which have been widely implemented into high-resolution CPMs. It is not often clear that the assumptions implicit in these schemes are valid for CPMs, especially for grid-lengths larger than 100 m, indicating the need for evaluation.

Previous studies have focused on identifying the sensitivity of simulated convection (e.g. cloud size, precipitation) to the sub-grid turbulence scheme configuration. Although such investigations are very useful to quantify the (varied) sensitivity of simulated convection and to identify the tuning necessary to improve a forecast, they can only provide limited insight

into the validity and overall suitability of the chosen turbulence scheme. Of primary importance is to demonstrate that a turbulence scheme is able to perform consistently with its design when adopted for use in a CPM. To accomplish this, turbulence diagnostics in clouds simulated in CPMs should be directly evaluated using observations of turbulence in real clouds – an investigation which has yet to be presented.

The following section (1.4) details methods to estimate the eddy dissipation rate ε, in convective clouds using a high-resolution Doppler weather radar capable of sampling within the inertial sub-range. Section 2.3.2 outlines the necessary steps to determine ε from the Smagorinsky-Lilly scheme used in the MetUM. Detailed comparisons of ε between model simulations and observations of mutual case studies (presented in Chapter 5) can be used to determine whether the scheme is dissipating realistic amounts of TKE, while providing insight into whether the resolved scales of the model are within the inertial sub-range; as assumed by the scheme.

1.4 Turbulence retrieval with radar

1.4.1 Velocity measurements with Doppler radar

When sampling a meteorological target (i.e. a hydrometeor) with a Doppler radar, comparison of the phase θ (in radians), of the returned signal from a pair of transmitted electromagnetic pulses (pulse-pair processing) can provide information about the component of the target's velocity that is parallel to the radar beam axis (in the radial direction).

If a stationary target exists at a distance r, from the radar, transmitted pulses of wavelength, λ will travel a two-way distance ($2r$) comprised of $2r/\lambda$ wavelengths. Since one wavelength is equivalent to 2π radians, the phase delay of the returned pulse (in radians) D, can be given by:

$$D = \left(\frac{2r}{\lambda}\right) 2\pi \tag{1.14}$$

If the phase of the transmitted pulse is given by θ_0, and the phase of the received pulse by θ_1:

$$\theta_1 = \theta_0 + D \tag{1.15}$$

This states that the transmitted and returned pulses are in phase if D is a multiple of 2π. When sampling a stationary target, the transmitted and received pulses remain in phase as they travel the same number of complete wavelengths. This is demonstrated by differentiating (1.15) with respect to time, t:

$$\frac{d\theta}{dt} = \frac{4\pi}{\lambda}\frac{dr}{dt} \tag{1.16}$$

Equation (1.16) states that there is no change in the phase of the transmitted and returned pulses if the radial velocity of the target (given by $\frac{dr}{dt}$) is zero. If the target is moving with a component of velocity either towards or away from the radar, a phase shift will be detected. Pulse-pair processing involves comparing the phase of the returned signal from two transmitted pulses separated by a very small time difference (one divided by the pulse-repetition frequency (PRF)). From this, the target (Doppler) velocity v, can be found from re-arranging (1.16):

$$v = \frac{\lambda}{4\pi}\frac{d\theta}{dt} \tag{1.17}$$

If only a single meteorological target is present within a radar resolution volume (the volume of atmosphere sampled by a single pulse, V_6), v can be measured from a single pair of pulses. When observing clouds and precipitation however, there are many targets within V_6, with different backscatter cross sections, and individual velocities that are variable in space and time. In these circumstances, the mean Doppler velocity $\bar{v}$, is estimated as the mean of v returned from many successive pairs of radar pulses. In this sense, $\bar{v}$ represents a weighted average of point velocities within V_6.

When scanning through clouds with Doppler radar, fields of $\bar{v}$ provide information regarding the features of the flow on scales larger than V_6. Details of velocity scales within V_6 are not directly measurable but characteristics can be estimated by examining the variability of v over many pulse-pairs. Doppler radars often use 32 or 64 pulse-pairs at a prescribed PRF to sample a V_6. The time duration over which V_6 is sampled can be calculated as the number of pulses divided by the PRF, commonly referred to as the *dwell time*. The variability in v throughout the dwell time reflects the variability of target velocities within V_6. This is quantified in the variance of the Doppler velocity spectrum σ_v^2 ($\mathrm{m^2\ s^{-2}}$). For the observations with CAMRa used in this thesis, σ_v^2 is estimated by measuring the rate of decorrelation of v in 32 adjacent pairs of pulses throughout the dwell time; this is explained in more detail in Section 2.1.2. The contribution to σ_v^2 from turbulence has been shown to be independent of the sampling direction when viewed by radar in the horizontal plane (Lee and Thomas, 1989; Nastrom *et al*., 2004). This is important to note for scanning radar such as CAMRa which collects observations from a range of azimuths.

1.4.2 Turbulence from Doppler velocity variance

The presence of turbulence on spatial scales within V_6 will cause fluctuations in the velocity of meteorological targets that contribute to σ_v^2. If the spatial scales of V_6 are smaller than the largest scale of the inertial sub-range Λ_0, then σ_v^2 will include velocity variance from isotropic turbulence with a known energy spectrum (1.11). Under the assumptions of Kolmogorov (1941), this range of turbulence scales are characterised by a constant downscale transfer of TKE – the eddy dissipation rate, ε.

Similar theoretical approaches to infer ε from σ_v^2 using the same key assumptions are presented by Frisch and Clifford (1974) and Labitt (1981). They derive the same relationships between ε and σ_v^2 but differ slightly on the simplification of the final expression. This application follows the derivation of Frisch and Clifford (1974) to the point

where full expressions relating ε to σ_v^2 are presented ((1.24a) and (1.24b)). The simplification of these is instead performed based on the specifications of CAMRa, to determine the final expression used in this thesis (1.25).

They begin with an expression for the spatial spectrum of velocities sampled by V_6, $\Phi_{\overline{V}}$, taken from Srivastava and Atlas (1974):

$$\Phi_{\overline{V}}(\mathbf{k}) = (2\pi)^6 \, \Phi_V(\mathbf{k}) \, |F_P(\mathbf{k})|^2 \tag{1.18}$$

Where $\Phi_V(\mathbf{k})$ is the spectral density (in terms of spatial wavenumber, $\mathbf{k}$) of point-velocities within V_6, and $F_P(\mathbf{k})$ represents the Fourier transform of the 3-D beam pattern, P. In (1.18), reflectivity is assumed to be constant across V_6 so that $\Phi_{\overline{V}}$ is determined purely by the weighting of P on the spatial spectrum of point-velocities. Following these conventions, σ_v^2 is then described as the difference between the variance of point-velocities that exist within V_6 (σ_V^2), and the variance of these velocities once weighted by the beam pattern ($\sigma_{\overline{V}}^2$):

$$\sigma_v^2 = \sigma_V^2 - \sigma_{\overline{V}}^2 \tag{1.19}$$

If the beam is suitably narrow, $\Phi_V(\mathbf{k})$ is assumed to be approximately equal to the spatial spectrum of *radial* (Doppler) point-velocities within V_6, $\Phi_v(\mathbf{k})$. This assumption is especially appropriate for CAMRa given the extremely narrow one-way half-power beam width of 0.28° (see Section 2.1.1). Expressed in spectral terms, (1.19) is given as:

$$\sigma_v^2 = \int \Phi_v(\mathbf{k})(1 - (2\pi)^6 \, |F_P(\mathbf{k})|^2) \, d^3\mathbf{k} \tag{1.20}$$

where $d^3\mathbf{k}$ represents an integral with respect to $\mathbf{k}$ over the volume of V_6.

The beam profile (including that of CAMRa) is assumed to be well approximated by a 3-D Gaussian distribution (Doviak and Zrnic, 1984). Frisch and Clifford (1974) apply the following 3-D Gaussian beam pattern:

$$P(x,y,z) = \frac{\exp\left\{-\left[\frac{y^2+z^2}{2\alpha^2} + \frac{x^2}{2\beta^2}\right]\right\}}{(2\pi)^{\frac{3}{2}}\beta\alpha^2} \tag{1.21}$$

Where x, y and z are directions parallel to, horizontally across, and vertically across the beam axis, respectively, and α and β refer to the standard deviation of the transverse and radial beam profile, respectively. The beam weighting function $|F_P(\mathbf{k})|^2$, is then derived from (1.21) as:

$$|F_P(\mathbf{k})|^2 = (2\pi)^{-6}\exp\{-[(k^2 - k_x^2)\alpha^2 + k_x^2\beta^2]\} \tag{1.22}$$

Where k is the 3-D wavenumber with subscripts referring to directional wavenumbers.

Under the assumption the velocity fluctuations within V_6 are due solely to isotropic, inertial sub-range turbulence, and turbulence is homogeneous, $\Phi_v(\mathbf{k})$ is stated as (Panchev, 1971):

$$\Phi_v(\mathbf{k}) = \frac{E(k)}{4\pi k^2}\left(\frac{k_x^2}{k^2} - 1\right) \tag{1.23}$$

Where $E(k)$ is the energy spectrum of inertial sub-range turbulence (1.13) derived in Section 1.1.3. By substituting (1.23) and (1.22) into (1.20), performing the integral, converting from a Cartesian to a polar co-ordinate system and re-arranging for ε:

$$\varepsilon = \frac{1}{\alpha}\left[\frac{\sigma_v^2}{1.35A\left(1 - \frac{\gamma^2}{15} - \frac{\gamma^4}{105}\right)}\right]^{\frac{3}{2}} \quad ; \quad \text{where} \quad \gamma^2 = 1 - \left(\frac{\beta}{\alpha}\right)^2 \tag{1.24a}$$

And:

$$\varepsilon = \frac{1}{\beta}\left[\frac{\sigma_v^2}{1.35A\left(1 + \frac{\xi^2}{15} + \frac{\xi^4}{105}\right)}\right]^{\frac{3}{2}} \quad ; \quad \text{where} \quad \xi^2 = 1 - \left(\frac{\alpha}{\beta}\right)^2 \tag{1.24b}$$

Where (1.24a) applies only when $\alpha > \beta$, and (1.24b) only when $\alpha < \beta$. The constant A is the universal constant of isotropic turbulence stated in Frisch and Clifford (1974) as 0.47, however, a more recent and widely-used value of 1.6 is selected from Gossard and Strauch (1983).

For a radar with the specifications of CAMRa (Section 2.1.1), $\alpha > \beta$ at distances further than 17.9 km from the radar. Given that the cloud observations used for turbulence retrieval in this thesis were almost always collected between 30 and 150 km from the radar (see Section 2.2.4), only (1.24a) is required. As an additional simplification, $\frac{\gamma^4}{105}$ remains less than 15% of $\frac{\gamma^2}{15}$ between 30 and 150 km range, so $\frac{\gamma^4}{105}$ is omitted from (1.24a). For conditions typically observed (a Doppler variance of $\sigma_v^2 = 4\ \mathrm{m^2\ s^{-2}}$ observed at 60 km range), the omission of the γ^4 term in (1.24a) results in ~ 1% difference in ε, suggesting the effect on the retrieval is negligible.

Although the high resolution of CAMRa means that variance from inertial sub-range turbulence will be included in σ_v^2 (see Section 2.1.2), this is not the only process that can contribute to Doppler variance. Values of σ_v^2 can have contributions from radial wind shear (Atlas *et al*., 1969; Battan and Theiss, 1973), the distribution of target fall-velocities (Atlas *et al*., 1973), antenna rotation (Doviak and Zrnic, 1984), hydrometeor oscillations (Oguchi 1983; Zrnic and Doviak, 1989), beam broadening (Nathanson, 1969) and the effects of hydrometeor rotation (Meyer and Jank, 1989), break-up and coalescence. A thorough investigation into the removal of variance contributions to σ_v^2 from these mechanisms is presented and applied to CAMRa in Chapter 3. By assuming each contribution to σ_v^2 is statistically independent (Doviak and Zrnic, 1984), σ_v^2 is described as a sum of each variance contribution (3.1) so that variances from mechanisms aside from turbulence can be subtracted from σ_v^2, leaving the turbulent contribution σ_t^2, to be converted to ε using:

$$\varepsilon = \frac{1}{\alpha}\left[\frac{\sigma_t^2}{1.35A\left(1-\frac{\gamma^2}{15}\right)}\right]^{\frac{3}{2}} \quad ; \quad \text{where} \quad \gamma^2 = 1-\left(\frac{\beta}{\alpha}\right)^2 \tag{1.25}$$

In summary, the variance of the Doppler velocity spectrum due to turbulence can be related to the dissipation rate of turbulent kinetic energy using the theoretical approach described in this section. However, this approach is applicable only under a set of assumptions (summarised by Labitt, 1981). The key assumptions are now listed and discussed in the context of CAMRa. These include that:

1) Reflectivity is uniform throughout V_6.
2) Turbulence is homogeneous within V_6.
3) The largest scale of V_6 is smaller than Λ_0.
4) The effect of turbulence is reflected in the motions of hydrometeors within V_6.

Assumptions (1), (2) and (3) become increasingly likely when V_6 is small and so are considered especially safe assumptions for a radar with such a narrow beam as CAMRa. As highlighted in Labitt (1981), the horizontal motions of hydrometeors are expected to reflect the effects of turbulence more so than the vertical motions. By scanning with CAMRa at low elevation angles (less than 15°; see Section 2.2.1), horizontal velocity fluctuations will dominate the radial velocity spectrum, so assumption (4) is considered to be suitable for this application.

1.4.3 Benefits and evaluation of the Doppler variance method

Observations of turbulence in the atmospheric boundary layer can be collected using a variety of in situ or remote measurements aside from Doppler radar. Turbulence probes can be attached to aircraft to analyse the fluctuations in wind along the flight vector (e.g. MacCready, 1962; Grandia and Marwitz, 1975; Sand, 1976; Meischner *et al*., 2001). Similar measurements can be collected by turbulence probes attached to a radiosonde in atmospheric

ascent experiments (e.g. Harrison and Hogan, 2006; Martini *et al.*, 2017). Fluctuations in refractive index caused by turbulence can be measured using scintillometers (e.g. Chonacky and Deuel, 1988).

In situ methods using aircraft and radiosonde ascents are of particular benefit when collecting simultaneous observations of many small-scale microphysical and thermodynamic processes alongside turbulence. However, such methods can only collect time-series observations from single points in space. To estimate ε using these methods, the distance over which the fluctuating wind is measured (often referred to as the *analysis length*) must be smaller than Λ_0, limiting the spatial extent of data collection. In contrast to in situ methods, Doppler radar is used to estimate ε from velocity variance on spatial scales within V_6. As long as the largest dimension of V_6 is less than Λ_0, ε can be retrieved from any V_6 with a reliable value of σ_v^2 (i.e. suitably high signal-to-noise ratio). This means that scanning with Doppler radar can retrieve turbulence across large swathes of atmosphere over short timescales. Simultaneous measurements of microphysical and thermodynamic processes are, however, not practically attainable with Doppler radar without the use of other instruments. Therefore, in isolation, the Doppler variance method is not currently suited to the investigation of turbulence in relation to cloud processes on very small scales (e.g. microphysics and entrainment) but is of particular benefit to studies (such as this thesis) aiming to investigate turbulence in the context of larger scale cloud processes (e.g. cloud dimensions and updraft characteristics) for model evaluation.

The approach to retrieving ε with Doppler radar requires numerous assumptions regarding the properties of turbulence, the motions of scatterers and the relationship between V_6 and the range of length scales associated with the isotropic inertial sub-range. Further to this, details of turbulent motion are not measured directly; the accuracy by which turbulent velocity variance (and therefore ε) is inferred from the Doppler spectrum depends on the accurate removal of variance from all other contributors. Given the potential limitations to

accuracy, validation of ε from the Doppler variance method has previously been required through direct comparison with other methods.

Comparison of ε from Doppler radar with in situ measurements is particularly difficult. For example, simultaneous measurements of ε by aircraft and Doppler radar cannot be made without returning a very strong echo from the aircraft in the sampled V_6. Even so, such verification experiments have been attempted by Labitt (1981) and Meischner *et al.* (2001). Labitt (1981) made measurements of ε in a severe storm with a ground-based S-band Doppler radar using the Doppler variance approach and co-ordinated these with aircraft measurements. By scanning across the flight path and ignoring data where the aircraft was sampled in V_6, they found strong agreement between radar and aircraft ε indicated by a correlation coefficient of 0.81. Meischner *et al.* (2001) performed a more accurate comparison of ε estimated with C-band Doppler radar and aircraft measurements in thunderstorm anvils. There were time differences of up to 5 minutes between aircraft and radar measurements of particular cloud regions. By assuming that the characteristics of the cloud did not change during these time intervals, but were simply advected by the mean flow, the location of the aircraft measurements were moved to the location predicted by the mean horizontal velocity measured in the time between radar and aircraft measurements. Although they identified significant differences in ε between aircraft and radar over small distances, this was attributed to the uncertainty of simply advecting aircraft measurements. They found values of ε sampled by radar broadly agreed with those measured by aircraft, albeit with a general over-estimation of ε (and Doppler variance) using the radar method; median values were larger by a factor of 1 – 4 when observed with radar. However, this study employed a radar with a 1° one-way half-power beam-width and involved cloud observations out to typical distances of 80 km. The largest dimension of V_6 at 80 km range is 1400 m and no estimation of Λ_0 is presented for comparison. Although steps have been taken to filter out variance from shear on scales outside V_6, it appears at least possible that

the over-estimation of ε results from the inclusion of variance in V_6 from turbulent eddies on scales outside the inertial sub-range.

Values of ε retrieved under the Doppler variance method have also been tested against other Doppler radar techniques, namely, the spatial spectra method. This method entails taking the Fourier transform of a dataset of Doppler velocity measurements sampled along a single ray. If this dataset of V_6 comprises an analysis length that is within the inertial sub-range, the Fourier transform can be approximated by the $k^{-\frac{5}{3}}$ spectrum using the Kolmogorov assumption, and ε can be estimated. The spatial spectra method is synonymous with in situ measurements in that it involves analysing the spectrum of velocity fluctuations in one dimension along a fixed distance. However, Doppler velocity observations along a ray are collected near-instantaneously. The benefit of this, as highlighted by Brewster and Zrnic (1986), is that the assumption of Taylor's frozen turbulence (that turbulence is advected only by the mean flow) necessary for in situ measurements, is not required.

Brewster and Zrnic (1986) compared estimates of ε in a severe thunderstorm from the spatial spectra and Doppler variance methods. Based on the 10-km scale of the main updraft they initially estimated Λ_0 to be about 5 km. The spatial spectra method was applied to 32 Doppler velocities collected along a ray, separated by 150 m, constituting an analysis length of 4.8 km. They found good agreement with the $k^{-\frac{5}{3}}$ spectrum close to the radar, concluding that the estimates of ε were reliable. Values of ε were found to be largely consistent between the two methods. Median values of ε estimated from Doppler variance were approximately 10% larger than those estimated from spatial spectra which was attributed to small variance contributors to σ_v^2 that were neglected; such as beam broadening and hydrometeor oscillations (see Section 3.2). The difference in ε between the two methods increased with range from the radar. This was attributed to the filtering of mean Doppler velocities by V_6; which has dimensions that increase with range. They conclude, given that the filtering by V_6 (i.e. the weighting of the beam pattern) is implicit in the Doppler variance approach, that it

is increasingly better to use ε from Doppler variance the further from the radar observations are collected. Bouniol *et al.* (2003) performed a similar evaluation of the Doppler variance method using the spatial spectra method with a vertically-pointing 95 GHz Doppler cloud radar. The spectrum found by applying a Fourier transform to a sample of 30 Doppler velocities along a ray was again well approximated by the $k^{-\frac{5}{3}}$ spectrum, giving credibility to retrieved ε. Point-for-point comparison with ε from Doppler variance showed a high level of agreement, especially for larger values. They conclude that the Doppler variance provides a reliable estimate of ε.

No such validation methods have been applied directly to retrievals of ε with CAMRa as part of this thesis (although the sensitivity of retrievals is tested – see Section 3.5.1). However, the Doppler variance method is widely used, and has been shown to give very reliable estimates of ε when compared with in situ and spatial spectra methods, as discussed in this section. Of key importance is that the assumptions made in the theoretical approach apply well to CAMRa; which was discussed at the end of Section 1.4.2. The suitability of CAMRa to retrieve ε is examined in more detail in relation to the dataset of radar observations used in this thesis in Section 2.1.2.

1.5 Characteristics of ε in clouds

1.5.1 Wider context for ε values

Conventions for the severity of atmospheric turbulence are desired to establish context for the discussion of ε retrieved in observed clouds for this thesis. Generally, and particularly in aviation, turbulence is classified into three categories: “light”, “moderate” and “severe”. However, these are often defined from fluctuations in aircraft velocity resulting from flight through turbulent air (e.g. Federal Aviation Administration, 2012). The classification of turbulent intensity by this method is subjective in that these fluctuations are dependent on

the characteristics of the aircraft. The severity of turbulence expressed purely in terms of ε is not clearly defined in the literature. To address this, Sharman *et al.*, (2014) collected over 137 million values of ε sampled at cruising altitude by ~ 200 commercial aircraft and analysed these together with the subjective reports of turbulent intensity. They established that ε corresponding to light, moderate and severe turbulence had median values of 10^{-6}, 10^{-2} and 10^{-1} m^2 s^{-3}, respectively. These classifications were made predominantly from clear-air measurements of ε, however, they are adopted for this thesis to provide context for the severity of ε values in convective clouds. By loosely applying this classification to clouds observed with CAMRa, values of ε are considered to represent weak turbulence when $\varepsilon < 10^{-2}$ m^2 s^{-3} and strong turbulence when $\varepsilon > 10^{-1}$ m^2 s^{-3}.

1.5.2 Values of ε in clouds

Values of ε can vary by many orders of magnitude in different cloud types, but also within individual clouds. For example, Bouniol *et al.* (2003) used a 94 GHz cloud radar to retrieve values ranging from $10^{-8} - 10^{-4}$ m^2 s^{-3} in cirrus clouds and $10^{-4} - 10^{-2}$ m^2 s^{-3} in stratocumulus clouds. Kollias *et al.*, (2001) measured, again with a 94 GHz cloud radar, values of $10^{-3} - 10^{-2}$ m^2 s^{-3} in fair weather cumulus clouds. Values of ε in cumulonimbus clouds were found to range from as low as 10^{-6} m^2 s^{-3} (aircraft measurements) to 0.05 m^2 s^{-3} (Doppler radar measurements) in anvil regions by Meischner *et al.* (2001). Sand (1976) found values of ε to vary from $0.006 - 0.4$ m^2 s^{-3} in hailstorms observed by aircraft. Using Doppler radar, Frisch and Strauch (1976) found ε values to range from $0.003 - 0.06$ m^2 s^{-3} in a Colorado thunderstorm (revised using an updated $A = 1.6$ instead of $A = 0.53$), Knupp and Cotton (1982) found values as large as 0.15 m^2 s^{-3} in a quasi-steady mountain thunderstorm, and Istok and Doviak (1986) found values as large as 3 m^2 s^{-3} in an Oklahoma supercell. In this particular supercell storm, 50% of ε values exceeded 0.1 m^2 s^{-3}, indicating that strong turbulence was widely distributed.

The lowest values of ε that can be sampled in clouds depends on the sensitivity of the instrumentation. This is highlighted in particular by Meischner *et al.* (2001) who compared aircraft and radar measurements of ε in individual storm anvils. Values of ε estimated by aircraft were as low as 10^{-6} m^2 s^{-3}, while co-ordinated radar estimates fell no lower that $\sim 10^{-3}$ m^2 s^{-3}, leading to the conclusion that Doppler weather radar is suitable for estimating ε above a threshold value. For CAMRa (see Section 2.1.2), the lowest ε that can be sampled at the typical 60-km range of observations is also $\sim 10^{-3}$ m^2 s^{-3}. The similarity in this value with Meischner *et al.* (2001) appears to be that 32 pulse-pairs were used in both cases to sample each V_6. In Section 6.2.3, the sensitivity of CAMRa to small values of ε is shown to improve by increasing the number of pulse-pairs. Chapman and Browning (2001) used CAMRa to retrieve values of ε closer to 10^{-4} m^2 s^{-3} by sampling with 128 pulse-pairs.

1.5.3 Features of ε in relation to cloud characteristics

Mature cumulonimbus clouds can reach heights that can exceed typical cruising altitudes of commercial flight aircraft (~ 12 km). Owing to the danger posed to aviation by severe turbulence, deep convective clouds have provided the focus for many previous turbulence retrieval studies. These often take the form of detailed examinations of the turbulent properties of individual clouds in relation to broad cloud characteristics. In this thesis, the retrieval of ε is performed in precipitating convective clouds over the south of England to assess statistics of ε for model evaluation. Although this focus differs from the majority of previous applications, it is the relationships between ε and the characteristics of deep convective clouds that are appropriate for discussion in this section.

The production of TKE in convective clouds is primarily from the shear and buoyancy associated with vertical motion. It could therefore be expected that the largest values of ε in the cloud are located within updrafts. For individual cloud cases, the largest values of ε have

been identified within the region of the main updraft (Sand, 1976; Istok and Doviak, 1986; Kollias *et al.*, 2001; Meischner *et al.*, 2001) and around the edges of updrafts (Grandia and Marwitz, 1975). Strong turbulence was also indicated by high Doppler variance around the periphery of updrafts by Donaldson and Wexler (1969). The highest values of ε have also been found between the main updraft and downdraft (Frisch and Strauch, 1976; Knupp and Cotton, 1982). Both Knupp and Cotton (1982) and Istok and Doviak (1986) note that strong turbulence exists immediately downstream of the main updraft. Measurements of ε using aircraft in flights directly through updrafts have shown that only weak turbulence can exist in close proximity to vertical velocity maxima (Grandia and Marwitz, 1975). It is clear from these independent studies that the strongest turbulence in convective clouds is often associated with updrafts. However, the specific location of ε maxima can vary from within and around the edges of updrafts to regions immediately downstream of the updraft core.

Study	**Maxima in updraft velocity ($\mathbf{m\ s^{-1}}$)**	**Maxima in ε ($\mathbf{m^2\ s^{-3}}$)**
Istok and Doviak (1986)	50	3
Knupp and Cotton (1982)	25	0.15
Meischner *et al.* (2001)	17	0.1
Sand (1976)	14	0.3
Frisch and Strauch (1976)	12	0.06
Grandia and Marwitz (1975)	7	0.006
Kollias *et al.* (2001)	6	0.004

Table 1.1: Comparison of maxima in ε and updraft velocity for a selection of independent studies. Values of ε from Grandia and Marwitz (1975) and Sand (1976) have been converted to $m^2\ s^{-3}$ units and the value from Frisch and Strauch (1976) has been revised using an updated value for universal constant of isotropic turbulence A, of 1.6 instead of 0.53.

As suggested by (1.7), the TKE in a cloud increases through the buoyancy term when the vertical velocity is positive. Values of ε could therefore be expected to increase with updraft strength. For the studies discussed so far in this section that report ε values in updrafts, Table 1.1 lists the maxima in ε together with the maximum updraft velocity. Values of ε from Sand (1976) and Grandia and Marwitz (1975) have been converted to $m^2\ s^{-3}$. Aside from Sand (1976), Table 1.1 shows a consistent increase in reported ε maxima with updraft strength. However, this appears to be nonlinear; an approximate factor-of-10 increase in updraft velocity corresponds to an increase in ε by ~ 10^3.

Further suggested by (1.7) is the production of TKE from gradients in velocity. The largest value of ε found by Frisch and Strauch (1976) was located in a region of strong horizontal shear in the vertical velocity (0.03 s^{-1}). Istok and Doviak (1986) note large velocity gradients towards the upper levels of the cloud which are spatially correlated with large ε, with lower values of ε found where shear is weaker. Knupp and Cotton (1982) attributed the lower values of ε found later in the storm life-cycle to reduced shear in the magnitude of horizontal and vertical shear in the Doppler velocity. A loose association between ε and the magnitude of the vertical shear of the Doppler velocity was also identified by Donaldson and Wexler (1969).

There are consistent indications in these individual cloud case studies that the intensity of turbulence is not distributed linearly in the vertical. In measurements with aircraft, the intensity of turbulence at the base of clouds has been shown to be weak (Sand, 1976), while turbulence has been shown to increase with height from the cloud base to the level of free convection by Grandia and Marwitz (1975). They suggested that this resulted from the interaction between the updraft and entrained environmental air, noting that turbulence decreased again above the level of free convection. With Doppler radar, Knupp and Cotton (1982) found weak turbulence in the lower levels of the updraft which increased with height. Donaldson and Wexler (1969) found an increase in values of Doppler variance within the

cloud, implying a vertical gradient in turbulent intensity. Larger values of ε have also been identified in the upper regions of the cloud by Frisch and Strauch (1976). Istok and Doviak (1986) found that the spatial coverage of large ε also increases with height in the cloud.

The advection of turbulence throughout the cloud has been speculated to affect its spatial distribution by Istok and Doviak (1986). They noticed that regions of strong shear over small scales (less than 3 km) were not always accompanied by high ε. This was also observed in some cases by Knupp and Cotton (1982). Istok and Doviak (1986) speculated that some turbulent eddies produced by shear will not yet have attained the scales within V_6 that contribute to ε, i.e. the Richardson cascade has not fully developed. In other cases, regions of high dissipation could be advected away from the region where turbulence was produced. This could serve to explain why the location immediately downstream of updrafts has been reported to include strong turbulence; turbulent eddies generated by the updraft are advected downwind before reaching dissipation length scales.

1.5.4 Summary and discussion

In summary, measurements of turbulence in convective clouds by aircraft and Doppler radar have revealed that ε can vary by many orders of magnitude in individual clouds. Turbulence is strongly associated with regions of shear and buoyancy, as expected from (1.7). The strongest turbulence is often found within close proximity of updrafts and appears to scale in intensity with the updraft strength (Table 1.1). There is a consistent trend across many of these studies that the intensity of turbulence increases with height in the cloud. The precise location of high ε does not always correspond spatially with production mechanisms owing to the combination of cascade timescales and eddy advection.

Broad, qualitative relationships between ε and cloud characteristics have been identified in individual case studies in the literature. The degree to which these findings can be compared and analysed together is substantially limited by the diversity of instruments, radar

specifications and methods used to estimate ε in clouds. The current state of research is therefore not sufficient to provide the quantitative relationships between ε and cloud characteristics required to reliably evaluate the use of turbulence parametrisations in CPMs. New research is required to derive quantified relationships (through statistical assessment) between ε and observed cloud characteristics such as shear, updraft strength, updraft size, cloud region and cloud depth. A reliable statistical analysis will require measurements of ε to be performed consistently across many cloud cases. As discussed in Section 1.4, scanning Doppler weather radar is well suited to this application. If it can be demonstrated that the assumptions required for accurate turbulence retrieval are valid given the radar specifications, such instruments can be used to retrieve ε across large swathes of atmosphere over short timescales. Consistent retrieval of ε over many radar scans requires the development of a comprehensive turbulence retrieval algorithm to estimate ε from Doppler variance under a wide range of conditions. The statistical features of ε can then be reliably examined across many cloud cases. Such an approach will provide deeper insights into the characteristics of turbulence in convective clouds while providing turbulence statistics with a suitable level of detail and reliability to test against those identified in CPMs.

1.6 Thesis outline

This thesis aims to address the current short-comings in observations of turbulence in convective clouds which, until now, have been insufficient to conduct a thorough evaluation of the parametrisation of turbulence in CPMs. A comprehensive turbulence retrieval algorithm is developed and applied to radar observations of convective clouds. These were collected during the Dynamical and Microphysical Evolution of Convective Storms (DYMECS) project, using the Chilbolton Advanced Meteorological Radar (CAMRa). By examining many cloud cases together, a detailed statistical assessment of turbulence in convective clouds is presented for two contrasting case studies. Statistical relationships are

compared with equivalent turbulence statistics from high-resolution simulations of observed case days, performed in the Met Office Unified Model (MetUM) to evaluate the Smagorinsky-Lilly sub-grid turbulence scheme.

This thesis is organised as follows: Chapter 2 provides descriptions of CAMRa and its suitability to turbulence retrieval, the DYMECS radar observations used for analysis, and the simulations performed in the MetUM. Chapter 3 details a comprehensive approach to the retrieval of ε using Doppler weather radar; ultimately discussed in the context of CAMRa. Chapter 4 presents retrievals of ε for cloud cases observed with CAMRa in two contrasting case days of observations. A thorough statistical assessment of the relationships between ε and cloud characteristics is presented. In Chapter 5, details of the MetUM simulations of the observed cases are presented. A statistical assessment of ε in simulated clouds (using methods consistent with those used in observations) is performed to evaluate the parametrisation of turbulence using the Smagorinsky-Lilly sub-grid scheme. Lastly, the results and conclusions are summarised and future work is proposed in Chapter 6.

Chapter 2

Data and Methods

2.1 Observing turbulence with CAMRa

This section details the specifications of the Chilbolton Advanced Meteorological Radar (CAMRa), which was used to collect the observations analysed in this thesis (Section 2.1.1). This is followed by a description of how the Doppler velocity spectrum is estimated by CAMRa, and why this can be used to quantify characteristics of turbulence in clouds (Section 2.1.2).

2.1.1 CAMRa overview and specifications

Radar observations used in this project were collected with CAMRa, the 3 GHz (S-Band) weather radar located at the Chilbolton Observatory in Hampshire, UK (see Figure 2.1). CAMRa has dual-polarisation capability allowing the alternate transmission of horizontally and vertically polarised pulses, receiving co-polar and cross-polar signals simultaneously. It is also Doppler-capable, permitting measurements of the radial velocity component of a wind field. The sensitivity of CAMRa is -37 dBZ at 1 km range, and the far-field begins at a range of 12.5 km. The large diameter antenna (25 m) makes CAMRa the largest fully steerable meteorological radar in the world. The antenna can be used to scan with maximum rotation speeds of $3° \ s^{-1}$ in the azimuthal direction, and $1° \ s^{-1}$ in elevation. Such a large antenna permits very high-resolution measurements; the one-way half-power beam width of 0.28° provides transverse (and elevation) resolutions of 100 m at 20 km range, and 500 m at 100 km range. A detailed overview of the radar hardware and signal processing scheme for

CAMRa is summarised in Goddard *et al*. (1994), and a summary of radar specifications is provided in Table 2.1.

Figure 2.1: The 25-m antenna of the 3 GHz Chilbolton Advanced Meteorological Radar (CAMRa) located at the Chilbolton Observatory, Hampshire, UK.

Specification	Value
Frequency	3.0765 GHz
Peak power	600 kW
Pulse repetition frequency	610 Hz
Pulse duration	0.5 μs
Wavelength	9.75 cm
Antenna diameter	25 m
Half-power beam width	0.28°
Range resolution	75 m
Maximum unambiguous velocity	14.9 m s^{-1}
Maximum unambiguous range	246 km

Table 2.1: Technical specifications of CAMRa.

2.1.2 Measurements of turbulence from CAMRa

To enable the estimation of turbulent intensity (expressed as the eddy dissipation rate, ε), the Doppler velocity spectrum variance σ_v^2, must include velocity variances from turbulent eddies of spatial scales within the inertial sub-range. As detailed in Section 1.1.3, the inertial sub-range has a characteristic largest scale Λ_0, whereby turbulence on smaller scales than Λ_0 is isotropic and transfers energy downscale to dissipation scales. The spectral form of turbulent energy associated with eddy wavelengths larger than Λ_0 is not known. Therefore, variance contributions to σ_v^2 from turbulence that is outside the inertial sub-range of scales

cannot be converted to ε. Such variances are removed from σ_v^2 as a correction for shear, σ_s^2. As long as the largest dimension of the radar resolution volume V_6, is less than Λ_0, σ_v^2 will contain velocity variance from inertial sub-range turbulence, σ_t^2 (Frisch and Clifford, 1974), which can then be isolated from σ_v^2 and converted to ε (see Chapter 3).

The suitability of CAMRa for the retrieval of turbulence can be determined by comparing Λ_0 to the spatial dimensions of V_6. The range resolution of CAMRa (75 m, see Table 2.1) is constant owing to the fixed pulse length; however, the transverse dimension increases with range due to the angular beam-width of 0.28°. Section 2.2.1 summarises the scanning strategy used to collect the dataset of observations with CAMRa, and Section 2.2.4 details the subset of these observations selected as cases for turbulence retrieval. As stated in Section 2.2.4, clouds were rarely closer than 30 km from CAMRa, or at ranges further than 150 km. Between 30 – 150 km, the beam broadens from 147 - 733 m. In Section 3.4, Λ_0 is estimated to be ~ 1 km for the cloud observations selected for turbulence retrieval, suggesting that Doppler velocity spectra from CAMRa will almost always include details of inertial sub-range turbulence, and can be used to estimate ε.

As described in Section 1.1.4, turbulence, expressed as ε, can be derived from the Doppler velocity spectrum width, σ_v. Although σ_v represents the standard deviation in target velocities within V_6, the individual velocities of hydrometeors within V_6 are not measured directly. In the case of CAMRa, σ_v is estimated through the analysis of the phase of the radar echo over successive radar pulses used to sample V_6. For the observations selected for turbulence retrieval, 32 pairs of pulses (64 individual pulses) were used to sample each V_6 at a PRF of 610 Hz (see Table 2.1), which corresponds to an integration time of 0.1 s for each V_6.

Methods to estimate σ_v for CAMRa (Goddard *et al.*, 1994), involve recording the amplitude A, and phase θ, of each pulse. Using this information, σ_v is estimated through the

rate of decorrelation of θ during the period of sampling. Assuming the Doppler spectrum is Gaussian, the correlation ρ, between pairs of pulses tends to:

$$\rho(t) = \exp\left[-8\left(\frac{\sigma_v \pi t}{\lambda}\right)^2\right] \tag{2.1}$$

In (2.1), λ is the radar wavelength, and $\rho(t)$ is the correlation coefficient between $e^{i\theta}$ of a given radar pulse, and that of a pulse after time, t. Pulses decorrelate with $\exp(-t^2)$, and at a rate that increases with σ_v^2. Re-arranging (2.1) provides the expression that is used to determine σ_v.

$$\sigma_v = \frac{\lambda}{2\sqrt{2}\pi t}[-\ln(\rho)]^{1/2} \tag{2.2}$$

The range of σ_v observable for a given radar is determined by the maximum unambiguous velocity interval (Nyquist velocity). Keeler and Passarelli (1990) state that reliable measurements of the Doppler spectrum width can only be made between $0.02 - 0.2$ of the Nyquist interval. CAMRa has a Nyquist interval of 30 m s^{-1}, so σ_v can only be reliably observed between $0.6 - 6$ m s^{-1}, corresponding to a range in Doppler spectrum variance σ_v^2, of $0.36 - 36$ m^2 s^{-2}. In the extreme case where this variance is due only to inertial sub-range turbulence ($\sigma_v^2 = \sigma_t^2$), such a range in σ_t^2, observed at a range of 60 km (the typical range of observed clouds), would correspond to a maximum detectable range in ε of $10^{-3} - 1$ m^2 s^{-3} (using (1.25)). Only in the most turbulent of the observed clouds are values of σ_v close to 6 m s^{-1}. In these cases, however, there is no evidence that values of σ_v would be larger than 6 m s^{-1} if observed using a larger Nyquist interval (widespread areas of σ_v equal to 6 m s^{-1} would suggest values were capped). Although an observable limit to σ_v exists, it is not suppressing values of ε that may otherwise be larger than 1 m^2 s^{-3}. For turbulence retrieval in clouds that are significantly more turbulent than those observed in DYMECS,

using a radar with the Nyquist velocity of CAMRa may not be suitable to detect the full range of ε in the cloud.

The Nyquist interval (given by $\pm\frac{1}{4}\lambda \cdot \mathrm{PRF}$) can be extended by increasing the PRF. However, by doing this, both the upper and lower limits to reliable values of σ_v increase. For example, doubling the PRF of CAMRa from 610 Hz to 1220 Hz would double the Nyquist interval to $60\ \mathrm{m\ s^{-1}}$, and alter the range of reliable σ_v to $1.2 - 12\ \mathrm{m\ s^{-1}}$. This suggests that an increased PRF would have to be accompanied by other methods to improve reliable detection of small σ_v, e.g. increasing the number of pulses (see Section 6.2.3). Large increases to the PRF would also decrease the maximum unambiguous range. Doubling the PRF of CAMRa would halve the maximum unambiguous range to only 123 km. With high-resolution measurements desirable for turbulence retrieval (improved chance to sample within the inertial sub-range), this is not a significant disadvantage when collecting observations. Another method includes using two staggered PRFs with a small separation in the time between pulses, as outlined in Section 7.4.3 of Doviak and Zrnic (1984). No experiments have been performed with CAMRa to extend the Nyquist interval for this thesis. However, due to the confidence that CAMRa is reliably sampling the range of σ_v (with the exception of $\sigma_v < 0.6\ \mathrm{m\ s^{-1}}$) within the observed clouds, these should not be essential.

2.2 Data

2.2.1 Data collection in DYMECS

The radar observations used for turbulence retrieval were collected during the Dynamical and Microphysical Evolution of Convective Storms (DYMECS) project (Stein *et al*., 2014; Stein *et al*., 2015). The primary objective of DYMECS is to apply a statistical approach to investigate the dynamics, morphology and evolution of convective storms over southern

England, both in radar observations and in high-resolution Met Office Unified Model (MetUM) simulations.

During DYMECS, an automated scanning procedure was used to obtain radar observations with CAMRa of hundreds of convective storms in 2011-2012. Initially, this involved running an algorithm to detect and track rainfall features over southern England, based on a threshold rainfall rate of 4 $\mathrm{mm\,hr^{-1}}$. These were identified in radar fields of rainfall provided every 5 minutes by the UK Met Office network of C-band radars (Harrison *et al*., 2011). This algorithm recorded details of the detected rainfall features, collecting information regarding storm size, velocity vectors, rainfall intensity and location every 5 minutes. A second "scan scheduler" algorithm was then applied; this used rainfall intensity and size information to prioritise storms for scanning with CAMRa. Sets of four Range-Height Indicator (RHI) scans (elevation scanning at fixed azimuth yielding vertical cross-sections through the atmosphere) were performed for the three most intense storms diagnosed by the tracking software. This was achieved by performing RHIs along azimuths that bisected rainfall rate maxima, taking into account the advection of storms between the times of detection and scanning. This was followed by volume scanning using a sequence of Plan-Position Indicator (PPI) scans (azimuthal scanning at fixed elevation) at a variety of elevations separated by 0.5°. This procedure was carried out on 40 non-consecutive days between July 2011 and August 2012, building a dataset of over 1000 convective storm observations. RHIs were collected with an elevation scanning speed of 0.4° $\mathrm{s^{-1}}$, with an azimuthal scanning speed of 2° $\mathrm{s^{-1}}$ for PPIs. Although the largest elevation of individual RHIs varied (intentionally overshooting storms to ensure full coverage by the scan), the typical maximum elevation is 15°. For further details regarding the scanning strategy used during DYMECS, see Stein *et al*. (2014).

2.2.2 Case studies: Overview

Two particular case days have provided the focus for investigation in DYMECS research both before and during this project, owing to the contrast in the characteristics of observed convection. These are the 20 April and 25 August 2012, hereafter referred to as the shallow "showers", and "deep convection" cases, respectively.

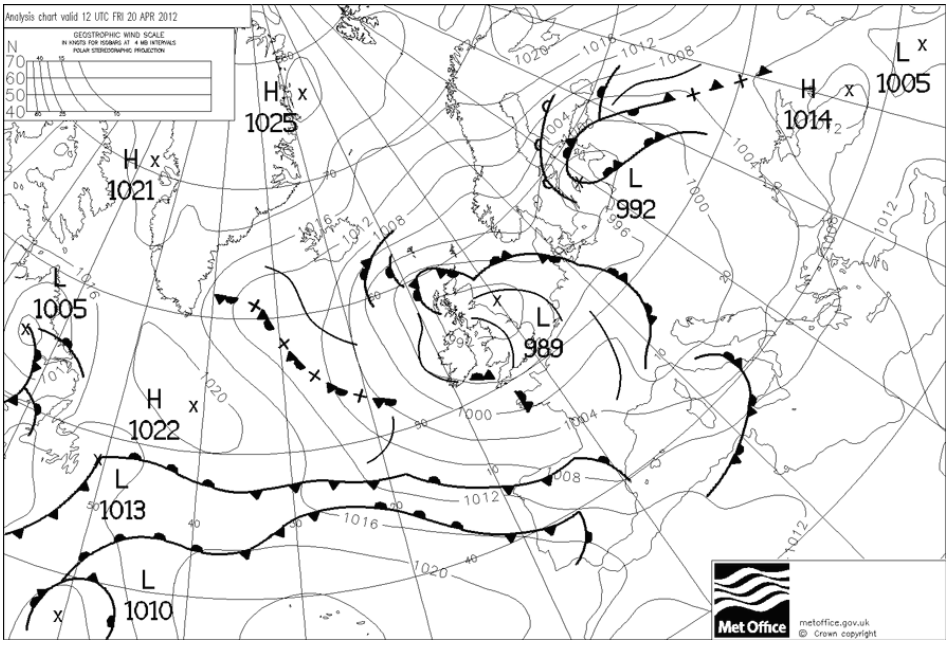

Figure 2.2a: Met Office 12 UTC synoptic chart for 20 April 2012.

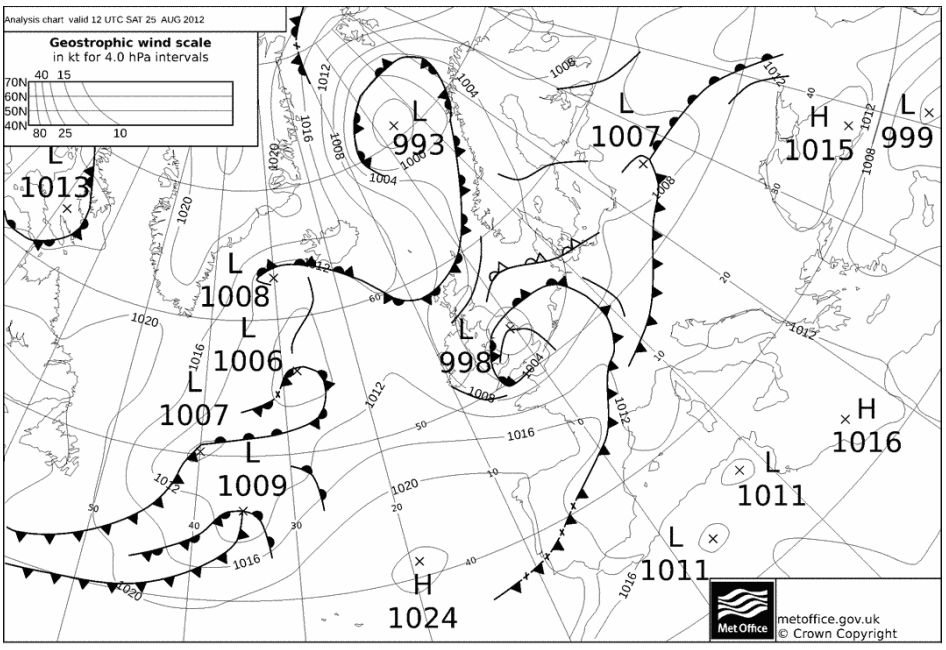

Figure 2.2b: Met Office 12 UTC synoptic chart for 25 August 2012.

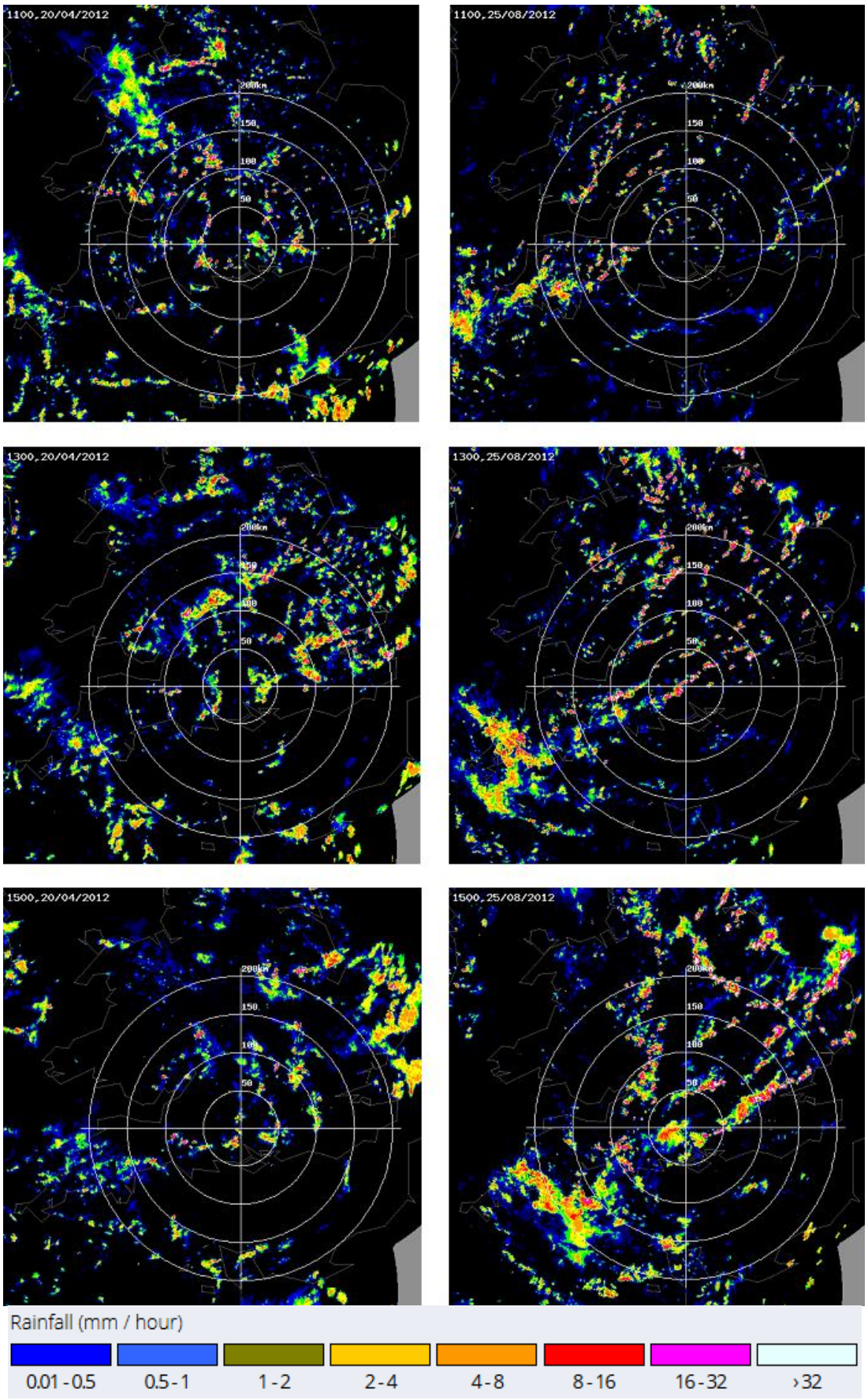

Figure 2.3: Chilbolton Observatory rainfall radar observations for 1100 UTC, 1300 UTC, and 1500 UTC on 20 April 2012 (left) and 25 August 2012 (right), showing the evolution of convective precipitation throughout the day.

The Met Office synoptic scale chart for 1200 UTC on 20 April 2012 is shown in Figure 2.2a. An area of low pressure was centred on the east coast of the UK, with a shortwave trough oriented roughly north-south across central areas. Convective showers developed in response to surface heating through the late morning hours, becoming widespread across central and southern UK by 1100 UTC (see Figure 2.3), and moving northeast throughout the day. By 1300 UTC, convection had begun to grow upscale into small clusters, becoming more isolated from the west. Using the methodology summarised in Section 2.2.1, CAMRa was used to perform 149 RHIs and 269 PPIs of convection between 1030 and 1600 UTC. An example RHI scan performed at 238° azimuth at 1252 UTC is presented in Figure 2.4, showing the radar reflectivity and vertical velocity retrieval (Nicol *et al*., 2015, see Section 2.2.3 for details of these retrievals). These fields (and those in Figure 2.5 for deep convection) are selected to be representative of the typical strength and depth of convection on the respective days. Figure 2.4a shows that shower clouds grew to a maximum height of 5.5 – 6 km, with observed radar reflectivity generally no larger than 35 dBZ. Maximum updraft velocities (Figure 2.4b) generally ranged from 2 – 4 m s^{-1}, with a largest recorded value of 6.5 m s^{-1}.

25 August 2012 was characterised by the strongest and deepest convection of any day observed during the DYMECS project. The 1200 UTC synoptic chart (Figure 2.2b) shows a weakening low-pressure system, with associated occlusion, moving east across the UK. During the late morning hours, breaks in cloud cover led to the initiation of scattered convective storms. By 1300 UTC (see Figure 2.3), storms had become much more widespread over central and southern England, organising into lines and clusters. Thunderstorms were reported widely across southern England by 1500 UTC, as upscale growth of convection continued through to early evening. Between 0900 and 1700 UTC, CAMRa was used to perform 263 RHIs and 339 PPIs through convective clouds. Figure 2.5 displays the marked differences in the characteristics of convection from the shower case. The example RHI presented was performed at 1250 UTC at 262° azimuth, through a line of

convection located 50 – 100 km west of Chilbolton (see Figure 2.3 at 1300 UTC). Clouds grew to over 10 km in depth, with reflectivity in excess of 50 dBZ common in stronger cells. Updrafts were far stronger on this day; vertical velocity maxima typically ranged from 6 – 10 m s^{-1}, with a largest recorded value of 14.9 m s^{-1} (Nicol *et al*., 2015).

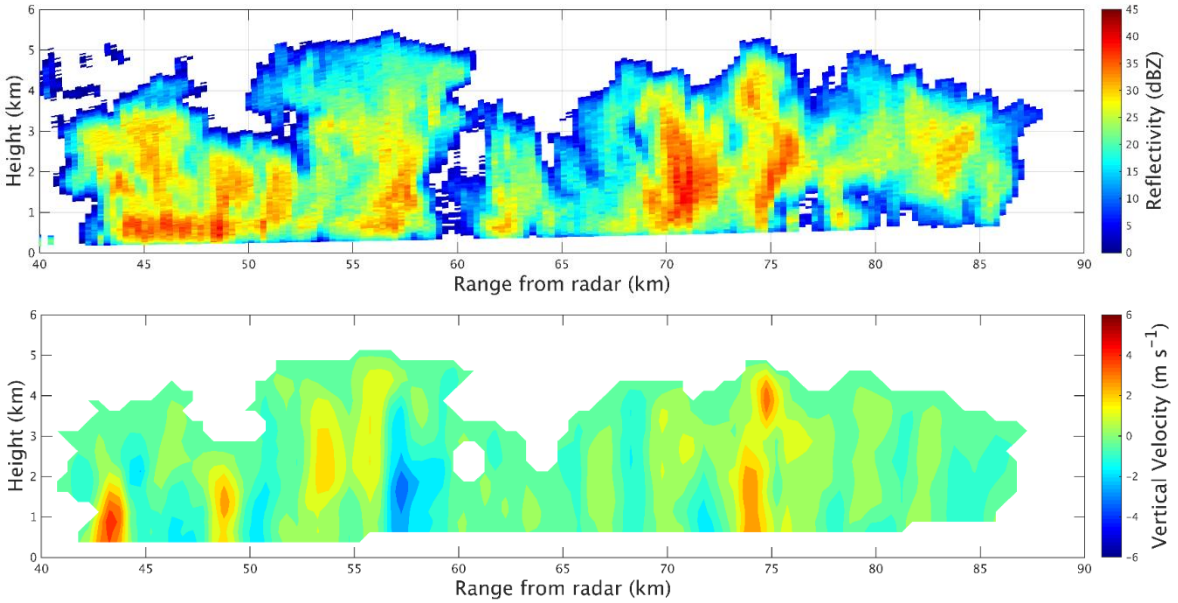

Figure 2.4: (a): (Top panel) Example radar reflectivity and (b): (Bottom panel) Vertical velocity retrieval (Nicol *et al*., 2015), for an RHI scan through convection on 20 April 2012, performed at 1252 UTC at an azimuth of 238°.

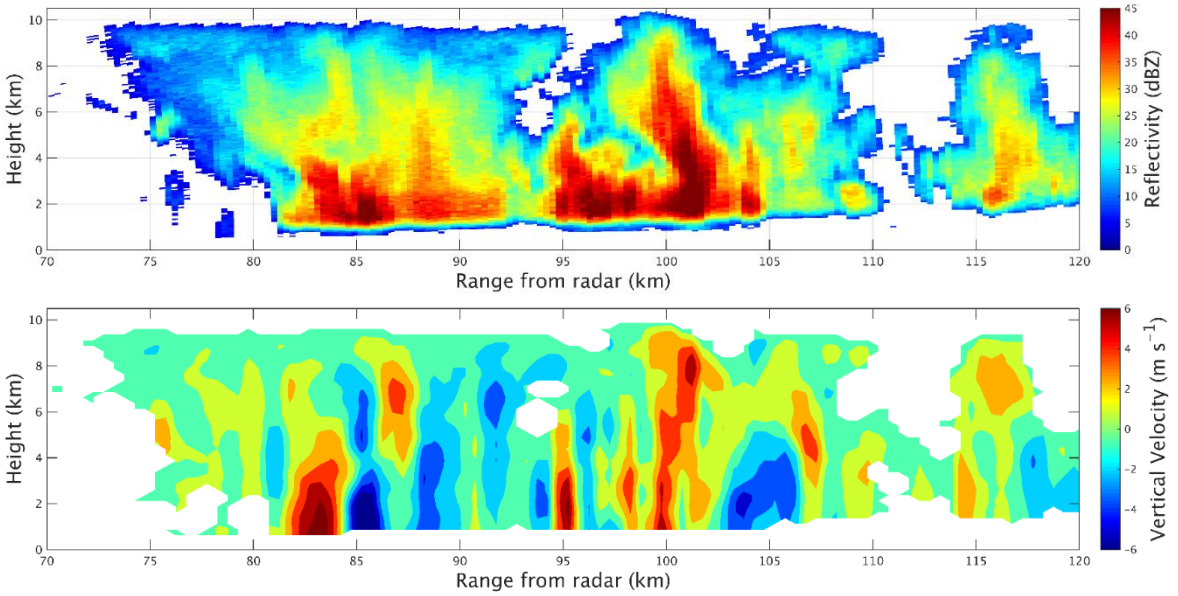

Figure 2.5: (a): (Top panel) Example radar reflectivity and (b): (Bottom panel) Vertical velocity retrieval (Nicol et al., 2015), for an RHI scan through convection on 25 August 2012, performed at 1250 UTC at an azimuth of 262°.

2.2.3 Case studies: Analysis of cases in previous DYMECS research

As mentioned, these two case days have formed the focus for other research in DYMECS. Hanley *et al*. (2015) used high-resolution Met Office Unified Model (MetUM) simulations of these two cases to investigate the sensitivity of storm morphology to changes in the Smagorinsky-Lilly turbulence parametrisation (see Section 1.3.2 for details of this paper and Section 2.3.2 for details of the Smagorinsky-Lilly scheme). The model suites used to perform these simulations were also used by Stein *et al*. (2015) to evaluate the evolution and morphology of simulated clouds with observations collected with CAMRa for both cases. For both case days, Hanley *et al.* (2015) demonstrated that the UKV, 500-m and, in particular, 200-m models do a good job of simulating the correct amount of domain-averaged rainfall when compared to Met Office network radar composite data. The number and intensity of convective cells improved towards that observed with radar as the resolution was increased. In both cases, there was also good agreement between cell equivalent diameter in the 200-m model and radar observations. These studies show that the models provide good quality forecasts of both cases, albeit with some variability in the timing of convective initiation, cloud characteristics and precipitation with model grid-length and the configuration of the turbulence parametrisation. In both studies, the 200-m models produced simulated convection with characteristics that were in strongest agreement with observations. For this thesis, the same model suites are used to perform new simulations for both cases with a focus on comparing turbulence diagnostics in 100-m and 55-m simulations with observations. The 100-m and 55-m models are nested within the 200-m model and, as such, derive lateral boundary conditions from an accurate simulation that has been tested against observations. The details of these suites and the selected modelling framework for this project are summarised in Section 2.3.1.

In this thesis, retrievals of vertical velocity (as shown in Figures 2.4 and 2.5) are used for analysis with ε, which have been produced for all RHI scans on both case days by Nicol *et*

al. (2015). These velocities were estimated from the Doppler velocity by vertically integrating local changes in horizontal convergence, under the assumption of flow continuity, accounting for the changes in density with height. The method required a zero-velocity boundary condition, either at the surface or cloud echo top. A weighted combination of velocity derived under both conditions was developed to minimise the vertical propagation of errors. In using only single-Doppler measurements, these errors were found both in the initial convergence estimation, and in using convergence measured in only one plane (the plane of the scan). The omission of convergence in the direction perpendicular to the scanning plane would lead to a consistent under-estimation of the vertical velocity. To correct for this under-estimation, the suitable scaling for the vertical velocity was estimated from correspondingly high-resolution simulations of the MetUM for each case. These were made under assumptions that the simulated three-dimensional wind flows were suitably realistic, and that the range of observed vertical velocities was represented in the model. After model-guided rescaling of the single-Doppler retrievals, vertical velocities remained under-estimated, and to a degree that increased with the retrieved velocity (15% when vertical velocity was 10 $\mathrm{m\,s^{-1}}$). In the circumstance that updrafts were symmetrical and were sampled directly through the centre by the radar, the two orthogonal components of convergence would be the same. In this sense, a simple doubling of retrieved velocities was proposed, which would not require corresponding model simulations for each case. However, it was concluded that the correction by mapping the observed retrievals to model simulations produced a result with a lower error.

The analysis of these two case studies summarised above offers both the means to perform well-initialised MetUM simulations for each case, and vertical velocities for analysis with fields of turbulence, as tools to improve the investigations in this project. Vertical velocity retrievals for other DYMECS days were not available at the start of this project. Due to the questionable reliability of simply doubling vertical velocities derived from single-Doppler measurements, accurate retrievals for other DYMECS days are not

possible without the laborious step of running MetUM simulations for each case to obtain the correct scaling functions. Instead, the same two case studies provide the focus for analysis in this thesis, benefitting from the tools and insights provided through the depth of the preceding analysis.

2.2.4 Details of RHI subsets

For the analysis of turbulence in convective clouds included in this thesis, a subset of RHI scans was drawn from the case study observations. As described in Section 2.2.1, sequential RHIs were quickly performed in sets of at least 4 for a given target storm. For example, scanning from 0° to 15° to 0° twice took only 150 seconds, and provides 4 RHIs over such a time resolution that the internal structure of storms changes only slightly. As the data in these scans are very similar (e.g. see Figure 2.6), biases are possible in statistical analyses by including observations that are correlated. To demonstrate the consistency in sequential RHIs, Figure 2.6 displays fields of retrieved turbulence for two RHIs (from the surface) performed 75 seconds apart for a storm case on 25 August 2012. On the scale of individual data points, there is variability in values of ε between the two scans, though they remain positively correlated ($r = 0.41$). However, the broad-scale values and general distribution of ε remain very similar; the mean and standard deviation of ε in both scans is $0.018\ m^2\ s^{-3}$ and $0.022\ m^2\ s^{-3}$, respectively. To ensure this subset consists only of statistically independent cloud observations, only one RHI from each sequential set is included.

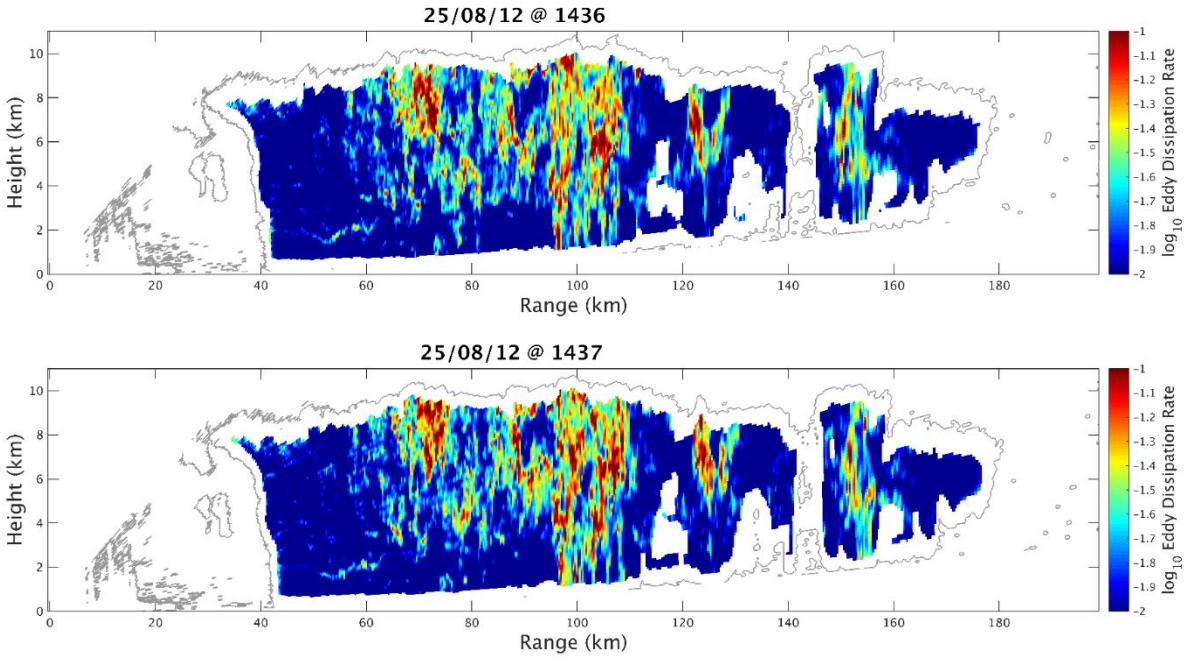

Figure 2.6: Comparison of ε retrieved in two RHIs performed 75 seconds apart for the same storm case on 25 August 2012. The grey contour is the boundary of detected reflectivity, dissipation rates are expressed as $\log_{10}$ ε.

During certain time periods during the case days (especially in the morning hours), the coverage of convection in scanning range of Chilbolton was sparse. Observations were still collected by the automated detection and scanning algorithm, however, the prioritised storms at these times were often insignificant, and in some cases, very little cloud was observed. Such RHI sets were qualitatively removed from consideration, ensuring only high-quality cloud observations were included in RHI subsets for both cases. The scanning algorithm prioritises storms with more intense rainfall, as a result CAMRa was often directed back to perform a set of RHIs for storms that had been scanned a period of time before. However, the motion of the target clouds relative to the radar in this time period means the incident angle of the RHI changes, potentially scanning through the same precipitation cores, but sampling different areas of the surrounding cloud. Together with the general evolution of the clouds in the time period, these scan sets are treated as new cloud observations, as

opposed to repeated, and considered for the subset. From each RHI set, the selection of a scan to include in the subset is made through qualitative inspection of fields of radar reflectivity and Doppler velocity (independent of the Doppler spectrum width to avoid selection biases). For example, scans that displayed evidence of skipped rays, or any other irregularities, were omitted to ensure only the scans with the highest data quality were included.

Based on the above considerations, the final subset of observations for the deep convection case includes 44 RHIs performed between 1030 and 1630 UTC. For the shower case, this includes 33 RHIs performed between 1030 and 1550 UTC. In these RHIs, clouds were rarely observed closer than 30 km from CAMRa, or at ranges further than 150 km. Although the range resolution of CAMRa is 75 m, the radial resolution of data collected in DYMECS was subsequently averaged to 300 m.

2.3 Met Office Unified Model (MetUM)

2.3.1 The MetUM: Overview and selected modelling framework

The Unified Model is the operational weather forecast model based at the Met Office in Exeter, United Kingdom. The MetUM is used internationally to perform deterministic and ensemble simulations ranging from short-range regional scales to global climate scales. As summarised in Davies *et al*. (2005), the MetUM dynamical core (introduced in 2002) solves the compressible, non-hydrostatic, deep-atmosphere equations of motion. In the vertical, the model uses a vertically-staggered Charney-Phillips grid (Charney and Phillips, 1953), with a terrain-following height coordinate. In the horizontal, the model employs Arakawa C staggering on a regular latitude-longitude grid system which, for limited domain simulations, is rotated so the domain is centred on the equator to ensure a consistent grid-length. Semi-Lagrangian advection is used for all prognostic variables aside from density, with semi-implicit time-stepping. The model uses the radiation scheme from Edwards and Slingo

(1996), the microphysics scheme developed by Wilson and Ballard (1999), the Joint UK Land Environment Simulator (JULES) surface exchange scheme (Best *et al.*, 2011), and a non-local boundary layer mixing scheme developed by Lock *et al.* (2000).

From 2009, the Met Office has run a convection-permitting operational configuration of the MetUM for weather forecasting for the UK at 1.5 km grid-length, called the UK variable-resolution model (UKV). At the time of DYMECS, the UKV derived boundary conditions from the 12-km North Atlantic and Europe (NAE) model and used 3-hourly 3D-Var data assimilation of observations. However, the UKV currently derives boundary conditions from the 10-km global model and uses hourly 4D-Var data assimilation. The model uses 70 vertical levels with a quadratic increase in level spacing with height throughout the 40-km depth of the model. As noted in Section 1.3.1, for MetUM models with a grid-length equal to or lower than the UKV, the convection scheme otherwise used in the MetUM (Gregory and Rowntree, 1990) is switched off, allowing convection to take place explicitly.

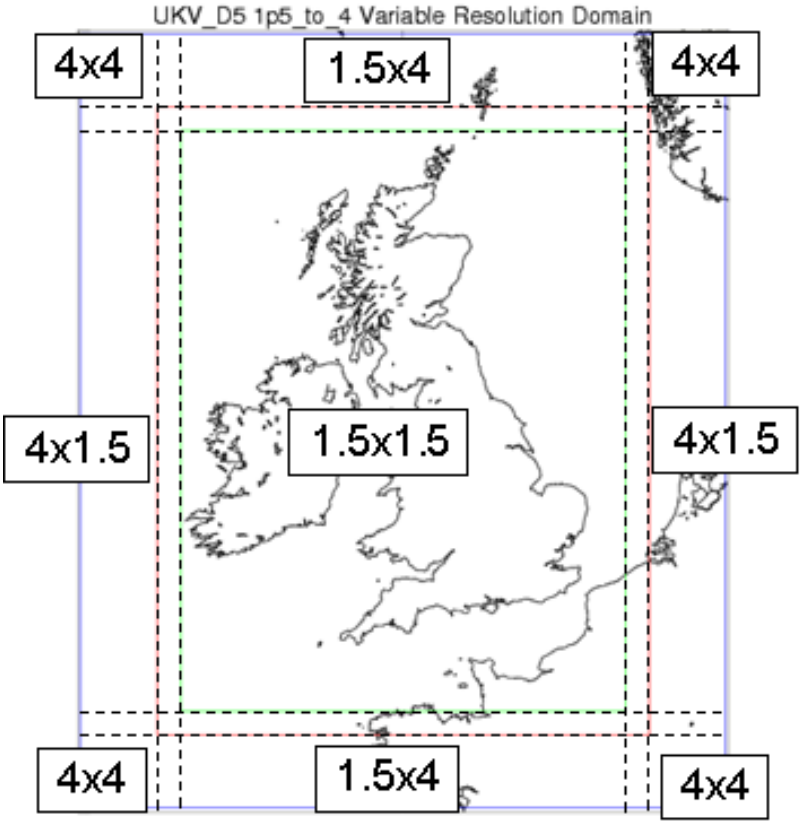

Figure 2.7: The UK variable-resolution (UKV) model domain, indicating the resolution transition to distance the forecast area (green) from the boundaries (UK Met Office).

The full domain of the UKV is presented in Figure 2.7, which displays the forecast area of 1.5 x 1.5 km grid-length (green dashed line) covering the whole of the UK. The large increase in resolution from the 10-km global model to the 1.5-km model can have substantial impacts on the resulting high-resolution forecast. The transition from parametrised convection in the global model, to resolved convection in the UKV takes a finite amount of time and can lead to poor representation of convection near the boundaries. To help ameliorate this issue, the central 1.5 km domain is surrounded by a zone of variable resolution (hence UK variable-resolution), where the grid-length increases smoothly up to 4 km (between green and red dashed lines). This increase occurs independently in the x and y directions, leading to regions with grid-length of 1.5 x 4 km above and below the domain, 4 x 1.5 km to the sides, and 4 x 4 km in the corners. By using this approach, the boundaries with the surrounding global model are shifted away from the forecast area, ultimately improving the quality of the simulation over the UK.

To make reliable comparisons between turbulence in clouds observed with CAMRa for the two case studies, and those simulated in the MetUM, simulations with a similar resolution to CAMRa are preferred. The spatial resolution of CAMRa changes as the beam broadens with range from the radar. Clouds were typically observed between 30 and 100 km from the radar; between these ranges, the width of the beam increases from ~ 150 – 500 m. Comparable features in the model are resolved by a number of grid points (see Section 1.3.1). Therefore, to resolve features of similar spatial scale to those observed by CAMRa, radar observations are compared with simulations using grid-lengths of 50 – 100 m. Following the summary in Section 1.3.2, models using grid-lengths of 100 m or smaller should satisfy the assumptions made in the implementation of the sub-grid turbulence scheme. This should allow for a more reliable comparison of turbulence diagnostics with observations.

As mentioned in Section 2.2.3, a suitable modelling suite developed previously in the DYMECS project is used in this project to perform MetUM simulations at varying resolutions for the chosen case studies (this model is described in detail in Section 2 of

Hanley *et al*., 2015). For this application, the model setup is edited in a Rose suite which runs version 10.1 of the MetUM, using the ENDGame dynamical core, and submits jobs to the shared partition of the Met Office supercomputing node (MONSooN2). The suite will first run a 1.5 km UKV forecast for the selected case, followed by a series of nested models over the south of the UK. The sequential simulations are run with a grid-length from 1.5 km (UKV), downscale to 500 m, 200 m, 100 m, and 55 m, with each nested simulation run over an increasingly smaller domain. Initial and boundary conditions for each of the nested models is sourced from the forecast of the preceding resolution. Although observations are only compared to turbulence generated by the 100-m and 55-m models, all preceding model steps (UKV, 500 m and 200 m) need to be performed to provide the correct initial and boundary conditions for the 100-m, and then 55-m models. Figure 2.8 shows the location and relative size of the nested domains compared to the UKV (full figure), indicating the location of CAMRa. The Chilbolton Observatory is located approximately 40 km north-east of the centre of the 100-m domain; situated just outside the north-east corner of the 55-m domain. Both 100-m and 55-m domains lie within scanning range of CAMRa. All models nested within the UKV run with 140 vertical levels, instead of 70. This change is stated in Hanley *et al*. (2015) as to remove excessive small-scale structure in precipitation generated in the 200-m model when 70 vertical levels were used; the change having little effect on precipitation in the 500-m model. Table 2.2 lists the number of vertical levels used for each model, and the domain size described in terms of grid points and spatial extent.

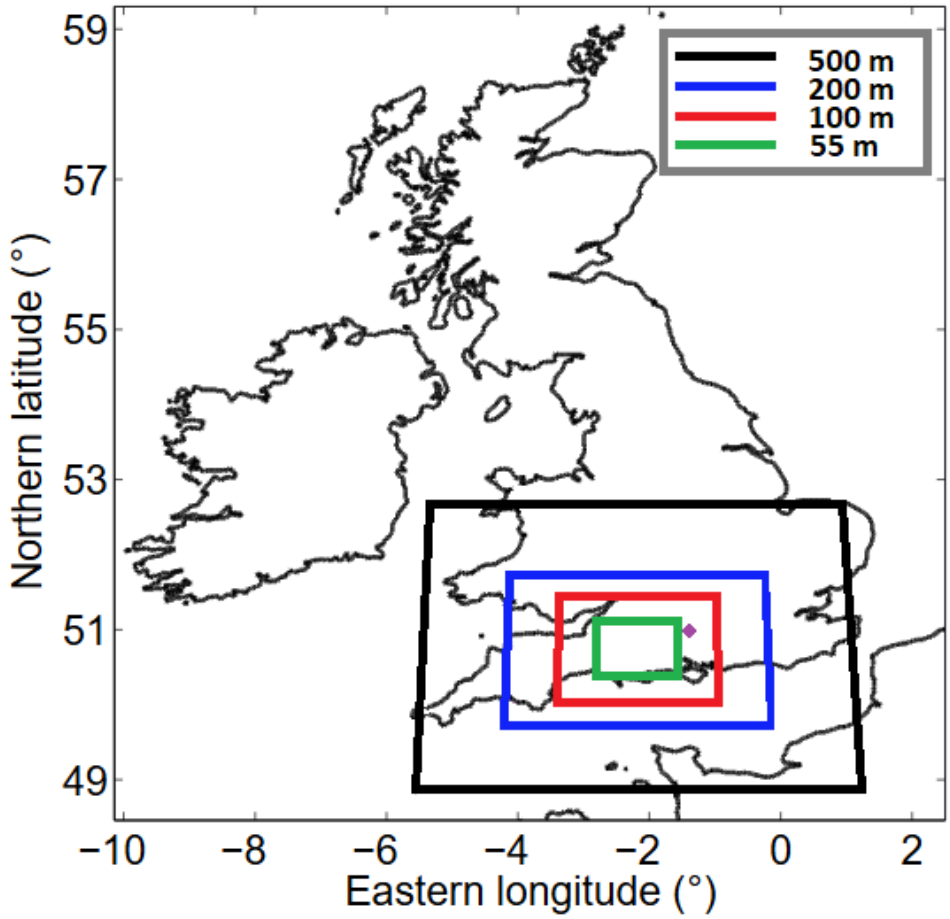

Figure 2.8: Comparison of the size of the domains in the nested suite with the UKV domain (full map). The location of the CAMRa at the Chilbolton Observatory is indicated by the purple dot. Original map is from Hanley *et al*. (2015) with the addition of the 100- and 55-m domains.

Model	**Vertical Levels (up to 40 km)**	**Latitude-longitude grid points (domain size)**
UKV 1.5 km (inner)	70	622 × 810 (933 × 1215 km)
500 m	140	1000 × 850 (500 × 425 km)
200 m	140	1500 × 1125 (300 × 225 km)
100 m	140	1750 × 1500 (175 × 150 km)
55 m	140	1500 × 1364 (82.5 × 75 km)

Table 2.2: Overview of the vertical levels and domain sizes for the model domains displayed in Figure 2.8.

High resolution (grid-length ~ 1 km) versions of the MetUM employ a sub-grid turbulence scheme to account for turbulent mixing occurring on scales below the grid-length. Convection-permitting configurations of the MetUM use the Smagorinsky-Lilly sub-grid scheme. The details of this parametrisation and how turbulence diagnostics are derived are summarised in Section 2.3.2. In operational versions of the UKV, for example, the sub-grid turbulence scheme is only used to parametrise horizontal mixing, with the vertical mixing handled by the 1-D non-local boundary layer scheme. For this thesis, modelling experiments are conducted to directly evaluate the characteristics of turbulence from Smagorinsky-Lilly sub-grid scheme using radar observations. The model runs performed to accomplish this are therefore configured to allow Smagorinsky mixing in both horizontal and vertical directions (3-D Smagorinsky mixing), with the non-local boundary layer scheme switched off. For consistency, 3-D Smagorinsky mixing is turned on for each model, including the UKV.

2.3.2 The Smagorinsky-Lilly sub-grid turbulence scheme

To account for turbulent mixing on spatial scales smaller than the model grid-length, the MetUM employs the Smagorinsky-Lilly sub-grid mixing scheme; based on Smagorinsky (1963). This section includes the derivation of this scheme and a summary of the available outputs and how these are used to compute ε for comparison with observations.

As described in Section 1.1.2, under the assumption of homogenous, steady-state turbulence in co-ordinates aligned with the flow, the TKE equation (1.7) reduces to a balance between the sum of the TKE production from shear and production/destruction from buoyancy, and the viscous dissipation given by ε (1.9). The Smagorinsky-Lilly scheme is derived from this formulation by first expressing (1.9) as:

$$\tau_{ik}^{d} s_{ik}^{r} + s(w, b) = \varepsilon \tag{2.3}$$

Where $s(w,b)$ is the buoyancy term, ε is the eddy dissipation rate, τ_{ik}^{d} is the deviatoric stress and s_{ik}^{r} is a resolved (indicated by superscript r) shear term is given by:

$$s_{ik}^{r} = \frac{1}{2}\left(\frac{\partial u_i}{\partial x_j} + \frac{\partial u_j}{\partial x_i}\right)^{\mathrm{r}} = \frac{1}{2} S_{ik}^{r} \tag{2.4}$$

The subscripts i and j refer to the horizontal dimensions of the model grid, and k refers to the vertical dimension.

Assuming a homogeneous diffusivity, τ_{ik}^{d} is expressed as:

$$\tau_{ik}^{d} = a_m e^{\frac{1}{2}} \lambda 2 s_{ik}^{r} = \nu_m S_{ik}^{r} \tag{2.5}$$

And $s(w,b)$ as:

$$s(w,b) = -\frac{g}{\theta_{vB}} a_h e^{\frac{1}{2}} \lambda \frac{\partial \theta_v^{r}}{\partial z} = -\frac{g}{\theta_{vB}} \nu_h \frac{\partial \theta_v^{r}}{\partial z} \tag{2.6}$$

In (2.5) and (2.6), TKE is given by e, the terms a_m and a_h include stability dependence, g is the acceleration due to gravity, θ_v is the virtual potential temperature and λ is the mixing length. In physical terms, λ (in m), can be described as the distance an eddy can travel while retaining its characteristics before they blend with the surrounding flow, i.e. a mean free path for a turbulent eddy. In (2.5) and (2.6), the kinematic viscosity ν_m, and molecular diffusivity ν_h, have also been defined.

Substituting (2.5) and (2.6) into (2.3) provides the TKE equation, assuming steady state and homogenous diffusivity, in gradient diffusion form:

$$a_m e^{\frac{1}{2}} \lambda 2 s_{ik}^{r} s_{ik}^{r} - \frac{g}{\theta_{vB}} a_h e^{\frac{1}{2}} \lambda \frac{\theta_v^{r}}{\partial z} = \varepsilon \tag{2.7}$$

The eddy dissipation rate ε can be expressed as TKE over a dissipation timescale, τ_d:

$$\varepsilon = \frac{e}{\tau_d} \tag{2.8}$$

Where τ_d describes the time taken for a turbulent eddy with a velocity scale $e^{\frac{1}{2}}$, to travel the mixing length before it is dissipated, such that:

$$\tau_d = \frac{\lambda}{e^{\frac{1}{2}}} \tag{2.9}$$

Substituting (2.9) into (2.8), then substituting this into (2.7) and re-arranging for e provides:

$$e = a_m \lambda^2 2 s_{ik}^r s_{ik}^r - \frac{g}{\theta_{vB}} a_h \lambda^2 \frac{\theta_v^r}{\partial z} = a_m \lambda^2 \left(2 s_{ik}^r s_{ik}^r - \frac{a_h}{a_m} \frac{g}{\theta_{vB}} \frac{\theta_v^r}{\partial z} \right) \tag{2.10}$$

Which can be simplified further to:

$$e = a_m \lambda^2 2 s_{ik}^r s_{ik}^r \left(1 - \frac{\mathrm{Ri}}{\mathrm{Pr}} \right) \tag{2.11}$$

Where Ri is the shear gradient Richardson number:

$$\mathrm{Ri} = \frac{\frac{g}{\theta_{vB}} \frac{\theta_v^r}{\partial z}}{2 s_{ik}^r s_{ik}^r} \tag{2.12}$$

And Pr is the turbulent Prandtl number given by:

$$\mathrm{Pr} = \frac{\nu_m}{\nu_h} = \frac{a_m}{a_h} \tag{2.13}$$

In the Smagorinsky-Lilly scheme in the MetUM, ν_m and ν_h are given by:

$$\nu_m = \lambda_{\mathrm{UM}}^2 S f_m(\mathrm{Ri}) \tag{2.14}$$

$$\nu_h = \lambda_{\mathrm{UM}}^2 S f_h(\mathrm{Ri}) \tag{2.15}$$

where f_m and f_h are Richardson number dependent stability functions. When $\mathrm{Ri} < 0$, the 'LEM Conventional' unstable functions are used for f_m and f_h:

$$f_m = (1 - c\mathrm{Ri})^{\frac{1}{2}} \tag{2.16}$$

$$f_h = a(1 - b\mathrm{Ri})^{\frac{1}{2}} \tag{2.17}$$

Where $a = 1/\mathrm{Pr_N}$, $\mathrm{Pr_N}$ is the neutral Prandtl number of 0.7, and $b = c = 1.43$. When $\mathrm{Ri} > 0$, the 'Sharpest' stable functions are used:

$$f_m = (1 - 0.5 g_0 \mathrm{Ri})^2 \qquad \text{for } 0 < \mathrm{Ri} < \frac{1}{g_0} \tag{2.18}$$

$$f_m = \left(\frac{1}{2 g_0 \mathrm{Ri}}\right)^2 \qquad \text{for } \mathrm{Ri} \geq \frac{1}{g_0} \tag{2.19}$$

$$f_h = a f_m \tag{2.20}$$

Where $g_0 = 10$ and $a = 1/\mathrm{Pr_N}$. The shear term S, is given by:

$$S = \frac{|S_{ij}|}{\sqrt{2}} = \left(\frac{1}{2} S_{ij} S_{ij}\right)^{\frac{1}{2}} = \left(2 s_{ij}^r s_{ij}^r\right)^{\frac{1}{2}} \tag{2.21}$$

In the MetUM, λ_0 is defined only as a function of the model horizontal grid-length Δx, by:

$$\lambda_0 = C_s \Delta x \tag{2.22}$$

where C_s is a constant that typically ranges from 0.2 – 0.3 and has a default value of 0.2 in the MetUM. It is often more suitable to determine λ_0 instead from the geometric mean of Δx, Δy and Δz. Experiments in the MetUM that define λ_0 using the geometric mean approach have shown only small differences to using Δx alone. If $\Delta x \gg \Delta z$ for the majority of the vertical profile, very little difference would be seen between the two methods. However, for 100-m resolution simulations, Δz exceeds Δx above 3.7 km, suggesting for very high-resolution simulations, the geometric mean approach may be more suitable.

The mixing length used in (2.14) and (2.15) is reduced near the surface so that:

$$\frac{1}{\lambda_{\mathrm{UM}}^2} = \frac{1}{\lambda_0^2} + \frac{1}{[\kappa(z + z_0)]^2} \tag{2.23}$$

By first re-arranging (2.11) for a_m, and substituting this into (2.5), and then substituting (2.14) into (2.5) gives:

$$e^{\frac{3}{2}} = \lambda_{\mathrm{UM}}^3 S f_m(Ri) S_{ik}^r 2 s_{ik}^r \left(1 - \frac{\mathrm{Ri}}{\mathrm{Pr}}\right) \tag{2.24}$$

Which can be simplified further using (2.4) and (2.21) to provide:

$$e = \lambda_{\mathrm{UM}}^2 S^2 f_m^{\frac{2}{3}} \left(1 - \frac{\mathrm{Ri}}{\mathrm{Pr}}\right)^{\frac{2}{3}} \tag{2.25}$$

Using (2.8) and (2.9), ε is then given by:

$$\varepsilon = \lambda_{\mathrm{UM}}^2 S^3 f_m \left(1 - \frac{\mathrm{Ri}}{\mathrm{Pr}}\right) \tag{2.26}$$

For each of the model simulations performed, the Smagorinsky-Lilly scheme outputs diagnostics consisting of ν_m, ν_h, S and λ_{UM}, that are defined for each grid point. To compute ε from (2.26), Ri, Pr and the stability function f_m, remain to be determined. Equations (2.14) and (2.15) can be used to calculate f_m and f_h directly. The Prandtl number is stated as the ratio of ν_m and ν_h in (2.13), which itself equates to the ratio of f_m and f_h. The Richardson number is determined by inverting the stability functions for f_m given by (2.16), (2.18) and (2.19):

$$\mathrm{Ri} = \frac{1 - f_m^2}{c} \qquad \text{for} \quad f_m > 1 \tag{2.27}$$

$$\mathrm{Ri} = \frac{2(1 - f_m^{0.5})}{g_0} \qquad \text{for} \quad 0.5 < f_m^{0.5} < 1 \tag{2.28}$$

$$\mathrm{Ri} = \frac{1}{2 g_0 f_m^{0.5}} \qquad \text{for} \quad f_m^{0.5} \leq 0.5 \tag{2.29}$$

2.3.3 Experiments using the MetUM

In Chapter 5, a thorough evaluation of ε produced by the MetUM is performed using radar observations for the shower and deep convection case studies described in Section 2.2.2. The majority of this evaluation involves two simulations (one for each case study) performed with a horizontal grid-length that is most similar to the resolution of CAMRa ($\Delta x = 100$ m) and the default value for C_s (0.2). The representation and evolution of convection in the MetUM has been shown to be sensitive to changes in λ_0 and Δx for DYMECS case studies in Hanley *et al*. (2015). To test the sensitivity of ε to λ_0 and Δx (Section 5.6), three additional simulations are performed for each case study. The sensitivity of ε to λ_0 is investigated by repeating the control simulations after doubling the prescribed value of C_s (see (2.22)) from 0.2 to 0.4 (and hence doubling λ_0 with respect to Δx). Simulations using C_s of 0.2 and 0.4 are then performed at $\Delta x = 55$ m to test the sensitivity of ε to model grid-length. The 8 simulations are summarised in Table 2.3 where 1 and 5 are referred to as "control" simulations and the remainder as "sensitivity" simulations in Chapter 5. Figure 2.9 outlines the procedure to perform simulations 1 – 8. All models in the suite use 3-D Smagorinsky mixing (1-D boundary layer scheme switched off), and each 100-m simulation derives initial and boundary conditions from a 200-m forecast performed with a C_s of 0.2.

In analysing observations of ε in Chapter 4, comparisons are made between ε in clouds (defined by the spatial extent of the radar reflectivity, Z) with convective updraft characteristics detected in retrievals of vertical velocity, w. To perform an analysis consistent with this in MetUM simulations, 3-D fields of corresponding variables are required from each of the 8 simulations. In terms of diagnostics, these are ν_m, ν_h, S and λ_{UM} from the Smagorinsky-Lilly scheme used to derive ε using (2.26)), w to detect updrafts, and the total (all hydrometeor types) radar reflectivity Z_{T}, to detect clouds. Fields of Z_{T} are produced by a forward model developed from the MetUM microphysics scheme outlined in

Appendix A of Stein *et al*. (2014). For both case studies, 3-D fields of ν_m, ν_h, S, λ_{UM}, w and Z_{T} are output hourly in each model from 0900 to 1900 UTC in the 100-m model, and from 1000 to 1900 UTC in the 55-m model. These time-frames comfortably overlap the periods of data collection using CAMRa over both case days.

Simulation Number	**Case Study**	**Model grid-spacing, Δx (m)**	**Mixing length constant, C_s**	**Mixing length, λ_0 (m)**
1	20 April 2012	100	0.2	20
2	-	55	0.2	11
3	-	100	0.4	40
4	-	55	0.4	22
5	25 August 2012	100	0.2	20
6	-	55	0.2	11
7	-	100	0.4	40
8	-	55	0.4	22

Table 2.3: Summary of the simulations performed for both case days. Control simulations (1 and 5) are performed using grid-lengths of 100 m and a C_s of 0.2. Sensitivity simulations (remaining numbers) involve various combinations of doubling C_s and reducing the grid-length to 55 m.

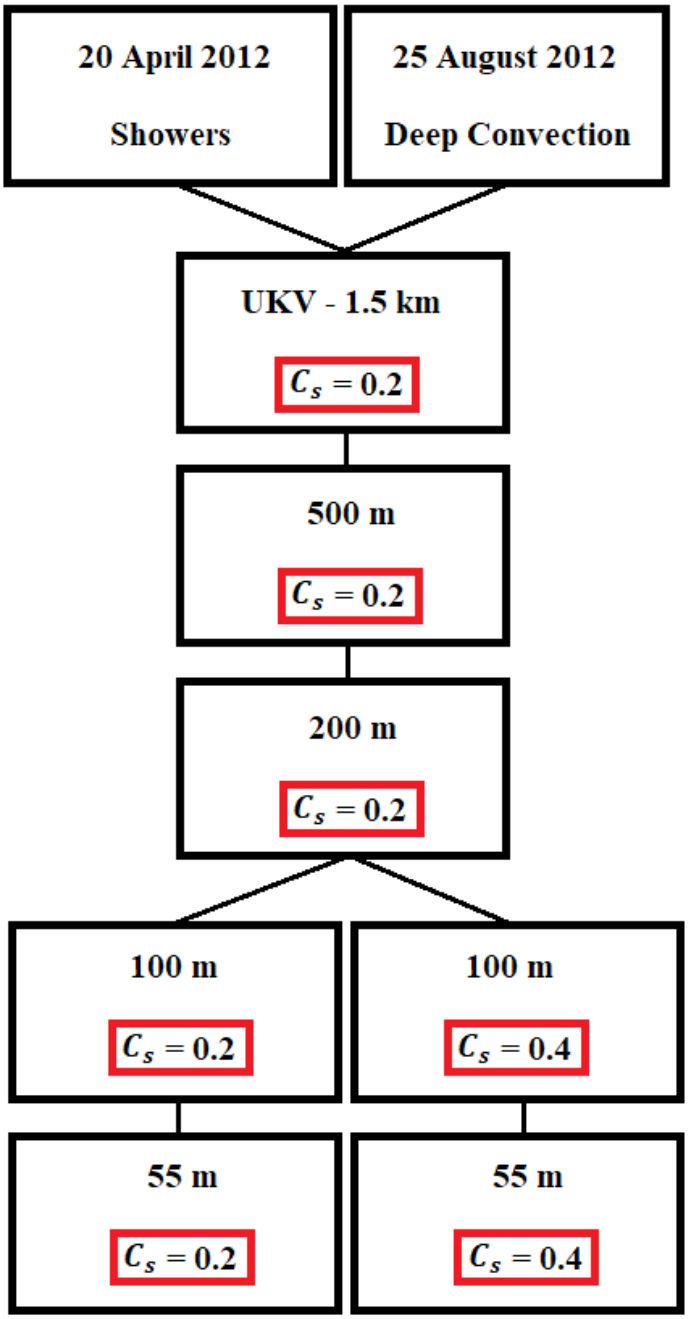

Figure 2.9: Flow diagram illustrating the modelling experiments performed for each case study, indicating where changes to C_s occur for each nested model. Each link between models can be read as "…derives boundary and initial conditions from…".

Chapter 3

Turbulence retrieval with CAMRa

3.1 Introduction and aims of method

This section provides a summary of the characteristics and assumptions associated with turbulence and weather radar that permit methods to retrieve turbulence accurately with CAMRa, together with the main aims of the retrieval method (Section 3.1.1). Section 3.1.2 provides an outline of the radar fields involved in the retrieval and methods used in data preparation. In Section 3.1.3, a threshold value of Doppler velocity variance is introduced to justify neglecting small variance contributions, and to estimate the potential size of resulting errors in ε.

3.1.1 Overview and aims

In previous sections of this thesis, the following points have been established:

- The Doppler spectrum variance σ_v^2, can only be used to accurately estimate dissipation rates ε, if the largest dimension of the radar resolution volume V_6, is smaller than the largest scale of the inertial sub-range Λ_0, i.e. the radar only samples variance due to inertial sub-range eddies.
- Under assumptions of $\Lambda_0 \sim 1$ km, CAMRa has suitably high resolution to sample velocity variance from inertial sub-range turbulence σ_t^2, over the typical distances of cloud observations collected in DYMECS (30 – 150 km).

- The range of σ_v^2 values that are detectable based on the Nyquist velocity of CAMRa appears to be sufficiently broad to provide an accurate representation of ε in the observed clouds.

Together, these statements justify the suitability of CAMRa to retrieve accurate estimates of ε throughout case study observations.

As described in Section 1.4.2, in a given V_6, σ_v^2 is comprised of velocity variances associated with various physical processes, as well as factors intrinsic to radar sampling. By assuming these variances are statistically independent (Doviak and Zrnic, 1984), σ_v^2 can be described as a linear sum of each contribution:

$$\sigma_v^2 = \sigma_s^2 + \sigma_{\mathrm{t}}^2 + \sigma_{\mathrm{TV}}^2 + \sigma_\alpha^2 + \sigma_{\mathrm{o}}^2 + \sigma_{\mathrm{B}}^2 + \sigma_{\mathrm{H}}^2 \tag{3.1}$$

Where σ_v^2 has contributions from radial wind shear across V_6, σ_s^2; turbulence, σ_{t}^2; the distribution of hydrometeor fall-velocities, σ_{TV}^2; antenna rotation, σ_α^2; hydrometeor oscillations, σ_{o}^2; beam broadening, σ_{B}^2; and the combined effects of hydrometeor rotation, break-up and coalescence, σ_{H}^2. As the details of turbulent motion cannot be found directly from σ_v^2, σ_{t}^2 is inferred from σ_v^2 by accounting for all other variance contributions in (3.1). This is accomplished either by measuring and subtracting the variance contributions from σ_v^2, or by demonstrating that they are negligibly small compared to σ_{t}^2.

The primary aim of this chapter is to detail the considerations made for each term in (3.1), to develop an algorithm that can be performed consistently across all RHIs in the observations, to isolate σ_{t}^2 from σ_v^2, and convert to ε. To accomplish this, the value of terms in (3.1) have been investigated thoroughly under a broad range of conditions, with an eventual focus on the scanning strategy and specifications of CAMRa. In doing this, the algorithm can be applied without change to future observations collected by CAMRa. By evaluating the terms in (3.1) in a sufficiently broad context, a further aim of this chapter is

to provide a reliable framework for turbulence retrieval with other high-resolution radars capable of sampling inertial sub-range turbulence.

3.1.2 Data preparation

To perform the retrieval of ε, only fields of radar reflectivity Z, the mean Doppler velocity $\bar{v}$, and Doppler variance σ_v^2, are required for each storm case. When selecting the subset of RHIs for statistical analysis of ε (see Section 2.2.4), a degree of initial data quality has been ensured through the qualitative selection of these fields. In a quantitative sense, it is necessary to remove data in regions where the ratio of returned signal to noise level is low; high values of σ_v^2 can result from signal noise rather than true variability in $\bar{v}$. To accomplish this, the ratio of the noise level of CAMRa ($Z_{\mathrm{N}} = -37$ dBZ at a range of 1 km), to the returned signal Z, is determined for each V_6. Fields of reflectivity are converted into linear units Z_{lin}, and then to P (a quantity proportional to echo power), using the following:

$$Z_{\mathrm{lin}}\ [\mathrm{mm^6\ m^{-3}}] = 10^{\frac{Z}{10}} \quad ; \quad P = \frac{Z_{\mathrm{lin}}}{R^2} \tag{3.2}$$

Where R is the range of the reflectivity observation in m. The noise power, P_{N} is constant at all points and determined in (3.2) using $Z = -37$ dBZ and $R = 10^3$ m. The ratio of signal to noise (SNR) is then determined at all points from:

$$\mathrm{SNR} = \log_{10}\left(\frac{P - P_{\mathrm{N}}}{P_{\mathrm{N}}}\right) \tag{3.3}$$

Values in Z, $\bar{v}$ and σ_v^2 that are co-located with $\mathrm{SNR} < 0$ are removed, i.e. where $P \leq 2P_{\mathrm{N}}$. This is performed identically for each storm case before turbulence retrieval methods are applied.

Figure 3.1 provides an example of this correction to RHIs of Z and σ_v^2 for observations through a line of convective cloud observed on 25 August 2012. Figure 3.1a displays Z before SNR correction with a contour overlay for $\mathrm{SNR} = 0$. The field of Z after thresholding

by SNR is shown in Figure 3.1b. The equivalent for σ_v^2 is presented in Figure 3.1c and 3.1d, showing the location of values removed corresponding to regions of low SNR. In Figure 3.1c, high values of σ_v^2 are found around the edge of clouds where signal is weak, but also in low-SNR regions within and between clouds. Some examples of this are apparent between 115 and 135 km in range, and 2 – 6 km in height, where regions of high σ_v^2 due to weak signal have been removed, which would have otherwise appeared genuine in Figure 3.1c. If thresholding by SNR was not performed, σ_v^2 due to weak signal would be included as turbulence, ultimately leading to biases in the statistics of ε.

During RHI data collection, CAMRa's slow scan rate, combined with short integration times, led to an angular resolution in the elevation direction that is approximately one sixth of the beam-width. To reduce the resulting noise in σ_v^2, data is smoothed in the elevation direction using a 6-point moving average. By doing this, σ_v^2 becomes correlated over a spatial scale similar to the true width of the beam, without re-gridding the data.

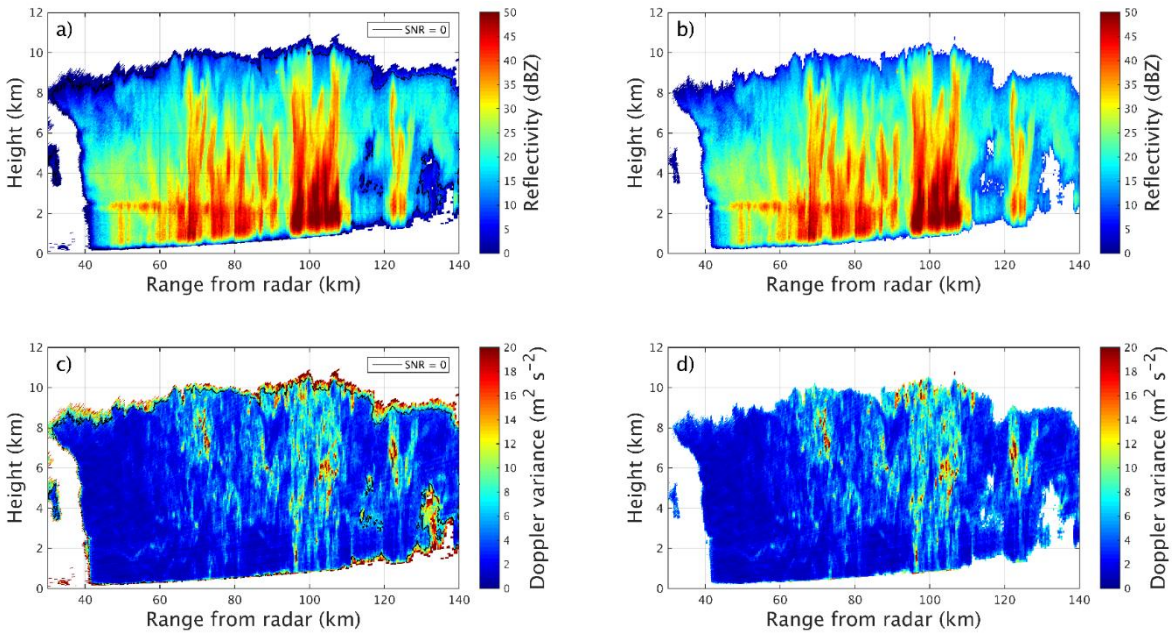

Figure 3.1: Effects of thresholding by signal-to-noise ratio on the radar reflectivity ((a) and (b)), and the Doppler variance ((c) and (d)), for an RHI performed on 25 August 2012. High Doppler variance in areas of low signal is removed.

3.1.3 Negligibility thresholds and biases in ε

Observed values of σ_v^2 generally range from 1 – 25 $m^2\ s^{-2}$. In reality, the negligibility of terms in (3.1) depends on their value relative to σ_t^2, and as a result, no fixed variance value will always be negligibly small. Assuming that turbulence is only significant when $\sigma_t^2 > 5\ m^2\ s^{-2}$ (this translates to $\varepsilon > 0.04\ m^2\ s^{-3}$ at 60 km from the radar; the typical range of cloud observations), a negligibility threshold σ_{neg}^2, of 0.5 $m^2\ s^{-2}$ is selected for the purpose of this application. Whereby, variance contributions that are less than σ_{neg}^2 can be neglected.

By considering the maximum combined variance from terms that may be neglected, the potential errors in ε can be estimated. The variance contributions from σ_α^2 and σ_B^2 are small enough to be ignored completely (σ_α^2 and σ_B^2 contribute less than $10^{-2}\ m^2\ s^{-2}$, see Section 3.2). No element of σ_s^2 is neglected, regardless of value compared to σ_{neg}^2, as this contribution can be measured directly (Section 3.4). However, contributions from σ_{TV}^2, σ_o^2 and σ_H^2 are not simple to measure directly. Contributions from σ_{TV}^2 can be larger than σ_{neg}^2 for rain and hail (Section 3.3), while σ_o^2 and σ_H^2 are both expected to contribute less than $0.25\ m^2\ s^{-2}$ (Section 3.2). The potential error in σ_t^2 that is incurred when neglecting σ_{TV}^2, σ_o^2 and σ_H^2 is therefore limited to 1 $m^2\ s^{-2}$. If $\sigma_t^2 = 5\ m^2\ s^{-2}$, this would translate to a 28.4% positive error in ε (See Figure 3.2). The error then decreases to only 5.9% when $\sigma_t^2 = 25\ m^2\ s^{-2}$, and is independent of the range of the σ_t^2 observation from the radar. Figure 3.2 shows how the error in ε changes as a function of σ_t^2 when the error in σ_t^2 is 1, 0.75 and 0.5 $m^2\ s^{-2}$. Importantly, the percentage error in ε is inversely proportional to σ_t^2, meaning large errors are only found when turbulence is not significant.

The maximum potential error of $1\ m^2\ s^{-2}$ considers the largest contributions from each term, which may result in a significant over-estimation in ε when $\sigma_t^2 < 5\ m^2\ s^{-2}$. However, the true error in ε is expected to be considerably lower than this. In the case of σ_{TV}^2, under the assumption that rain and hail only exist below 3 km, σ_{TV}^2 will not exceed σ_{neg}^2 when

scanning at any elevation for storms located further than 15 km from the radar. Given that the minimum distance of observed storms was 30 km, with a more typical distance of 50 – 80 km, the true contribution from σ_{TV}^2 is likely to be far less than 0.5 $m^2\ s^{-2}$. The continuous processes involved in σ_o^2 and σ_H^2 are assumed to provide a contribution to Doppler variance that is consistent in time and space when scanning through cloud and precipitation, and independent of scanning angle. Therefore, the lowest variances observable by CAMRa may provide an indication of the size of these contributions. When scanning through ice cloud and rain drops with 128 pulse-pairs (see Figure 6.1), CAMRa detects the Doppler spectrum width as low as 0.6 m s^{-1}, corresponding to a variance of 0.36 $m^2\ s^{-2}$. In the case where variance due to shear and turbulence is zero, the combined contribution from σ_o^2 and σ_H^2 (and σ_{TV}^2) could only be 0.36 $m^2\ s^{-2}$. The true error in σ_t^2 is therefore expected to be closer to 0.5 $m^2\ s^{-2}$, indicated by the red line in Figure 3.2. In this case, the positive bias in ε will only be 15% when $\sigma_t^2 = 5\ m^2\ s^{-2}$, and decrease as turbulence becomes more intense.

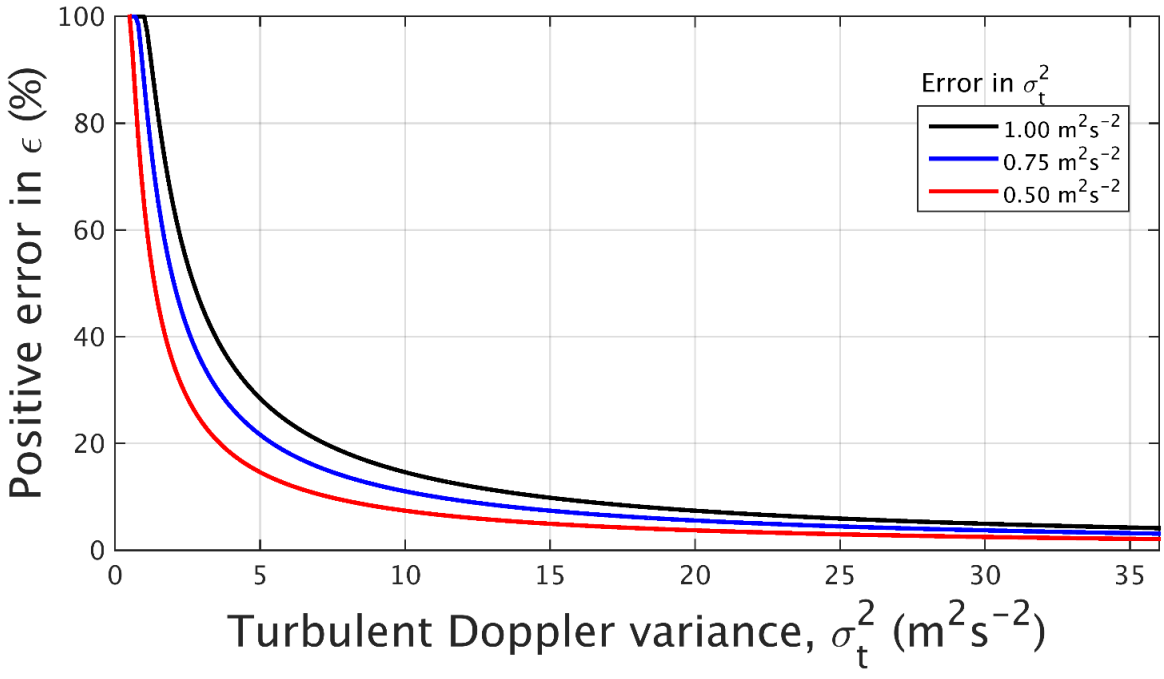

Figure 3.2: Positive errors in ε resulting from neglected terms that contribute to σ_v^2. The maximum incurred error as a function of σ_t^2 is shown in black, with more realistic errors in blue and red.

3.2 Beam broadening, antenna rotation and hydrometeor oscillation

This section includes the estimation and discussion of contributions to Doppler velocity variance σ_v^2, from mechanisms that are intrinsic to either scanning weather radar or falling hydrometeors when scanning through clouds or precipitation. The continuous movements of a radar during data collection, a finite beam-width, and the small-scale movements of falling hydrometeors can all contribute to σ_v^2. The aim of this section is to detail these mechanisms and assess them for significance for applications with CAMRa.

3.2.1 Doppler variance due to beam broadening

If the angular width of a radar beam is not infinitesimally small, radiation will propagate at a range of angles relative to the beam axis in a radar resolution volume, V_6. As noted in Gossard (1990), this effect (referred to as "beam broadening") will result in the sampling of a distribution of radial velocities even when the wind across V_6 is uniform; which contributes a variance (given by σ_B^2) to σ_v^2. To isolate this contribution, the horizontal plane of V_6 is analysed under specific conditions. Constant reflectivity and uniform wind is assumed across V_6, with a non-zero, transverse velocity vector v_T, that is perpendicular to the central beam axis, i.e. the radial velocity v_r, along the beam axis is zero. Contributions to σ_v^2 from shear, turbulence, antenna rotation or hydrometeor fall-speed distribution are assumed to be zero, i.e. $\sigma_v^2 = 0$ in the absence of beam broadening. Within a given V_6, radiation propagating from the radar will be incident to v_T at a range of angles determined by the one-way half-power beam-width, θ_1. This is illustrated in the schematic of the horizontal plane of V_6 presented in Figure 3.3. In the absence of variance contributions from all other mechanisms, a range of v_r will be observed, weighted by the Gaussian beam pattern between half-power

points. The resulting contribution to σ_v^2 is dependent only on θ_1 and v_T, and does not vary with range from the radar.

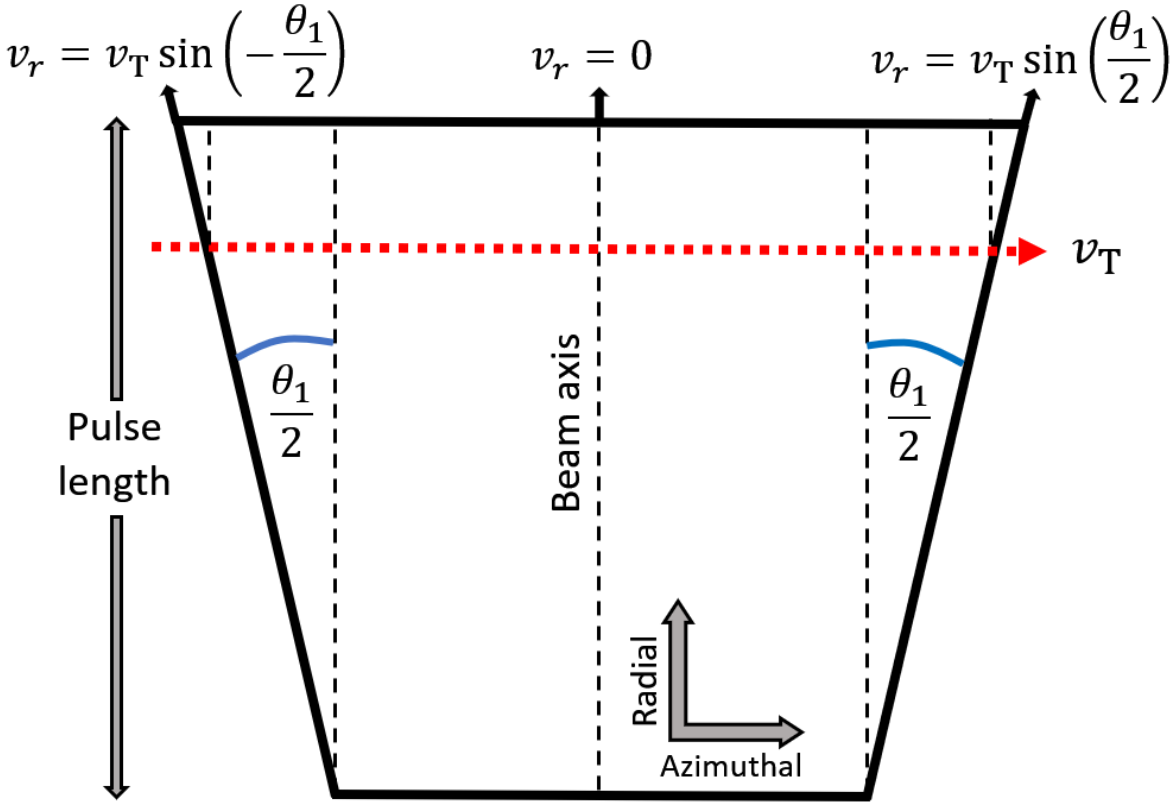

Figure 3.3: Horizontal plane of a resolution volume illustrating the change in sampling of a transverse velocity v_T, across a beam of one-way half-power beam-width of θ_1.

An equation to calculate the variance contribution due to beam broadening is stated in Gossard (1990):

$$\sigma_\mathrm{B}^2 = \frac{v_\mathrm{T}^2 \theta^2}{2.76} \tag{3.4a}$$

In (3.4a), v_T is the uniform velocity perpendicular to the beam axis in m s^{-1}, and $\theta = \frac{1}{2}\theta_1$, measured in radians. However, (3.4b) is used as an equivalent expression to (3.4a) that is more consistent with the conventions used in this chapter:

$$\sigma_\mathrm{B}^2 = \frac{v_\mathrm{T}^2 \theta_1^2}{16 \ln 2} \tag{3.4b}$$

In (3.4b), θ has been replaced with $\frac{1}{2}\theta_1$, and the factor 2.76 is assumed to be an approximation of $4 \ln 2$. The resulting equation describes a velocity variance that arises due to the weighting of v_T^2 by $\frac{\theta_1^2}{16 \ln 2}$; which is the variance of the Gaussian two-way beam pattern (see (3.25) in Section 3.4.1).

Observed radial velocity was no larger than 15 m s^{-1} in observations with CAMRa ($\theta_1 = 4.9 \times 10^{-3}$ rad). Assuming a similar maximum applies to velocities perpendicular to the beam, this would result in a variance contribution of only 4.9×10^{-4} $\mathrm{m}^2\ \mathrm{s}^{-2}$, which is far below the threshold for negligibility ($\sigma_\mathrm{neg}^2 = 0.5\ \mathrm{m}^2\ \mathrm{s}^{-2}$). To observe $\sigma_\mathrm{B}^2 > \sigma_\mathrm{neg}^2$ with a radar with such a narrow beam as CAMRa would require an extreme transverse velocity of 481 m s^{-1}, which was not observed. Contributions from σ_B^2 are therefore neglected when retrieving turbulence with CAMRa. If using a radar with a 1° beam-width, v_T would have to be 135 m s^{-1} for σ_B^2 to contribute more than 0.5 $\mathrm{m}^2\ \mathrm{s}^{-2}$. This indicates that σ_B^2 is always negligible for radar capable of sampling within the inertial sub-range for turbulence retrieval.

3.2.2 Doppler variance due to antenna rotation

The movements of the radar antenna while scanning will broaden the Doppler velocity spectrum. Assuming a constant antenna scan rate α, in $\mathrm{rad\ s}^{-1}$, the variance contribution due to antenna rotation σ_α^2, is provided by Doviak and Zrnic (1984):

$$\sigma_\alpha^2 = \left(\frac{\alpha \lambda \cos \theta_\mathrm{el} \sqrt{\ln(2)}}{2\pi\theta_1} \right)^2 \tag{3.5}$$

Where λ is the wavelength of the radar in metres, θ_el is the elevation angle from the surface, and θ_1 is the one-way half-power beam width in radians.

For CAMRa, $\lambda = 0.0975$ m and $\theta_1 = 5 \times 10^{-3}$ rad. During DYMECS, RHI and PPI observations were made using scan speeds of $\alpha_\mathrm{RHI} = 7 \times 10^{-3}\ \mathrm{rad\ s}^{-1}$ and $\alpha_\mathrm{PPI} =$

35×10^{-3} rad s^{-1}. The contribution from σ_α^2 is largest when scanning horizontally ($\cos(\theta_{el} = 0) = 1$); in this case $\sigma_\alpha^2 < 0.01$ m^2 s^{-2} for both RHI and PPI observations, making a negligible ($\sigma_\alpha^2 < \sigma_{neg}^2$) contribution to σ_v^2. Observations collected at non-zero elevations (up to 15° in DYMECS) would only reduce the value of σ_α^2, therefore contributions from σ_α^2 are neglected in this application. For lower resolution radar (where θ_1 is larger), σ_α^2 decreases further still, suggesting that contributions from this term are only significant in cases of extreme scanning speed (for CAMRa, $\sigma_\alpha^2 > \sigma_{neg}^2$ only when $\alpha >$ 4.1 rad s^{-1}; close to one revolution per second).

3.2.3 Doppler variance due to hydrometeor oscillations

By simulating the oscillations of falling hydrometeors in a perturbation model, Zrnic and Doviak (1989) investigated the axisymmetric oscillations of raindrops, and the resulting effects on σ_v^2 among other Doppler radar parameters. The choice of axisymmetric oscillations is important; the spectral broadening due to drop oscillations will be the same independent of the angle of observation by the radar. In the case of raindrops with a normalised r.m.s axial ratio (ratio of the standard deviation in axial ratio due to oscillations, with the reference axial ratio on a non-oscillating raindrop) of 0.1, they find $\sigma_o^2 < \sigma_{neg}^2$ for all rain-rates larger than 5 mm hr^{-1}, while more generally σ_o^2 is less than 0.25 m^2 s^{-2}. Variance contributions from σ_o^2 are small enough to be neglected when retrieving turbulence, but an assumed maximum value of σ_o^2 = 0.25 m^2 s^{-2} is included when estimating the potential biases in ε due to neglected terms (Section 3.1).

The rotation of hydrometeors and the break-up and coalescence of rain-drops, are thought to further contribute to σ_v^2 (Zrnic and Doviak, 1989). These effects are poorly understood, and the combined variance contribution (σ_H^2) has yet to be quantified in the literature. Zrnic and Doviak (1989) speculate that contributions will be similar in value to σ_o^2; therefore, σ_H^2

is assumed to be no larger than $0.25\ \mathrm{m^2\ s^{-2}}$. An investigation into quantifying these effects is not included as part of this thesis, however, as for σ_o^2, a maximum value of $\sigma_H^2 = 0.25\ \mathrm{m^2\ s^{-2}}$ is included when estimating potential biases in ε in Section 3.1. Until the variance contribution from σ_H^2 is understood in more detail, estimated values should always be included to assess potential errors in ε.

3.3 Doppler variance due to a distribution of hydrometeor fall-speeds

3.3.1 Introduction and aims

When scanning through cloud and precipitation, hydrometeors of various size may fill a radar resolution volume, V_6. The presence of a distribution of hydrometeor diameters will lead to a distribution of hydrometeor fall velocities. In the circumstance where the radar beam is not perpendicular to hydrometeor velocity, this contributes to the variance of the Doppler velocity spectrum. The observed variance contribution (σ_{TV}^2 in (3.1)) is largest for a vertically pointing radar beam and decreases with angle from zenith.

Previous studies to estimate turbulence characteristics from Doppler velocity spectra typically assume σ_{TV}^2 to be negligible (e.g. Frisch and Clifford, 1974; Chapman and Browning, 2001; Meischner *et al*., 2001) unless observations were made at vertical incidence (Brewster and Zrnic, 1986). The expected variance due to σ_{TV}^2 is reduced significantly by scanning at lower elevations (often the reason σ_{TV}^2 is assumed negligible), however, this does not ensure the contribution is always negligibly small. Some attempts at quantifying the effects of falling hydrometeors on Doppler spectra exist in the literature. In the case of falling rain-drops, Martner and Battan (1976) present an equation (without derivation) to determine σ_{TV} from the radar reflectivity, Z (in linear units) alone:

$$\sigma_{\mathrm{TV}_{\mathrm{rain}}} = 0.79\, Z^{0.07} \tag{3.6}$$

However, without the details of its derivation, or equivalent expressions governing effects from other hydrometeor types under mutual assumptions, this section approaches the problem of quantifying σ_{TV}^2 directly, under consistent assumptions, for application in turbulence retrieval.

The primary aim of this section is to determine specific conditions under which σ_{TV}^2 is negligibly small (less than σ_{neg}^2), for three common hydrometeor types. This includes the derivation of Doppler velocity variance equations for each hydrometeor classification as a function only of the reflectivity in V_6, and the elevation angle of the radar. Doing this provides: (1) a means to estimate σ_{TV}^2 when necessary; (2) justification when neglecting σ_{TV}^2; and (3) suggestions for how future scanning strategies for turbulence retrieval can be tailored to ensure σ_{TV}^2 is always negligible.

3.3.2 Formulation and derivation of σ_{TV}^2 equations

For application to RHI radar observations, two hydrometeor types are classified based on the height of the 0°C isotherm, $z_{0°\mathrm{C}}$, which is estimated from the location of bright-band radar reflectivity in the observations. Though $z_{0°\mathrm{C}}$ varies for different DYMECS case days, the average height is ~ 1.5 km. For simplicity, any reflectivity returned from below this level is assumed to be due to liquid rain-drops, and any reflectivity from above is due to ice aggregates. By making this simple distinction, σ_{TV}^2 can be estimated in all areas of an RHI scanning domain. Owing to the potential for significant localised spectral broadening from large hydrometeors falling at high terminal velocity, considerations for hail are included.

The reflectivity in a given V_6 is assumed to be dominated by a single hydrometeor type, and hydrometeors are assumed to be falling vertically downwards at terminal velocity.

Hailstones are assumed to be dry and to consist of solid ice with homogeneous density. For hydrometeor mass calculations, raindrops and hailstones are assumed to be spherical.

To estimate the relative size of σ_{TV}^2 when compared to σ_v^2, σ_{TV}^2 is characterised as the variance of the reflectivity-weighted mean fall velocity in V_6. For a vertically-pointing radar beam:

$$\sigma_{\mathrm{TV}_j}^2 = \overline{W_j^2} - \bar{W}_j^2 \tag{3.7}$$

Where $\sigma_{\mathrm{TV}_j}^2$ has units $\mathrm{m}^2\ \mathrm{s}^{-2}$, W is the reflectivity-weighted hydrometeor fall velocity, and j refers to the hydrometeor type. $\overline{W_j^2}$ and $\bar{W}_j^2$ are estimated by evaluating the following integrals:

$$\overline{W_j^2} = \frac{\int_0^\infty V_j(D)^2\, M_j(D)^2\, n_j(D)\, dD}{\int_0^\infty M_j(D)^2\, n_j(D)\, dD} \tag{3.8}$$

$$\bar{W}_j^2 = \left(\frac{\int_0^\infty V_j(D)\, M_j(D)^2\, n_j(D)\, dD}{\int_0^\infty M_j(D)^2\, n_j(D)\, dD} \right)^2 \tag{3.9}$$

Where $V_j(D)$, $M_j(D)$ and $n_j(D)$ are terminal velocity-diameter, mass-diameter and particle-size distribution (PSD) relationships for hydrometeor j, respectively, and D is the hydrometeor diameter in metres.

In (3.8) and (3.9), particle reflectivity is assumed to be proportional to $M_j(D)^2$. This is a reasonable assumption if in the Rayleigh scattering regime, which is almost always the case for a 3 GHz radar. For hydrometeor j, the radar reflectivity Z_j, is determined in linear units of $\mathrm{mm}^6\ \mathrm{m}^{-3}$ from the integral $Z_j = R_j \int_0^\infty M_j(D)^2\, n_j(D)\, dD$. The variable R_j (which is cancelled out in (3.8) and (3.9)) is a function of constants given by:

$$R_j = 10^{18} \frac{|K_j|^2}{|K_{\mathrm{water}}|^2} \left(\frac{6}{\pi \rho_j} \right)^2 \tag{3.10}$$

Where $\left|K_j\right|^2$ and ρ_j are the dielectric factor and density of hydrometeor j.

Terminal velocity-diameter relationships are commonly expressed as simple power laws:

$$V_j(D) = p_j D^{q_j} \tag{3.11}$$

Where V is the fall velocity and D is the drop diameter. For ice aggregates, D is the melted diameter. Values of p and q for raindrops, ice aggregates and hailstones are taken from Atlas and Ulbrich (1977), Gunn and Marshall (1958) and Cheng and English (1982), respectively. These have been converted into S.I. units (See Table 3.1).

The hydrometeor mass M, as a function of particle diameter D, can be expressed in the form:

$$M_j(D) = a_j D^{b_j} \tag{3.12}$$

Where M and D are in S.I. units.

The PSD of each hydrometeor class is assumed to be well approximated by an exponential distribution of form given by Marshall and Palmer (1948):

$$n_j(D) = N_{0_j} \exp\left(-\lambda_j D\right) \tag{3.13}$$

Where N_{0_j} and λ_j are the intercept ($n_j(D=0)$) and slope parameters, respectively, for hydrometeor type j. This is considered a suitable approximation; spectral broadening owing to a distribution in fall velocity has been shown to be nearly independent of the functional form of the hydrometeor PSD (Lhermitte, 1963).

For rain and ice aggregates, values of ρ, $|K|^2$, a, b and N_0, are sourced from the UK Met Office Unified Model microphysics scheme, as summarised in Stein *et al*. (2014) (See Table 3.1). For hail, an intercept parameter of $N_0 = 1.2 \times 10^4$ m^{-4} is taken from Waldvogel *et al*. (1978). As there is variability in values of N_{0_j} presented in the literature, the sensitivity of $\sigma^2_{\mathrm{TV}_j}$ to N_{0_j} is tested in Section 3.3.4.

Variable	Units	Rain	Aggregates	Hail
$\boldsymbol{\rho}$	kg m^{-3}	1000	917	917
$\lvert\boldsymbol{K^2}\rvert$	kg^2 m^{-6}	0.930	0.174	0.174
$\boldsymbol{p}$	m$^{1-\mathrm{q}}$ s^{-1}	386.6	8.34	142.6
$\boldsymbol{q}$	-	0.67	0.31	0.50
$\boldsymbol{a}$	kg m$^{-\mathrm{b}}$	523.6	0.0444	480.1
$\boldsymbol{b}$	-	3	2.1	3
$\boldsymbol{N_0}$	m^{-4}	8×10^{6}	6.8×10^{6}	1.2×10^{4}
$\boldsymbol{R}$	kg^2 m^{-6}	3.65×10^{12}	8.12×10^{11}	8.12×10^{11}

Table 3.1: Parameter values used in $\sigma^2_{\mathrm{TV}_j}$ calculations. The value of N_0 was calculated for aggregates using $N_0 = 2 \times 10^6 e^{(-0.1222 T_{\max})}$ from Cox (1988), assuming $T_{\max} = -10°\mathrm{C}$. The variable $\rho_j = 917$ kg m^{-3} is the density of solid ice, as assumed density for hail and ice aggregates.

To evaluate (3.7), (3.11) – (3.13) is first substituted into (3.8) and (3.9) using values from Table 3.1. By using a gamma function solution for the integrals resulting after substitution of this into (3.7), expressions are derived for the Doppler spectral variance contribution from the three hydrometeor types. At this point, they are functions only of PSD parameter, λ_j. An expression for λ_j is determined as a function of Z_j by evaluating $Z_j = R_j \int_0^\infty M_j(D)^2\, n_j(D)\, dD$ using (3.12) and (3.13), and rearranging for λ_j:

$$\lambda_j = \left(\frac{R_j a_j^2 N_{0_j} \Gamma\left(1 + 2b_j\right)}{Z_j} \right)^{\frac{1}{1+2b_j}} \tag{3.14}$$

Substituting (3.14) into the $\sigma^2_{\mathrm{TV}_j}(\lambda_j)$ expressions and simplifying using values from Table 3.1, produces spectral variance equations for rain, ice aggregates and hail:

$$\sigma^2_{\mathrm{TV}_{\mathrm{rain}}} = 0.62\, Z^{0.191} \sin^2 \theta_{\mathrm{el}} \tag{3.15}$$

$$\sigma^2_{\mathrm{TV}_{\mathrm{agg}}} = 0.029\, Z^{0.119} \sin^2 \theta_{\mathrm{el}} \tag{3.16}$$

$$\sigma^2_{\mathrm{TV}_{\mathrm{hail}}} = 1.7\, Z^{0.143} \sin^2 \theta_{\mathrm{el}} \tag{3.17}$$

Where Z is in $\mathrm{mm}^6\ \mathrm{m}^{-3}$, $\sigma^2_{\mathrm{TV}_j}$ has units of $\mathrm{m}^2\ \mathrm{s}^{-2}$ and θ_{el} is the elevation angle of the reflectivity observation measured from the surface. Together, these expressions can be used to estimate the Doppler variance contribution due to the distribution of hydrometeor fall speeds in V_6.

3.3.3 Analysis of $\sigma^2_{\mathrm{TV}_j}$

Reflectivity measurements in the observations with CAMRa are generally no less than -20 dBZ, and no more than 60 dBZ. In this application, the minimum and maximum potential variances considered are $\sigma^2_{\mathrm{TV}_j}(Z_j = -20\ \mathrm{dBZ})$ and $\sigma^2_{\mathrm{TV}_j}(Z_j = 60\ \mathrm{dBZ})$.

Equations (3.15) – (3.17) show that $\sigma^2_{\mathrm{TV}_j}$ increases with radar reflectivity and elevation angle of observation. For a vertically pointing radar beam, and given Z_j in the range of -20 dBZ to 60 dBZ, $\sigma^2_{\mathrm{TV}_{\mathrm{rain}}}$ increases from 0.26 to 8.62 $\mathrm{m}^2\ \mathrm{s}^{-2}$, $\sigma^2_{\mathrm{TV}_{\mathrm{agg}}}$ from 0.02 to 0.15 $\mathrm{m}^2\ \mathrm{s}^{-2}$ and $\sigma^2_{\mathrm{TV}_{\mathrm{hail}}}$ from 0.90 to 12.53 $\mathrm{m}^2\ \mathrm{s}^{-2}$. In the DYMECS observations, RHIs scanned at a maximum elevation angle of 15°. Figure 3.4 displays (3.15) – (3.17) for a vertically pointing beam (solid lines) and corresponding values at 15° elevation ('+' lines). Compared with a vertically pointing beam, if Z_j is sampled at 15° elevation, values of $\sigma^2_{\mathrm{TV}_j}$ are respectively reduced by a factor of 14.

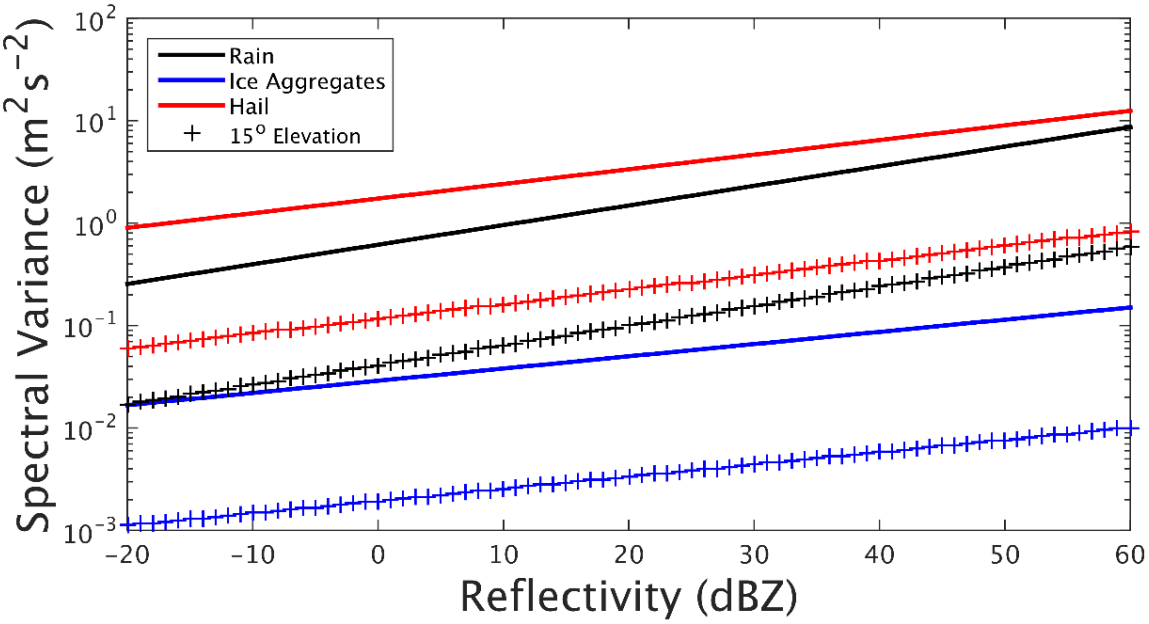

Figure 3.4: Change in $\sigma^2_{\mathrm{TV}_j}$ for rain, ice aggregates and hail, with radar reflectivity and elevation angle of observation. Solid lines refer to observations made at vertical incidence; '+' lines represent corresponding values when sampled at $\theta_{\mathrm{el}} = 15°$.

A maximum $\sigma^2_{\mathrm{TV_{agg}}}$ of 0.15 $\mathrm{m^2\ s^{-2}}$ suggests that the contribution from ice aggregates is always less than σ^2_{neg}. Assuming that ice aggregates constitute all hydrometeors above $z_{0°\mathrm{C}}$, then σ^2_{TV} is negligible for all observations made above this level. For rain, which is assumed to be limited to below $z_{0°\mathrm{C}}$, the equivalent maximum of 8.62 $\mathrm{m^2\ s^{-2}}$ is comparably large, and so $\sigma^2_{\mathrm{TV_{rain}}}$ cannot always be neglected. Equation (3.15) shows $\sigma^2_{\mathrm{TV_{rain}}}(60\ \mathrm{dBZ}) < \sigma^2_{\mathrm{neg}}$ for all rain observed at $\theta_{\mathrm{el}} < 13.9°$.

Under the circumstances that: $\sigma^2_{\mathrm{TV_{agg}}}$ is always negligible, $\sigma^2_{\mathrm{TV_{rain}}}$ is negligible when $\theta_{\mathrm{el}} < 13.9°$, $z_{0°\mathrm{C}}$ can be estimated, and hail is not present, the negligibility of σ^2_{TV} can be described purely in terms of distance from the radar. A minimum distance from the radar R_{min}, is estimated whereby if the range of a reflectivity observation is larger than R_{min}, σ^2_{TV} can be assumed negligible. This is a simple function of $z_{0°\mathrm{C}}$ such that:

$$R_{\mathrm{min}} = \frac{z_{0°\mathrm{C}}}{\tan(13.9°)} \tag{3.18}$$

Where both $R_{\min}$ and $z_{0°C}$ are in kilometres. In the case of the DYMECS RHI observations ($z_{0°C} \sim 1.5$ km), σ^2_{TV} is negligibly small everywhere at ranges further than 6.1 km from the radar. Due to rain occurring nearer than $R_{\min}$, but below $z_{0°C}$, σ^2_{TV} can still be significant due to rain occurring nearer than $R_{\min}$, below $z_{0°C}$, but remains conditional on both Z_{rain} and θ_{el}. The minimum range of observed clouds in DYMECS was approximately 30 km from the radar, and so σ^2_{TV} contributions from rain and ice aggregates are neglected under the assumption that liquid raindrops exist only below $z_{0°C}$.

Supercooled liquid raindrops can exist above $z_{0°C}$, especially in vigorous convective clouds. However, when scanning at $\theta_{\text{el}} = 13.9°$, the beam reaches a height of 7.4 km at 30 km range from the radar (the nearest observations), and 10 km (the approximate maximum observed cloud height) at 40 km range. This suggests that supercooled liquid raindrops would need to be observed with $Z = 60$ dBZ at least 7.4 km above the surface, and only between 30 – 40 km from the radar, for $\sigma^2_{TV_{\text{rain}}}$ to exceed σ^2_{neg}. This suggests that it is extremely likely that $\sigma^2_{TV_{\text{rain}}}$ can always be neglected in the DYMECS observations.

According to (3.17), hail can contribute more to σ_v^2 than rain. However, hail is generally a much less common, more localised occurrence than rain. As a result, the detection of hail using retrieved radar parameters (e.g. hail differential reflectivity H_{DR}, Depue *et al*. (2007)) is necessary before (3.17) can be reliably applied. If observations do indeed include hail, (3.17) suggests that $\sigma^2_{TV_{\text{hail}}}(60 \text{ dBZ})$ falls below σ^2_{neg} for all hail observations made at $\theta_{\text{el}} < 11.5°$. Due to the potential for hail presence both above and below $z_{0°C}$, negligibility based on range from radar is not stated. However, as the minimum range of observations was 30 km, hail would need to be observed at 6 km altitude for $\sigma^2_{TV_{\text{hail}}}$ to exceed σ^2_{neg}, which is unlikely to have occurred.

Based on the threshold for negligibility σ^2_{neg}, the estimation of $z_{0°C}$, and the assumptions made in the derivation of (3.15) – (3.17), variance contributions from σ^2_{TV} are neglected in the DYMECS observations.

3.3.4 Sensitivity of $\sigma^2_{\mathrm{TV}_{\mathrm{rain}}}$ and $\sigma^2_{\mathrm{TV}_{\mathrm{hail}}}$ to assumptions

This section summarises the sensitivity testing of (3.15) and (3.17) to some of the assumptions made in their derivation. For ice aggregates, no reasonable sensitivity testing (an order of magnitude increase and decrease in $N_{0_{\mathrm{agg}}}$, and reducing density to $500\ \mathrm{kg\ m^{-3}}$) has resulted in the factor three increase in $\sigma^2_{\mathrm{TV}_{\mathrm{agg}}}$ required to even conditionally exceed σ^2_{neg}. As a result, sensitivity tests involving ice aggregates have been omitted from this discussion, concluding that $\sigma^2_{\mathrm{TV}_{\mathrm{agg}}}$ is always negligible.

For rain and hail, little uncertainty is expected in the majority of values in Table 3.1. The first potential source of uncertainty lies with the treatment of hail as dry with the density of solid ice. Sensitivity to this assumption is tested by comparing $\sigma^2_{\mathrm{TV}_{\mathrm{hail}}}$ when hailstones are dry with the density of solid ice (as assumed in the derivation of (3.17)), to $\sigma^2_{\mathrm{TV}_{\mathrm{hail}}}$ from low-density and melting hailstones. Melting hailstones will possess a thin outer layer of liquid water, appearing to the radar as large raindrops. To simulate this effect, the dielectric factor $|K_{\mathrm{hail}}|^2$, in (3.10) is changed from 0.174 to 0.93. Resulting variance contributions are 21% lower than for dry hailstones for any given reflectivity. Assuming all hailstones below $z_{0°\mathrm{C}}$ have a liquid water layer, this reduction leads to $\sigma^2_{\mathrm{TV}_{\mathrm{hail}}}(60\ \mathrm{dBZ}) \approx \sigma^2_{\mathrm{TV}_{\mathrm{rain}}}(60\ \mathrm{dBZ})$ below $z_{0°\mathrm{C}}$. For observations made below $z_{0°\mathrm{C}} = 1.5\ \mathrm{km}$, (3.18) can be used to show that $\sigma^2_{\mathrm{TV}} < \sigma^2_{\mathrm{neg}}$ at all ranges further than 6.5 km from the radar, regardless of hydrometeor type. If further considering melting hailstones consisting of low-density ice ($\rho_{\mathrm{hail}} = 500\ \mathrm{kg\ m^{-3}}$), this leads to a combined reduction in $\sigma^2_{\mathrm{TV}_{\mathrm{hail}}}$ of 34%, at which point $\sigma^2_{\mathrm{TV}_{\mathrm{hail}}}(60\ \mathrm{dBZ}) < \sigma^2_{\mathrm{TV}_{\mathrm{rain}}}(60\ \mathrm{dBZ})$.

A second source of uncertainty lies with the chosen values of N_0; with respective values for rain and hail assumed constant. For rain, $N_{0_{\mathrm{rain}}} = 8 \times 10^6\ \mathrm{m^{-4}}$ is taken from Marshall and Palmer (1948), who demonstrate its independence of rainfall intensity. The assumption

of a constant $N_{0_{\text{hail}}}$ is not as safe as for raindrops as it depends on the largest hail diameter, $D_{\max}$, and has been shown to vary from 10^3 – 10^5 m^{-4} (Ulbrich, 1974). The value of $N_{0_{\text{hail}}} = 1.2 \times 10^4$ m^{-4} selected from Waldvogel *et al*. (1978) is roughly in the centre of this range and is very similar to values of $1.1 - 1.4 \times 10^4$ m^{-4} presented by Ulbrich (1977). To test the sensitivity of results to N_0, respective values for rain and hail are reduced by an order of magnitude. This decrease is chosen to be large enough to roughly account for the maximum potential variability in N_0. The result is a 55% increase in $\sigma^2_{\text{TV}_{\text{rain}}}$ and a 39% increase in $\sigma^2_{\text{TV}_{\text{hail}}}$. Such a large increase in $\sigma^2_{\text{TV}_{\text{rain}}}$ is unlikely given the confidence in the selection of $N_{0_{\text{rain}}}$ (Marshall and Palmer, 1948). However, the corresponding increase for $\sigma^2_{\text{TV}_{\text{hail}}}$ is more likely realised given the stated uncertainty in $N_{0_{\text{hail}}}$. Such an increase would imply that $\sigma^2_{\text{TV}_{\text{hail}}}(60\ \text{dBZ}) < \sigma^2_{\text{neg}}$ only if observed at $\theta_{\text{el}} < 9.8°$. By instead increasing values of N_0 by an order of magnitude (not shown), $\sigma^2_{\text{TV}_{\text{hail}}}$ and $\sigma^2_{\text{TV}_{\text{rain}}}$ are respectively reduced by 36% and 28%. In summary, only decreasing N_0 by an order of magnitude has resulted in larger variance contributions from rain and hail. The resulting percentage increase in $\sigma^2_{\text{TV}_{\text{hail}}}$ is not large enough to significantly change the criteria for negligibility, and for rain, the percentage increase is likely to be unrealistic given the confidence in the selected value of $N_{0_{\text{rain}}}$.

A final source of uncertainty lies with the selected velocity-diameter relationship for hail, $V_{\text{hail}}(D)$. There is broader diversity in $V_{\text{hail}}(D)$ in the literature than for rain; the $V_{\text{rain}}(\text{D})$ power law provided by Atlas and Ulbrich (1977) is assumed to be accurate. Figure 3.5 compares $\sigma^2_{\text{TV}_{\text{hail}}}$ derived using $V_{\text{hail}}(D)$ from Cheng and English (1982), Ulbrich (1977), and Pruppacher and Klett (1978). As the $V_{\text{hail}}(D)$ relationship provided by Ulbrich (1977) involves the same exponent ($q = 0.5$) as that used for (3.17), the resulting effect is a 29% increase in $\sigma^2_{\text{TV}_{\text{hail}}}$ for all reflectivity owing to the different values of p. The $V_{\text{hail}}(D)$ relationship from Pruppacher and Klett (1978) however, involves $q = 0.8$. This leads to a

change in exponent in (3.17), causing a decrease in $\sigma^2_{\mathrm{TV}_{\mathrm{hail}}}(Z < 40\ \mathrm{dBZ})$ and an increase for $\sigma^2_{\mathrm{TV}_{\mathrm{hail}}}(Z > 40\ \mathrm{dBZ})$. $\sigma^2_{TV_{\mathrm{hail}}}(60\ \mathrm{dBZ})$ is increased by 43%. Figure 3.5 suggests that the selection of $V_{\mathrm{hail}}(D)$ can have a substantial and varied effect on $\sigma^2_{\mathrm{TV}_{\mathrm{hail}}}$, which limits the precision of conditions under which $\sigma^2_{\mathrm{TV}_{\mathrm{hail}}}$ is negligible.

Listed among the four key assumptions required for the retrieval of ε using radar (see Section 1.4.2; assumption 4), the effects of turbulence must be reflected in the velocity of hydrometeors sampled within the beam. Hailstones falling at terminal velocity are the least likely hydrometeor type to satisfy this assumption, indicating that the retrieval of turbulence in falls of hail may be unreliable. Combining this with the discussed sources of uncertainty and the potential for high values of $\sigma^2_{\mathrm{TV}_{\mathrm{hail}}}$, sufficient care should be taken to identify the presence of hail in scanned clouds to ensure reliable retrievals of ε.

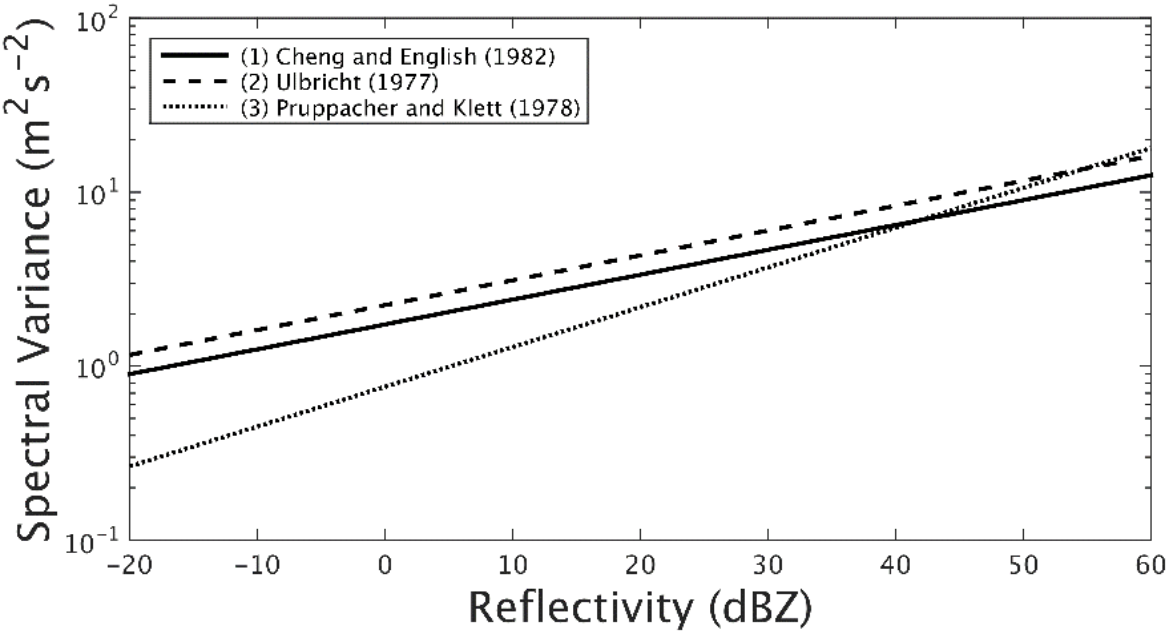

Figure 3.5: The impact on $\sigma^2_{\mathrm{TV}_{\mathrm{hail}}}$ of using different $V_{\mathrm{hail}}(D)$ relationships in the derivation of (3.17); (1) $p = 142.6,\ q = 0.5$; (2) $p = 162.0,\ q = 0.5$; (3) $p = 359.0,\ q = 0.8$. All plotted lines correspond to values of $\sigma^2_{\mathrm{TV}_{\mathrm{hail}}}$ sampled at vertical incidence ($\theta_{\mathrm{el}} = 90°$).

3.3.5 Conclusions

Equations (3.15) – (3.17) suggest that at vertical incidence, σ^2_{TV} can constitute a large proportion of σ^2_v, especially when sampling through heavy rain and hail. However, the contribution falls sharply with reflectivity and $\sin^2 \theta_{\mathrm{el}}$. Although a considered approach has been taken to ensure values stated in Table 3.1 are suitable, $\sigma^2_{\mathrm{TV}_{\mathrm{hail}}}$ is sensitive to N_0 and $V(D)$. Variation in these can lead to a 39%, and more than a 29% increase in $\sigma^2_{\mathrm{TV}_{\mathrm{hail}}}$, respectively.

Under the assumptions made in the derivation of (3.15) – (3.17):

- The variance contribution from ice aggregates is always negligibly small.
- In the absence of hail, σ^2_{TV} is negligible if observations are made at $\theta_{\mathrm{el}} < 13.9°$. If $z_{0°\mathrm{C}} < 1.5$ km, σ^2_{TV} is negligible at ranges further than 6.1 km from the radar. Equation (3.18) can be used to revise this distance for different values of $z_{0°\mathrm{C}}$.
- If wet hail is present but confined to below $z_{0°\mathrm{C}} = 1.5$ km, σ^2_{TV} is negligible at ranges further than 6.5 km from the radar.
- If dry hail is present (not confined to below $z_{0°\mathrm{C}}$), σ^2_{TV} is negligible if $\theta_{\mathrm{el}} < 11.5°$. If observations of dry hail are made at $\theta_{\mathrm{el}} > 11.5°$, (3.17) can be used to determine the variance contribution as a correction to σ^2_v will be required.
- The negligibility of σ^2_{TV} is considerably simpler to declare in the absence of hail. If there is potential for hail in observations, measures should be taken to identify its presence, especially in regions of high σ^2_v.

For DYMECS observations, clouds were rarely observed closer than 30 km from the radar, so contributions from σ^2_{TV} are neglected.

3.4 Doppler variance from shear of the radial wind

This section outlines methods to calculate the velocity variance due to shear of the radial wind across the radar beam, σ_s^2. This involves: (1) establishing the correct equations to calculate σ_s^2; (2) developing methods to calculate shear across a fixed scale throughout all observations; and (3) deriving statistical relationships between shear along the beam and shear in the azimuthal (transverse across the beam) direction – a dimension not sampled using RHIs, but that contributes to σ_v^2.

3.4.1 Equations for σ_s^2

So far in this chapter, variance terms σ_{TV}^2, σ_α^2, σ_{o}^2, σ_{B}^2 and σ_{H}^2 have been examined for significance relative to σ_{t}^2. When applied to observations collected with CAMRa, these terms individually provide a negligible variance in σ_v^2. When the effects are combined, the variance potentially included in σ_{t}^2 is expected to result in an over-estimation of ε by no more than 15% when $\sigma_{\mathrm{t}}^2 = 5\ \mathrm{m}^2\ \mathrm{s}^{-2}$, with the error decreasing as turbulence becomes more significant (red line in Figure 3.2). The remaining task, which is detailed in this section, is to separate the contributions to σ_v^2 from shear and turbulence, so that σ_{t}^2 can be found from:

$$\sigma_{\mathrm{t}}^2 \simeq \sigma_v^2 - \sigma_s^2 \tag{3.19}$$

and used in (1.25) to calculate ε.

In (3.19), σ_s^2 represents the sum of variance contributions from the shear of the mean Doppler velocity $\bar{v}$, in the elevation θ, azimuthal φ, and radial r, directions. Similar to σ_v^2, σ_s^2 can be decomposed into a sum of statistically independent variances from shear in each direction:

$$\sigma_s^2 = \sigma_{s\theta}^2 + \sigma_{s\varphi}^2 + \sigma_{sr}^2 \tag{3.20}$$

Various equations have been used in past literature to calculate $\sigma_{s\theta}^2$ and $\sigma_{s\varphi}^2$ that are not mutually consistent (e.g. Chapman and Browning, 2001). Due to the uncertainty in the literature, these equations are derived and presented here.

In the elevation, θ and azimuthal, φ dimensions of the beam, the Doppler variance contribution from shear, $\sigma_{\theta,\varphi}^2$, can be calculated from:

$$\sigma_{\theta,\varphi}^2 = (RS\sigma_2)^2 \tag{3.21}$$

Where S is the shear of $\bar{v}$ in the respective dimension, with units s^{-1}, R is the distance from the radar in metres, and σ_2 is the standard deviation of the two-way beam profile.

Assuming a circularly symmetric Gaussian beam pattern, the beam profile can be considered the same in both elevation and azimuthal dimensions. The one-way beam pattern, B can be described as,

$$B = e^{-\left(\frac{\theta^2}{2\sigma_1^2}\right)} \tag{3.22}$$

Where θ is the angle away from the beam axis, and σ_1 is the standard deviation of B. The two-way beam pattern is therefore simply:

$$B^2 = e^{-\left(\frac{2\theta^2}{2\sigma_1^2}\right)} = e^{-\left(\frac{\theta^2}{2\sigma_2^2}\right)} \tag{3.23}$$

Where it can be seen that $\sigma_2 = \frac{\sigma_1}{\sqrt{2}}$.

The one-way and two-way half-power beam widths are defined as θ_1 and θ_2, respectively, so that when $\theta = \pm\frac{\theta_1}{2}$, $B = \frac{1}{2}$. By substituting these values into (3.22) and rearranging, the variance of the one-way beam pattern is found in terms of θ_1:

$$\sigma_1^2 = \frac{\theta_1^2}{8\ln 2} \tag{3.24}$$

Since $\sigma_2 = \frac{\sigma_1}{\sqrt{2}}$, the variance of the two-way beam pattern, again in terms of θ_1, is found to be:

$$\sigma_2^2 = \frac{\theta_1^2}{16 \ln 2} \tag{3.25}$$

Which agrees with that stated in Doviak and Zrnic (1984; page 118, Equation 5.75). Substituting (3.25) into (3.21) provides equations to calculate Doppler variance due to shear of $\bar{v}$ in the elevation $\sigma_{s\theta}$, and azimuthal $\sigma_{s\varphi}$, directions:

$$\sigma_{s\theta}^2 = \frac{(|S_\theta| R\theta_1)^2}{16 \ln 2} \tag{3.26}$$

$$\sigma_{s\varphi}^2 = \frac{\left(|S_\varphi| R\theta_1\right)^2}{16 \ln 2} \tag{3.27}$$

An expression for variance due to shear along the beam σ_{sr}^2, is also taken from Doviak and Zrnic (1984), which assumes a rectangular transmitted pulse:

$$\sigma_{sr}^2 = \left(\frac{0.35 |S_r| c\tau}{2}\right)^2 \tag{3.28}$$

As the beam profile is the same in the θ and φ planes, (3.26) and (3.27) differ only by the observed shear. In (3.28), c is the speed of light in m s^{-1}, and τ is the pulse duration in seconds (for CAMRa, $\tau = 0.5$ µs). The shears S_θ, S_φ and S_r are found by differentiating $\bar{v}$ in the respective planes $\left(\frac{d\bar{v}}{d\theta}, \frac{d\bar{v}}{d\varphi}, \frac{d\bar{v}}{dr}\right)$, and have units of s^{-1}. For shear to be measured consistently along each plane, the length of $d\theta$, $d\varphi$ and dr is held to one constant, and each plane is centred on the beam axis. As the variance contribution is independent of the sign of S, magnitudes are used in (3.26) – (3.28). In each V_6, velocity gradients are assumed to be linear, and reflectivity is assumed to be uniform.

The variability of each component of σ_s^2 with $|S|$ is plotted in Figure 3.6, with a comparison made with σ_{neg}^2. In the case of $\sigma_{s(\theta,\varphi)}^2$, the curves are identical and are plotted corresponding to $|S|$ observed at 30 km and 150 km, which is the approximate minimum and maximum range of observed clouds. Variance from σ_{sr}^2 is independent of range owing to the fixed pulse length. For $|S_r|$ in the range of 0 to 0.02 s^{-1}, σ_{sr}^2 increases with $|S_r|^2$ from 0 to 0.28 $m^2\ s^{-2}$. If $|S_r| < 0.027\ s^{-1}$ then $\sigma_{sr}^2 < \sigma_{\text{neg}}^2$, indicating that for observations with CAMRa, σ_{sr}^2 is negligibly small except in cases of extreme shear. Although σ_{sr}^2 is generally small enough to neglect, the chosen method of calculating shear (Section 3.4.3) allows the direct measurement of $|S_r|$ to be made simply. Contributions from σ_{sr}^2 are therefore included in σ_s^2, and removed from σ_v^2.

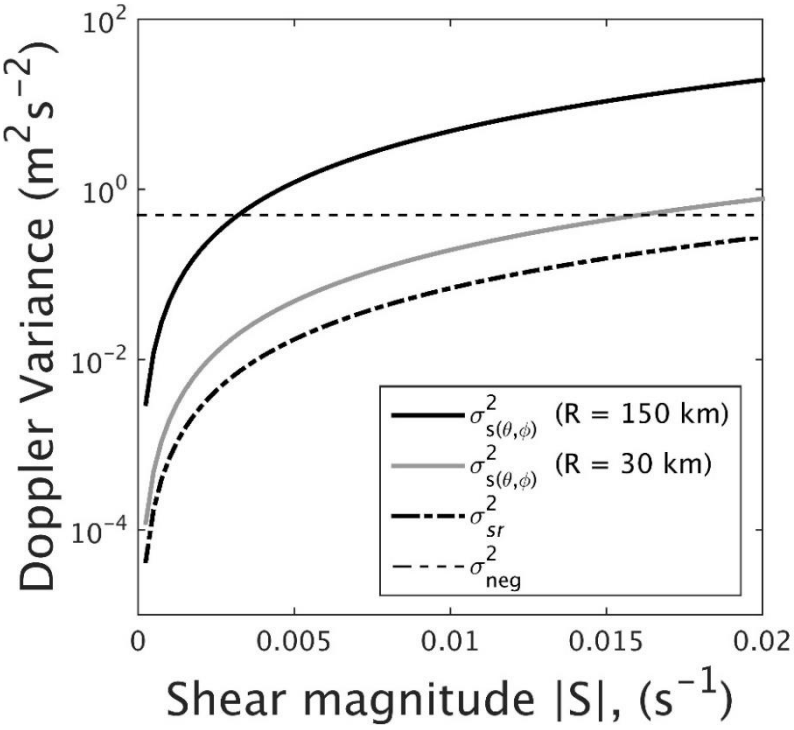

Figure 3.6: Doppler variance contribution from components of σ_s^2 as a function of observed shear magnitude $|S|$. For a given shear, $\sigma_{s\theta}^2$ and $\sigma_{s\varphi}^2$ are identical, and are plotted at the approximate minimum and maximum range of observations. The threshold of negligibility σ_{neg}^2, is plotted as a dashed line at 0.5 $m^2\ s^{-2}$ for comparison.

For shear observed in θ and φ directions at 30 km range, $\sigma^2_{s(\theta,\varphi)}$ increases from 0 to 0.75 $m^2\ s^{-2}$ for $|S_{\theta,\varphi}|$ in the range of 0 to 0.02 s^{-1}. At 150 km range, $\sigma^2_{s(\theta,\varphi)}$ increases to as much as 18.7 $m^2\ s^{-2}$ when $|S_{\theta,\varphi}|$ is 0.02 s^{-1}. This suggests that, even at the minimum range of 30 km, if $|S_{\theta,\varphi}| > 0.016\ s^{-1}$, then $\sigma^2_{s(\theta,\varphi)}$ is always greater than σ^2_{neg} for observations with CAMRa. Given that shears of this magnitude are quite possible (especially in the elevation direction), $\sigma^2_{s(\theta,\varphi)}$ will be considered for all of observations.

The high resolution of CAMRa means that radial velocity shears are often measured over small distances, and result in negligible contributions to σ_v^2, however, as shown, this is not true for shear of sufficient values. To ensure accuracy in point-to-point values of ε, and consistency in application across full RHI scans, σ_s^2 is measured and removed for every V_6 in the observations.

3.4.2 The separation of shear and turbulence - theory

The separation of shear and turbulence is a significant challenge. The high resolution of CAMRa means that the spatial scales of V_6 are likely to be within the inertial sub-range of turbulence. The calculation of σ_s^2 is necessary to remove velocity variance contributions to σ_v^2 from outside the range of scales sampled by the radar. This section aims to determine a suitable scale over which to calculate shear for DYMECS observations.

Methods to distinguish σ_s^2 from σ_t^2 are guided by the framework employed to derive ε from σ_v^2 summarised in Section 1.1.4. The scale over which to calculate shear in (3.26) – (3.28) (hereafter referred to as Λ_s), must be larger than the dimensions of V_6. If Λ_s is similar to the outer scale of the inertial sub-range Λ_0, then shear will largely arise from features in the flow that have scales outside the inertial sub-range. Variance due to these gradients are then removed from σ_v^2 using (3.26) – (3.28). However, Λ_s should not be larger than Λ_0,

otherwise variance from outside the inertial sub-range may be included in σ_t^2, leading to an over-estimation of ε.

Without the means to routinely determine Λ_0 for each of the convective storm observations collected in DYMECS, an estimation is made based on past literature. As summarised in Section 1.1.3, Λ_0 can vary from 0.4 – 3 km in storms of different scale and intensity and vary spatially within the cloud. The larger estimates of Λ_0 were made in severe thunderstorms/hailstorms with strong, large-scale circulations. In comparison, the convective storms constituting the DYMECS dataset are generally much weaker, which may limit how applicable these values are to these observations. An assumption is made that Λ_0 scales with the size of the largest eddy-generating mechanisms in a convective cloud, i.e. the main updraft circulation. If this circulation is shallow, Λ_0 is expected to be small as the downscale cascade to isotropic turbulence begins at a smaller eddy scale. As updraft heights on DYMECS case days generally ranged from 3 – 8 km (Nicol *et al*., 2015), Λ_0 is assumed to be ~ 1 km for this application. This includes a further assumption that Λ_0 remains constant throughout individual clouds. Chapman and Browning (2001) found a factor two change in Λ_0 to have very little effect on their resultant values of ε. However, this involved assuming a Λ_0 of only 200 m for shallow shear layers, so the sensitivity of retrieved ε to Λ_s is tested in Section 3.5.1.

3.4.3 The separation of shear and turbulence – velocity surface model

The application of methods to distinguish σ_s^2 from σ_t^2 will depend on the relationship between the spatial dimensions of V_6, and Λ_0. For CAMRa, the largest dimension of V_6 is less than the estimate of Λ_0, therefore σ_s^2 must be determined from gradients in $\bar{v}$ calculated in each plane over enough contiguous V_6 volumes to constitute a spatial scale of Λ_0. In RHI

data, only S_θ and S_r can be calculated directly, although variance due to S_φ will still contribute to σ_v^2. This section outlines methods to directly measure S_θ and S_r from RHI fields of $\bar{v}$, to determine $\sigma_{s\theta}^2$ and σ_{sr}^2. The variance from $\sigma_{s\varphi}^2$ is estimated through investigating a statistical relationship between S_φ and S_r in PPI observations; this is covered in Section 3.4.4.

To evaluate shear over a constant spatial scale in data with polar co-ordinates is not straight-forward. With two-dimensional radar data, the most effective way to achieve this is to use least-squares regression to fit a velocity surface to Doppler velocity data. A suitable framework for this velocity surface is taken from Neter and Wasserman (1974) and has been applied in previous turbulence retrieval studies (Istok and Doviak 1986, Meischner *et al*., 2001). When applied to RHIs, the velocity surface is given by:

$$v_i = v_0 + S_\theta \, l_{\theta_i} + S_r l_{r_i} + E_i \tag{3.29}$$

Where l_{θ_i} and l_{r_i} are the elevation and radial distances between v_i and v_0, given by:

$$l_{\theta_i} = R_0(\theta_i - \theta_0) \quad ; \quad l_{r_i} = R_i - R_0$$

In (3.29), R is the range from the radar, and θ is the elevation angle in radians, and S_θ and S_r are linear shears found by the model. This velocity model is applied individually to each V_6 in the RHI. Centred to best approximation on a selected Doppler velocity point, neighbouring data points are used to constitute (as closely as is possible) a Λ_s – by – Λ_s grid of data, G. Approximation is required in cases where G is not symmetrical about the central V_6, e.g. using $\Lambda_s = 1200$ m would require one extra 300-m radial cell on one side of the central point. In these cases, the bias is directed in the positive radial and elevation directions. The velocity found at the central point of G, v_0, is located at (θ_0, R_0), and v_i is the Doppler velocity at the point (θ_i, R_i).

This formulation aims to find S_θ, S_r and v_0 (hereafter referred to as output parameters) such that the error in velocity between G and the model, given at each data point by E_i, is minimised. The total square error is given by:

$$T = \sum_i E_i^2 \tag{3.30}$$

Where (3.29) is re-arranged to find:

$$E_i = v_i - v_0 - S_\theta \, l_{\theta_i} - S_r l_{r_i} \tag{3.31}$$

To minimise the total square error, T is differentiated with respect to the output parameters using (3.30) and (3.31) and set to zero:

$$\frac{\partial T}{\partial v_0} = \sum_i 2E_i \frac{\partial E_i}{\partial v_0} = \sum_i -2E_i = 0 \tag{3.32}$$

$$\frac{\partial T}{\partial S_\theta} = \sum_i 2E_i \frac{\partial E_i}{\partial S_\theta} = \sum_i -2l_{\theta_i} E_i = 0 \tag{3.33}$$

$$\frac{\partial T}{\partial S_r} = \sum_i 2E_i \frac{\partial E_i}{\partial S_r} = \sum_i -2l_{r_i} E_i = 0 \tag{3.34}$$

Applying the result of (3.32) – (3.34) to (3.31), produces three simultaneous equations that are most conveniently represented in the following matrix operation, where the constant factor of 2 cancels:

$$\begin{pmatrix} \sum_i 1 & \sum_i l_{\theta_i} & \sum_i l_{r_i} \\ \sum_i l_{\theta_i} & \sum_i l_{\theta_i}^2 & \sum_i l_{r_i} l_{\theta_i} \\ \sum_i l_{r_i} & \sum_i l_{\theta_i} l_{r_i} & \sum_i l_{r_i}^2 \end{pmatrix} \begin{pmatrix} v_0 \\ S_\theta \\ S_r \end{pmatrix} = \begin{pmatrix} \sum v_i \\ \sum v_i l_{\theta_i} \\ \sum v_i l_{r_i} \end{pmatrix} \tag{3.35}$$

The output parameters are then found from:

$$\begin{pmatrix} v_0 \\ S_\theta \\ S_r \end{pmatrix} = \begin{pmatrix} n & \sum l_{\theta_i} & \sum l_{r_i} \\ \sum l_{\theta_i} & \sum l_{\theta_i}^2 & \sum l_{r_i} l_{\theta_i} \\ \sum l_{r_i} & \sum l_{\theta_i} l_{r_i} & \sum l_{r_i}^2 \end{pmatrix}^{-1} \begin{pmatrix} \sum v_i \\ \sum v_i l_{\theta_i} \\ \sum v_i l_{r_i} \end{pmatrix} \tag{3.36}$$

Where n is the number of data points in G.

Each component on the right of (3.36) can be calculated directly from G, meaning the only prescribed variable for this model is the spatial scale over which it is applied, Λ_s. The lengths l_{θ_i} and l_{r_i} are calculated as absolute distances between the central points of v_0 and v_i. The output parameters are then attributed to the data point at the centre of G. By completing this process for all points in a scan, fields of S_θ and S_r are obtained for each V_6 in an RHI, which represent shear over a fixed spatial scale, Λ_s.

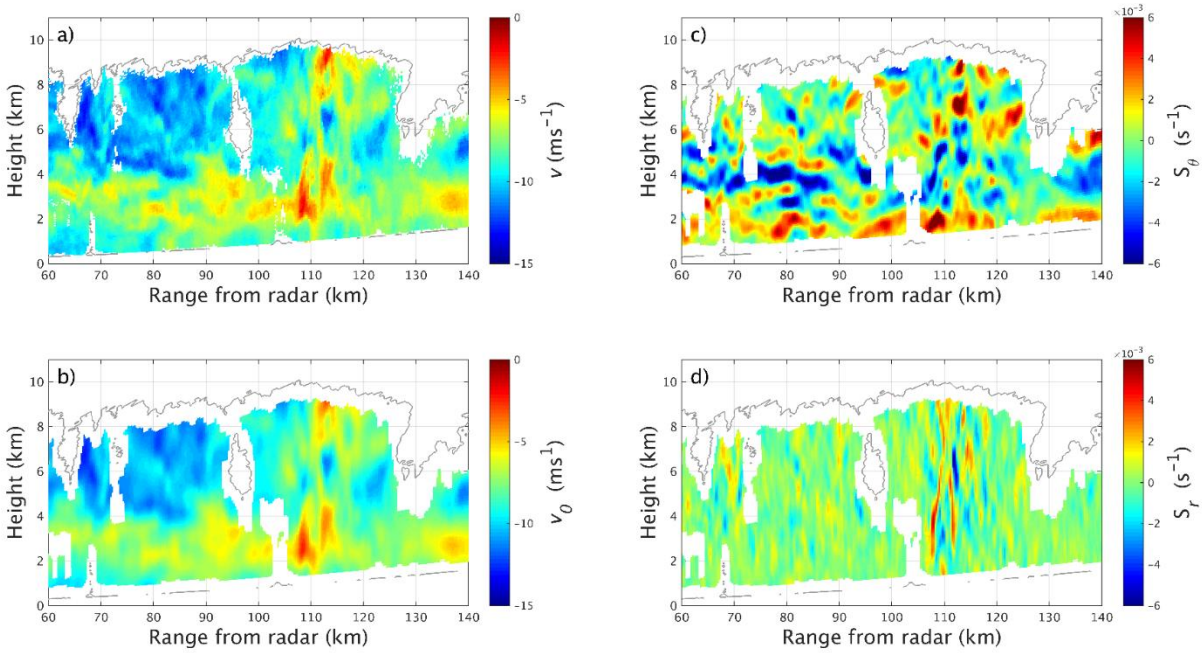

Figure 3.7: Application of velocity surface to determine shear in Doppler velocity over a scale of 900 m. (a) The mean Doppler velocity $\bar{v}$, from CAMRa, (b) the Doppler velocity v_0 from the velocity model synonymous with applying a 2-D smoothing to $\bar{v}$ over 900 m scale, (c) and (d) S_θ and S_r evaluated over 900 m scale in $\bar{v}$. The grey contour outlines the reflectivity returns to CAMRa for this case, data loss in (a) is due to removal by SNR, additional data loss in (b) – (d) is due to incomplete surface fitting at cloud edges.

Figure 3.7 shows an application of this model to a wind field observed on 25 August 2012, where Λ_s is set to 900 m. The Doppler velocity from CAMRa is shown in Figure 3.7a, and model outputs v_0, S_θ and S_r are shown in subplots (b), (c) and (d), respectively. In (b), v_0 is a comparable Doppler velocity to (a), however, it has been reconstructed using the gradients in the surrounding velocity. As a result, v_0 essentially results from smoothing (a) over 900 m in range and elevation, strongly attenuating velocity gradients on the scale of V_6. The shears in (c) and (d) represent the gradients in the smoothed velocity field that, if $\Lambda_s \sim \Lambda_0$, are associated with velocity scales outside the inertial sub-range of turbulence. The magnitude of these shears can therefore be used in (3.26) and (3.28) to remove Doppler variance due to shear. In applying this method, S_θ and S_r are defined for each data point in (a), this enables the point-for-point calculation, and removal, of shear-induced Doppler variance.

In applying (3.29) to observations, G will only be partially filled with data for those v located on the periphery of reflectivity echoes, meaning (3.36) cannot be performed. Data located less than $\sim \frac{\Lambda_s}{2}$ from the edge of observed clouds is lost, therefore the degree of data loss increases with Λ_s. In Figure 3.7, the grey contour outlines the full extent of reflectivity returns before removal of data by signal-to-noise ratio (SNR). In (a), the Doppler velocity has been corrected by SNR, however, the additional loss in data found in the fields from the velocity model result from application of (3.29) within $\sim \frac{\Lambda_s}{2}$ of the cloud edge. As σ_s^2 can only be accounted for where shear can be measured, this data loss is carried through to fields of ε.

The 300-m range resolution of the observations collected during DYMECS restricts values of Λ_s to multiples of 300 m in order to include whole radial cells, and a minimum of 600 m to include at least two radial cells for the calculation of shear. Under these restrictions, assuming $\Lambda_0 \sim 1$ km, a value of $\Lambda_s = 900$ m is applied to DYMECS observations.

3.4.4 Doppler variance from shear in the azimuthal direction, $\sigma_{s\varphi}^2$

When RHI or PPI scans are performed, the radial velocity field is observed in two dimensions, the radial direction and the scanning direction. Although displayed in two dimensions, these fields include data from three-dimensional sample volumes. In terms of RHIs, Doppler variances from azimuthal velocity gradients $\sigma_{s\varphi}^2$, will contribute to σ_v^2, but direct estimation is not possible due to scanning in the elevation direction. Unless an adjacent RHI is performed, separated from the first scan by an angular distance comparable to the width of the beam, S_φ cannot be determined directly. As shown in Section 3.4.1, variance contributions from $\sigma_{s\varphi}^2$ cannot be ignored for this application. To account for $\sigma_{s\varphi}^2$ in circumstances where it cannot be measured directly, statistical relationships are sought between $|S_\varphi|$ and $|S_r|$ using PPI radar observations.

PPI scans were performed alongside RHIs scans on DYMECS case days. Doppler velocity fields from PPI scans can be differentiated in the radial and azimuthal directions to determine fields of $|S_\varphi|$ and $|S_r|$. By collecting many co-located pairs of $|S_\varphi|$ and $|S_r|$ from these fields, $|S_\varphi|$ can be parametrised as a function of $|S_r|$. Applying the result to RHIs, each $|S_r|$ can be used to estimate a corresponding value of $|S_\varphi|$, and its uncertainty. This accounts for all components of σ_s^2, removing variance that would otherwise have been included in σ_t^2.

In order for relationships derived between $|S_\varphi|$ and $|S_r|$ to be of most benefit, shear must be calculated over a mutual spatial scale. This must also be consistent with that used to calculate $|S_\theta|$ and $|S_r|$ in RHIs, i.e. Λ_s = 900 m. To achieve this, a version of (3.29) tailored to PPI scans is used, where $S_\theta l_{\theta_i}$ is replaced by $S_\varphi l_{\varphi_i}$, and l_{φ_i} is the azimuthal distance between v_i and v_0. By generating pairs of $|S_\varphi|$ and $|S_r|$ values for each V_6 across many PPIs, a dataset of co-located values of $|S_\varphi|$ and $|S_r|$ was produced for statistical assessment.

Figure 3.8a shows the combined two-dimensional distribution of approximately 10^6 pairs of S_φ and S_r sourced from 31 PPIs performed on 20 April 2012, at angles of elevation

ranging from $\theta_{\mathrm{el}} = 0.5 - 5°$. The distribution is approximately 2-D Gaussian in shape, and roughly centred on $S_r = S_\varphi = 0$. The circular, symmetrical shape reveals that there is little correlation between the sign and magnitude of S_φ and S_r. However, it does suggest that the same range of shear values are observed in each direction, which appear normally distributed around $S_r = S_\varphi = 0$. This further suggests that there is little discernible bias in the data. Which indicates that, together, the PPIs include observations of wind vectors made at a full range of sampling angles. Figure 3.9a displays an equivalent 2-D histogram for 5×10^5 pairs of S_φ and S_r sourced from 31 PPIs performed on 25 August 2012. The resulting distribution is very similar in shape to Figure 3.8a (albeit with fewer data points), indicating that the shear statistics are consistent between the two cases. As a result, statistical relationships between $|S_\varphi|$ and $|S_r|$ derived from the shower cloud data later in this section can be reliably applied to retrievals for both cases.

The independent distributions of S_φ and S_r in the shower cloud, shown in Figure 3.8b, were produced by integrating the 2-D distribution along lines of $S_r = 0$ and $S_\varphi = 0$, respectively. Both S_φ and S_r are approximately normally distributed, however, a small positive bias is evident in S_r. Closer inspection reveals that 52.7% of S_r values are positive, compared to only 50.4% of S_φ values. This is a notable bias considering the sample size (5.4×10^4 more positive values, than negative), and one that primarily seems to affect S_r. To investigate this, any inconsistencies between the sampling of S_r and S_φ were considered.

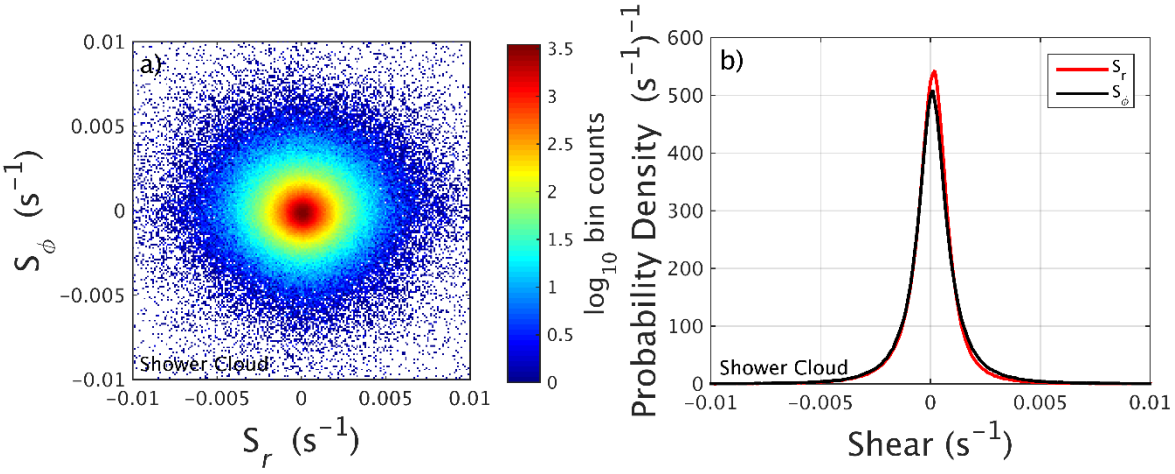

Figure 3.8: (a) 2-D histogram comprised of ~ 10^6 pairs of S_φ and S_r from 31 PPIs performed on 20 April 2012. A bin-width of 10^{-4} s^{-1} is used, and counts are expressed in $\log_{10}$ units. (b) The independent distributions of S_φ and S_r.

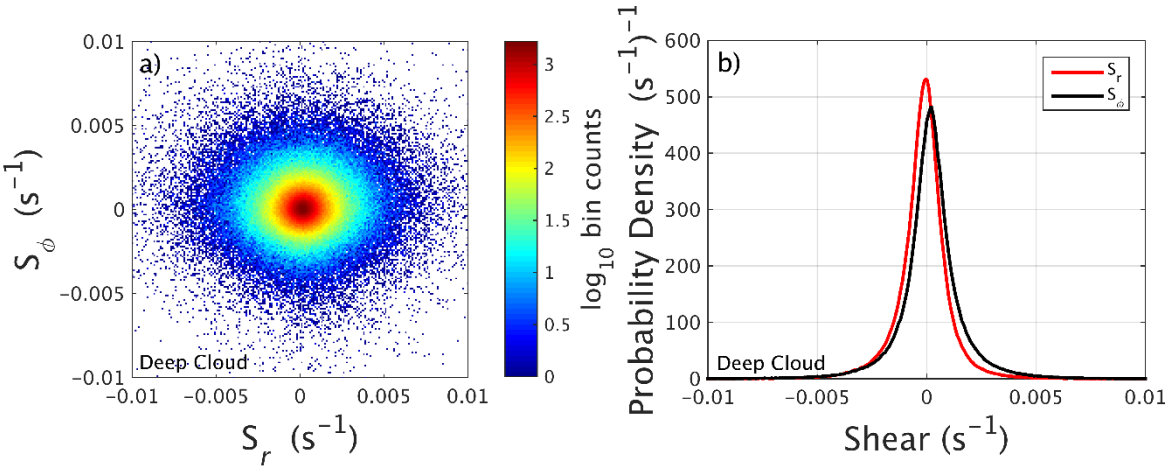

Figure 3.9: Equivalent to Figure 3.8 for deep cloud S_φ and S_r.

A likely reason for the 2.7% positive bias in S_r (hereafter referred to as ΔS_r) appears to be contamination of radial gradients in v by a positive background vertical shear, owing to scanning at non-zero elevation. Figure 3.10 provides a simplified plan view of a 90° PPI sector scan performed at a non-zero elevation, with the radar located in the bottom-left. For a given V_6 (shown in purple), the gradient in velocity between v_1 and v_2 (S_r) will sample any vertical shear that exists between z_2 and z_3, at an angle of θ_{el}. However, the gradient in velocity between v_3 and v_4 (S_φ) will not be affected due to its measurement along an arc of equal height. If the background vertical shear is non-zero, a bias will result in S_r that is not seen in S_φ.

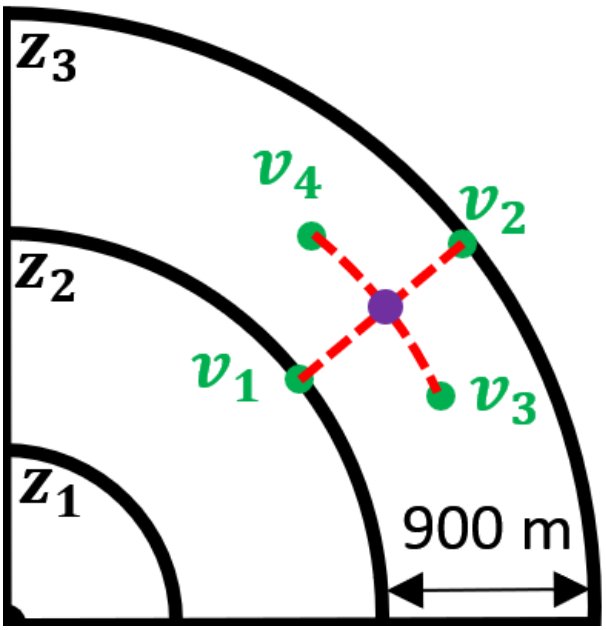

Figure 3.10: A plan view of a 90° PPI sector scan performed at non-zero elevation. Radial gradients in velocity S_r, (v_1 to v_2) are made over an increase in height ($Z_3 - Z_2$), whereas azimuthal gradients are not. If environmental vertical shear is non-zero, this introduces biases in S_r.

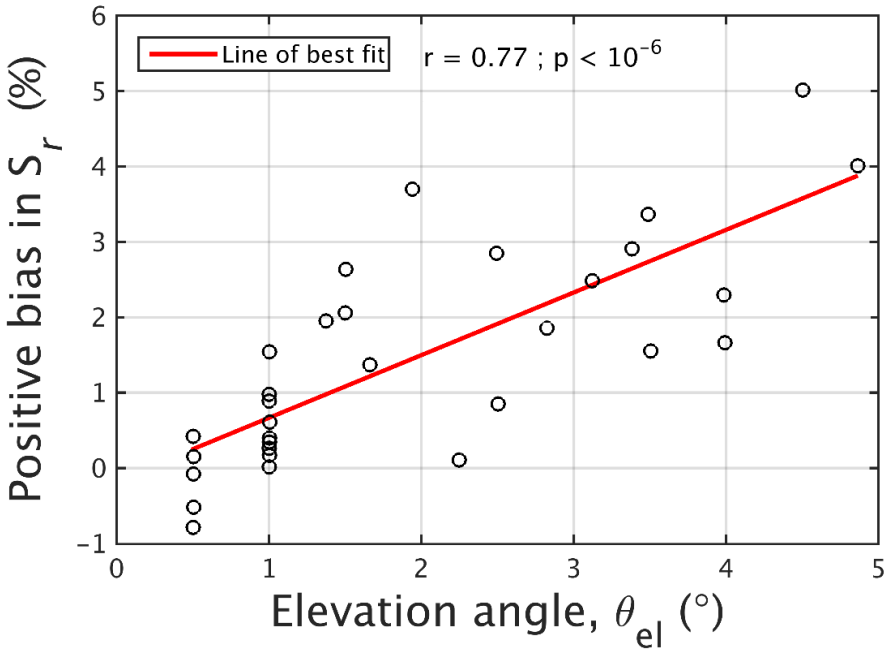

Figure 3.11: Significant positive correlation between the degree of positive bias in radial shear S_r, and elevation angle, θ_{el}.

Any S_r observed at non-zero elevation will be a function of horizontal shear S_x, vertical shear, S_z and θ_{el}:

$$S_r = S_x \cos(\theta_{\text{el}}) + S_z \sin(\theta_{\text{el}}) \tag{3.37}$$

The degree to which S_z is responsible for ΔS_r can be estimated using (3.37) for $\theta_{\text{el}} = 1.95°$ – the average elevation of the 31 PPIs. The observed bias only results when S_x is negative, and S_r is turned positive by the influence of S_z. The distribution of S_x is unknown, but due to low elevation scanning, it is assumed to be very similar to that of S_r. By setting $S_r = 0$ in (3.37) and setting S_x to the 47.3th percentile of S_r, the S_z required to result in $\Delta S_r = 2.7\%$, is estimated to be a realistic value of 1.4×10^{-3} s^{-1}. As θ_{el} increases, a larger component of S_z would be sampled. Therefore, ΔS_r would be expected to increase with θ_{el}. Figure 3.11 displays a scatter plot of ΔS_r and θ_{el} from each of the 31 PPIs. The result is a statistically significant positive correlation ($r = 0.77; p < 10^{-6}$), which strongly suggests ΔS_r results from contamination by S_z. It is worth noting that when sampling clouds against the mean flow, the radar will observe a negative elevation shear in Doppler velocity when S_z is positive. On 20 April 2012, the mean flow was south-westerly. For the 31 PPIs considered in this analysis, the mean azimuthal scanning angle weighted by the data counts contained in each scan was 3.5° (approximately northerly). Therefore, on average, scans were collected in the direction of the flow (albeit at an angle of 40°), providing further evidence that the observed positive bias in S_r has resulted from contamination from positive background vertical shear. Interestingly, a 2.7° positive bias in S_r was also found in the deep cloud analysis (see Figure 3.9b). In this case, the weighted mean azimuthal scanning angle (119.4°) was at a similar angle (30°) to the eastward cloud motion.

Once the magnitude of S_φ and S_r is taken, which is the quantity relevant to σ_s^2, ΔS_r will translate to a small positive bias in $|S_r|$ that varies with the sampling elevation. Statistical relationships between $|S_\varphi|$ and $|S_r|$ will reflect this bias for an average θ_{el} of 1.95°.

However, because the bias is small, and $|S_r|$ is sampled at a range of elevations in RHIs, these relationships are expected to remain accurate.

To derive statistical relationships between $|S_\varphi|$ and $|S_r|$, $|S_r|$ is first divided into contiguous intervals of width $1 \times 10^{-4}\ \mathrm{s}^{-1}$. For each of these intervals, the associated dataset of $|S_\varphi|$ is extracted, and its probability density function (PDF) in generated. Figure 3.12 demonstrates that the resulting PDFs are very well approximated by the gamma distribution, given for a random variable x, by:

$$\gamma(x|k,l) = \frac{x^{k-1}e^{-\frac{x}{l}}}{\Gamma(k)l^k} \tag{3.38}$$

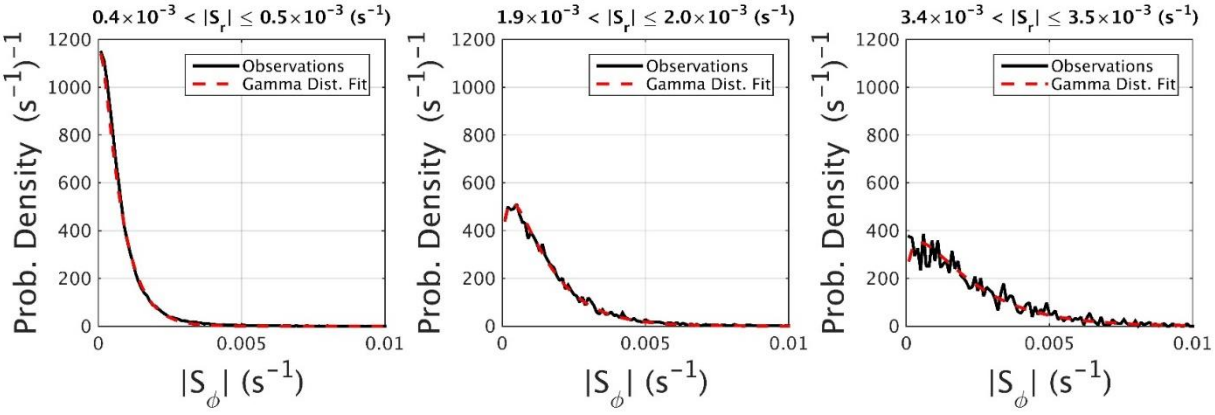

Figure 3.12: Change in the PDFs of observed $|S_\varphi|$ for three selected intervals of $|S_r|$ (solid black lines). Distributions of $|S_\varphi|$ are well approximated by Gamma PDFs (3.38). The width of each $|S_r|$ interval is $1 \times 10^{-4}\ \mathrm{s}^{-1}$, and the interval of $|S_r|$ for each distribution is displayed in the figure titles.

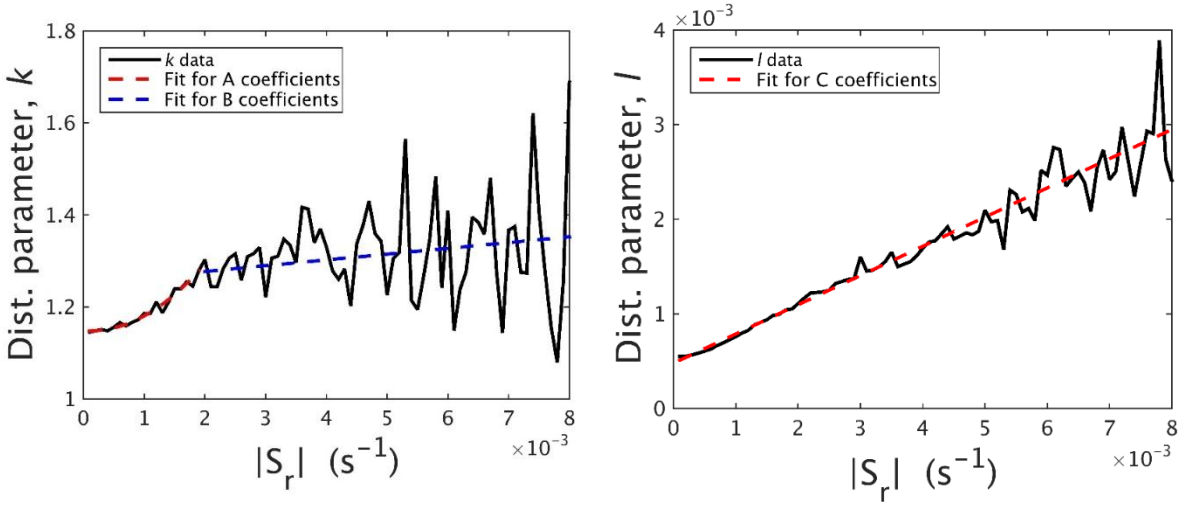

Figure 3.13: (Left) Quadratic ($|S_r| < 0.0017$ s^{-1}) and linear ($|S_r| > 0.0017$ s^{-1}) functions fit to k (3.39). (Right) Linear function fit to l (3.40).

Figure 3.12 further illustrates that the change in the distribution of $|S_\varphi|$ with $|S_r|$ can be accurately simulated using (3.38). For each $|S_r|$ interval, the gamma distribution parameters k (shape) and l (scale) are extracted from the corresponding distribution of $|S_\varphi|$. Figure 3.13 displays the change in these distribution parameters with $|S_r|$. By numerically fitting functions to relationships between (k, l) and $|S_r|$, k and l are defined in terms of $|S_r|$. A quadratic function is used to model k for $|S_r| < 0.0017$ s^{-1}, with a linear function fit to k for $|S_r| < 0.0017$ s^{-1}. The quadratic function is chosen to more closely model k for small values of $|S_r|$, which are far more frequently encountered (88% of $|S_r|$ values). A linear function is applied to approximate k for $|S_r| > 0.0017$ s^{-1}, where k is variable owing to corresponding $|S_\varphi|$ data becoming increasingly sparse. A linear function accurately models l throughout all values of $|S_r|$. The resulting quadratic and linear expressions are a function only of $|S_r|$, with coefficient values included in Table 3.2:

$$k = \begin{cases} |S_r|(A_1|S_r| + A_2) + A_3, & \text{if } |S_r| \leq 0.0017 \text{ s}^{-1} \\ B_1|S_r| + B_2, & \text{otherwise} \end{cases} \tag{3.39}$$

$$l = C_1|S_r| + C_2 \tag{3.40}$$

Coefficient	Value	Coefficient	Value
$\boldsymbol{A_1}$	40212.80	D_1	5.77
$\boldsymbol{A_2}$	-7.91	D_2	0.39
$\boldsymbol{A_3}$	1.15	D_3	0.00057
$\boldsymbol{B_1}$	18.65	E_1	5.73
$\boldsymbol{B_2}$	1.22	E_2	0.29
$\boldsymbol{C_1}$	0.31	E_3	0.00043
$\boldsymbol{C_2}$	0.00048	-	-

Table 3.2: Coefficient values A – C used in (3.39) and (3.40) to determine $|S_\varphi|$ distribution parameters from $|S_r|$. Coefficient values D – E used in (3.41) and (3.42), respectively, to calculate mean and median values of $|S_\varphi|$ from $|S_r|$.

For a given value of $|S_r|$, (3.39) and (3.40) are used to produce a corresponding PDF of $|S_\varphi|$. An estimate of $|S_\varphi|$ is then derived as the mean of this PDF, where the mean of the gamma distribution is simply the product of k and l. The median, and 25th and 75th percentiles of the distribution are also determined. By recording these statistics from distributions corresponding to a spectrum of $|S_r|$ values, and least-squares fitting quadratic functions to the result, (3.39) and (3.40) can be refined into expressions relating the mean, $|S_\varphi|_{\mathrm{mn}}$, and median, $|S_\varphi|_{\mathrm{md}}$, with $|S_r|$:

$$|S_\varphi|_{\mathrm{mn}} = |S_r|(D_1|S_r| + \mathrm{D}_2) + D_3 \tag{3.41}$$

$$|S_\varphi|_{\mathrm{md}} = |S_r|(E_1|S_r| + \mathrm{E}_2) + E_3 \tag{3.42}$$

where coefficient values are again provided in Table 3.2.

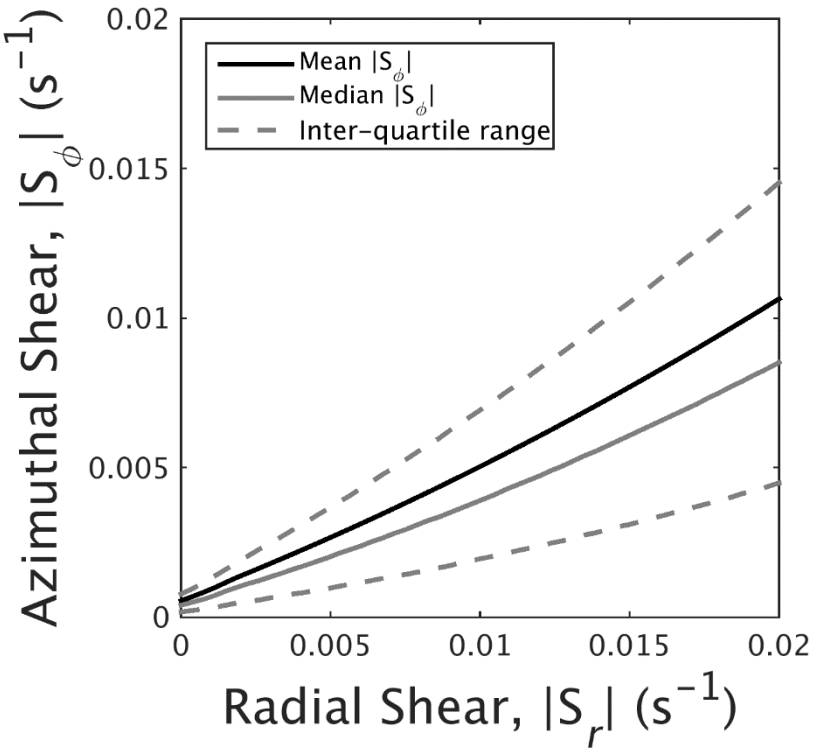

Figure 3.14: The change median (3.41), mean (3.42) and inter-quartile range values of $|S_\varphi|$ with $|S_r|$.

Figure 3.14 shows the change in mean, median and inter-quartile range (IQR) percentiles of $|S_\varphi|$ with $|S_r|$. Distributions of $|S_\varphi|$ get broader with $|S_r|$ (as displayed in Figure 3.12), and as a result, the size of the IQR increases with $|S_r|$. Values of $|S_\varphi|_{\mathrm{md}}$ increase with $|S_r|$ according to (3.42), with $|S_\varphi|_{\mathrm{mn}}$ values approximately 25% larger than $|S_\varphi|_{\mathrm{md}}$. The skew of the gamma distribution towards small values results in mean and median values that are lower than the $|S_r|$ used to generate the $|S_\varphi|$ distribution. This effect is illustrated in Figure 3.14, where $|S_\varphi|_{\mathrm{mn}}$ and $|S_\varphi|_{\mathrm{md}}$ values are roughly half of $|S_r|$, becoming ~ 0.01 s^{-1} for the largest observed values of $|S_r| = 0.02\ \mathrm{s}^{-1}$. This apparent limit to $|S_\varphi|$ is likely to lead to under-estimation of $|S_\varphi|$ in cases where $|S_\varphi|$ is otherwise larger than 0.01 s^{-1}. Due to the increased potential for including biases in ε when shear correction has been significantly

under-estimated, $|S_\varphi|_{\text{mn}}$ is chosen to estimate $|S_\varphi|$, due to the capacity of (3.41) to predict larger shear values.

The standard deviation of $|S_\varphi|_{\text{mn}}$ (given by $|S_\varphi|_{\text{SD}}$) provides an indication to the degree of uncertainty in $|S_\varphi|_{\text{mn}}$ and can be determined by using (3.39) and (3.40) to compute $l\sqrt{k}$. Figure 3.15 displays the ratio of $|S_\varphi|_{\text{SD}}$ to $|S_\varphi|_{\text{mn}}$, expressed as a function of $|S_\varphi|_{\text{mn}}$. The ratio decreases from 0.93 – 0.79 for $|S_\varphi|_{\text{mn}}$ in the range of 0 – 0.02 s^{-1}. This indicates that the uncertainty in $|S_\varphi|_{\text{mn}}$ is large, reflecting the apparent lack of correlation in S_φ and S_r illustrated in the 2-D distribution displayed in Figure 3.8a.

To estimate the error in σ_s^2 resulting from this uncertainty, typical shear values are selected for $|S_r|$ and $|S_\theta|$, observed at the typical 60-km range of observations. In the case where $|S_r| = |S_\theta| = 5 \times 10^{-3}\ \text{s}^{-1}$, $|S_\varphi|$ is determined from (3.41) to be $2.7 \times 10^{-3}\ \text{s}^{-1}$, with an error of 89% from Figure 3.15. Substituting these shears into (3.26) – (3.28), (3.20) is then used to determine the change in σ_s^2 when $|S_\varphi|$ is both 89% larger and smaller than $2.7 \times 10^{-3}\ \text{s}^{-1}$. When 89% larger, σ_s^2 increases by 54%, and when 89% smaller, σ_s^2 decreases by 21%. This suggests that σ_s^2 is sensitive to the uncertainty in $|S_\varphi|$ when $|S_r| \sim |S_\theta|$. However, $|S_r|$ is typically much smaller than $|S_\theta|$ in observations. By repeating this procedure for $|S_\theta| = 5 \times 10^{-3}\ \text{s}^{-1}$ and $|S_r| = 1 \times 10^{-3}\ \text{s}^{-1}$, an 89% increase in $|S_\varphi|$ only results in a 9% increase in σ_s^2, and a 4% decrease when $|S_\varphi|$ reduced by 89%. This indicates that σ_s^2 is insensitive to the uncertainty in $|S_\varphi|$ when $|S_r| \ll |S_\theta|$; which is typical for these observations.

Using (3.41), $|S_\varphi|_{\text{mn}}$ can be determined from $|S_r|$ alone, which is then used in (3.27) to calculate its variance contribution, $\sigma_{s\varphi}^2$. All components of σ_s^2 in (3.20) can be accounted for and subtracted from σ_v^2 to find $\sigma_\mathfrak{t}^2$ using (3.19), which in turn is applied in (1.25) to find ε.

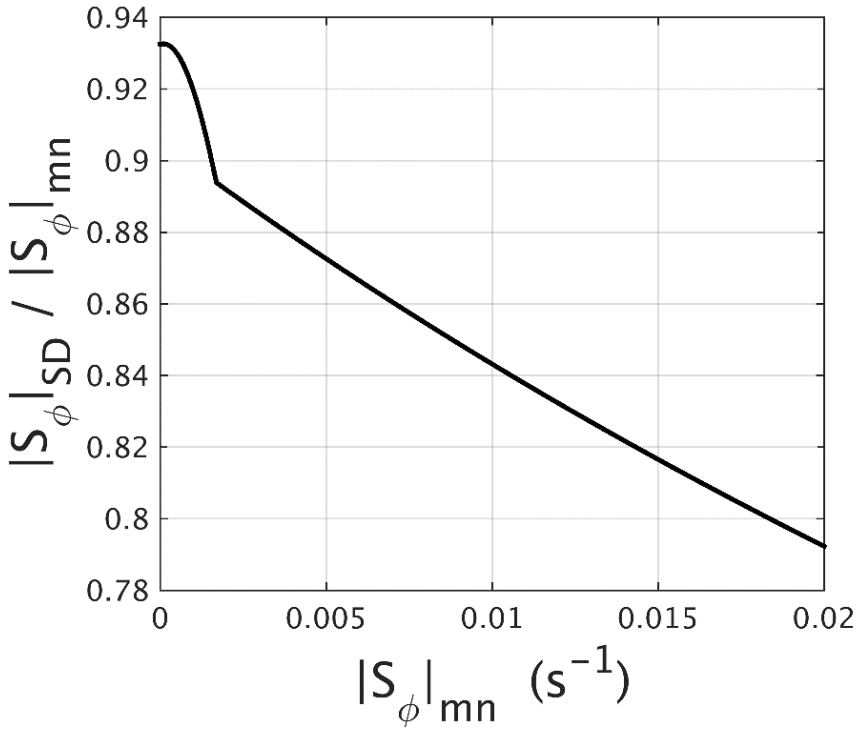

Figure 3.15: The standard deviation $|S_\varphi|_{\mathrm{SD}}$, normalised by the mean shear value, $|S_\varphi|_{\mathrm{mn}}$, and expressed as a function of $|S_\varphi|_{\mathrm{mn}}$. The ratio decreases with $|S_\varphi|_{\mathrm{mn}}$ from 0.93 – 0.79 for $|S_\varphi|_{\mathrm{mn}}$ of 0 – 0.02 s^{-1}.

3.5 Eddy dissipation rates

Based on the uncertainty in the scale over which to calculate shear Λ_s in Section 3.4, this brief section examines the sensitivity of retrievals of ε to Λ_s.

3.5.1 Sensitivity of ε to Λ_s

The selection of the scale over which to calculate shear Λ_s, was made through estimation of the outer-scale of the inertial sub-range Λ_0, for the DYMECS observations (see Section 3.4.2). This considered reference values for Λ_0 determined for various convective scenarios from the literature. By assuming Λ_0 scales with the depth of convective motions, and under

limitations from data resolution, an estimation of $\Lambda_0 = 900$ m was made for DYMECS observations, which was then selected for Λ_s. Due to the uncertainty in this value, and the assumption that Λ_0 is the same throughout all observed clouds, the sensitivity of retrieved ε to Λ_s is investigated.

To perform this sensitivity test, ε is determined in RHI scans of convective clouds using different values of Λ_s in methods to calculate σ_s^2. This analysis involves 44 RHI scans performed on 25 August 2012 which provide 3.5×10^5 comparable values of ε for each Λ_s applied. For each RHI, $\varepsilon(\Lambda_s)$ is determined where Λ_s is 600 m, 900 m, 1500 m, 2100 m, and 2700 m, where $\varepsilon(\Lambda_s = 900 \text{ m})$ is chosen as a control ε_c, to assess the impact of changing Λ_s on the retrievals of ε. As described in Section 3.4.3, the degree of data loss on the periphery of reflectivity echoes increases with Λ_s when fitting the velocity surface. To ensure the comparison of ε is consistent across different Λ_s, the largest data loss (when $\Lambda_s = 2700$ m) is imposed on all $\varepsilon(\Lambda_s)$ for each RHI scan.

Figure 3.16 displays the PDFs of $\varepsilon(\Lambda_s)$ using the combined data from all RHIs. It shows that the distribution of ε is largely insensitive to Λ_s, though there is a small reduction in the likelihood of low values of ε (less than 0.01 m^2 s^{-3}) with decreases in Λ_s. When calculating shear over a smaller Λ_s, the shear magnitude, and therefore σ_s^2, is likely to be higher. This means more of σ_v^2 is removed due to shear, and the derived ε is subsequently lower, with the converse true if Λ_s is large. To quantify the sensitivity of ε_c to this effect beyond the qualitative interpretation of PDFs, the ratio of $\varepsilon(\Lambda_s)$ to ε_c is recorded for each individual data point. Through determining the mean of this ratio for data points falling in intervals of ε_c, the effect is further expressed as a function of ε_c.

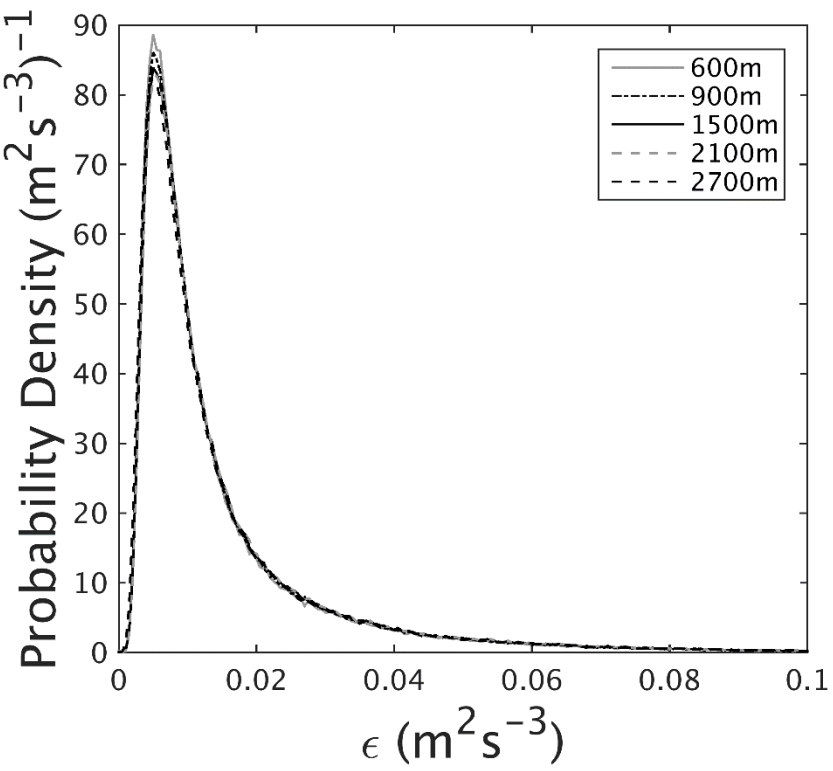

Figure 3.16: The insensitivity of probability density distributions of ε to the scale Λ_s, over which shear is calculated for σ_s^2.

Figure 3.17 and Figure 3.18 show the change in the mean and standard deviation, respectively, of $\varepsilon(\Lambda_s)/\varepsilon_c$ with ε_c for different values of Λ_s. When $\Lambda_s < 900$ m, the resulting mean ε is smaller than ε_c. This results from the removal of more variance from σ_v^2 when shear is calculated over a finer scale, i.e. σ_s^2 is larger due to stronger velocity gradients measured over smaller scales, meaning σ_t^2, and therefore ε, is reduced. Conversely, when $\Lambda_s > 900$ m, mean ε is larger than ε_c due to weaker shears observed over larger scales, leading to smaller corrections to σ_v^2 from σ_s^2, and therefore larger ε.

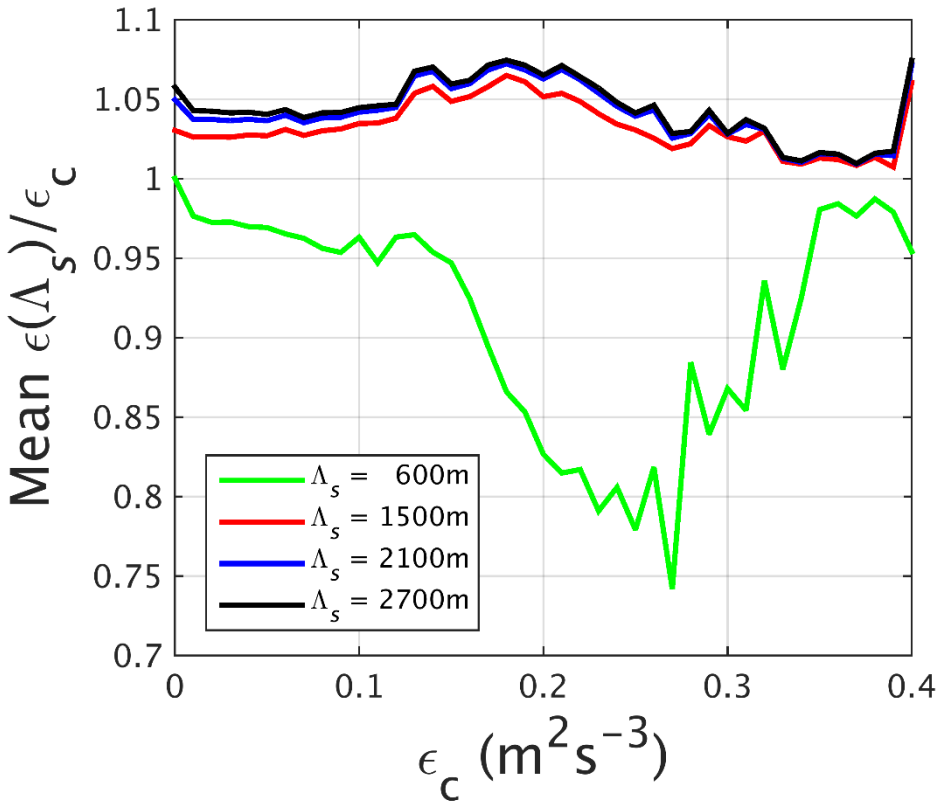

Figure 3.17: The sensitivity of ε_c to Λ_s determined by calculating the mean ratio of $\varepsilon(\Lambda_s)$ to ε_c for different intervals of ε_c. Each interval has a width of 0.01 m^2 s^{-3}.

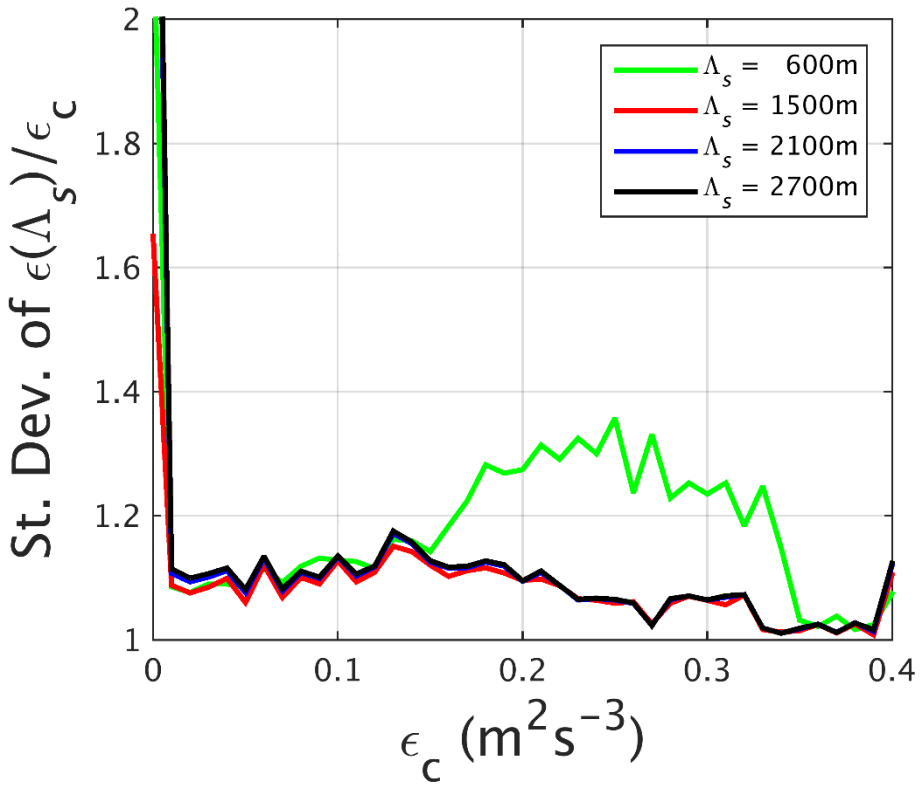

Figure 3.18: The standard deviation of the mean ratio of $\varepsilon(\Lambda_s)$ to ε_c for different intervals of ε_c. Each interval has a width of 0.01 m^2 s^{-3}.

For $\varepsilon_c < 0.1\ m^2\ s^{-3}$ (which contains 98.7% of ε_c observations), mean $\varepsilon(\Lambda_s)$ differs from ε_c by less than 5%, with a near-constant standard deviation of 10% (shown in Figure 3.18). This suggests that when $\varepsilon_c < 0.1\ m^2\ s^{-3}$, ε_c is insensitive to any change in Λ_s. For $\varepsilon_c > 0.1\ m^2\ s^{-3}$ however, mean $\varepsilon(\Lambda_s)$ differs from ε_c by an increasing, and then decreasing amount with ε_c. For $\Lambda_s > 900$ m, $\varepsilon(\Lambda_s)$ does not differ from ε_c by any more than 8% for all values of ε_c, and does not change by more than 2 – 3% when Λ_s is increased from 1500 m to 2700 m. This suggest that ε_c is always insensitive to increases in Λ_s, regardless of the value of ε_c. When $\Lambda_s = 600$ m, mean ε can be 15 – 25% less than ε_c for $\varepsilon_c > 0.1\ m^2\ s^{-3}$, with a standard deviation of up to 30%. This indicates that large values of ε_c can be sensitive to decreases in Λ_s. The higher sensitivity to Λ_s in regions of high ε_c may reflect the importance of local shear in generating strong turbulence on length scales within V_6.

In summary, ε_c only appears sensitive to changes in Λ_s when $\varepsilon_c > 0.1\ m^2\ s^{-3}$, and then only to decreases in Λ_s. This demonstrates that the crude estimate of Λ_0 (and therefore Λ_s), made in the absence of direction measurements, does not lead to large errors in ε. However, assumptions of small Λ_s should not be made without suitable justification (e.g. measurements of Λ_0) to avoid under-estimating large values of ε.

3.6 Summary and Conclusions

A comprehensive analysis of processes contributing to the variance of the Doppler velocity spectrum σ_v^2, has been performed, with the objective of developing a rigorous algorithm to estimate turbulence intensity expressed as eddy dissipation rate, ε. To perform this retrieval method, only three simple radar fields are required, these are the radar reflectivity, the mean Doppler velocity, and the Doppler spectrum variance. The method involves quantifying, or demonstrating the negligibility of, terms in (3.1), where a threshold for negligibility of $0.5\ m^2\ s^{-2}$ has been established in Section 3.1. Combining the realistic

contributions to σ_v^2 from terms that are neglected results in a maximum positive bias in ε of 15% when $\sigma_t^2 = 5\ \mathrm{m^2\ s^{-2}}$; this bias decreases as σ_t^2 becomes larger.

New equations to quantify the Doppler variance due to a distribution of hydrometeor fall-speeds (σ_{TV}^2) have been presented for ice aggregates, raindrops and hail. Contributions from ice aggregates $\sigma_{TV_{agg}}^2$, are concluded as negligibly small in all circumstances. Variance due to rain and hail ($\sigma_{TV_{rain}}^2$ and $\sigma_{TV_{hail}}^2$) are negligible when observed at elevations lower than 13.9° and 11.5°, respectively. When assuming the height of the melting layer is 1.5 km, σ_{TV}^2 is negligible at distances further than 6.5 km from the radar. If scanning vertically through heavy rain or hail, σ_{TV}^2 can be larger than 8 $\mathrm{m^2\ s^{-2}}$. High-elevation scanning is therefore not recommended when attempting to retrieve turbulence from σ_v^2, though (3.15) – (3.17) can be used to correct for σ_{TV}^2 if necessary. In DYMECS, observations were rarely made closer than 30 km from the radar, so σ_{TV}^2 was neglected for this application.

Methods have been presented to remove contributions to σ_v^2 from shear over scales larger than those sampled by the radar. This was achieved through computing shear over a constant spatial scale (Λ_s), using linear velocity surface fitting techniques, as employed in past studies. Resulting values of ε have been found to be largely insensitive to Λ_s. To permit the estimation of ε from σ_t^2, it is of key importance that the largest dimension of V_6 is lower than Λ_0. To account for contributions to σ_v^2 from shear in the azimuthal dimension of the radar beam, σ_φ^2, new equations have been presented for the mean and median azimuthal shear as a function of radial shear alone. This can be used to account for 3-D shear-induced Doppler variance in 2-D radar scans, and can be used simply to further improve the accuracy of retrieved ε. After noting inconsistency in the equations for the calculation of $\sigma_{(\theta,\varphi)}^2$ in the literature, a full derivation has been presented in Section 3.4.1.

The method presented in this chapter has sourced, developed, and added to many decades of turbulence retrieval research to form the most comprehensive approach to date. Though ultimately applied to a specific radar and observational dataset, the considerations made are

suitably general to form a reliable framework for turbulence retrieval with other high-resolution Doppler weather radars capable of sampling within the inertial sub-range. The results of this chapter have been used to guide changes to the scanning strategy and radar configuration used for collecting observations with CAMRa for turbulence retrieval (see Section 6.2.3).

Chapter 4

Turbulence in observed clouds

4.1 Introduction, aims and overview

Following from the development of a method to retrieve turbulence characteristics, expressed in terms of the dissipation rate ε, in radar observations in Chapter 3, this section introduces and motivates methods to investigate turbulence in convective clouds (Section 4.1.1). An overview of the analysis methods used in subsequent sections is then provided in Section 4.1.2.

4.1.1 Introduction and aims

The method to retrieve ε in Chapter 3 was developed so that it could be applied identically across many RHIs, independent of the day of observation. This consistency allows the variation in ε between different scans to be more reliably attributed to the characteristics and physical processes of each cloud. Although the retrieved ε refers to the dissipation of turbulence, it acts as a proxy for turbulent intensity under the assumption that turbulence is locally dissipated, i.e. intense turbulence is expected in regions of high ε. On this foundation, the strength of in-cloud turbulence can be reliably compared between observed clouds; ranging from individual cloud cases to datasets of observations for different DYMECS case days. As outlined in Section 2.2, the analysis of ε in observations (and MetUM in Section 2.3) is focused on two case studies: 20 April 2012 “showers” case, and 25 August 2012 “deep cloud” case. Any mention of radar observations hereafter refers to those collected for these case studies.

The DYMECS RHIs provide only snapshot vertical cross-sections of radar fields, so it is not possible to analyse ε in the context of the three-dimensional circulations and processes within the cloud. The retrieved turbulence in a specific RHI might be influenced by features of the flow which are out of the plane of the scan, and hence not observed. A comprehensive explanation for ε observed in each RHI is therefore difficult to make. However, more general relationships between ε and cloud characteristics are expected to be represented within the RHI data. Given these factors, and the breadth of the RHI datasets available, a statistical approach is chosen to relate ε to the characteristics of observed clouds. Such an approach provides an assessment of observed turbulence that is representative of all observations for both case studies, providing relationships that can be tested against corresponding simulations in the MetUM.

This chapter has two primary aims: (1) to apply the turbulence retrieval detailed in Chapter 3 throughout large datasets of radar observations to investigate the characteristics of turbulence in observed clouds, and (2) to ensure that analyses can be performed consistently with MetUM data to evaluate turbulence from the Smagorinsky-Lilly scheme in Chapter 5. Under these primary aims, this chapter intends to address to following questions as part of a statistical investigation:

- What are the typical values of eddy dissipation rate in observed clouds?
- How does the intensity of turbulence change with height in observed clouds? How does this vertical distribution differ between shower and deep clouds?
- How is turbulence spatially distributed in clouds with a single convective circulation? Which cloud features control this distribution?
- What is the relative impact of different cloud characteristics on turbulent intensity? How is the intensity of turbulence related to the strength of convective updrafts?
- What are the spatial scales of turbulent features in observed clouds? Do these scales differ in shower and deep clouds?

4.1.2 Chapter overview

This chapter includes the detailed statistical analysis of ε in observed clouds to improve understanding of how turbulence is related to the characteristics of convection, and to provide a reliable framework to evaluate the parametrisation of turbulence in the MetUM.

In Section 4.2, retrievals of ε are presented for individual shower and deep clouds. A detailed comparison is made to identify the features of ε in observed clouds, how these relate to other retrieved radar fields, and how they differ between the two cases. This comparison is extended to all observed clouds on both days, to investigate differences in the vertical distribution of ε.

To begin to relate ε to the characteristics of observed clouds, Section 4.3 outlines an investigation into turbulence in single-cell convective clouds, i.e. those that exhibit a single updraft-downdraft circulation. The simple motions in this variant of convective storm (compared to those in multicell or linear convection) offer the best opportunity to attribute ε to specific cloud processes. The spatial distribution of ε in individual clouds is presented, together with statistical relationships between ε and cloud characteristics, e.g. updraft strength and cloud size.

Owing to the importance of convective motion in generating turbulence, Section 4.4 presents a more focused analysis of ε associated with convective updrafts. This section includes details of the automated detection of updrafts, and a statistical examination of ε found within many of these regions over both case days.

The spatial characteristics of coherent ε features are presented in Section 4.5. This involves the automated detection of ε features at varying threshold values to examine the change in their spatial scales with intensity, and how features of similar intensity vary between shower and deep clouds.

4.2 General features of ε in observed clouds

This section commences the analysis of ε in convective clouds observed with CAMRa. This is achieved through applying the retrieval method to radar observations collected for the two contrasting case studies summarised in Section 2.2. More specifically, this section provides an overview of the general features of retrieved ε. This includes a detailed comparison of ε in two contrasting cloud cases (Section 4.2.1), and the change in the vertical distribution of ε between the datasets of shower and deep convective clouds (Section 4.2.2).

4.2.1 Analysis of retrievals for single cloud cases

For a given cloud observation, vertical velocities (see Section 2.2.3) together with radar fields measured directly with CAMRa provide a detailed picture of each case. When combined with fields of ε, the turbulence within each cloud can be analysed in the context of many storm characteristics. This section provides a detailed comparison of two observed clouds; a typical example from both cases days. The example from shower case day will be referred to as the "shower cloud", and the example from the deep convection case day as the "deep cloud".

Figures 4.1 and 4.2 compare retrieved ε to various radar fields for the shower and deep clouds, respectively. These examples have been selected to reflect the typical size and strength of convective storms observed on both days. Both figures include panels of (a) radar reflectivity Z, (b) mean Doppler velocity $\bar{v}$, (c) vertical velocity w, (d) Doppler velocity variance σ_v^2, (e) Doppler variance due to shear σ_s^2, and (f) ε expressed in $\log_{10}$ units. Table 4.1 lists the mean and 99.9th percentile values (99th for w) of each field except $\bar{v}$, as well as for shear magnitudes $|S_\theta|$, $|S_\varphi|$ and $|S_r|$. High percentiles are chosen to represent the largest value of each field instead of the maximum observed value, which is susceptible to error from noise. The data counts of each field are included in Table 4.1 to illustrate the suitability

of the chosen percentiles to approximate the largest values for each parameter. The data counts for w are roughly a factor of 10 lower than for other parameters, due to the coarser grid of the retrieval. As a result, the 99th percentile is selected to represent the largest value of w, instead of the 99.9th percentile.

		Data Counts		Mean		99.9th pctl. (99th for w)	
Parameter	**Unit**	**Shower**	**Deep**	**Shower**	**Deep**	**Shower**	**Deep**
$\boldsymbol{Z}$	**dBZ**	4754	16528	25.7	25.2	49.6	57.2
$\boldsymbol{w}$	$\mathbf{m\ s^{-1}}$	513	1197	0.7	0.4	3.6	12.1
$\boldsymbol{\sigma_v^2}$	$\mathbf{m^2\ s^{-2}}$	4731	16476	2.30	3.15	8.43	20.30
$\boldsymbol{\sigma_s^2}$	$\mathbf{m^2\ s^{-2}}$	3700	14129	0.04	0.05	0.26	0.65
$\boldsymbol{\varepsilon}$	$\mathbf{m^2\ s^{-3}}$	3700	14129	0.02	0.04	0.09	0.61
$\boldsymbol{\lvert S_\theta \rvert}$	$\mathbf{s^{-1}}$	3700	14129	0.0017	0.0027	0.0063	0.0155
$\boldsymbol{\lvert S_\varphi \rvert}$	$\mathbf{s^{-1}}$	3700	14129	0.0010	0.0013	0.0026	0.0045
$\boldsymbol{\lvert S_r \rvert}$	$\mathbf{s^{-1}}$	3700	14129	0.0011	0.0017	0.0048	0.0089

Table 4.1: Mean and 99.9th percentile values (99th for w) of various retrieved parameters for the examples of shower cloud, and deep convective cloud shown in Figure 4.1 and Figure 4.2, respectively. Data counts are listed to provide context for percentiles, and to illustrate the data loss through signal-to-noise thresholding and velocity surface fitting, as well as the coarser resolution of w.

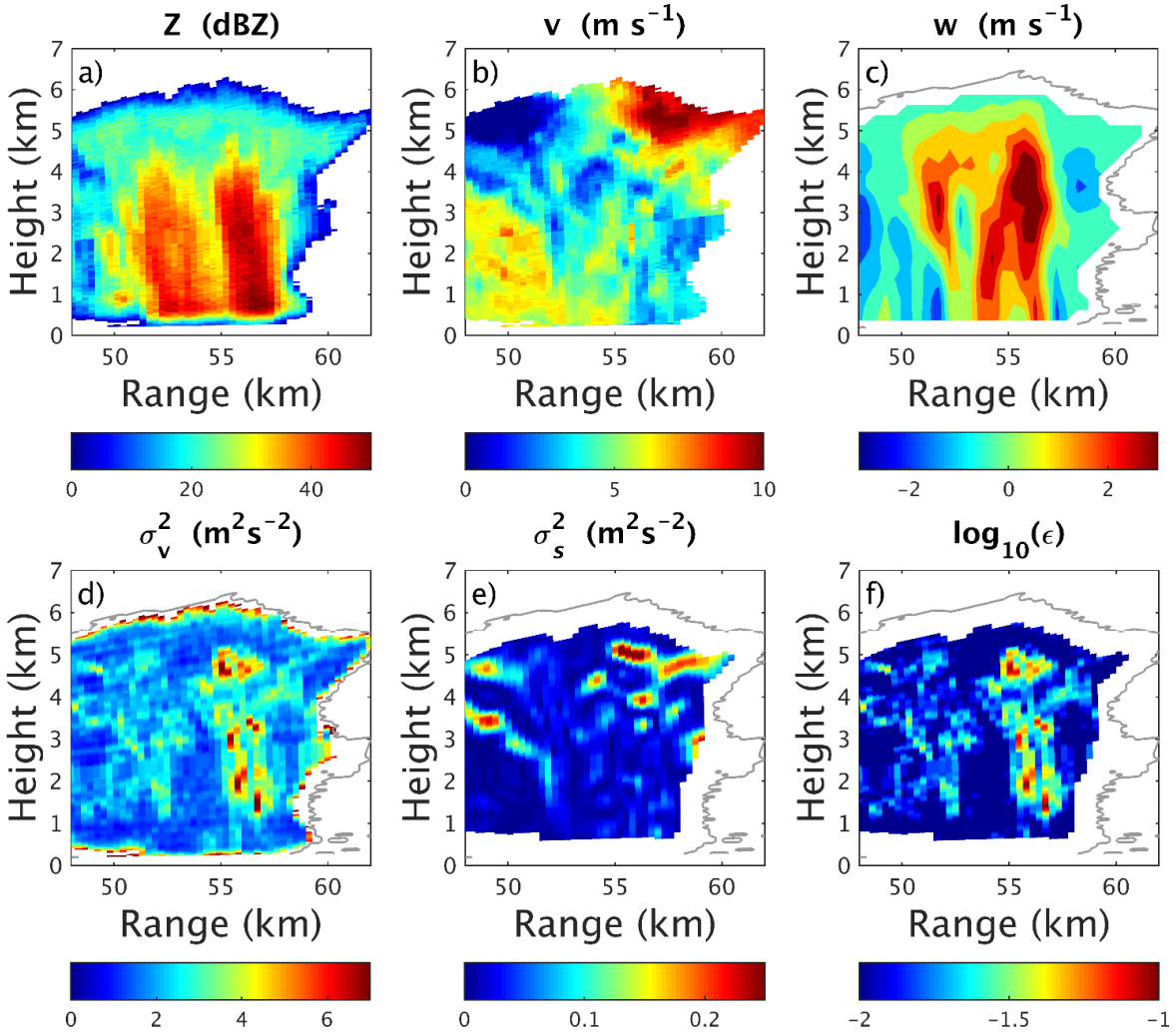

Figure 4.1: Example ε retrieval for an RHI scan of a convective storm performed on the 20 April 2012 (showers). Included is (a) radar reflectivity, (b) Doppler velocity, (c) vertical velocity, (d) total Doppler variance, (e) Doppler variance due to shear, and (f) eddy dissipation rate displayed in $\log_{10}$ units. The grey contour outlines reflectivity returns before correction by SNR.

In Figure 4.1, the observed shower cloud is approximately 10 km wide at the base, and 6 km in height. As shown in Figure 4.1c, the main updraft region is located between ranges $R = 53$ km and $R = 57$ km, and spans the surface to 5 km in height. Within the updraft region, w generally ranges from 1 – 3 m s^{-1}, with a largest value of 3.6 m s^{-1}. The highest reflectivity (see Figure 4.1a) is observed in and below the location of the main updraft, where Z is as large as 50 dBZ, indicating heavy precipitation at the surface. A second region of positive w is found at an approximate range of $R = 52$ km, between 2 – 4 km from the surface. A column of enhanced reflectivity (~ 40 dBZ) is again found in and below the

feature, indicating a second, weaker core of precipitation within the cloud. The majority of the observed central area of the cloud is dominated by rising motion, which leads to divergence at the top of the cloud indicated in $\bar{v}$ (Figure 4.1b).

The Doppler velocity variance shown in Figure 4.1d has a mean of 2.30 $\mathrm{m^2\ s^{-2}}$, with values up to 8.43 $\mathrm{m^2\ s^{-2}}$. A correction is made to σ_v^2 due to the effects of shear (Figure 4.1e) before the residual σ_t^2 is converted to ε using in (1.25). In this case, all corrections are negligibly small (less than $\sigma_{\mathrm{neg}}^2 = 0.5\ \mathrm{m^2\ s^{-2}}$), generally amounting to less than 10% of σ_v^2. The largest values of σ_s^2 are mostly associated with regions of vertical shear resulting from the divergence in $\bar{v}$ above 4 km.

Figure 4.1f displays ε within the cloud, which has a mean value of 0.02 $\mathrm{m^2\ s^{-3}}$, and a largest value of 0.09 $\mathrm{m^2\ s^{-3}}$. Of particular interest is the spatial distribution of turbulence within the cloud; a large proportion of the cloud area is only weakly turbulent ($\varepsilon \leq 0.01\ \mathrm{m^2\ s^{-3}}$), with stronger turbulence localised to specific cloud regions. The strongest, and most spatially consistent region of turbulence is found in a 2-km wide, 4-km deep column roughly co-located with the main updraft region between $R = 55$ km and $R = 57$ km. Strong turbulence could generally be expected here due to the shear and buoyancy associated with vertical motion. However, the intensity of turbulence is still varied within this region and does not strictly scale with the strongest w. For example, insignificant turbulence is associated with the region of $w \sim 2\ \mathrm{m\ s^{-1}}$ located between $R = 54$ km and $R = 55$ km, in the lowest 3 km of the cloud. This serves to highlight the limitations of the data discussed in Section 4.1.1; a comprehensive explanation of observed ε cannot be made from vertical cross-sections alone. Instead, patterns in ε can be identified over many of these cases to form a statistical assessment.

A corresponding set of retrieved fields for the deep cloud is displayed in Figure 4.2. The cloud is considerably larger than the shower cloud in Figure 4.1; approximately 15 km wide at the base, extending to 10 km in height. Updrafts are taller than in the shower cloud,

displaying multi-cell characteristics with numerous updraft-downdraft circulations present in Figure 4.2c. The dominant updraft region is located approximately between $R = 33$ km and $R = 34$ km, and is narrower, deeper and much stronger than the main updraft of the shower cloud. The updraft extends to nearly 9 km in height, with w generally ranging from 5 – 10 m s^{-1}, and as large as 12.1 m s^{-1} in the lowest 2 km of the cloud. Reflectivity exceeds 50 dBZ in the region associated with the main updraft, increasing to 57 dBZ in the lowest 3 km indicating the likelihood of intense precipitation to the surface.

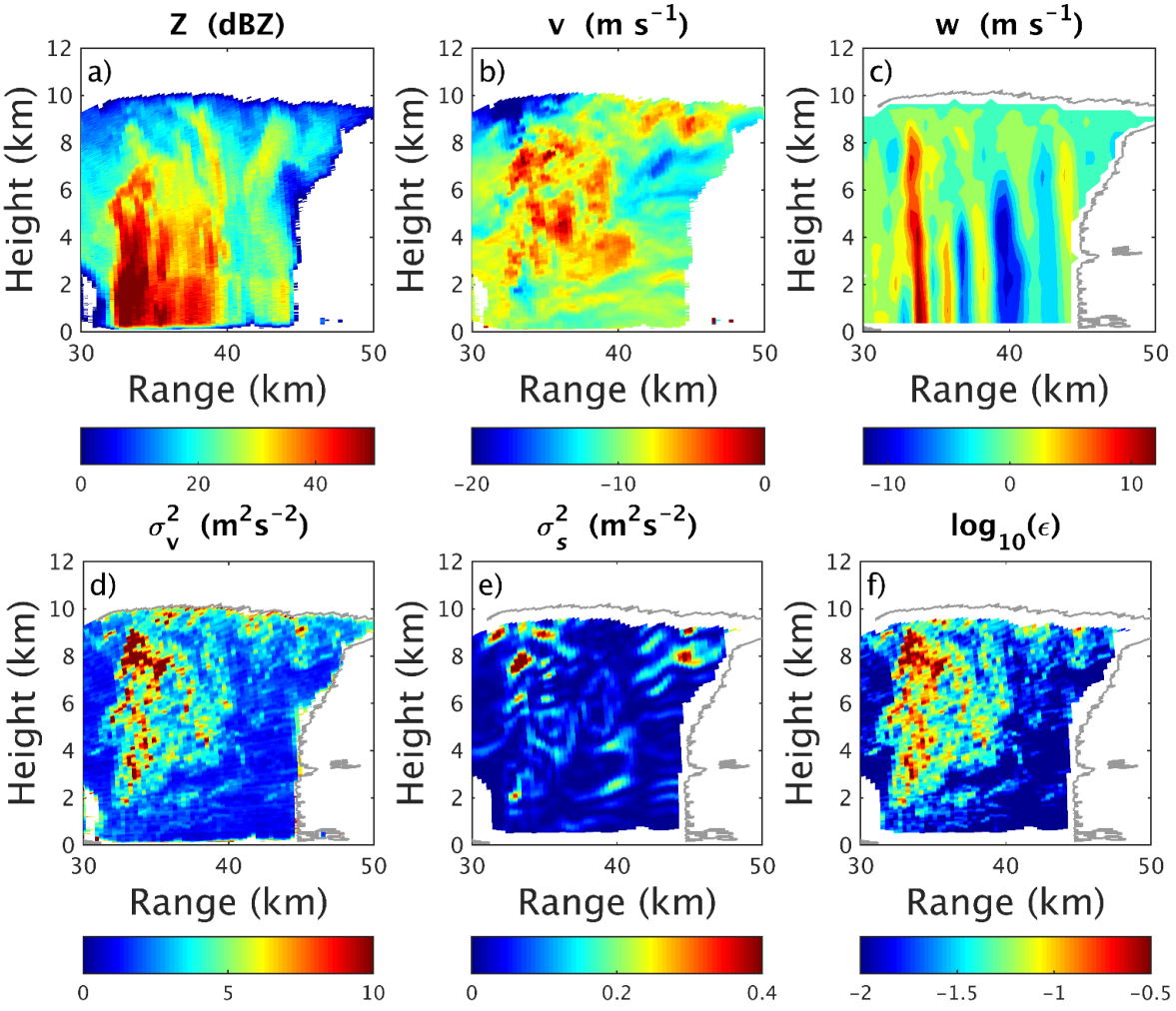

Figure 4.2: Equivalent to Figure 4.1; an example retrieval of ε for an RHI scan of a convective storm performed on the 25 August 2012 (deep cloud case).

The mean values of σ_s^2 are similarly small in both cases (~ 0.05 m^2 s^{-2}), suggesting the average correction to σ_v^2 is much less than σ_{neg}^2. However, the largest σ_s^2 in Figure 4.2e is 0.65 m^2 s^{-2}, which is more than twice the largest observed in the shower cloud, and not a negligible correction. At small distances from the radar, σ_s^2 is more likely to be negligibly small due to its scaling with R^2 (see (3.26) and (3.27)). For example, if $|S_\theta| = |S_\varphi| = |S_r|$, σ_s^2 will be a factor of 2.5 smaller at 35 km range than at 55 km (range of shower cloud). Figure 4.2e suggests that even when observed at 35 km from the radar (one of the closest observed clouds in the DYMCES data), values of σ_s^2 can still exceed σ_{neg}^2. This provides a practical example of the need to consider shear corrections for all cases, as outlined in Section 3.4.1.

Although observed closer to the radar than the shower cloud, higher values of σ_s^2 are found in the deep cloud; this results from the presence of stronger gradients in $\bar{v}$. Table 4.1 displays the average and largest values of the three components of shear magnitude used in the calculation of σ_s^2. Both the mean and largest values of each shear component are higher in the deep cloud, with the largest values of $|S_\theta|$ a factor of 2.5 higher than in the shower cloud. In Figure 4.2e, the location of $\sigma_s^2 = 0.65$ m^2 s^{-2} ($\sim R = 33$ km at a height 8 km) is characterised by high spatial variability in $\bar{v}$. This appears to be associated with the interaction of the top of the main updraft with the air in the surrounding environment, generating strong local shear.

The mean value of σ_v^2 in Figure 4.2d is larger than in the shower cloud at 3.15 m^2 s^{-2}. The largest value of 20.3 m^2 s^{-2} is more than twice that observed in the shower cloud. As for the shower cloud in Figure 4.1, σ_s^2 is subtracted from σ_v^2, before the residual σ_t^2 is used in (1.25) to determine ε; which is displayed in Figure 4.2f. Qualitative inspection of Figure 4.2f indicates that turbulence is more intense and widespread within the deep cloud when compared to Figure 4.1f. The mean ε is 0.04 m^2 s^{-3}, which is twice as large as in the shower cloud, with values as large as 0.61 m^2 s^{-3}; more than a factor of six larger than in Figure

4.1d. Similar to Figure 4.1, strong turbulence in the deep cloud is associated with the main updraft region, with the largest values of ε found at the top of the updraft. However, in this case, strong turbulence is also more widely distributed in and around the updraft region. Figure 4.3 displays the probability density function (PDF) of ε for both clouds. In the deep cloud, low values of ε (less than 0.01 $m^2\ s^{-3}$) appear to be much less common than in the shower cloud. The probability of values of ε greater than 0.02 $m^2\ s^{-3}$ is higher in the deep cloud, with values extending far above the largest observed in the shower cloud. The higher values of ε within the deep cloud suggest that turbulence is more intense due to the much stronger updraft, and the broader PDF of ε suggests that more turbulent energy is being dissipated within the cloud as a result.

This detailed comparison between two contrasting cloud cases has highlighted the following:

- A retrieval of ε can be analysed together with other available radar fields to begin to explain the strength and spatial distribution of turbulence within observed clouds.
- Vertical cross-sections alone are insufficient to comprehensively explain all the features of ε, indicating a statistical assessment of ε across many cases is the optimal approach with this data.
- Turbulence within the two cloud cases appears to be spatially correlated with the main updraft region and appears to increase in intensity with the updraft strength. Strong turbulence is more widely distributed within deep convective cloud.
- The largest values of ε appear more likely to be located towards the top of the cloud, especially in the upper regions of the main updraft.

These findings suggest that relationships between ε and cloud characteristics can be identified in the DYMECS data, providing indications of the cloud features most important in generating turbulence. The depth of the available dataset suggests that methods can be applied to represent these relationships statistically to investigate the features of ε in

observed clouds. This will ultimately provide a framework of results that can be replicated in data from MetUM simulations to test ε produced by the Smagorinsky-Lilly sub-grid turbulence scheme in Chapter 5.

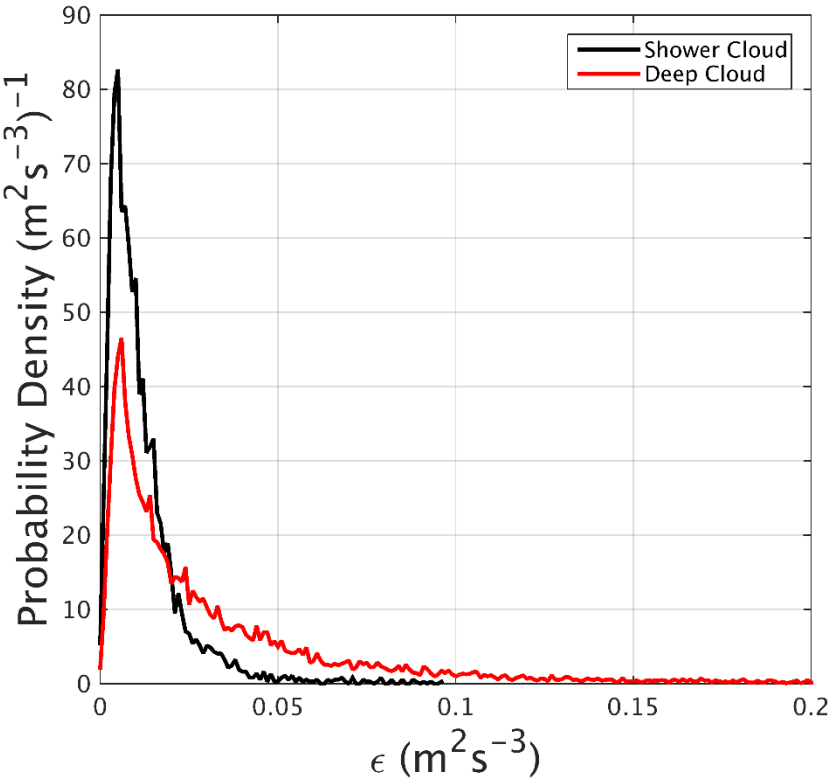

Figure 4.3: Comparison of the probability distribution of ε displayed in Figure 2.1f and Figure 2.2f for shower and deep cloud cases.

4.2.2 Vertical distribution of ε in observed clouds

In Section 4.2.1, the analysis of ε in single cloud cases suggests that the strength and depth of convective updrafts may impact the vertical distribution of turbulence within the cloud. This is highlighted especially in the deep cloud case, where large ε is more widely distributed towards the top of the cloud, and in particular above the main updraft. To investigate this observation in more detail, the vertical distribution of ε has been determined from all clouds observed on the two case days. In doing this, location of the strongest turbulence can be determined in the context of cloud depth and compared for clouds with different updraft strength.

This analysis uses the subset of RHI scans described in Section 2.2.4, which was derived from the full DYMECS observations to consist only of high quality, statistically independent scans for both case days. This subset includes 44 RHI scans of deep cloud and 33 scans of shower cloud. For each RHI, retrievals of ε are separated into vertical levels of 1-km depth up to the maximum cloud height; 0 – 6 km in the shower clouds, and 0 – 10 km in the deep clouds. For each vertical level, values of ε are collected together from each RHI (separately for shower and deep cloud). The 25th, 50th, 75th and 95th percentiles of ε are then determined from the ε associated with each vertical level to observe how the average and largest values of ε vary with height, and how this differs between the two case studies. These statistics are plotted at the midpoint of each vertical level and compared in Figure 4.4.

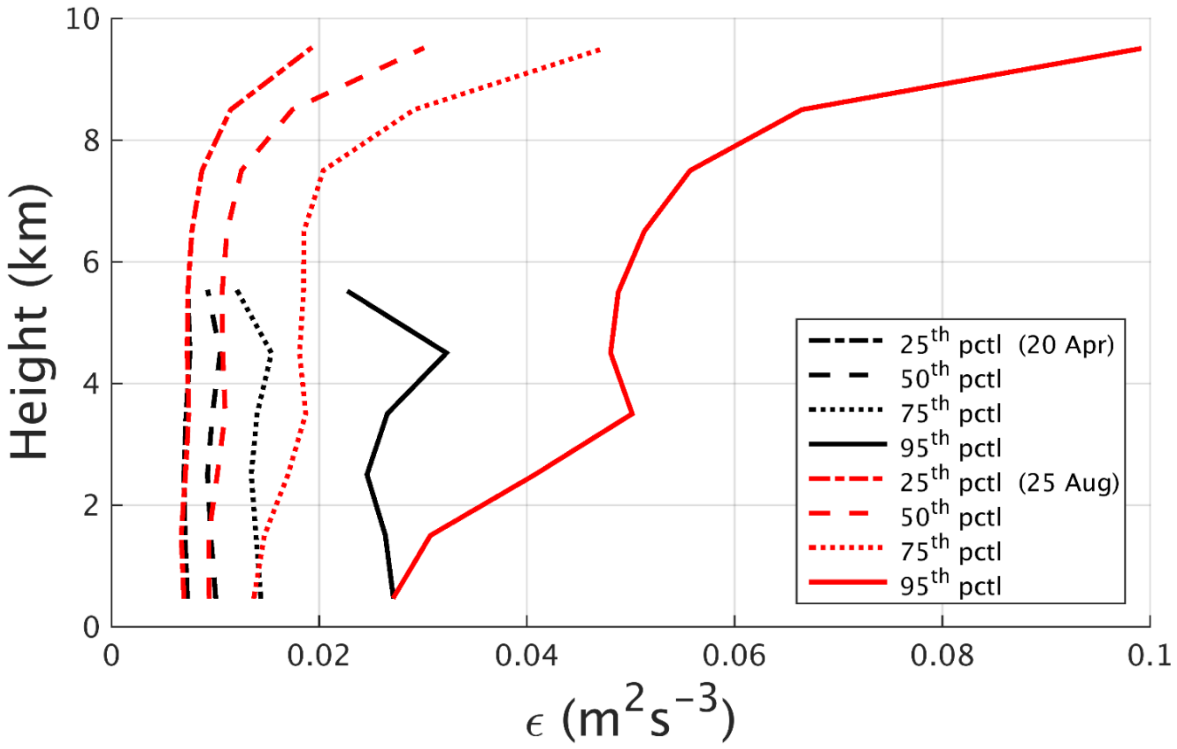

Figure 4.4: Comparison of the vertical distribution of various percentiles of ε in convective clouds observed on 20 April (showers) and 25 August (deep cloud), 2012. Percentiles are determined for each 1-km vertical layer and then plotted at the midpoint of each layer.

The 95th percentiles of ε (hereafter ε_{95}) between 0 – 1 km are approximately the same in shower and deep clouds, at ~ 0.025 $m^2\ s^{-3}$. In shower clouds, ε_{95} remains approximately constant with height, varying only between 0.02 – 0.035 $m^2\ s^{-3}$, and peaking slightly between 4 – 5 km, near the cloud top. In deep clouds, ε_{95} increases by an approximate factor of four from the surface to the cloud top, where ε_{95} approaches 0.1 $m^2\ s^{-3}$, however, the increase is not linear. From 0 – 4 km in deep cloud, ε_{95} doubles to 0.05 $m^2\ s^{-3}$; a factor of 2 larger than for shower cloud at 4 km. In the central regions of deep cloud from 4 – 7 km, ε_{95} remains approximately constant with height, before increasing by a further factor of 2 from 7 – 10 km to 0.1 $m^2\ s^{-3}$. This indicates significant differences in the vertical profile of ε_{95} between shower and deep cloud. The updrafts in shower cloud produce turbulence with intensity that is approximately constant with height. However, the stronger, deeper updrafts in the deep clouds generate more intense turbulence and introduce a positive vertical gradient in ε_{95}.

Median ε values are approximately constant at 0.01 $m^2\ s^{-3}$ throughout the 6-km depth of shower cloud. In the same depth of deep cloud, the median is almost identical to this, but then increases by a factor of three from 0.01 – 0.03 $m^2\ s^{-3}$ from 6 – 10 km. The 25th and 75th percentiles of ε (which indicate the typical values of ε within the cloud) follow a very similar pattern to this, indicating that from 0 – 6 km the average intensity of turbulence is very similar for both cases. A reason for this is suggested in Figures 4.1f and 4.2f; turbulence is locally strong, but a large proportion of the cloud area is only weakly turbulent in both cases ($\varepsilon \leq 0.01\ m^2\ s^{-3}$). This was often the case throughout observed clouds on both days, which serves to explain why the bulk of ε values are so similar. The strong turbulence in the upper regions of deep cloud is represented similarly in the lower percentiles of ε, indicating a broad increase in the spatial distribution of strong turbulence in this location of deep cloud.

Figure 4.4 provides a convenient way to simultaneously compare the differences in turbulent intensity and distribution with height between the two cloud types, building on

features identified in Section 4.2.1. Further to this, a comparison can be made simply to the vertical distribution of ε in MetUM simulations for the corresponding days in Chapter 5. However, this analysis is limited to a broad comparison, and does not provide statistical relationships between ε and the characteristics of individual clouds, which forms the focus of the remainder of this chapter.

4.3 Turbulence in single-cell convective clouds (SCCCs)

This section summarises initial attempts to explore the potential for statistical relationships between ε and cloud characteristics in DYMECS observations. More specifically, to determine whether it is possible to explain the intensity and spatial distribution of ε in terms of in-cloud convective circulations, and more general cloud characteristics.

The DYMECS observations are comprised of many cloud varieties, including discrete single-cells (one dominant updraft-downdraft circulation), multi-cell clusters, and linear convective features. The direct attribution of ε to specific cloud characteristics is made difficult in cloud cases with complex interior circulations, or where otherwise separate clouds are clustered together, appearing as a single cloud mass to radar. For example, the small spacing of multiple updraft circulations observed in multi-cell clouds (e.g. Figure 4.2) would lead to difficulty in relating ε to specific updraft features. Furthermore, observing multiple clouds as a single cloud area would bias any relationships between ε and cloud size. Given the limitations of using only vertical cross-sections of cloud to explain features of turbulence (see Section 4.2.1), a perfect analysis of ε for each cloud is not possible. However, the discussed problems are reduced, and the ability to explain ε is improved, by initially limiting the analysis of ε to more simple, discrete clouds with a single, dominant updraft-

downdraft circulation. For the remainder of this section, these are referred to as single-cell convective clouds (SCCCs).

Details of the SCCC dataset are summarised in Section 4.3.1, and the spatial distribution of ε relative to the main updraft is investigated for SCCCs in Section 4.3.2. Potential relationships between ε in various cloud regions, and cloud characteristics, are then determined using correlation techniques in Section 4.3.3.

4.3.1 Subset of SCCCs

A subset of SCCCs are derived from the dataset of shower and deep cloud RHIs summarised in Section 2.2.4. SCCCs are determined qualitatively in these scans by identifying discrete clouds that exhibit a single, dominant updraft. Discrete clouds that contain more than one updraft of similar strength are omitted, as are clouds that possess single updrafts, but have edges that are not clearly defined due to close proximity to other clouds. Under these constraints, 25 SCCC cases have been extracted from the full dataset; 8 shower clouds and 17 deep clouds. As only a small proportion of the total observed clouds, the size of the dataset reflects the rarity of SCCCs on the case days relative to more complex and clustered cloud varieties. The combined 25-case dataset is suitably large to investigate the potential for relationships between ε and cloud characteristics. However, with only 8 shower clouds included, reliable comparisons between the two case days are difficult to make. Examples of SCCCs for shower and deep cloud are shown in Figure 4.5 and Figure 4.6, respectively. In both cases, the cloud possesses one main updraft, with cloud boundaries that are suitably well defined. This allows the analysis of observed ε (right panel) to be made in the context of a discrete cloud environment, with measurable characteristics.

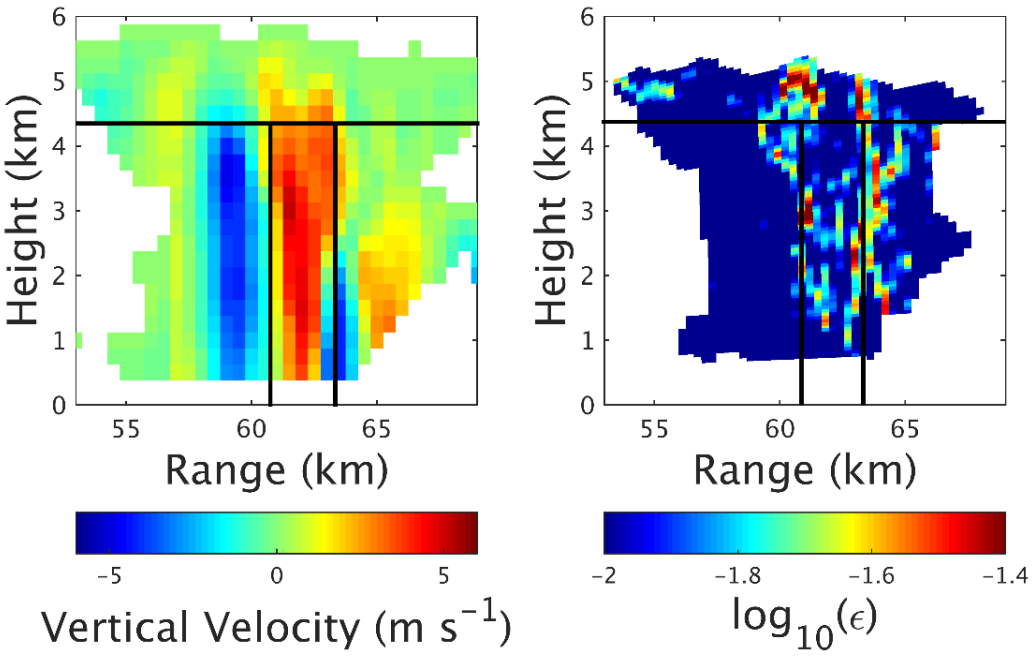

Figure 4.5: Example single-cell shower cloud characterised by a single, dominant updraft (left panel). In the right panel, ε has units of m^2s^{-3} but is expressed on a $\log_{10}$ scale. The overlaid black lines indicate the separation of the cloud into regions (for Section 4.3.2) based on the updraft location.

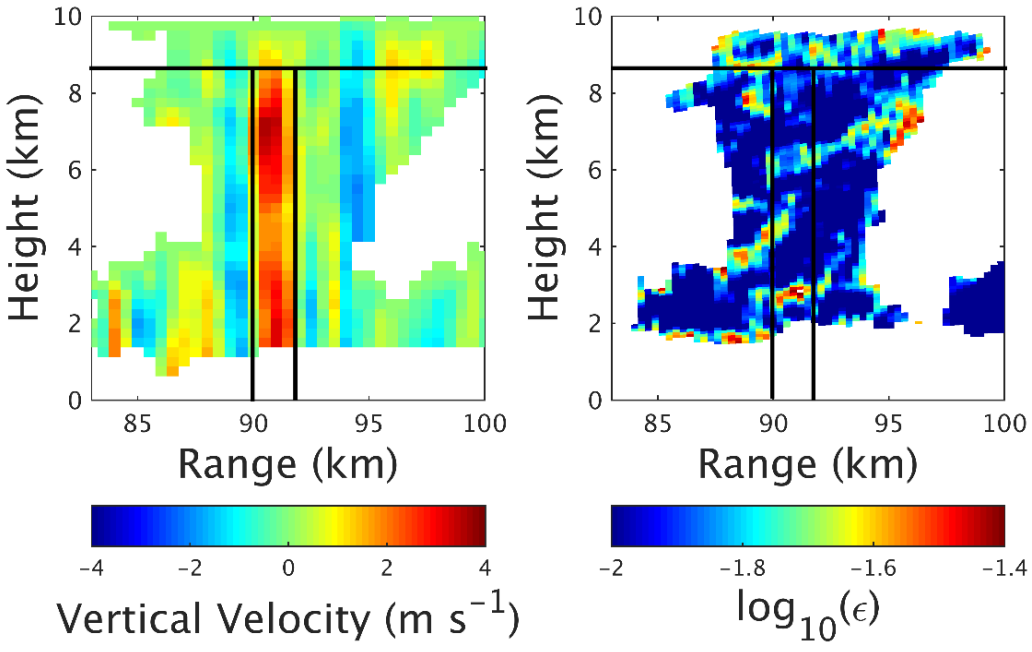

Figure 4.6: An example single-cell deep cloud; equivalent to Figure 4.5.

4.3.2 Spatial distribution of ε in SCCCs

The analysis of ε in SCCCs begins by assessing the spatial distribution of turbulence within the cloud, with the aim of revealing the locations that are typically most turbulent. This is achieved by dividing SCCCs into different cloud regions based on the location of the main updraft, and comparing mean values of ε observed in each region.

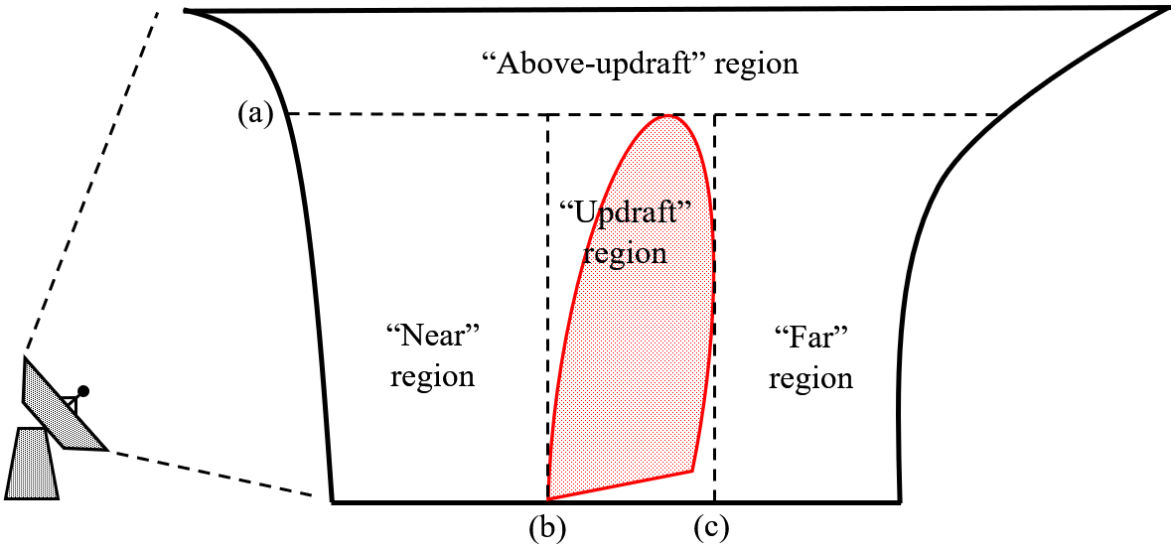

Figure 4.7: Schematic showing the separation of single-cell clouds into regions based on the location of the updraft. The "near" and "far" regions are named relative to the location of the radar during data collection.

Figure 4.7 provides a schematic representation of the separation of SCCCs into four regions based on the location of the main updraft. This schematic has been applied to the SCCC examples shown in Figure 4.5 and Figure 4.6, indicating the location of each region, and the corresponding values of ε. For consistency across all cases, regions are determined by simply placing three lines of division approximately around the main updraft. Line (a) (see Figure 4.7) is placed horizontally at the top of the updraft, with lines (b) and (c) placed from this height down to the surface on either side of the updraft. The area enclosed by (a), (b) and (c) is named the "updraft" region, and the area above (a) is named the "above-updraft" region, which spans the horizontal extent of the cloud. In the case where the updraft

reaches the cloud top, the upper 1-km of the cloud is named the above-updraft region. Two more regions are defined either side of the updraft, below (a), which are named the "near" and "far" regions, based on the location of the radar during data collection. Due to the range of sampling directions during the DYMECS data collection, these regions have no specific definition aside from being nearer to, or further from, the radar. Any observed differences in turbulent intensity between these regions cannot be reliably attributed to cloud characteristics. Therefore, the comparison of turbulence statistics in these areas is not of immediate interest. However, they are analysed in the context of the main downdraft location later in this section.

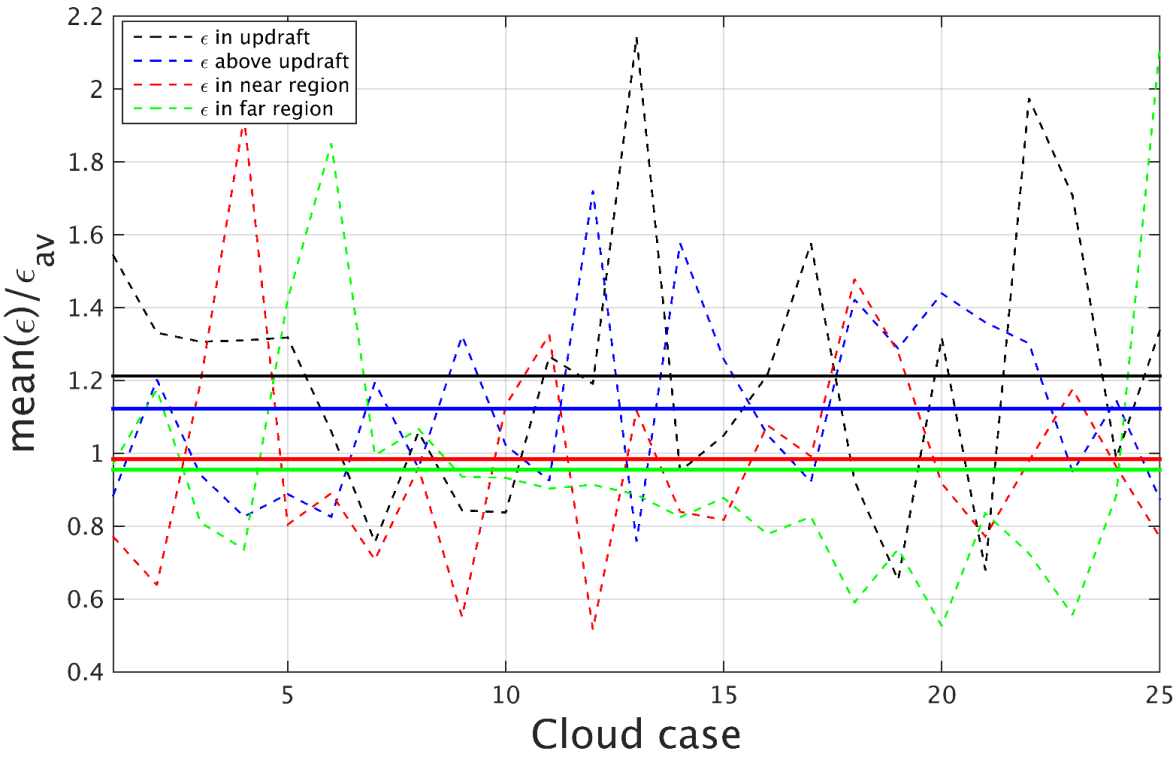

Figure 4.8: (Dashed lines) Mean ε in the "near", "far", "updraft" and "above updraft" regions normalised by the cloud-average (ε_{av}) for each of the 25 cloud cases (1 – 8 refers to shower clouds; 9 – 25 refers to deep clouds). The solid lines represent the mean of the dashed lines, indicating the regions of largest ε relative to the cloud-average.

For each SCCC, mean values of ε are determined in each of the four regions. These values are then normalised by the mean of all ε observed in each cloud, ε_{av}. Values expressed as factors of ε_{av} better represent the spatial distribution of ε, and can be compared between different clouds. Figure 4.8 compares the normalised means for each of the SCCC cases (1 – 8 refers to shower clouds; 9 – 25 refers to deep clouds). The mean of each dashed line is indicated by solid lines, revealing the region of the largest ε relative to ε_{av}.

Although values in individual clouds appear to vary substantially, turbulence in the updraft, and above-updraft regions, are on average 21% and 12% higher than ε_{av}, respectively. In 17 of the 25 SCCCs, turbulence is strongest in either the updraft or above-updraft region. In both shower and deep clouds, turbulence in the updraft region is 21% larger than ε_{av}. In only deep cloud examples, turbulence above the updraft is 20% larger than ε_{av}, however, corresponding values in shower clouds are 3% lower than ε_{av}. This suggests that although $\varepsilon/\varepsilon_{av}$ is similar in the updraft regions of both cloud types, the stronger updrafts in deep clouds are more effective at producing (or possibly re-distributing) strong turbulence towards the cloud top. The small number of cases in the dataset limit the reliability of this observation, however, it is highly consistent with results comparing the vertical distribution of ε in both cloud types in Figure 4.4.

Turbulence in the near and far regions are approximately the same; lower than ε_{av} by 2% and 4%, respectively. In defining these regions based on the location of the radar, this similarity could be expected as there was no preferred scanning direction when collecting data with CAMRa. However, these cloud regions can be used to investigate the turbulence associated with convective downdrafts. For the SCCCs where the main downdraft is clearly defined (20 out of 25 cases), the near and far regions can be redefined to those with and without the main downdraft – for this analysis, these regions are referred to as A and B, respectively. Figure 4.5 provides an example of a cloud case where the downdraft is clearly

defined in the near region. In Figure 4.6 however, the main downdraft is not clearly defined, so the cloud is not included in this analysis.

Figure 4.9 compares $\varepsilon/\varepsilon_{av}$ between regions A and B in the 20 observed SCCCs. Results indicate that in region A, ε is 17% lower than the cloud average, while values are 17% higher in region B. Turbulence in region A is only larger than ε_{av} in 3 out of 20 cloud cases, compared to 11 out of 20 for region B. This may suggest that downdrafts are significantly less important in generating turbulence than updrafts. Figure 4.5 (cloud case 2 in Figure 4.9), provides an example that is consistent with this result; turbulence is far weaker in the downdraft than in the updraft, even though the magnitude of the vertical velocity is approximately the same. However, the reliability of this result is limited by the smaller number of cloud cases analysed, the limitations of vertical cross-section data, and the lack of a clear explanation for the corresponding positive bias to ε in region B.

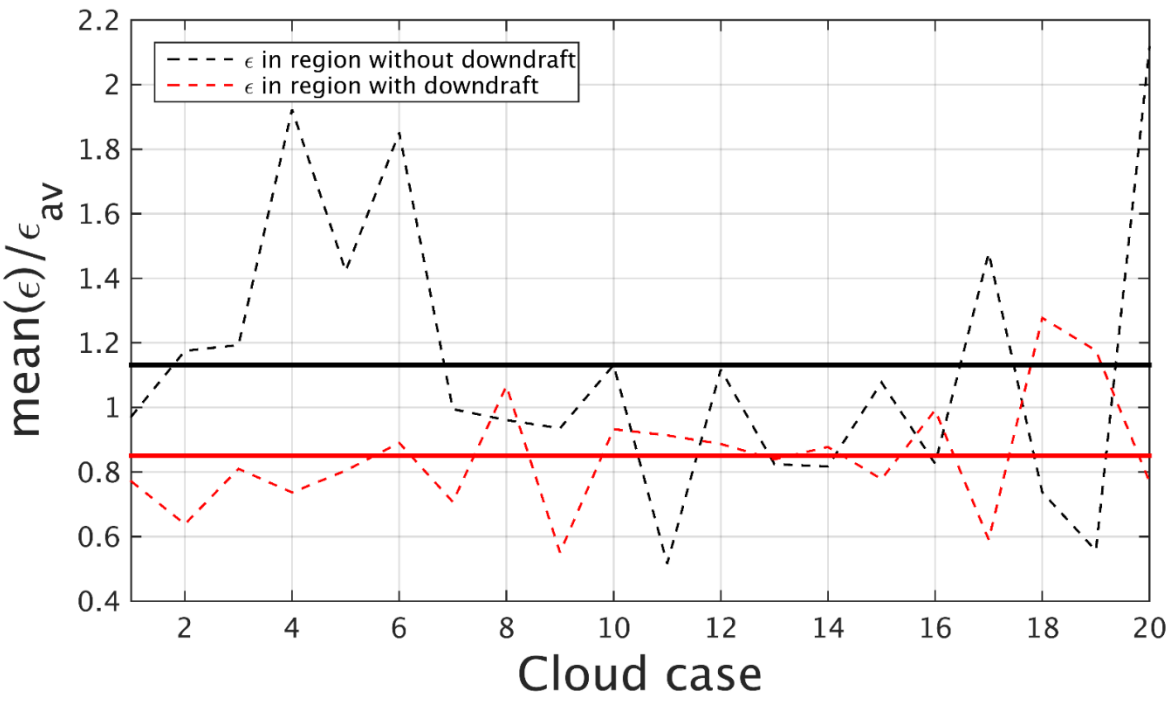

Figure 4.9: (Dashed lines) The mean ε (normalised by the cloud-average, ε_{av}) within the cloud region containing the main downdraft (region A), compared to the region without (region B). (Solid lines) Mean of dashed lines. This is only assessed for cloud cases where the main downdraft is clearly defined (20 out of 25 cases).

To summarise, the spatial distribution of ε in observed clouds has been investigated in a subset of 25 SCCCs. When compared to the average ε in each cloud ε_{av}, turbulence is strongest in the updraft region, with mean values that are 21% larger than ε_{av}. Values of turbulence above the updraft are 12% larger than ε_{av}, however, positive biases are mostly found in the deep cloud examples, indicating the importance of strong updrafts in distributing large ε near the cloud top. Turbulence associated with the downdraft region of the cloud is lower than ε_{av} by 17%, suggesting (with limitations to reliability) significant differences between the turbulence associated with updrafts and downdrafts.

4.3.3 Relationships between ε and cloud characteristics in SCCCs

The analysis in Section 4.3.2 has indicated how the intensity of turbulence varies spatially within SCCCs, with the largest ε found in and above convective updrafts. This section aims to investigate the degree to which the spatial distribution and intensity of ε can be explained in terms of the vertical motion and spatial characteristics of SCCCs.

To perform this investigation, 10 variables are recorded from each SCCC; these are listed in Table 4.2 together with a description of how each is determined. The mean values of ε in all four cloud regions are included together with ε_{av}, as well as five cloud characteristics. The cloud area A_c, and updraft area A_u, are selected to determine whether turbulence is stronger in larger clouds, and/or in cases with larger scale vertical motion. The maximum (95th percentile) updraft velocity w_{95}, is selected to compare turbulence in different cloud regions to the updraft strength. The mean magnitude of vertical motion $\overline{|w|}$, is calculated from all w in each cloud to determine the combined effect of updraft-downdraft circulations on ε. Lastly, $\overline{|S_{el}|}$ is calculated by differentiating the Doppler velocity in the elevation direction in each cloud, and calculating the mean magnitude of the resulting shear. This is used to assess whether the average strength of velocity gradients have a significant impact on ε.

Variable number	Variable name	Description for a given cloud
1	Updraft size	The product of the updraft width and height (km^2)
2	Max. updraft velocity	The 95th percentile of vertical velocity in the updraft region
3	Mean magnitude of vertical velocity	Determined from all vertical velocity associated with a given cloud
4	Mean magnitude of vertical shear	Vertical shear is determined by differentiating the Doppler velocity in the elevation direction
5	Cloud size	The product of approximate cloud width and depth (km^2)
6	Cloud-averaged ε	Mean of ε measured in all regions combined
7	Updraft region ε	Mean of ε measured within the updraft region
8	Near region ε	Mean of ε measured within the "near" region
9	Far region ε	Mean of ε measured within the "far" region
10	Above-updraft region ε	Mean of ε measured above the updraft region

Table 4.2: Details of the variables used for the correlations presented in Figure 4.10, together with a description of how they were determined for in a given SCCC.

The values collected for each variable are correlated with all other variables to detect significant relationships. The resulting correlation coefficients r, are presented in Figure 4.10. Values of r have been filtered out by significance where the corresponding p-value is larger than 0.05, i.e. where the probability of obtaining the observed r by random chance is less than 0.05. The final result is set of significant positive correlations between many of the variables. By relating the data in this format, Figure 4.10 includes significant correlations between the cloud characteristics (variables 1 – 5), e.g. A_c is related to A_u, and between ε in different cloud regions (variables 6 – 10), e.g. updraft ε is related to ε_{av}. These are often intuitive, and offer little direct value to the analysis of turbulence.

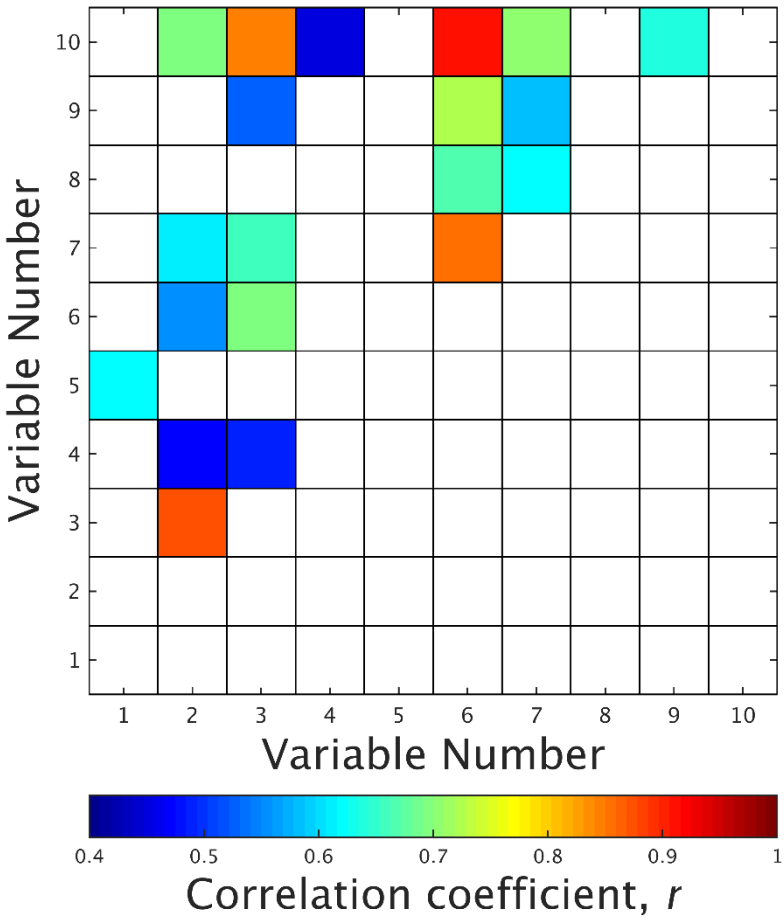

Figure 4.10: Correlation coefficients between cloud characteristics and ε in different regions of SCCCs. Correlations have been filtered out where the corresponding p-value is larger than 0.05, i.e. where the probability of obtaining the observed correlation by random chance is greater than 0.05. Details of how variables were determined are summarised in Table 4.2. Correlations below the diagonal have been removed to avoid duplication of results.

Therefore, these inter-correlations will not provide the focus for this discussion. However, when trying to determine causative factors for ε, it remains useful to know which cloud characteristics are inter-correlated.

The spatial area of both cloud and updraft (A_c and A_u) have no significant correlation with ε in any cloud region. This indicates that cloud area, and perhaps more importantly, updraft area, has no significant effect on the intensity of turbulence within the cloud. The updraft strength w_{95}, has significant positive correlation with ε in the updraft and above-updraft cloud regions. This is consistent with the result suggested in Section 4.3.2, which

indicated the effects of updraft strength in generating turbulence within the updraft, but also near the top of the cloud when updrafts were stronger. Unsurprisingly, turbulence in these two regions is strongly correlated with ε_{av}, which explains the significant, but weaker, correlation between w_{95} and ε_{av}. Due to the strong relationship between $\overline{|w|}$ and w_{95}, $\overline{|w|}$ is correlated to ε in similar cloud regions, however, these correlations are stronger in each case. This would suggest that the degree of vertical motion throughout the cloud (which includes the downdraft) is more important in generating turbulence than the strength of the main updraft alone. The final cloud characteristic $\overline{|S_{el}|}$, is only correlated with ε above the updraft, however, this is assumed to be indirect due to the inter-correlation of $\overline{|S_{el}|}$ with both w_{95} and $\overline{|w|}$.

In summary, by recording and comparing various statistics of SCCCs, it has been possible to demonstrate that significant statistical relationships exist between turbulence and cloud features. Correlations suggest that the vertical velocity characteristics $\overline{|w|}$ and w_{95} are the most important in generating strong turbulence. These correlations are generally strongest with ε in the updraft and above-updraft regions of the cloud. These are areas commonly associated with strong buoyancy and velocity gradients which are important in the production of turbulent kinetic energy. The spatial characteristics of the cloud and main updraft, and the effects of vertical shear, appear to have little effect on values of ε. There are indications that turbulent production in downdraft regions is significantly less than in updraft regions of similar $|w|$. Although using a correlation-based approach has proved useful in identifying which dependencies exist for ε, further quantitative detail is required to examine these dependencies using methods that are more easily applied to data from MetUM model simulations; this is addressed in Section 4.4.

4.4 Turbulence in convective updrafts

Recalling the two primary aims of this chapter, methods developed to analyse turbulence in observed clouds should not only aim to improve understanding of turbulence in observations but should ideally be developed to allow for a consistent application with model data from the MetUM.

The results of Section 4.3 provide useful insights into the relative importance of various cloud features in controlling the intensity and distribution of turbulence in observed clouds. Such an analysis was made possible by subsampling a dataset of clouds that conformed to a qualitative framework for single-cell convection. The framework of a discrete cloud with clearly defined features allowed the attribution of ε to cloud characteristics to be made with improved reliably. However, the resulting dataset consisted of only 25 cloud cases, which represents a small proportion of the combined observations collected over the two case days. Both this, and adopting a specific framework for clouds, limits the potential for comparison with clouds simulated in the MetUM. A new approach is therefore required to derive statistics that are more representative of the full dataset of observations and can be derived consistently in MetUM data.

By focusing only on turbulence associated with convective updraft regions, the rigid single-cell structure for clouds can be abandoned, while allowing a more detailed examination of the features found (in Section 4.3) to be most important in generating turbulence. The approach considers all updrafts observed in the DYMECS data (selecting those that exceed certain thresholds, see Section 4.4.1), providing a much larger, more representative dataset for both case days. By using automated methods to detect updrafts, data can be collected consistently in observations and in data from MetUM simulations.

Section 4.4.1 outlines the application of an algorithm used to detect updraft regions, building a dataset of updrafts with associated statistics. In Section 4.4.2, the statistics of turbulence in updraft regions is compared between shower and deep clouds.

4.4.1 Detection of updraft regions

In Section 4.3, updraft regions were identified through qualitative inspection of fields of vertical velocity, w. This approach was sufficient to roughly separate different cloud regions in a small dataset of observations. However, a more precise and consistent method is designed to improve the comparison of observations between case days, and in Chapter 5, between observations and model.

To detect coherent updraft regions, a connected-component algorithm (Haralick and Shapiro, 2002) is applied to each vertical cross-section of w associated with the RHI dataset summarised in Section 2.2.4. This is used to automatically detect the co-ordinates of regions of (at least four) values of w that exceed a specified velocity threshold, where pixels can be connected either by edges or corners. By recording the four spatial extremes of these co-ordinates, a box is placed around an updraft – defined as the updraft region. This is similar to the definition of an updraft region demonstrated in Figure 4.7, except in this case, the spatial extremes of the updraft are numerically defined based on prescribed velocity thresholds. Observed updrafts are often irregular in shape, so this approach leads to the inclusion of some data surrounding the updraft in the defined region. As a result, updraft regions include information about turbulence along the periphery of an updraft, without it having to be co-located with specific values of w. As discussed in Section 1.5.3, previous studies have found the largest values of ε both within and along the edges of updrafts. By using this method to define updraft regions, any important features in ε along updraft edges are likely to be included. Therefore, the analyses in this section can be described more loosely in terms of the turbulence associated with convective updrafts, rather than turbulence precisely co-located with vertical motion within clouds.

The primary aim when applying the detection algorithm is to extract two separate datasets of updraft regions that are representative of the significant updrafts for each day. From this point, features initially detected by the connected-component algorithm will be referred to

as ‘objects’, while ‘updraft regions’ (or just ‘updrafts’) will be used to refer to detected objects that exceed prescribed size and velocity thresholds. These thresholds are applied to distinguish between all detected objects and the more substantial convective updrafts observed on each day. Owing to the marked differences in updraft strength and cloud depth between the two days, slightly different thresholds are used to identify significant updrafts. The first of these thresholds is applied to w, and represents the minimum vertical velocity the algorithm initially detects, $w_{\min}$. For deep clouds, $w_{\min}$ is selected to be 1.5 m s^{-1}. The updrafts are generally much weaker in shower cloud observations (2 – 4 m s^{-1}), compared to deep clouds (6 – 10 m s^{-1}). As a result, a lower $w_{\min}$ of 1 m s^{-1} is applied to better represent the smaller observed range in updraft velocity.

The algorithm identifies an object where at least four connected values of w exceed $w_{\min}$. The resolution of each RHI of w is 500 m in the horizontal direction, and 250 m in the vertical. This means that four connected values can represent very small features in w. As a result, detected objects are filtered by width and depth to remove small, insignificant areas of w from the dataset of updraft regions. This can be described in the context of the vertical velocity field presented in Figure 4.6 (in Section 4.3). Small areas of $w > 1.5$ m s^{-1} are located within the cloud, which are separate from the main updraft. These are too small to be defined as substantial convective updrafts, but which will still be detected by the algorithm. To account for this, objects detected in shower cloud with a depth less than 2 km are filtered out, while in deep clouds this threshold is 3 km. These values allow for the removal of objects that are less than approximately one third of the average cloud depth for both cases. Further to filtering by object depth, a threshold width of 1.5 km was introduced for both case days to remove objects that were less than three pixels wide.

When applied, the connected-component algorithm will sometimes resolve what is qualitatively one updraft region into many separate objects. This can occur in more diffuse updraft regions that are interspersed with areas of $w < w_{\min}$, which can lead to small objects

being recorded within, or on the periphery of, the main updraft region. By detecting several objects in a small spatial area, the associated updraft regions often overlap. This would lead to repeated sampling of the same ε when statistics are collected, potentially introducing biases to the resulting turbulence statistics. The combined effect of applying depth and width thresholds appears to be effective in removing any overlapping updraft regions.

Using this approach, 77 updraft regions were detected in shower cloud observations, and 101 regions for deep cloud. Although the fields of w exist on a Cartesian grid, the four spatial co-ordinates of each updraft region are defined in terms of range and height in the RHI domain. These co-ordinates can therefore be used to overlay the updraft region onto any other radar field in the DYMECS data, including retrievals of ε. This enables a statistical analysis of the turbulence associated with updrafts with different characteristics.

4.4.2 Statistics of updraft turbulence

By using automated procedures during data collection, a more detailed and quantified approach can be applied to investigate ε in observations. This section focuses on assessing statistical relationships between ε, and the spatial and velocity characteristics of updraft regions. These involve correlations of variables associated with individual updrafts (Section 4.4.2.2), but also investigates the change in the probability distribution of ε within updrafts of different strength (Section 4.4.2.3). This analysis begins with a broad comparison between the characteristics of updrafts observed in shower and deep cloud (Section 4.4.2.1)

4.4.2.1 Comparison of updrafts and turbulence in shower and deep clouds

In Figure 4.11a, the cumulative density function (CDF) of updraft area is compared for shower and deep clouds. Each area is the product of the width and depth of the rectangular updraft region placed around the co-ordinate extremes of $w > w_{\min}$. Due to the different

spatial thresholds used to detect updraft regions in the two cases, the minimum area of deep updrafts (4.5 km^2) is slightly different from that of shower updrafts (3 km^2). To provide a fair comparison of probability in Figure 4.11a, shower updrafts with an area less than 4.5 km^2 are not considered; this refers to 25 of the 77 shower updrafts. The median area of deep updrafts (12 km^2) is 60% larger than for shower updrafts (7.5 km^2). The proportion of deep updrafts larger than 10 km^2 (63%) is approximately double that for shower updrafts (29%), while the same is true for the largest observed updrafts (30 km^2 for showers; 58 km^2 for deep cloud). The spatial scale of vertical motion is much larger in the case of deep cloud, and the relationship between ε and updraft dimensions will be presented later in this section.

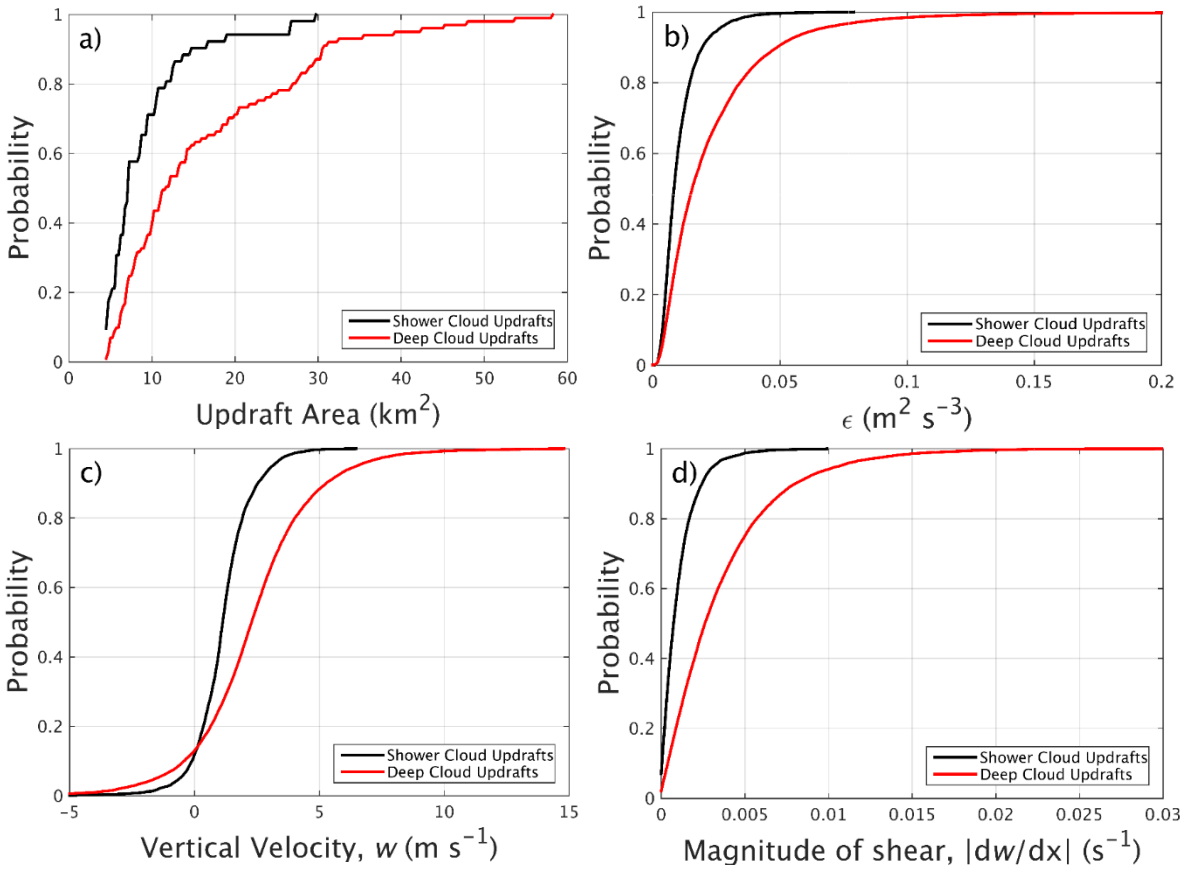

Figure 4.11: Comparison of the cumulative density functions (CDFs) of characteristics of convective updrafts between shower and deep clouds. These include: (a) Updraft area; (b) eddy dissipation rate ε; (c) vertical velocity w; (d) the magnitude of the horizontal shear in w, $\left|\frac{dw}{dx}\right|$. CDFs include values found in all updraft regions on each day. In (a), only shower cloud updrafts of area ≥ 4.5 km^2 are plotted for fair comparison with deep cloud updrafts. In (b) – (d), CDFs consist of 15334 deep updraft values and 4507 values for shower updrafts.

The turbulence associated with updrafts has been identified by overlaying the co-ordinates of each updraft region onto retrievals of ε. Figure 4.11b compares the CDF of all values of ε located within every updraft region in shower and deep clouds. Median values of ε are 60% larger in deep updrafts (0.016 $m^2\ s^{-3}$) than in shower updrafts (0.010 $m^2\ s^{-3}$). However, in terms of the range of ε values that are observed in these radar observations (typically $10^{-3} - 1\ m^2\ s^{-3}$), these values are similar, and relatively small. This indicates that a large proportion of the spatial area within updrafts on both days is only weakly turbulent. However, the proportion of values in deep updrafts that are considered weakly turbulent ($\varepsilon \leq 0.01\ m^2\ s^{-3}$) is only 29%, compared to 49% of values in shower updrafts. This is consistent with results from Section 4.2.2 which examined the vertical distribution of ε in all observed cloud over both days. This suggested that although the majority of the cloud area was weakly turbulent in both cases, significant turbulence was more widely distributed in deep clouds; this appears to hold true even for turbulence located within the cloud region most associated with turbulent production. There are significant differences between turbulence in shower and deep updrafts when inspecting values of $\varepsilon \geq 0.05\ m^2\ s^{-3}$. Only 0.4% of ε values in shower updrafts (corresponding to only 18 values across all updrafts) are larger than $0.05\ m^2\ s^{-3}$, while in deep updrafts this corresponds to 10% of all values. The largest observed value of ε in shower updrafts (0.08 $m^2\ s^{-3}$) is approximately one sixth of the corresponding maximum in deep updrafts (0.48 $m^2\ s^{-3}$, not shown in Figure 4.11b).

Figure 4.11c compares CDFs of w, indicating the distribution of vertical velocity within the updraft regions. As described in Section 4.4.1, the method used to define updraft regions leads to the inclusion of some peripheral data around the co-ordinates of $w > w_{\min}$. As a result, the CDFs in Figure 4.11c include some negative values of w, which are likely included in instances where regions of $w > w_{\min}$ are irregular in shape, and the updraft-downdraft separation distance is small. Negative values of w constitute very similar

proportions of the distribution in both shower updrafts (11%) and deep updrafts (12.5%), suggesting this effect is consistent across both datasets. The largest observed w in deep updrafts (14.9 m s^{-1}) is more than twice that observed in shower updrafts (6.5 m s^{-1}). The median updraft velocity (considering positive w only) is 2.6 m s^{-1} in deep updrafts, which is twice as large as for shower updrafts (1.3 m s^{-1}). This factor of two difference extends to good approximation (1.7 – 2.10) between the 20th and 80th percentiles of the CDFs, indicating that updraft strength is more generally twice as large in deep clouds. For the corresponding percentiles in Figure 4.11b, ε is larger in deep updrafts by a factor varying from 1.4 to 2.4, indicating a nonlinear relationship between turbulent intensity and updraft strength in these clouds. This was first evidenced in Section 4.2.2, where ε_{95} gained a positive vertical gradient with height in deep clouds while remaining constant with height in shower clouds. This resulted in deep cloud ε_{95} increasing nonlinearly with height from approximately equal to shower cloud ε_{95} near the surface, to a factor of four larger when comparing ε_{95} at the respective cloud top heights. The nonlinear relationship between ε and updraft strength was also evidenced in the literature by comparing values in independent studies in Section 1.5.3 (see Table 1.1).

Owing to the importance of shear in the production of turbulence, the horizontal gradient in the updraft velocity $\frac{dw}{dx}$, is also considered. This is determined by differentiating w in the positive x-direction (to the right as it appears in an RHI – away from the radar), over a consistent distance of 500 m; the horizontal resolution of w. To accomplish this for a data point at a distance of x from the radar w_x, the velocity difference between w_x and the data point immediately to the right w_{x+1}, is divided by 500 m. This shear is then attributed to the data point co-located with w_x. For values of w_x that lie along the right-hand edge of an updraft region, a single vector of w values (one pixel wide, extending to the depth of the updraft region) that lies adjacent to the right-hand edge (but outside) of the updraft region is used to compute shear. As any associated turbulence will be independent of the sign of the

shear, the magnitude of each value is taken to define $\left|\frac{dw}{dx}\right|$ for each point. This method is repeated for each updraft region to determine a value of $\left|\frac{dw}{dx}\right|$ for all data points in all updraft regions.

Figure 4.11d compares the CDF of all observed $\left|\frac{dw}{dx}\right|$ from shower and deep updraft regions. The median value of $\left|\frac{dw}{dx}\right|$ in deep updrafts is 0.0026 s^{-1}, which is more than twice the median of 0.0012 s^{-1} observed in shower updrafts. In deep updrafts, the largest shear observed (0.029 s^{-1}) corresponds to a change in w of 14.5 m s^{-1} over 500 m. This shear is therefore likely to be associated with the strongest w observed on the day (up to 14.9 m s^{-1}). The largest shear in shower updrafts of 0.014 s^{-1} is smaller in comparison, corresponding to a change in w of 7 m s^{-1} over 500 m, which is more consistent with the weaker shower updrafts observed. Only 0.3% of $\left|\frac{dw}{dx}\right|$ values in shower updrafts (13 values) are larger than 0.01 s^{-1}, whereas in deep updrafts, this corresponds to 5.3% of observed shears (813 values). For percentiles between the 20th and 80th, $\left|\frac{dw}{dx}\right|$ in deep updrafts varies from a factor of 2.2 to 4.3 larger than in shower updrafts. Although w in deep updrafts is more consistently a factor of two larger than in shower updrafts, the horizontal gradients in w can be stronger by a factor of more than four. This suggests that the increase in w is not accompanied by a corresponding increase in the updraft width; resulting in much stronger horizontal gradients. Evidence for this suggestion is found by correlating the 95th percentile of w with updraft width for the 101 deep cloud updrafts, which produces a correlation coefficient r, of only 0.24 ($r = 0.31$ for shower updrafts). This result is consistent with Anderson *et al*. (2005), who report r^2 values lower than 0.2 ($r < 0.44$) between updraft speed and width for updrafts in the tropics. The impact of the observed relationship between w and $\left|\frac{dw}{dx}\right|$ in these observations is investigated through correlation with ε in the next section.

4.4.2.2 Correlations of turbulence within updrafts

Following from the overview presented in the previous section, statistical relationships between turbulence and updraft characteristics are now examined. Initially, correlations are assessed between the features of updraft velocity (w and $\left|\frac{dw}{dx}\right|$), updraft width and depth, and ε. To accomplish this, the 95th percentile values of w, $\left|\frac{dw}{dx}\right|$, and ε, are recorded in each updraft region, to represent the largest values of each variable, together with the updraft dimensions. For the remainder of this section, the 95th percentile of w, $\left|\frac{dw}{dx}\right|$, and ε will be indicated through use of subscripts as w_{95}, $\left|\frac{dw}{dx}\right|_{95}$ and ε_{95}.

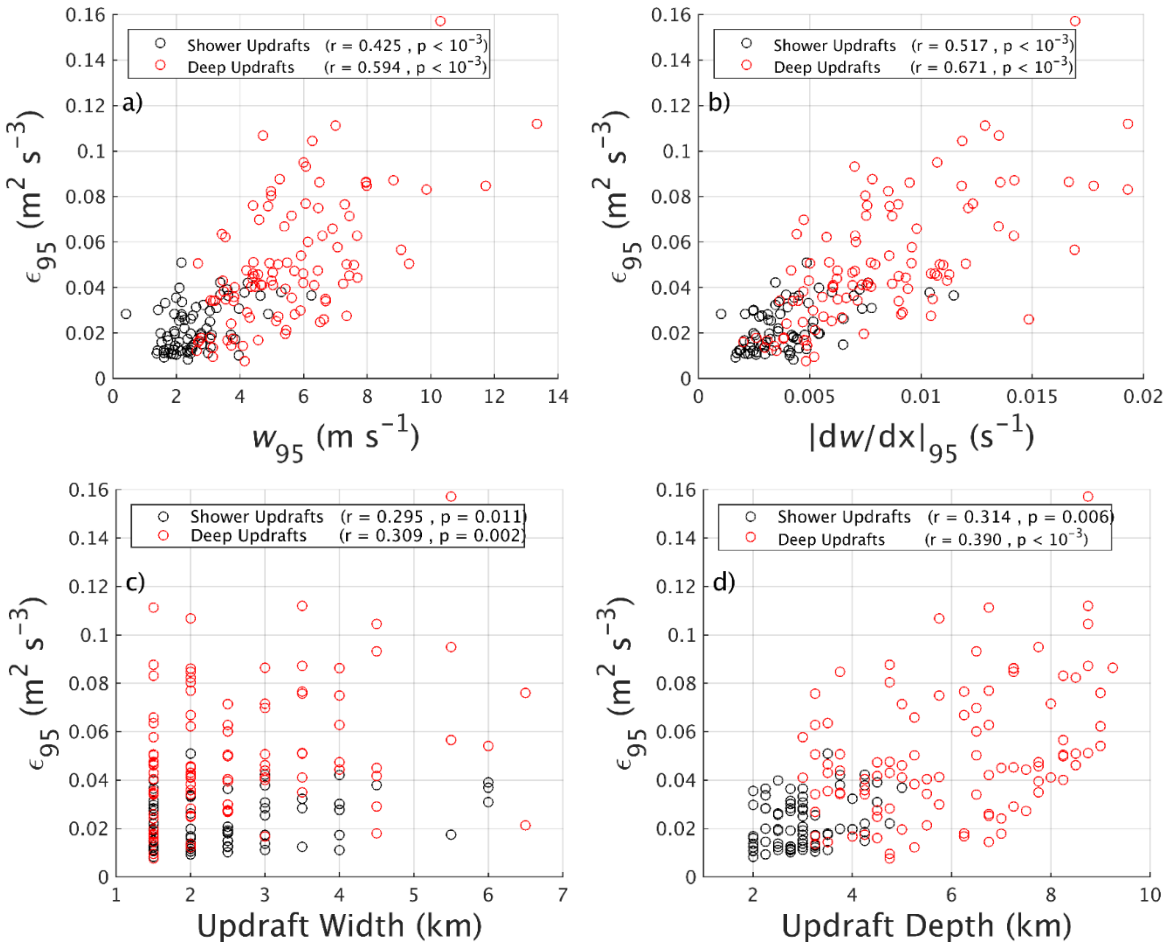

Figure 4.12: Scatter plots comparing the 95th percentile of ε for each updraft region ε_{95}, on the shower and deep cloud cases, to the following corresponding statistics: (a) the 95th percentile of vertical velocity w_{95}, (b) the 95th percentile of the magnitude of the horizontal gradient in vertical velocity $\left|\frac{dw}{dx}\right|_{95}$, (c) the updraft width, and (d) the updraft depth.

Figure 4.12 presents four scatter plots relating ε_{95} to, (a) w_{95}, (b) $\left|\frac{dw}{dx}\right|_{95}$, (c) updraft width, and (d) updraft depth, where each point plotted represents the statistics for one updraft region. Overlaid onto each plot are the correlation coefficient r, and significance statistic p, for both cases, indicating the degree of correlation and significance level between the two variables separately for both days. Figure 4.12a shows that ε_{95} has a significant ($p < 10^{-3}$) positive correlation with w_{95} in both shower updrafts ($r = 0.425$) and deep updrafts ($r = 0.594$). These are considerable correlations that suggest the strongest vertical velocity within convective updraft regions has a significant, and potentially predictable, impact on the peak intensity of turbulence. The correlation in deep updrafts is stronger, likely due to the smaller observed range in w_{95} for shower updrafts, where 72% of w_{95} values lie within a small interval of w ($1 - 3$ m s^{-1}). In comparison, only 5% of w_{95} values in deep updrafts lie within this velocity range. When the data from both days is considered together, in this case representing a broader range in w_{95}, the correlation improves further ($r = 0.718$; $p \ll 10^{-3}$). This suggests that ε_{95} relates to w_{95} in a way that is consistent across the range of w_{95} observed on individual case days and remains consistent between different days of observation. This could indicate that an increasingly stronger correlation may exist if further observations were included to reflect the turbulence associated with an even broader range in w_{95}. If true, this could allow for the parametrisation of ε_{95} in terms of variables associated with convective updrafts.

Figure 4.12b provides an equivalent scatter plot to Figure 4.12a, but for correlations with $\left|\frac{dw}{dx}\right|_{95}$. The resulting correlations with ε_{95} are positive and significant ($p < 10^{-3}$), but also stronger than those with w_{95} ($r = 0.517$ for shower updrafts, $r = 0.671$ for deep updrafts). Turbulence observed within convective updrafts appears to be more sensitive to gradients in w, than to w alone, although w_{95} and $\left|\frac{dw}{dx}\right|_{95}$ themselves are very strongly correlated ($r = 0.868$). The correlation with $\left|\frac{dw}{dx}\right|_{95}$ is again weaker in the case of shower updrafts, reflecting

the smaller range in observed shear; 80% of $\left|\frac{dw}{dx}\right|_{95}$ are smaller than 0.005 s^{-1}, compared with only 22% in deep updrafts. When $\left|\frac{dw}{dx}\right|_{95}$ values from both days are combined, r increases to 0.755, which represents the strongest observed correlation between ε_{95} and any characteristic of convective updrafts. This provides further evidence that it may be possible to parametrise ε_{95} as a function of updraft characteristics if, in this case, additional observations were collected to include ε_{95} from a broader range in $\left|\frac{dw}{dx}\right|_{95}$.

Weaker positive correlations exist between ε_{95} and the width and depth of updrafts for both showers ($r = 0.295$ for width, and $r = 0.314$ for depth), and deep cloud ($r = 0.309$ for width, and $r = 0.390$ for depth). When the data from both days is combined, the correlation with updraft width is not improved ($r = 0.281$). The correlation with updraft depth is improved to $r = 0.609$, however, this is assumed to be indirect due to the stronger correlation between updraft depth and w_{95} ($r = 0.678$). This suggests that the intensity of turbulence is not highly sensitive to the spatial dimensions of the updraft. This is consistent with results from Section 4.3, which performed a more limited and imprecise investigation into the relationship between ε and updraft dimensions in SCCCs.

4.4.2.3 Change in the distribution of ε with updraft strength

Correlation techniques are useful to identify the most important features of convective updrafts in generating strong turbulence, and to quantify the degree of sensitivity in a way that can be tested against both new observations, and MetUM simulations. However, there are limitations to the insights that can be provided by comparing one statistic from each updraft region. To further substantiate these results, the distribution of ε is compared within updraft regions of different strength. To accomplish this, all ε values within a given updraft region are added to a CDF based on its value of w_{95}. CDFs of ε are then combined for updraft regions with w_{95} falling in 2 m s^{-1} velocity intervals. This interval was selected to be large

enough to cover the range of w_{95} observed on both days, and to ensure a sufficient number of ε values constitute each CDF. By doing this, the full distribution of ε can be tested against w_{95}, instead of just the largest values. Figure 4.13 and Figure 4.14 shows the change in the CDF of ε with w_{95} in shower and deep updraft regions, respectively. The intervals of w_{95} are consistent between the two cases to aid comparison, although only the 2 – 4 m s^{-1} and 4 – 6 m s^{-1} intervals are represented by both cases. There were no deep updrafts with w_{95} less than 2 m s^{-1}, and no shower updrafts with w_{95} larger than 6 m s^{-1}.

In both shower and deep updrafts, there is a trend towards a lower probability of small ε, and a higher probability of large ε, with increasing w_{95}. For shower updrafts (Figure 4.13), the median value of ε increase from 0.009 m^2 s^{-3} when $w_{95} = 0 - 2$ m s^{-1}, to 0.015 m^2 s^{-3} when $w_{95} = 4 - 6$ m s^{-1}. The two CDFs associated with w_{95} between 0 – 4 m s^{-1} are very similar, while the difference between these distributions when w_{95} is 4 – 6 m s^{-1} is more considerable. This is particularly evident for small values of ε (less than 0.01 m^2 s^{-3}). For the two smallest intervals of w_{95}, 61% (0 – 2 m s^{-1}) and 47% (2 – 4 m s^{-1}) of ε values are less than 0.01 m^2 s^{-3}, whereas this falls to only 27% of values in updrafts of 4 – 6 m s^{-1}. The proportion of ε values that are larger than 0.03 m^2 s^{-3} is small for all shower updrafts but are more than twice as frequent when w_{95} is 4 – 6 m s^{-1} (9%), than when w_{95} is 2 – 4 m s^{-1} (4%). Together, these results suggest that when $w_{95} < 4$ m s^{-1}, the distribution of ε is largely insensitive to the updraft strength. However, a significant change in the distribution of ε is observed for updrafts of more than 4 m s^{-1}, which is characterised by an approximate factor two decrease in the proportion of $\varepsilon < 0.01$ m^2 s^{-3}, and a factor two increase in the proportion of $\varepsilon > 0.03$ m^2 s^{-3}.

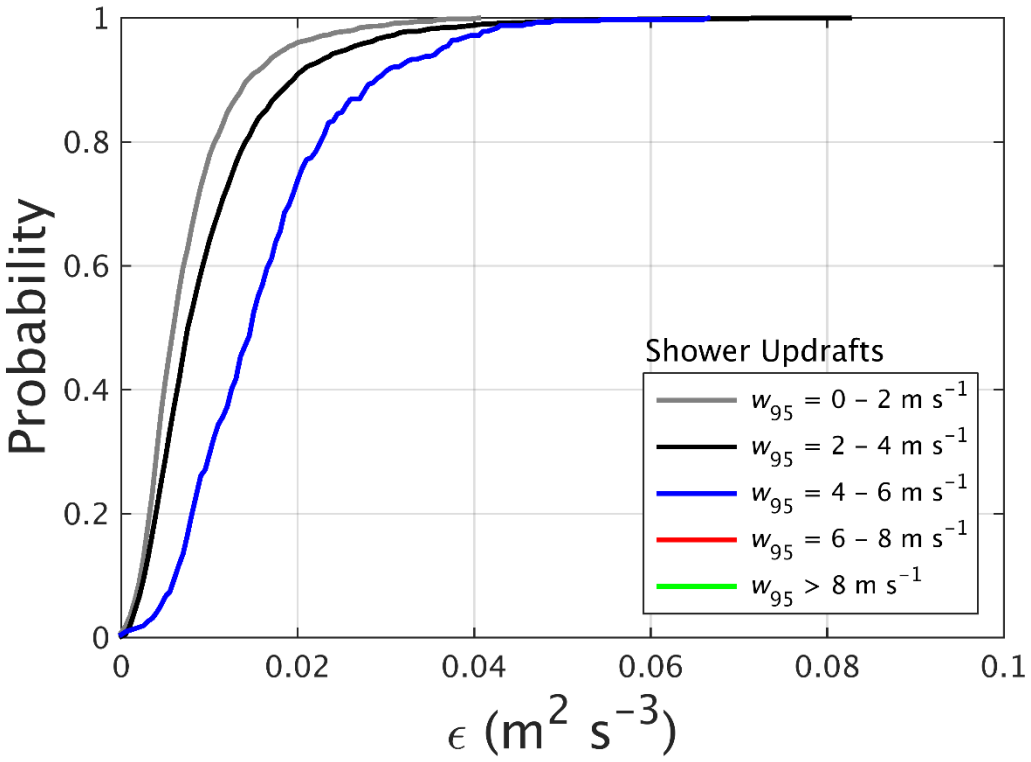

Figure 4.13: The change in the cumulative density function (CDF) of ε in updraft regions with different 95th percentile values of w (w_{95}), for shower clouds. Values of w_{95} did not exceed 6 m s^{-1} in any updraft region considered on this day, however these intervals are retained for comparison with Figure 4.14.

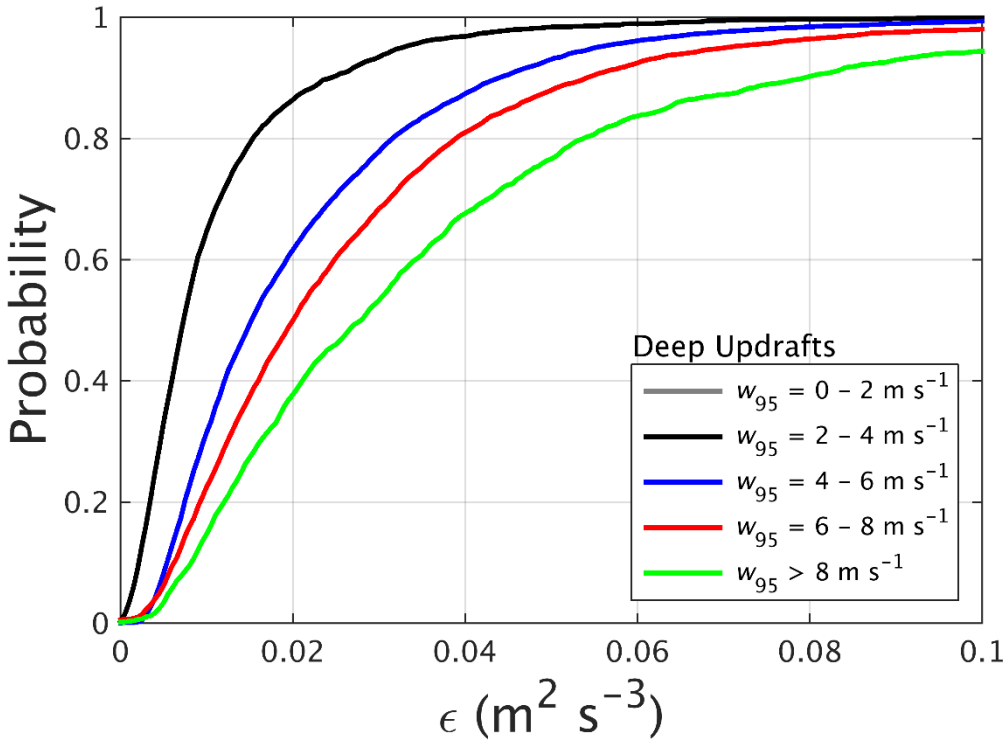

Figure 4.14: The change in the cumulative density function (CDF) of ε in updraft regions with different 95th percentile values of w (w_{95}), for deep clouds. Values of w_{95} smaller than 2 m s^{-1} were not found in any updraft regions on this day.

For deep updrafts (Figure 4.14), similarly to shower updrafts, median values of ε increase with w_{95}, with this trend extending $w_{95} > 8$ m s^{-1}. However, key differences exist for values of ε larger than 0.05 m^2 s^{-3}. These are very uncommon in shower updrafts, constituting only 0.5% of all observations, whereas in deep updrafts, this proportion increases from 1.7% in the weakest updrafts ($w_{95} = 2 - 4$ m s^{-1}), to as high as 24% of values in the strongest updrafts ($w_{95} > 8$ m s^{-1}). For the two intervals of w_{95} for which a distribution of ε is available over both days (between 2 – 6 m s^{-1}), the median values of ε are very similar. For updrafts of 2 – 4 m s^{-1}, median values of ε in both cases are approximately 0.01 m^2 s^{-3}, and for updrafts of 4 – 6 m s^{-1}, distributions of ε in both cases have median values of 0.015 m^2 s^{-3}. For updrafts of 2 – 4 m s^{-1}, 54% of ε values in deep updrafts are less than 0.01 m^2 s^{-3}, comparable to 47% for the same strength of shower updraft. A similar consistency is found for updrafts of 4 – 6 m s^{-1}, where the proportion of $\varepsilon < 0.01$ m^2 s^{-3} is 27% and 29% in shower and deep updrafts, respectively. This provides further evidence that the intensity of turbulence may be related to the specific characteristics of convection in a way that independent of the day of observation, or general convective scenario. However, the similarities for the average and low values of ε are not as clear for the larger ε in the distributions. In deep updrafts of 4 – 6 m s^{-1}, 7% of observed ε is larger than 0.05 m^2 s^{-3}, while, as mentioned, these values are very rare in shower updrafts (only 0.5% of values). This would suggest instead that turbulence is more intense in deep updrafts than in shower updrafts of the same strength, and not dependent solely on the updraft features.

These results raise an important question: is turbulent energy generated and dissipated on timescales that are small compared to the evolution of convective updrafts? Using only snapshot observations to investigate turbulence relies on the assumption that the observed turbulence is in response to the cloud characteristics observed simultaneously. In the case where a convective updraft is the production mechanism, the initial turbulent eddies,

generated on the scale of the updraft circulation, will require time in the downscale energy cascade to reach scales where turbulence is dissipated. However, during this time, the features of the updraft may have changed considerably. The rate of turbulent energy dissipation (given by ε) will be related to the strength of the updraft at the time of production. Therefore, turbulence will not always be observed together with the exact processes responsible for its production. Further to this, there are limitations associated with using only vertical cross-sections to investigate turbulence. The effects of advection within the cloud may introduce turbulence into a vertical cross-section from processes that are not observed. For example, in cases where an RHI was not performed directly through the centre of updraft (this is possible, scans were only guided by rainfall rates), turbulence may be observed that was associated with stronger w immediately adjacent to the scan. The strength of the correlations presented in Section 4.4.2.2 would suggest that the overall impacts of these effects is small; the observed turbulence is significantly related to the updraft features observed simultaneously. However, they may explain the more subtle difference in the distributions of ε in updrafts of the same strength, but observed on different days (Figure 4.13 and 4.14). Updrafts with w_{95} of 4 – 6 m s^{-1} (and higher) were much more common in deep clouds than shower clouds. It therefore becomes more likely that the effects of eddy timescales and advection introduce turbulence that is not entirely consistent with the updraft strength.

4.5 Spatial characteristics of coherent ε features

So far in this chapter, analyses of turbulence in observed clouds has included the vertical distribution of ε, the spatial distribution of ε relative to convective updrafts, and the statistical relationships between ε and characteristics within updraft regions. A final investigation is now performed into the appearance of turbulent structures within clouds. This is achieved

by applying the same connected-component algorithm as used to detect updraft regions, to retrievals of ε. By doing this, the size and shape of coherent features in ε can be found as a function of turbulent intensity and compared between shower clouds and deep clouds. By using automated detection methods, spatial characteristics of ε can be determined consistently between the two days of observations, and also in MetUM model simulations. The primary aim of this section is to determine the typical spatial scales of turbulent dissipation in observed clouds as a function of turbulent intensity. The spatial extent of dissipation features may reflect the typical scales of turbulent production within the clouds and provide a useful characterisation of the appearance of dissipation features to compare with parametrised turbulence in the MetUM (Chapter 5).

Section 4.5.1 outlines the data sources, methods used in data collection, and methods to determine spatial scales of turbulent features. Section 4.5.2 then presents and discusses the spatial scales of turbulent structures as a function of ε, and compares this across the two cloud types. The sensitivity of results to methods used to determine average size and shape is then examined.

4.5.1 Methods and data collection

The same connected-component algorithm used in Section 4.4.1 to detect updrafts is applied to fields of ε retrieved for the RHI subset described in Section 2.2.4. Objects of ε are detected from anywhere in the RHI domain between 30 – 170 km in range, where at least four connected values of ε exceed a prescribed threshold (referred to as ε_{thld}). Pixels can only be connected by edges; this is chosen (instead of both edges and corners, as for updraft detection) in an attempt to maximise the fill-fraction of $\varepsilon > \varepsilon_{thld}$ within the area defined by the spatial extremes of the object. A range of values for ε_{thld} are selected to enable the comparison of spatial scales as a function of turbulent intensity. In shower cloud, three thresholds of 0.01, 0.03 and 0.05 $m^2\ s^{-3}$ were selected to represent the range of ε observed.

For deep clouds, two additional thresholds of 0.1 and 0.2 $\mathrm{m^2\ s^{-3}}$ were included to reflect the larger values of ε. Objects detected at $\varepsilon_{\mathrm{thld}} = 0.03\ \mathrm{m^2\ s^{-3}}$, for example, will automatically include any regions of $\varepsilon > 0.03\ \mathrm{m^2\ s^{-3}}$ within its defined area. Objects are therefore referred to as including $\varepsilon > \varepsilon_{\mathrm{thld}}$, rather than $\varepsilon = \varepsilon_{\mathrm{thld}}$, in later analysis.

Using a similar method to that applied to updraft regions in Section 4.4, the object width W, and depth D, are determined from the four co-ordinates of the spatial extremes of each object. To find the average size and shape of ε objects, the median area and axial ratio (A_{m} and R_{m}) are first computed from all objects i, detected at a given $\varepsilon_{\mathrm{thld}}$:

$$A_{\mathrm{m}} = \mathrm{Median}(W_i \cdot D_i) \quad ; \quad R_{\mathrm{m}} = \mathrm{Median}\left(\frac{W_i}{D_i}\right) \tag{4.1}$$

These values are then used to estimate the average width and depth of objects for plotting purposes (referred to as W_{m} and D_{m}, although they are not strictly median values).

$$W_{\mathrm{m}} = \sqrt{A_{\mathrm{m}} \cdot R_{\mathrm{m}}} \quad ; \quad D_{\mathrm{m}} = \sqrt{\frac{A_{\mathrm{m}}}{R_{\mathrm{m}}}} \tag{4.2}$$

This approach was chosen instead of simply calculating the median of W and D independently in an attempt to pair the width and depth of each individual object when finding the average shape. If only W and D were used, the precision of the median width would be limited to multiples of 300 m due to the fixed radial resolution of the DYMECS data. This is avoided by allowing W_{m} (and D_{m}) to be found indirectly as a function of A_{m} and R_{m}. However, due to the numerous possible methods to determine the size and shape of ε objects, the sensitivity of results to other methods is in investigated in Section 4.5.3.

Two filters have been applied to the resulting dataset of objects to remove biases and improve data quality. The combined effects on the object counts for each $\varepsilon_{\mathrm{thld}}$ is summarised in Table 4.3. The first of these introduces a minimum threshold to A_{m}. The resolution of RHIs in the elevation direction becomes increasingly high at smaller distances from the radar due to the finite beam-width.

Deep Cloud		Shower Cloud	
$\boldsymbol{\varepsilon_{thld}}$ $(\mathbf{m^2\ s^{-3}})$	**Object counts (before filtering)**	$\boldsymbol{\varepsilon_{thld}}$ $(\mathbf{m^2\ s^{-3}})$	**Object counts (before filtering)**
0.01	1400 (2159)	0.01	618 (1061)
0.03	644 (1299)	0.03	150 (332)
0.05	391 (898)	0.05	34 (92)
0.1	125 (342)	-	-
0.2	11 (64)	-	-

Table 4.3: Final object counts for each threshold of ε in shower and deep clouds. Counts before filtering by area and location are indicated in parentheses.

Combining this with the effects of over-sampling described in Section 2.2.1, which results in an angular resolution a factor of six higher than the beam-width, four data points (the minimum for object detection) can constitute a very small spatial area. To remove the exceedingly small objects, a minimum threshold of 0.1 km^2 is applied to A_m. This results in a 38% and 31% reduction in the total object counts detected in deep and shower cloud, respectively. These are both large proportions of total objects, indicating that biases in the median object size would have resulted if a threshold to A_m was not applied.

The second filter refers to ε objects detected near the top and base of observed clouds. The spatial extent of objects in these regions is often curtailed by the edges of the data and are therefore susceptible to biases in shape. This is illustrated in Figure 4.15, which shows the change in R_m with height for objects detected in deep clouds. Objects detected in the top and bottom 1 km of cloud display a much higher R_m than for the rest of the vertical profile, for each $\varepsilon_\mathrm{thld}$ shown. This demonstrates that the ratio of width to depth is increased due to

incomplete vertical dimensions of objects near the cloud edge. Including objects from these locations would introduce biases to the average shape of objects. In shower clouds, the cloud top is generally no higher than 6 km, and 10 km for deep clouds. However, there is variability in the cloud tops of individual clouds, and also in the cloud base with range due to scanning at non-zero elevations. To account for this variability, objects are removed if detected within 1 km of the respective cloud tops for both days (5 – 6 km in shower cloud; 9 – 10 km in deep cloud), or within 1 km of the surface in both cases. This corresponds to a further reduction in total object counts of 13% and 19% in shower and deep clouds, respectively. No methods have been applied to remove objects located near the sides of clouds, or other cloud boundaries. The final data counts for each ε_{thld}, together with those before any filtering was applied, are listed in Table 4.3. Following from these methods to improve data quality, detected objects will be referred to as spatially coherent 'features' of turbulent dissipation.

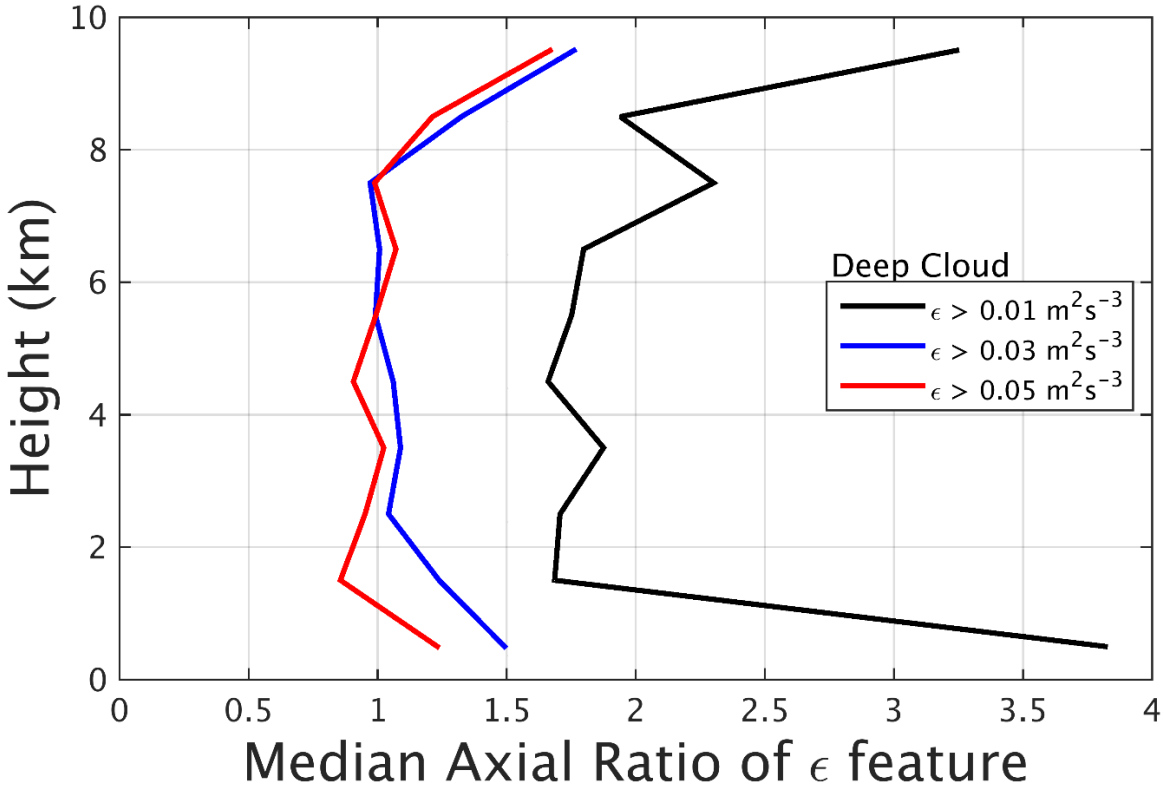

Figure 4.15: The change in the axial ratio (width to depth) of deep cloud objects with height, showing the bias to high axial ratio near the cloud top and base due to the suppressed vertical dimension.

4.5.2 Spatial characteristics of ε features

To better reflect the range of features sizes observed on both days, and to allow comparisons between average and large, the full dataset had been split into three, by terciles of area. For each ε_{thld}, average features are defined as those falling between the 33rd and 66th percentiles of area, and large features are those larger than the 66th percentile of area. Equations (4.1) and (4.2) are then applied separately to these, to determine W_m and D_m at each ε_{thld}. As W_m and D_m are the largest dimensions of (often irregularly shaped) features in ε, simply using a rectangular region defined by these scales would overstate the true spatial coverage of $\varepsilon > \varepsilon_{thld}$. The appearance is instead approximated by ellipses of width W_m, and depth D_m.

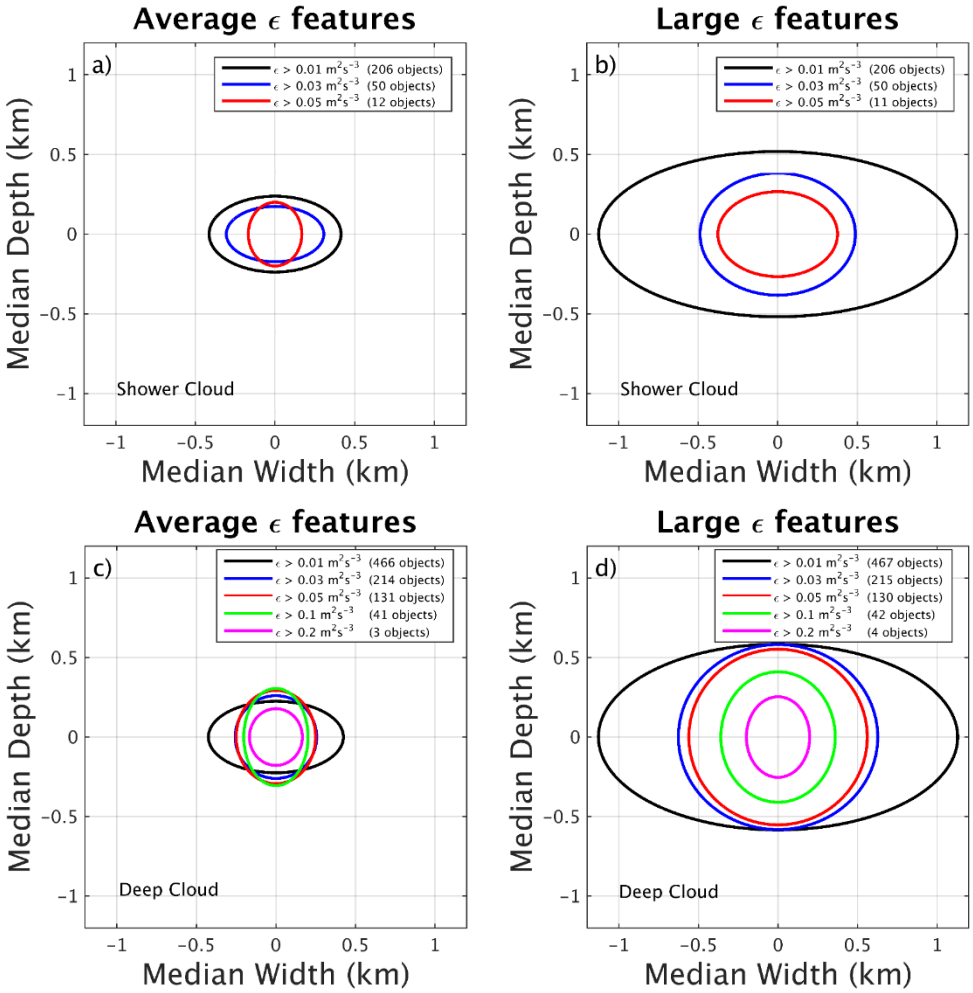

Figure 4.16: Median size of average and large ε objects in shower cloud ((a) and (b)), and deep cloud ((c) and (d)). Objects have been approximated by ellipses using W_m and D_m calculated from objects at each ε_{thld}, using (4.1) and (4.2).

Figure 4.16 compares the spatial characteristics of the average and large turbulent features, as a function of $\varepsilon_{\mathrm{thld}}$, between shower and deep cloud. When comparing the average features (Figures 4.16a and 4.16c), the spatial scales of the weakest turbulence ($\varepsilon > 0.01\ \mathrm{m^2\ s^{-3}}$) are approximately the same in both shower and deep cloud; $W_{\mathrm{m}} \sim 0.85$ km and $D_{\mathrm{m}} \sim 0.45$ km. Turbulence has been shown to be more widely distributed in deep clouds, suggesting that the spatial area of turbulent dissipation would be larger than in shower clouds. However, this result suggests that, for weak turbulence at least, the size and shape of discrete features in ε may be independent of cloud characteristics. The average spatial area of $\varepsilon > 0.03\ \mathrm{m^2\ s^{-3}}$ is approximately the same in shower (0.21 $\mathrm{km^2}$) and deep clouds (0.26 $\mathrm{km^2}$). However, the features in deep cloud are approximately circular with $W_{\mathrm{m}} \sim D_{\mathrm{m}} \sim 0.5$ km, while features in shower cloud retain the same $R_{\mathrm{m}} \sim 1.75$ as for those with $\varepsilon > 0.01\ \mathrm{m^2\ s^{-3}}$. The axial ratio of features of $\varepsilon > 0.05\ \mathrm{m^2\ s^{-3}}$ is the same in both shower and deep clouds ($R_{\mathrm{m}} \sim 0.85$), although A_{m} is more than a factor of two larger in deep clouds. This suggests that for features of average size, only small differences exist between shower and deep clouds, and only when $\varepsilon > 0.01\ \mathrm{m^2\ s^{-3}}$. The most significant difference appears to exist in the size of stronger dissipation features ($\varepsilon > 0.05\ \mathrm{m^2\ s^{-3}}$), where W_{m} and D_{m} are both 50% larger in deep clouds. The spatial characteristics of turbulence stronger than $0.05\ \mathrm{m^2\ s^{-3}}$ in deep clouds will be examined in the context of the largest features (Figure 4.16d).

When comparing the large dissipation features (Figures 4.16b and 4.16d), the difference in spatial characteristics between the cloud types becomes clearer as ε increases. The spatial scales of $\varepsilon > 0.01\ \mathrm{m^2\ s^{-3}}$ are again very similar between shower and deep clouds ($W_{\mathrm{m}} \sim 2.25$ km and $D_{\mathrm{m}} \sim 1$ km), again suggesting that scales of turbulent dissipation may only become dependent on cloud characteristics when $\varepsilon > 0.01\ \mathrm{m^2\ s^{-3}}$. The high R_{m} and large A_{m} of these weak dissipation features when compared to any other threshold of ε may reflect the effects of diffusion and horizontal advection of decaying turbulent features within

the cloud. In deep clouds, features of $\varepsilon > 0.03\ \mathrm{m^2\ s^{-3}}$ and $\varepsilon > 0.05\ \mathrm{m^2\ s^{-3}}$ have approximately the same characteristics ($W_\mathrm{m} \sim D_\mathrm{m} = 1.1 - 1.3$ km), with A_m only 15% smaller for $\varepsilon > 0.05\ \mathrm{m^2\ s^{-3}}$. For the same features in shower cloud, A_m is a factor of two smaller for features of $\varepsilon > 0.03\ \mathrm{m^2\ s^{-3}}$, and a factor of three smaller for $\varepsilon > 0.05\ \mathrm{m^2\ s^{-3}}$. This suggests that the scales of large dissipation features are considerably smaller in shower cloud, except for weak turbulence ($\varepsilon > 0.01\ \mathrm{m^2\ s^{-3}}$), which are almost identical in shape and size. When comparing Figures 4.16b and 4.16d, a key difference exists in the axial ratio of features; $R_\mathrm{m} > 1.25$ for all ε in shower cloud, while in deep cloud R_m decreases consistently with ε, from $R_\mathrm{m} = 1.9$ to $R_\mathrm{m} < 1$ when $\varepsilon > 0.1\ \mathrm{m^2\ s^{-3}}$ and $\varepsilon > 0.2\ \mathrm{m^2\ s^{-3}}$. Although data counts are significantly lower for these features, the vertical orientation of strong turbulent features may result from the stronger buoyant motion within the deep clouds.

4.5.3 Sensitivity to methods, and summary

As mentioned in Section 4.5.1, other methods exist to determine the average spatial scales of dissipation features. The selected method in Section 4.5.1 involved using the median area A_m, and median axial ratio R_m, of ε objects, to determine the median size and shape. This is now compared to two other methods: (1) computing the median width and depth scales independently, and (2) defining A_m in terms of the true spatial area of $\varepsilon > \varepsilon_\mathrm{thld}$ within each object. Method (1) involves simply calculating the median of W and D separately from a dataset of objects and using these values to define the shape of an ellipse.

For each object detected by the connected-component algorithm, A_m was determined from the median product of W and D, which represent the largest scales of each object. In cases where objects are not perfect squares of data, this approximation for area will include some values of $\varepsilon < \varepsilon_\mathrm{thld}$. This approximation is suitable only if the average proportion of $\varepsilon > \varepsilon_\mathrm{thld}$ is consistent for objects detected at different $\varepsilon_\mathrm{thld}$. If this is not true, A_m will

represent more of an over-estimation of the true spatial area of $\varepsilon > \varepsilon_{\text{thld}}$ for objects detected at particular $\varepsilon_{\text{thld}}$, introducing biases to Figure 4.16. To test the sensitivity of results to this effect, A_{m} is redefined to the median of the spatial area of $\varepsilon > \varepsilon_{\text{thld}}$ for each object. For each object i, the detection algorithm records the number of data points N, where $\varepsilon > \varepsilon_{\text{thld}}$, which are converted to a spatial area using the following expression:

$$A_i = N \cdot A_{\text{av}} = N \cdot 300\ \text{m} \cdot \left(\frac{(r_{\max} - r_{\min})}{2} \cdot (F_{\text{os}} \cdot \theta_1) \right) \tag{4.3}$$

Where A_i is the area of object i, and A_{av} is the average area of pixels within i. A_{av} is determined as the product of pixel width (the range resolution of CAMRa, 300 m), and average pixel depth. The product of the average range of pixels in i (given by $\frac{1}{2}(r_{\max} - r_{\min})$), and the one-way half-power beam-width, θ_1, provides the depth of the beam. This is then weighted by a factor $F_{\text{os}} = 0.174$, to account for the average oversampling of the radar in the elevation direction due to slow scan speeds. The median area of objects is then determined simply as the median of A_i, which then replaces A_{m} in (4.2) to determine the equivalent width and depth of ellipses for plotting.

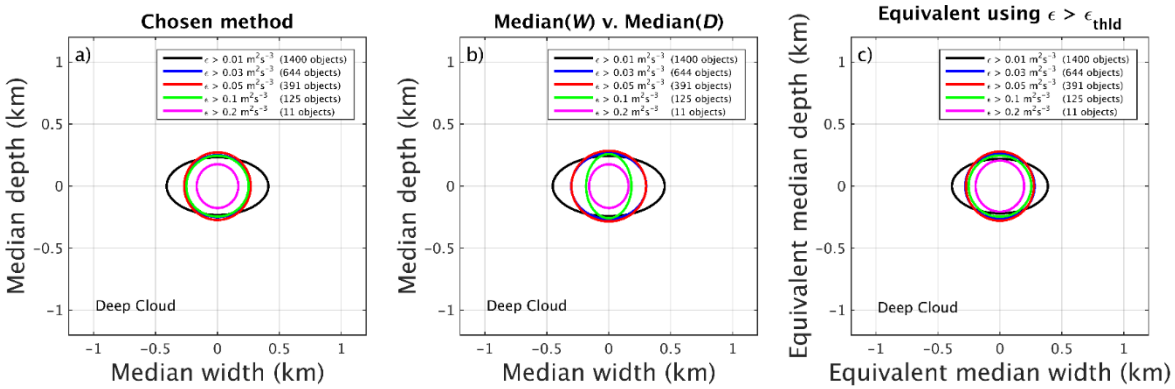

Figure 4.17: Comparison of median object sizes using three different methods for calculation. (a) Chosen method – as used in to produce Figure 4.16. (b) The median width and depth of all objects calculated independently. (c) Width and depth reconstructed from the spatial coverage of $\varepsilon > \varepsilon_{\text{thld}}$ within each object and the axial ratio of width to depth.

Figure 4.17 compares the median spatial scales derived from all deep cloud objects using the method described in Section 4.5.2, with those from methods (1) and (2). Figure 4.17b shows that simply calculating the median of W and D independently provides a very similar result to the chosen method. The depth of features is almost identical for all $\varepsilon_{\mathrm{thld}}$, but the widths are restricted to multiples of 300 m (the radial resolution of the data). When using A_{m} derived from only $\varepsilon > \varepsilon_{\mathrm{thld}}$ (Figure 4.17c), the resulting features are almost unchanged from the chosen method. The area of features in Figure 4.17c should be smaller than those in Figure 4.17a, as the area of $\varepsilon > \varepsilon_{\mathrm{thld}}$ will be less than the product of W and D. Instead these appear very slightly larger in some cases (e.g. $\varepsilon > 0.2\ \mathrm{m^2\ s^{-3}}$), which results from variability in the elevation resolution of the data. In some cases, where the over-sampling factor is much smaller than $F_{\mathrm{os}} = 0.174$, the area of individual pixels will be over-estimated by (4.3). However, the purpose of this comparison is to test the consistency of the effect for features detected at different values of $\varepsilon_{\mathrm{thld}}$. Features are almost identical in size, with no significant differences for any particular $\varepsilon_{\mathrm{thld}}$, suggesting that the average proportion of $\varepsilon > \varepsilon_{\mathrm{thld}}$ within the original features is consistent across all $\varepsilon_{\mathrm{thld}}$. Therefore, Figure 4.16 provides accurate representations of the spatial characteristics of dissipation features, that are insensitive to other methods of approximation.

In summary, the analysis in this section (4.5) provides useful insights into the typical spatial characteristics of dissipation features, relative to turbulent intensity. Features plotted in Figure 4.16 have been shown to be insensitive to different methods used to approximate size and shape. However, there are limitations to how these features can be analysed in the context of cloud characteristics. The differences between dissipation features in shower and deep cloud have been related to the main differences between the two cloud types. Although, without supporting evidence that relationships exist between turbulent production mechanisms, and the size of dissipation features, these conclusions remain speculative. Characterising the appearance of observed turbulence is perhaps more beneficial to the

evaluation of parametrised turbulence in Chapter 5, than to understand turbulent production processes in observations.

4.6 Summary and conclusions

By applying the turbulence retrieval method developed in Chapter 3 to radar observations collected with CAMRa, this chapter includes a thorough investigation into the characteristics of convective cloud turbulence. The analysis of ε was focused on vertical cross-section datasets collected for two contrasting cloud types; shallow shower cloud, and deep cloud with stronger updrafts. The breadth of the datasets available for both days, combined with the limitations of vertical cross-section data, suggested a statistical assessment of ε was the optimal approach. The methods used in this chapter have been developed to enable consistent application to clouds simulated in the MetUM.

Retrievals of ε for both days were presented and discussed in detail with several other radar fields in Section 4.2. Although only two individual clouds were compared, there were indications that the spatial distribution and intensity of observed turbulence could be related to the cloud characteristics. Mean values of ε were twice as large in the deep cloud (0.04 $m^2\ s^{-3}$) than in shower cloud. Values of ε up to 0.61 $m^2\ s^{-3}$ were observed in the deep cloud, more than a factor of six larger than the corresponding value in shower cloud 0.09 $m^2\ s^{-3}$. These values are within the range reported previously from observations of deep convective clouds (see Section 1.5.3 and Table 1.1). Turbulence was spatially correlated with the main updraft in both cases, however, strong turbulence appeared to be more widely distributed in the upper regions of deep cloud. This observation is consistent with results from Knupp and Cotton (1982) and Istok and Doviak (1986) (see Section 1.5.3) and was reflected in the analysis of the vertical distribution of ε in all clouds observed on both days. Turbulent intensity in shower clouds remained approximately constant with height, whereas

in deep clouds, 95th percentile values of ε increased by a factor of four with height throughout the 10-km cloud depth. Median ε in both cloud types were similarly small (~ 0.01 $m^2\ s^{-3}$), suggesting a large proportion of the spatial area of observed clouds is only weakly turbulent. An increase in ε with height was reported by numerous previous studies in Section 1.5.3; this has been quantified for shower and deep clouds with results that suggest the positive vertical gradient in ε increases with updraft strength.

Significant positive correlations were identified between ε and the characteristics of single-cell convective clouds (SCCCs) in Section 4.3. Features of vertical velocity (mean magnitude and 95th percentile) were found to be the most important in generating strong turbulence. No significant correlation was found between ε and the spatial dimensions of the cloud or updraft. Turbulence was strongest within the main updraft and above-updraft cloud regions; locations associated with strong buoyancy and velocity gradients. However, turbulence in cloud regions containing the downdraft was found to be significantly lower (17%) than the cloud-average, suggesting downdrafts are considerably less important than updrafts in producing turbulence within convective clouds. The SCCC framework restricted the dataset to only 25 cloud cases, which were determined qualitatively. Significant correlations could still be identified in this dataset; however, these limitations rendered the results insufficient for a reliable and detailed comparison with MetUM data.

By identifying the cloud characteristics that are most important in producing strong turbulence in SCCCs, a refined investigation into ε in convective updraft regions was performed in Section 4.4. Automated updraft detection methods were used examine updraft turbulence to improve the quantitative detail of the correlations identified in Section 4.3, and to enable a consistent application to MetUM data. Strong positive correlations were identified between ε_{95}, w_{95} and $\left|\frac{dw}{dx}\right|_{95}$ in updrafts of both cloud types, with weaker positive correlations with updraft dimensions. This is in agreement with both the positive correlation implied by maxima in ε and w from previous studies presented in Table 1.1, and the spatial

correlation between ε with regions of strong shear (Section 1.5.3). Correlations were strongest with $\left|\frac{dw}{dx}\right|_{95}$ suggesting the gradients in vertical velocity were more important in generating strong turbulence than w alone. Correlations identified from the combined updrafts of both days were stronger than for individual days ($r = 0.718$ for w_{95}; $r = 0.755$ for $\left|\frac{dw}{dx}\right|_{95}$). This suggests that consistent relationships may exist between ε and updraft characteristics that are independent of the day of observation. By examining probability distributions of ε, a consistent trend towards a lower probability of small ε, and higher probability of larger ε, was found with increasing w_{95}. In shower updrafts where $w_{95} < 4$ m s^{-1}, the distribution of ε was found to be largely insensitive to updraft strength, with more significant differences when $w_{95} > 4$ m s^{-1} for both cloud types. Approximately half of ε values were lower than 0.01 m^2 s^{-3} in updrafts of 2 – 4 m s^{-1} for both days. While this proportion fell consistently to 27% and 29% in shower and deep updrafts, respectively, when $w_{95} = 4 - 6$ m s^{-1}. This provided further evidence that ε may be function of cloud characteristics independent of the day of observation. If true, by including observations to reflect turbulence associated with a spectrum of cloud types, attempts could be made to parametrise ε as a function of updraft characteristics. This would help to isolate relationships from individual days of observation, removing the need to simulate corresponding days when evaluating turbulence in numerical models.

In Section 4.5, the spatial characteristics of coherent dissipation features in clouds were investigated as a function of turbulent intensity. For large features of ε in deep clouds, the median width doubles from 1.12 – 2.25 km when ε_{thld} decreases from 0.05 – 0.01 m^2 s^{-3}. For the same range of ε_{thld} in shower cloud, median width increases by a factor of three from 0.75 – 2.25 km. In deep clouds, when ε_{thld} increases from 0.1 – 0.2 m^2 s^{-3}, features become more deep than wide, with spatial scales less than 1 km. Without identifying that relationships exist between the spatial scales of turbulent features and cloud characteristics, comparisons between features and cloud processes are difficult to make. However, results

can used to identify the differences in the appearance of turbulence in the MetUM, as a function of turbulent intensity.

In this chapter, a rigorously derived turbulence retrieval method has been applied to improve understanding of turbulence in observed clouds, and to perform a statistical assessment of turbulence for model evaluation (in Chapter 5). In accomplishing this, results must be evaluated in the context of the limitations of the RHI dataset; vertical cross-sections taken from one instance. As discussed in Section 4.4.2.3, relationships between ε and cloud processes rely on the assumption that the turbulent energy cascade to dissipation scales occurs on timescales that are small compared to the evolution of convective processes. Further to this, it is assumed that the effects of eddy advection are small, i.e. ε can be attributed to the cloud processes observed simultaneously. Significant statistical relationships have been clearly identified in this chapter, suggesting the impact from these effects has been small. However, these effects will limit the precision to which ε can be explained in data of this type.

The results of this chapter suggest numerous improvements can be made to study turbulence in convective clouds for model evaluation. These should include using multiple high-resolution radars to observe the three-dimensional structures of turbulence, and utilise the turbulence retrieval method in Chapter 3, together with the improvements to scanning strategy suggested in Section 6.2.3. In doing this, turbulence can be investigated to higher precision in the context of three-dimensional cloud processes. Ultimately providing deeper insights into observed turbulence, together with improved tools for model evaluation.

Chapter 5

Evaluation of turbulence in simulated clouds

5.1 Introduction, aims and overview

5.1.1 Introduction and aims

In Chapter 4, a statistical assessment of turbulence, expressed in terms of the eddy dissipation rate ε, was performed in clouds observed in two contrasting case studies; a shallow shower cloud case and a deep cloud case. Chapter 4 had two primary aims; to investigate the statistical characteristics of turbulence in observed clouds, and to build a framework of results which can be used to reliably evaluate turbulence in clouds simulated for corresponding cases in the Met Office Unified Model (MetUM). To achieve the second of these aims, the methods used to analyse turbulence in observations were carefully chosen to enable a consistent application to data from the MetUM. Of the analyses in Chapter 4, the methods selected to investigate the vertical distribution of ε, the spatial characteristics of ε, and the statistics of ε in convective updrafts, can all be applied consistently to MetUM data. These tools for analysis will form the basis for a reliable comparison between parametrised and observed turbulence in this chapter.

Table 2.3 lists the MetUM simulations for the 20 April 2012 shower cloud and 25 August 2012 deep cloud cases. These have been performed to compare the statistical properties of turbulence in simulated clouds with observations (simulations 1 and 5), and to test the sensitivity of turbulence in the MetUM to grid-length Δx, and mixing length constant, C_s

(remaining 6 simulations). Simulations 1 and 5 use a horizontal grid-length of $\Delta x = 100$ m (similar to typical beam widths in CAMRa observations) and a mixing length constant of $C_s = 0.2$ (the default value used in the MetUM). As a result, these are referred to as the "control" simulations, which provide the focus for a detailed comparison with observed turbulence statistics in Sections 5.2 – 5.5. The remaining simulations (referred to as "sensitivity" simulations) are performed to test the change in the characteristics of ε with Δx and C_s; which is included in Section 5.6.

There are key differences between the characteristics of data collected with CAMRa, and data fields from MetUM simulations. For example, observations consist only of vertical cross-sections through clouds, compared with the three-dimensional data fields from the MetUM. Further to this, observations collected with radar are limited to clouds regions that exceed a threshold reflectivity, whereas data is defined at all points in the model domain. Due to such differences, a perfect comparison between turbulence in observed clouds and clouds simulated in the MetUM is difficult to perform. However, in Section 5.2.1, suitable constraints on the sampling of model data, prior to the application of analysis methods, are determined to ensure that the comparison between model and observations is as fair as possible. This improves the ability to distinguish true differences in turbulence characteristics between observations and model from those resulting from an imperfect comparison.

The primary aim of this chapter is to investigate how ε from the Smagorinsky-Lilly parametrisation differs from observed ε. Although explanations for precisely why characteristics of ε differ in the model are attempted, this does not provide the focus for this chapter. To accomplish the primary aim, this chapter includes four secondary aims: (1) to establish suitable constraints to model data sampling to ensure a fair comparison can be made with observations; (2) to perform a statistical analysis of parametrised turbulence in simulated shower and deep clouds using methods consistent with those applied to

observations in Chapter 4; (3) to discuss the resulting comparison with observations in the context of the limitations of both model and radar data to determine how turbulence differs in the MetUM; (4) to test the effect of changing model resolution and mixing length on ε in the MetUM.

Under these aims, this chapter intends to address the following research questions:

- What is the typical range of ε in the MetUM? How do these compare to the range of ε observed by radar?
- Do ε features appear in similar regions of model clouds? Where is the largest ε found in the MetUM? Is this similar to observations?
- Does ε have the same distribution with height as in observations?
- Does ε have a similar distribution within model updraft regions compared to observations? Do distributions change similarly with updraft strength? How does the strength of correlation between ε and model updraft characteristics differ from observations?
- Are the spatial scales of discrete ε features different from observations? Are there any differences between showers and deep cloud?
- What is the impact of model grid-length on values of ε? What is the impact of changing the model mixing length? Which model configuration produces ε most similar to those observed?

5.1.2 Chapter overview

This chapter details the evaluation of turbulence in the MetUM using the framework for statistical analysis of observed turbulence used in Chapter 4.

In Section 5.2, model data from the control simulations is presented in the form of vertical cross-sections and domain plots. These are used to identify and discuss the constraints to model data sampling that are necessary to ensure a fair comparison can be made with

observations. These include numerical thresholds such as those applied to ε and the simulated radar reflectivity to account for the limitations of sampling turbulence with radar.

In Section 5.3, a detailed comparison is made between single cases of simulated and observed clouds. The general characteristics of ε are compared with observations, including the appearance of ε features, typical values and spatial distribution. A broader evaluation of the range of ε values found in the control simulations is then conducted by comparing the vertical distribution of ε, determined from large datasets of simulated clouds, with observations.

In Section 5.4, an evaluation of ε in simulated updrafts is performed using the updraft detection and analysis methods from Section 4.4 to compare directly with observations. The general characteristics of simulated and observed updrafts are compared, together with correlations between ε and updraft characteristics, and the change in the distribution of ε with updraft strength.

In Section 5.5, the size and shape of coherent features of ε in simulated clouds are compared with those presented for observations in Section 4.5. The same automated detection technique as applied to observations is used to evaluate the change in the spatial characteristics of ε with turbulent intensity in the model.

To investigate the impact of assumptions made in model and sub-grid scheme configuration, the sensitivity of ε to the model grid-length Δx, and mixing length λ_0, is tested in Section 5.6. Values of ε in the control simulations are compared with those in a set of sensitivity simulations (see Section 2.3.3) with respect to updraft regions and vertical distribution.

5.2 Fair model evaluation

This section introduces data from the control simulations performed for the 20 April 2012 shower cloud case, and 25 August 2012 deep cloud case (see Section 5.1.1). In Section 5.2.1, these simulations are used to highlight the key differences between MetUM data and radar observations. From this, a series of constraints on the sampling of simulated clouds are developed to ensure a fair comparison can be made with observations in later sections of this chapter.

5.2.1 Conditions for fair model evaluation

Before any of the methods used in Chapter 4 can be applied to data from the control simulations, it is important to identify and account for both the intrinsic and meteorological differences between the characteristics of the model data, and radar observations. More specifically, this involves deciding on suitable methods to sample model data for appropriate comparison with observations, accounting for any simulated meteorological features that were not observed and applying numerical thresholds to model data to ensure a consistent comparison can be made with clouds observed by radar. These steps are necessary to ensure a fair evaluation of turbulence in the MetUM. The constraints and thresholds identified in this section are applied consistently to the sensitivity simulations in Section 5.6.

Initially, a constraint is applied to the model fields used for comparison to observations for practicality. As described in Section 2.3.3, the eddy viscosity ν_m, and mixing length λ, are output hourly from the Smagorinsky-Lilly scheme. This means that 3-D fields of ε (found from ν_m, ν_h, S, λ_{UM} using (2.26)) are available every hour between 0900 – 1900 UTC. For the purpose of making comparisons with observations, it has been both unnecessary and impractical to perform an analysis of 3-D fields of model data for each of the time-steps. Instead, the 1100, 1300 and 1500 UTC time-steps have been selected for analysis. These are

chosen to span a time period during which the majority of RHI observations were collected. Of the RHI datasets described in Section 2.2.4, 68% of deep cloud RHIs, and 76% of shower cloud RHIs were collected between 1100 and 1500 UTC. RHIs within this time interval contained 82% and 70% of updraft regions for deep and shower cloud, respectively.

At this point, an assumption is made that sampling many simulated clouds throughout the model domain every two hours can be considered comparable to observing fewer clouds with radar, but more regularly throughout the observation period. For the RHIs used for analysis in Chapter 4, clouds were observed, on average, every 9 minutes. If the broad characteristics of observed convection did not change considerably on hourly time-scales, this is considered a safe assumption.

The remaining constraints on model data sampling are discussed in the context of clouds sampled from the control simulations; both throughout the model domain, and in vertical cross-sections. Figure 5.1 displays the simulated total radar reflectivity Z_{T}, observed at a height of $z = 150$ m throughout the full model domain of both cloud cases at 1100 UTC and 1500 UTC. Towards the western boundary (left-hand in plot) of domains in Figure 5.1, reflectivity features are present with distinctly different characteristics to those in the remainder of the 100-m domain; appearing to be smoother and aligned with the mean wind. These are also found near southern boundaries in cases where the wind is from the south-west (e.g. Figure 5.1b), or near northern boundaries when the wind is from the north-west (e.g. Figure 5.1d). The 100-m model is nested within a 200-m model (see Section 2.3). In cases where clouds simulated in the 200-m model lie along the boundary of the 100-m domain at the beginning of the time-step, these can be advected into the 100-m domain. These features are more characteristic of the 200-m model, than for the clouds that were simulated in the remainder of the 100-m domain during the time-step. Therefore, data located in regions containing advected features are omitted from any analysis of ε. Variability in the strength and direction of the mean wind leads to variation in the location of advected features in different models and time-steps. For example, in Figure 5.1c, advected features are

roughly east-west oriented and extend approximately 20 km into the domain from the western boundary, also appearing close to the southern boundary. By 1500 UTC (Figure 5.1d), features are again located within 20 km of the western boundary, but now appear close to the northern boundary due an apparent change in the mean wind direction to a north-westerly, as indicated by the change in orientation of the advected features. Due to this variability, the domains at each time-step have been inspected individually to determine the regions with advected features, for both case studies. For example, in Figure 5.1b, no data was considered closer than 20 km to the western boundary, or closer than 10 km to the southern boundary.

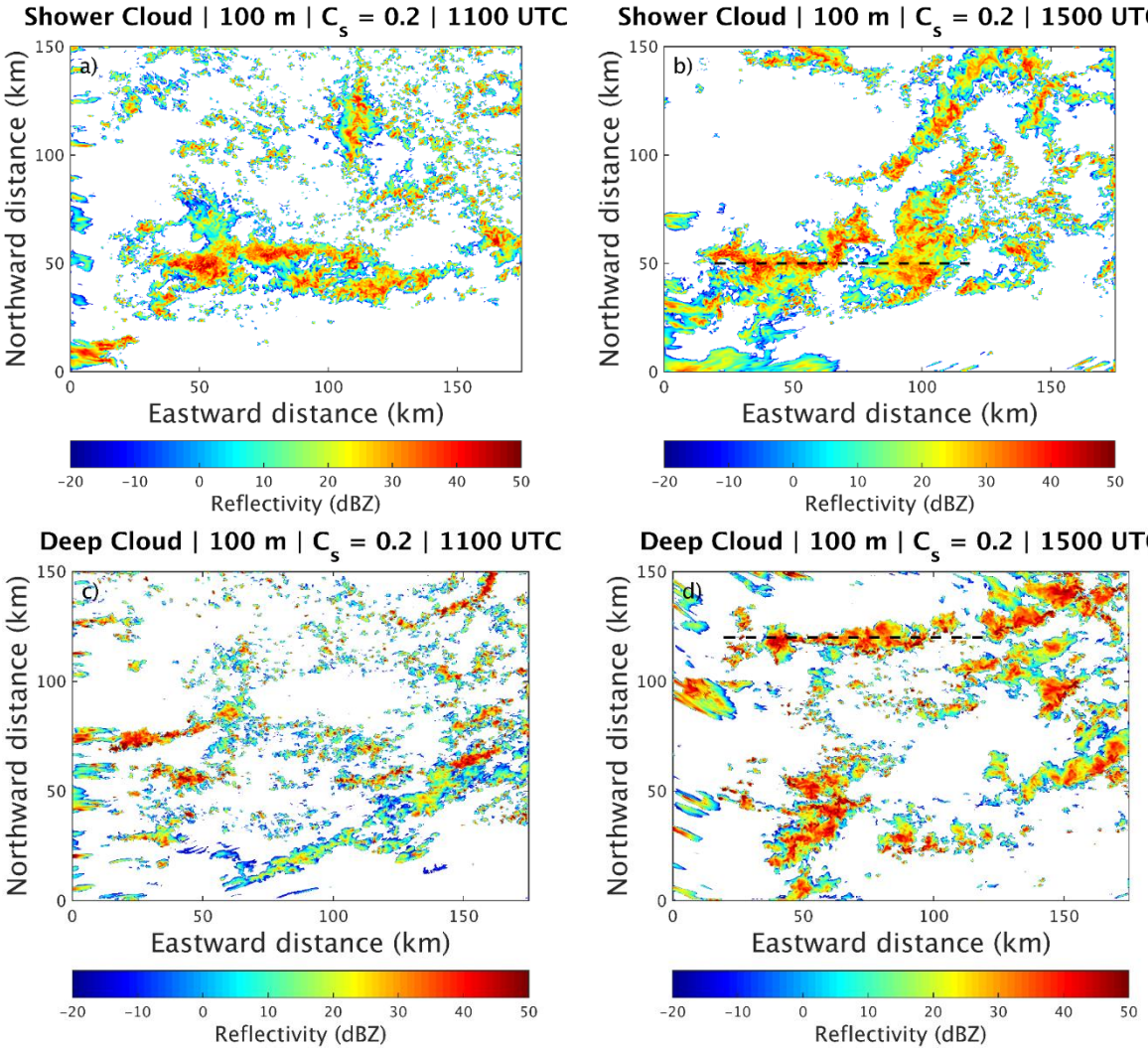

Figure 5.1: Total radar reflectivity Z_T, at 150 m height throughout the 100-m domain over southern England for: (a) shower cloud at 1100 UTC; (b) shower cloud at 1500 UTC; (c) deep cloud at 1100 UTC; (d) deep cloud at 1500 UTC. Dashed black lines in (b) and (d) indicate the location of vertical profiles in Figure 5.2. Values of Z_T lower than -20 dBZ are removed.

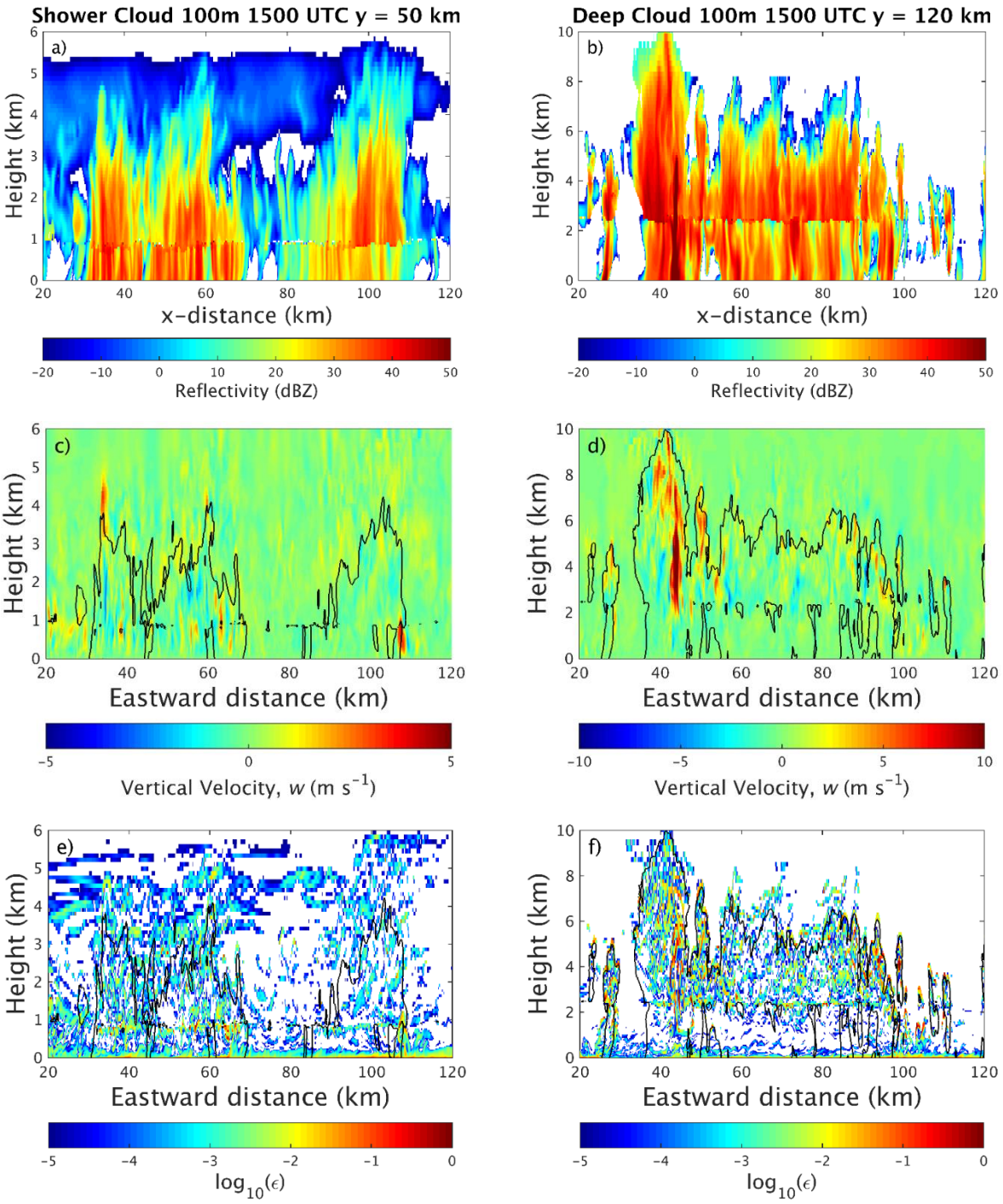

Figure 5.2: Vertical profiles of total radar reflectivity Z_T, vertical velocity w, and ε through simulated shower clouds (left) and deep clouds (right) at 1500 UTC. Location of vertical profiles are indicated by black dashed lines in Figure 5.1b and 5.1d. In (a) and (b) data has been removed where $Z_T < -20$ dBZ. In (e) and (f) data has been removed where $\varepsilon < 10^{-5}$ m^2 s^{-3}. The black contour in (c) – (f) represents the location of $Z_T = 20$ dBZ to indicate the location of convective cloud relative to vertical motion and turbulence.

A final constraint is applied to sample the 3-D model data in a way that is comparable to the observations with radar. Radar observations consist exclusively of RHIs, so vertical cross-sections through model data are collected for comparison. If the east-west direction is given by x, and the north-south direction by y, vertical cross-sections are sampled in x-z co-ordinates at regular intervals of y. This method is not consistent with the scanning strategy used in DYMECS, which identified maxima in rainfall features to define the azimuth of the RHI scan. However, an RHI bisecting a single rainfall feature will also sample any clouds along this azimuth up to 200 km from the radar. Due to this effect, it was uncommon for RHIs in the dataset used for analysis in Chapter 4 to include the target cloud alone. This indicates that the majority of clouds observed in the RHIs were sampled with no directional preference. Therefore, sampling vertical cross-sections of model data at regular intervals of y (which does not preclude sampling some clouds directly through rainfall maxima) is not expected to significantly impact the comparison with observations. The size of the y-interval differs depending on the application (e.g. 3 km for updraft analysis in Section 5.4 to minimise the oversampling of updrafts), so these are specified at the beginning of the corresponding sections.

With the necessary constraints applied to model data sampling, fixed numerical thresholds are now established to account for the limitations of radar observations. By applying thresholds to fields in vertical cross-sections of model data, the aim is to maximise their comparability with the RHI observations collected with CAMRa. Figure 5.2 includes vertical cross-sections of Z_{T}, vertical velocity w, and ε, for simulated shower and deep clouds at 1500 UTC. The locations of these are indicated in Figure 5.1 by dashed lines at $y = 50$ km for shower cloud (Figure 5.1b) and at $y = 120$ km for deep cloud (Figure 5.1d). In Figure 5.2a and 5.2b, values of $Z_{\mathrm{T}} < -20$ dBZ have been removed to better represent the location of simulated clouds and precipitation. In Figure 5.2e and 5.2f, values of $\varepsilon < 10^{-5}$ m^2 s^{-3} have been removed to better indicate the location of significant dissipation

rates. In Figure 5.2c – 5.2f, the black contour outlines regions of $Z_{\mathrm{T}} = 20$ dBZ to indicate the location of simulated convective clouds relative to turbulent dissipation and vertical motion. For the remainder of this section, Figure 5.2 is used for reference to discuss the application of numerical thresholds.

Retrievals of ε with CAMRa can only be made where reflectivity exceeds the minimum threshold for detection. At 1-km range this is -37 dBZ, although this increases with range from the radar. By inspecting RHIs that have been corrected by signal-to-noise ratio (using (3.3)) for the shower case, the smallest observed reflectivity increases from -4 dBZ to 3 dBZ between 30 km and 80 km (typical range of cloud distances). This suggests that applying a minimum threshold to Z_{T} in model data of $Z_{\mathrm{min}} = 0$ dBZ, and overlaying this onto fields of ε, would be suitably consistent with observations. Imposing a minimum threshold to Z_{T} has additional benefits to the shower case. As shown in Figure 5.2a, between 3 – 6 km in height, there is a layer of low-reflectivity cloud ranging from $Z_{\mathrm{T}} = -20$ dBZ to $Z_{\mathrm{T}} = 0$ dBZ. This feature (likely cirrus cloud) extends throughout the majority of the domain and persists for each of the three time-steps considered. However, there is no evidence of this in the RHI observations due to Z_{T} being largely lower than 0 dBZ. Figure 5.3 includes observations throughout the shower case day from the 35 GHz Copernicus cloud radar located at the Chilbolton Observatory. As indicated by the black box, there is an elevated layer (albeit shallow compared to Figure 5.2a) of low-reflectivity cirrus cloud ($Z_{\mathrm{T}} < -10$ dBZ) throughout the late-morning and early-afternoon hours. This suggests that the model is representing a layer of cirrus cloud that existed on the day of observation but to a larger extent than is indicated in radar observations. Sampling ε from within this simulated cloud region would be highly inconsistent with RHI observations; a benefit of applying the $Z_{\mathrm{min}} = 0$ dBZ threshold to model data.

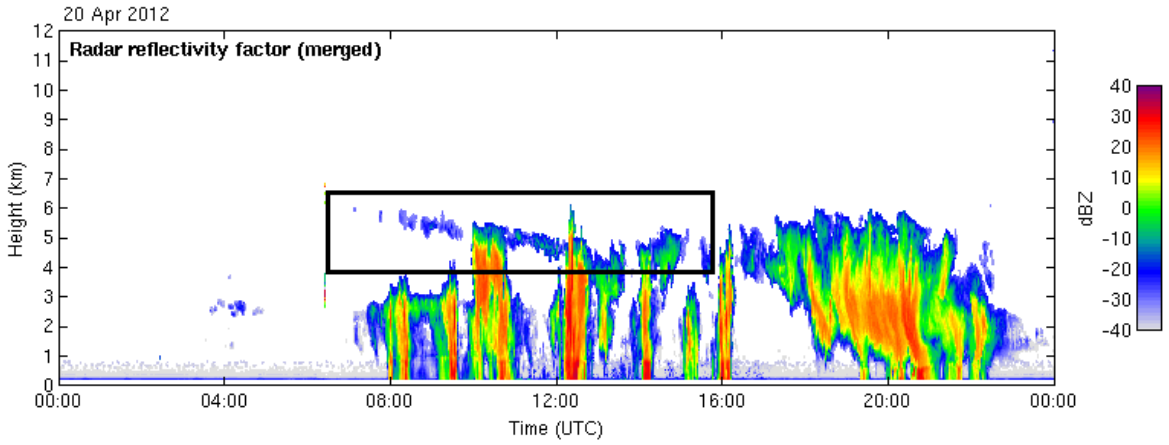

Figure 5.3: Radar reflectivity observations throughout the 20 April 2012 shower case day from the 35 GHz Copernicus cloud radar at the Chilbolton Observatory, indicating a shallow layer of low-reflectivity cirrus cloud (black box) not observed by the less sensitive CAMRa.

A second threshold is applied directly to model fields of ε due to the minimum ε observable with CAMRa. In Section 6.2.3, an apparent lower limit to observed values of σ_v was noted, with an approximate value of $0.9\ \mathrm{m\ s^{-1}}$. Subsequent experiments using a larger number of pulse-pairs while scanning succeeded in reducing this detection limit, but only closer to $\sigma_v = 0.6\ \mathrm{m\ s^{-1}}$; the lowest σ_v that can be reliably sampled due to the Nyquist velocity of CAMRa (see Section 2.1.2). A lower limit to σ_v of $0.9\ \mathrm{m\ s^{-1}}$ imposes a corresponding limit to ε (given by $\varepsilon_{\mathrm{lim}}$). In the extreme case where observed σ_v results only from turbulence ($\sigma_v = \sigma_{\mathrm{t}} = 0.9\ \mathrm{m\ s^{-1}}$), this translates to $\varepsilon_{\mathrm{lim}} = 2.9 \times 10^{-3}\ \mathrm{m^2\ s^{-3}}$ at a typical range of 60 km from the radar (using (1.25)). In the MetUM, ε has non-zero values defined for each grid point, which can fall to $10^{-10}\ \mathrm{m^2\ s^{-3}}$ (at which point they are practically zero). In Figure 5.2e and 5.2f, data has been removed where $\varepsilon < 10^{-5}\ \mathrm{m^2\ s^{-3}}$ to improve the visual representation of regions of significant turbulence. However, without applying this threshold, values of $\varepsilon < \varepsilon_{\mathrm{lim}}$ constitute 88% of all grid-points where $Z_{\mathrm{T}} > 0$ dBZ. Without applying a threshold to model data, the numerous values of $\varepsilon \ll \varepsilon_{\mathrm{lim}}$ would bias statistics such as percentiles and probability distributions, affecting the quality and fairness of comparison with observations. A fair evaluation of ε in simulated clouds can only be made for the range of ε that is reliably observed with CAMRa, however, this does not

refer to all $\varepsilon > \varepsilon_{\mathrm{lim}}$. Values lower than $\varepsilon_{\mathrm{lim}}$ in real clouds will be observed incorrectly as $\varepsilon_{\mathrm{lim}}$ with CAMRa. Therefore, observed values that are similar to $\varepsilon_{\mathrm{lim}}$ cannot be assumed to be reliable. Consequently, a threshold of $\varepsilon_{\mathrm{min}} = 5 \times 10^{-3}$ m^2 s^{-3} is selected, whereby only values larger than this threshold, in both model and observations, are compared. Although there is a maximum ε that can be reliably sampled by CAMRa of ~ 1 m^2 s^{-3} (see Section 2.1.2), there was little evidence to suggest this had imposed a restriction on observed ε. Therefore, no maximum threshold is applied to ε in simulated clouds.

A final threshold is applied to ensure that ε located very close to the surface is not sampled in the model. In both Figure 5.2a and 5.2b (and more generally in the control simulations), large ε is widespread close to the surface. However, due to scanning at non-zero elevations with CAMRa, observations are generally not collected from very close to the surface. This minimum height increases with range, however, at the minimum 30-km range of sampled clouds, observations are not collected nearer than 150 m from the surface. Therefore, a minimum height threshold of $z_{\mathrm{min}} = 150$ m is applied to model data.

In summary, to following constraints and thresholds have been applied to model data to ensure a fair comparison of ε can be made with observations:

- Model time-steps 1100, 1300 and 1500 UTC are selected for analysis to span the time period during which the majority of RHI observations were collected.
- Locations within domains of the control (and sensitivity) simulations that include advected features from boundaries with the surrounding 200-m model are omitted from analysis.
- Sampling model data by vertical cross-sections at regularly-spaced intervals is selected to provide the most suitable comparison with RHI observations. The interval size varies with analysis application and is prescribed at the start of each corresponding section.

- Only model data co-located with reflectivity larger than $Z_{\min} = 0$ dBZ is compared with observations to ensure consistency with the minimum reflectivity sampled by CAMRa.
- Due to the lower limit to ε observed with CAMRa, a minimum threshold of $\varepsilon_{\min} = 5 \times 10^{-3}$ m^2 s^{-3} is applied to model data.
- A minimum height of $z_{\min} = 150$ m is applied to model data to avoid sampling turbulence from regions that were not observed with CAMRa due to scanning at non-zero elevation.

5.3 General features of ε in simulated clouds

Thresholds and data sampling constraints were established in Section 5.2 to ensure a consistent comparison can be made between model and observations. This begins with a comparison of the general features of ε in cloud cases between the two control simulations, and between model and observations (Section 5.3.1). An approach is then taken to more broadly compare the values of ε in the control simulations with observations. This is achieved through examination of the vertical distribution of ε under the sampling constraints detailed in Section 5.2, affording a direct comparison with observations (Section 5.3.2).

5.3.1 Characteristics of ε in simulated clouds

In this section, cloud cases from the vertical cross-sections through simulated clouds in Figure 5.2 are examined in more detail to identify the differences between the general characteristics of ε between the control simulations. The intensity and probability distribution of ε, together with its spatial distribution and relation to vertical velocity *w* with the cloud, is then compared with corresponding examples of observed clouds for both case days. Simple cloud cases are used in this section to highlight the key differences between ε

in model and observations, which provide the focus for more detailed examination in later sections of this chapter.

To make these comparisons, the thresholds $Z_{\min} = 0$ dBZ, $\varepsilon_{\min} = 5 \times 10^{-3}$ m^2 s^{-3}, and $z_{\min} = 150$ m are first applied to Figure 5.2e and 5.2f. A simulated "cloud" is identified in both cases, defined by the contour of $Z_{\min}$. These are then compared with examples of observed cloud with similar spatial scales and strength of vertical motion. These are presented in Figure 5.4 and Figure 5.5, which compare ε and *w* for a shower cloud and deep cloud, respectively. To ensure a consistent comparison, $\varepsilon_{\min}$ has also been applied to the observed clouds. For the remainder of this section, acronyms are used to differentiate simply between the simulated deep cloud (SDC), simulated shower cloud (SSC), observed deep cloud (ODC) and observed shower cloud (OSC).

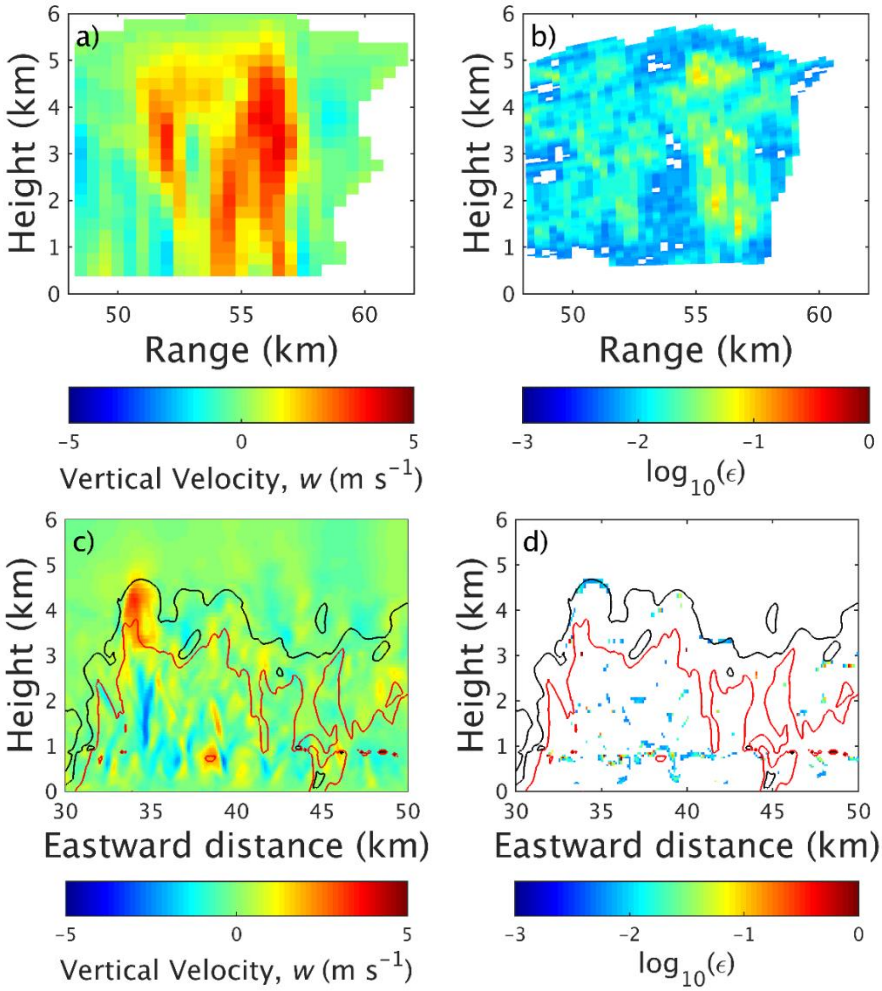

Figure 5.4: Comparison of *w* and ε in a single shower cloud in observations (a – b) and MetUM (c – d). Contours in (c) and (d) represent 0 dBZ (black) and 20 dBZ (red) reflectivity.

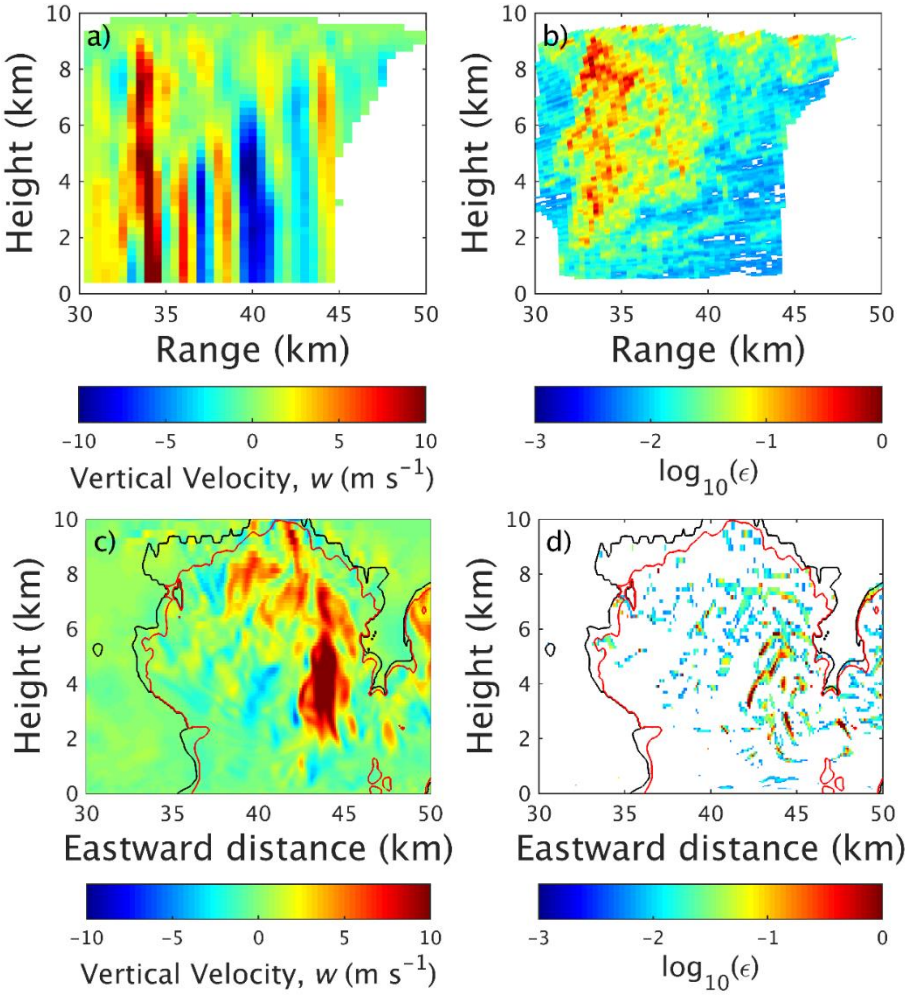

Figure 5.5: Equivalent comparison to Figure 5.4 for an example of deep cloud.

Qualitatively, Figure 5.4d and 5.5d show that $\varepsilon > \varepsilon_{min}$ is far less widespread within the cloud than for the observed clouds, which is especially true for the SSC. In the simulated clouds, large ε appears to be more strictly co-located with gradients in *w* than for observed clouds. This is most evident in the SDC, in which large ε (more than 0.1 $m^2\ s^{-3}$) is found in small discrete features along sharp gradients in *w* associated with the main updraft between 42 – 45 km eastward distance. Such strong gradients in *w* are not observed in the SSC and the resulting ε is weaker than less widespread. The strong association between ε and horizontal gradients in *w* was noted in observations (Section 4.4.4.2), where $\left|\frac{dw}{dx}\right|_{95}$ provided the strongest correlation with ε_{95} of any cloud characteristic. The statistical relationships

between ε and updraft characteristics in the control simulations are explored in more detail and compared with observations in Section 5.4.

In observed clouds, regions of ε are generally much more diffuse within the cloud (see Figure 5.5b); a clear difference to the localised, intense ε more strongly co-located with velocity gradients in the model. The Smagorinsky-Lilly scheme does not account for the advection of turbulence, rather ε is determined from shear and buoyancy processes occurring at the grid-scale. It would be reasonable to assume that the advection of turbulence within observed clouds results in a transition to broad, diffuse regions of weaker ε, occurring during the time-scale required to dissipate the turbulent kinetic energy (TKE) that has been produced in the cloud. This could explain the differences in spatial characteristics of ε in simulated clouds. The relationship between the spatial characteristics of ε, and the turbulent intensity, are explored in more detail and compared with observations in Section 5.5.

The larger intensity of ε features in Figure 5.5d combined with smaller spatial coverage might suggest that similar amounts of TKE are being dissipated, but over a much smaller spatial area. However, this makes the assumption that turbulent production mechanisms of a particular strength produce the same TKE in simulated and observed clouds. If this were the case, the mean TKE dissipated per second throughout a simulated cloud should be largely similar to that in an observed cloud if the strength of production mechanisms were approximately the same. The SDC and ODC are suitable for this comparison; they both contain a single main updraft region with w up to 8 – 12 m s^{-1}, and span approximately the same area (~ 150 km^2). However, the mean ε throughout the SDC (0.56 m^2 s^{-3}; see Table 5.1) is more than a factor of 10 larger than the mean ε in the ODC (0.041 m^2 s^{-3}). Such a result indicates that there may be significant differences in the production of TKE in the model, resulting in large differences found in the range of ε values between observed and simulated clouds that have similar characteristics; this will now be investigated in further quantitative detail.

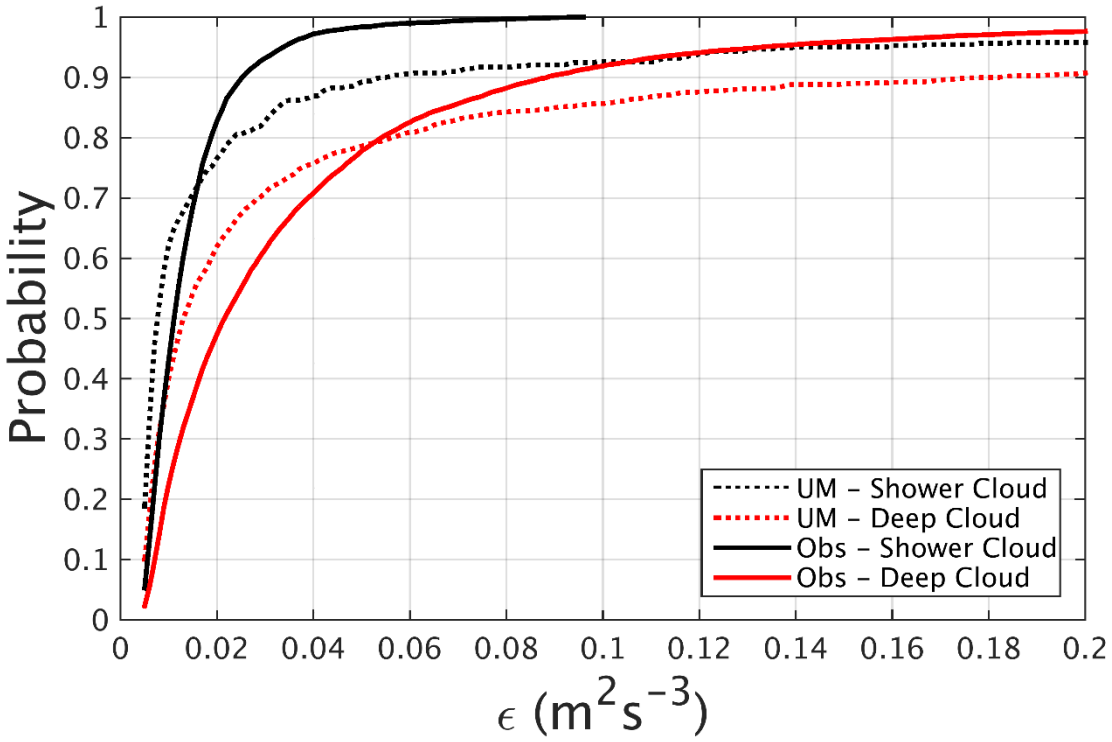

Figure 5.6: Comparison of the cumulative density function of ε as appears in Figures 5.4b (solid black), 5.4d (dotted black), 5.5b (solid red) and 5.5d (dotted red).

		Shower Cloud		Deep Cloud	
Statistic	**Unit**	**Obs**	**MetUM**	**Obs**	**MetUM**
Data count of $\boldsymbol{\varepsilon > \varepsilon_{min}}$	-	3569	530	13951	1991
Mean $\boldsymbol{\varepsilon}$	$m^2\ s^{-3}$	0.015	0.30	0.041	0.56
Median $\boldsymbol{\varepsilon}$	$m^2\ s^{-3}$	0.012	0.0087	0.023	0.014
95th pctl. $\boldsymbol{\varepsilon}$	$m^2\ s^{-3}$	0.035	0.14	0.13	0.46
Maximum $\boldsymbol{\varepsilon}$	$m^2\ s^{-3}$	0.097	110	1.0	317
$\boldsymbol{\varepsilon < 0.01\ m^2\ s^{-3}}$	(%)	37	58	19	36
$\boldsymbol{\varepsilon > 1\ m^2\ s^{-3}}$	(%)	0	1	0.007	4

Table 5.1: Statistics of ε for observed and simulated clouds in Figure 5.4 and 5.5.

Figure 5.6 includes the cumulative density functions (CDFs) of ε in each of the 4 cloud cases in Figure 5.4 and 5.5. Each CDF consists of a number of ε data points from each cloud that is listed in Table 5.1, together with various statistics associated with each distribution that will be referred to in this discussion. Figure 5.6 shows that small values of ε (less than 0.01 $m^2\ s^{-3}$) constitute a large proportion of total values in the SSC (58%) and SDC (36%). Further to this, large values ($\varepsilon > 0.1\ m^2\ s^{-3}$) are twice as frequent in the SDC (14%) than in the SSC (7%). Therefore, a large proportion of the simulated cloud area in both cases is only weakly turbulent, and strong turbulence is more widespread in deep clouds. Both of these features are consistent with those identified in observed clouds (see Section 4.2.1). However, Figure 5.6 also indicates key differences in the distribution of ε between the simulated and observed clouds. The percentage of ε values that are less than 0.01 $m^2\ s^{-3}$ is approximately twice as large in the SDC when compared to the ODC (36% for the SDC; 19% for the ODC). Large values of ε (more than 0.1 $m^2\ s^{-3}$) are also less common in the observed cases; most notably in the shower case where no ε larger than 0.1 $m^2\ s^{-3}$ was found in the OSC, while 14% of values exceeded 0.1 $m^2\ s^{-3}$ in the SSC. In summary, although the differences in the distribution of ε between the SDC and SSC are consistent with those between the OSC and ODC, the distribution of ε in the simulated clouds is far broader than in the observed clouds.

Interestingly, median values of ε are approximately 50% larger in the observed clouds, while mean values are substantially higher in the simulated clouds. The lower median values result from a larger proportion of small ε in the model, while the higher mean results from substantially larger ε produced in simulated clouds. The 95th percentile of ε is a factor of four larger in the SSC (0.14 $m^2\ s^{-3}$) than in the OSC (0.035 $m^2\ s^{-3}$), and more than a factor of three larger in the SDC (0.46 $m^2\ s^{-3}$) than in the ODC (0.13 $m^2\ s^{-3}$). Dissipation rates as large as 110 $m^2\ s^{-3}$ and 317 $m^2\ s^{-3}$ were found in the SSC and SDC, respectively. These are extremely large compared to the maximum ε found in the OSC (0.097 $m^2\ s^{-3}$) and ODC

(1 $m^2\ s^{-3}$). Importantly, these values are much larger than the maximum ε that can be reliably sampled by CAMRa of ~ 1 $m^2\ s^{-3}$ (see Section 2.1.2). In the SSC, only 1% of ε (5 values) were larger than 1 $m^2\ s^{-3}$, although 4% (71 values) exceeded this threshold in the SDC. Due to confidence that CAMRa was reliably sampling the full range of ε in observed clouds (see Section 2.1.2), the largest ε found in the simulated clouds far exceeds the ε that was present in the observed clouds.

In summary, by comparing individual cloud cases in detail, key differences have been identified in ε between simulated and observed clouds. A large proportion of the cloud area is only weakly turbulent in simulated clouds, and deep clouds are more turbulent that shower clouds; this is consistent with observations. Dissipation rates in simulated clouds are spatially correlated with areas of vertical motion as observed, however, large ε is more strongly co-located with shear around updrafts, resulting in localised, intense regions of dissipation. Although turbulence has significant correlation with features of updraft in observations, turbulence is generally found in weaker diffuse regions, possibly due to the effects of advection within the cloud which is not accounted for by the Smagorinsky-Lilly scheme. Although the CDFs of ε in the selected cloud cases are similar in appearance, distributions of ε are broader in simulated clouds. Values of ε produced by the model can far exceed the largest ε observed, and the largest ε reliably observable with CAMRa.

This investigation has compared only individual clouds, and so these conclusions are used as guidance for more detailed analyses in the following sections of this chapter. To more thoroughly compare the values of ε in simulated and observed clouds, the vertical distributions of ε are determined from many vertical cross-section of model data; this is presented following this section in Section 5.3.2. These are then compared directly to the observed vertical distributions presented in Section 4.3. To investigate the relationship between ε and features of convective updrafts in the MetUM, the updraft analysis performed for observations in Section 4.4 is replicated with model data in Section 5.4. To better

understand the differences in the spatial characteristics of ε features identified between model and observations in this section, methods used to analyse the size and shape of observed coherent ε features in Section 4.5 are applied identically to model data for a direct comparison in Section 5.5.

5.3.2 Vertical distribution of ε in simulated clouds

In Section 4.2.2, the vertical distribution of ε was investigated in observed clouds. This approach provided a convenient way to simultaneously compare intensity of ε and its distribution with height between the two cloud types. Such an approach is now applied to vertical cross-sections of model data to compare the change in various percentiles of ε with height, between the control simulations, and directly with observations. This will allow for a broader evaluation of the distribution of ε values in simulated clouds, building on the comparison of ε in individual clouds in Section 5.3.1. The acronyms established in Section 5.3.1 (e.g. SDC: simulated deep cloud) are used in this section to refer to all clouds sampled for analysis for each cloud type.

Following the constraints to model data sampling established in Section 5.2, vertical cross-sections of model data are sampled in x-z co-ordinates at regular intervals of y. A y-interval of 1 km is selected; however, the exact size of this interval is unimportant for purely sampling clouds as long as it is applied consistently throughout the model domain. This approach is applied throughout the three domains for both control simulations (corresponding to the 1100, 1300 and 1500 UTC timesteps), and 417 vertical cross-sections are collected through SDC, with 426 collected through SSC. The small difference results from differing constraints applied to the range of y considered. This results from the omission of domain regions with advected features from the surrounding 200-m model domain (see Section 5.2), which differ between both model and time-step. The thresholds of $Z_{\min} = 0$ dBZ, $\varepsilon_{\min} = 5 \times 10^{-3}$ m^2 s^{-3}, and $z_{\min} = 150$ m are applied to each vertical

cross-section to sub-sampled the ε that is comparable with observations. Consistent with methods applied to observations, resulting values of ε are recorded in each 1-km vertical level up to the maximum cloud height; 0 – 6 km for SSC, and 0 – 10 km for SDC. The 25th, 50th, 75th, 95th and 99th percentiles of ε are calculated for each vertical level and compared to corresponding values in observations; which have been re-calculated from the analysis in Section 4.2.2 to consider only $\varepsilon > \varepsilon_{min}$.

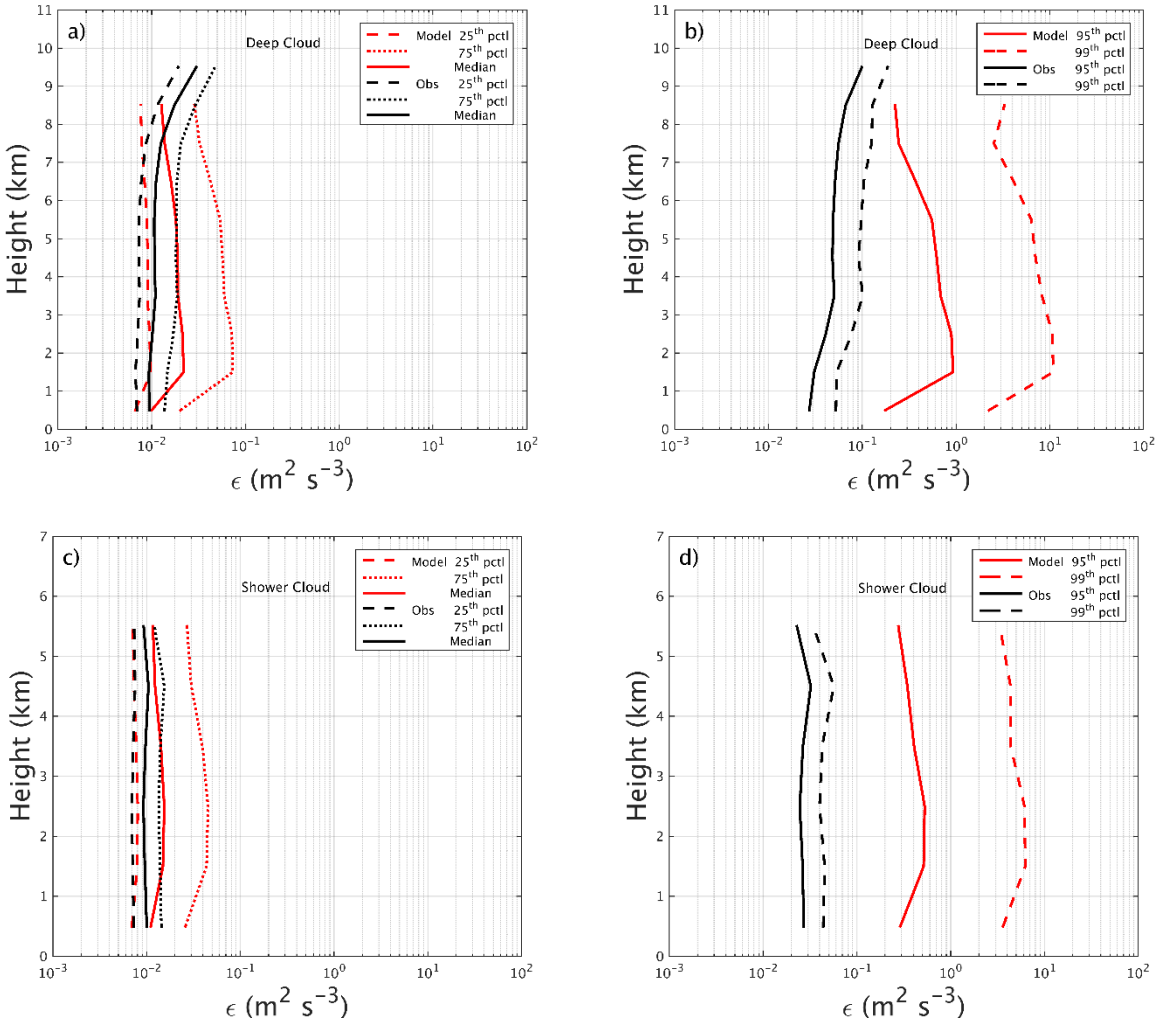

Figure 5.7: (a) Comparison of the vertical distribution of the median, 25th and 75th percentiles of ε in simulated and observed deep clouds, (c) equivalent for shower clouds. (b) Comparison of 95th and 99th percentiles of ε for deep clouds, (d) equivalent for shower clouds. Values of ε recorded in all simulated clouds where $Z > 0$ dBZ. Only $\varepsilon > 0.005$ m^2 s^{-3} considered in all clouds.

Figure 5.7a compares the change in the 25th, 50th and 75th percentiles of ε with height between ODC and SDC. Together, the 25th and 75th percentiles are used to represent the range of typical values of ε within each cloud, although only the median values of ε (given by $\varepsilon_{\mathrm{med}}$) will be discussed. For SDC, the number of values of ε collected for the 9 -10 km vertical level (103) was too small to derive reliable statistics, so no comparison is made with observations in Figure 5.7a (or 5.7b). In SDC, $\varepsilon_{\mathrm{med}}$ ranges from 0.01 – 0.02 $\mathrm{m^2\ s^{-3}}$ in the vertical profile, compared with 0.01 – 0.03 $\mathrm{m^2\ s^{-3}}$ in ODC. This indicates that values of $\varepsilon_{\mathrm{med}}$ are largely similar between model and observations. However, $\varepsilon_{\mathrm{med}}$ is larger in SDC for all vertical levels except 8 – 9 km. This is associated with a significant difference in the vertical distribution of $\varepsilon_{\mathrm{med}}$ between SDC and ODC; a general increase with height in observations compared with a general decrease with height in the model. An exception exists from 0 – 1 km in SDC, which contains the lowest $\varepsilon_{\mathrm{med}}$ of 0.01 $\mathrm{m^2\ s^{-3}}$. This is likely to reflect the turbulence within precipitation near the surface of the model, which is almost identical in intensity to observed values.

An equivalent comparison for shower clouds is presented in Figure 5.7c, which compares the same percentiles of ε from the surface to the 6-km cloud top. In OSC, $\varepsilon_{\mathrm{med}}$ is an approximately constant 0.01 $\mathrm{m^2\ s^{-3}}$ throughout the vertical profile, whereas for SSC, $\varepsilon_{\mathrm{med}}$ ranges from 0.010 – 0.015 $\mathrm{m^2\ s^{-3}}$. Again, this indicates that typical values of ε in simulated clouds are similar to observations. However, consistent with SDC, $\varepsilon_{\mathrm{med}}$ decreases with height from 1 km to the cloud top, and the lowest $\varepsilon_{\mathrm{med}}$ of 0.01 $\mathrm{m^2\ s^{-3}}$ is again found from 0 – 1 km. These results also indicate that the typical values of ε are very similar between the control simulations, both in value and in vertical gradient.

Although the typical values of ε are very similar between model and observations, significant differences exist in the largest values, as highlighted initially in the comparison of single cloud cases in Section 5.3.1. In Figure 5.7b, the change in the 95th and 99th percentiles of ε (referred to as ε_{95} and ε_{99}, respectively) with height is compared between

ODC and SDC. In SDC, ε_{95} varies from 0.2 – 1.0 $m^2\ s^{-3}$ in the vertical profile, compared with only 0.03 – 0.10 $m^2\ s^{-3}$ in ODC. This shows that ε_{95} is generally an order of magnitude larger in SDC. This difference is even greater when examining ε_{99}; values in SDC range from 2 – 11 $m^2\ s^{-3}$, whereas observed values range only from 0.05 – 0.20 $m^2\ s^{-3}$. This suggests that the largest ε is approximately two orders of magnitude greater in the model, far exceeding the values of ε that can be reliably sampled with CAMRa. Excluding values from 0 – 1 km, both ε_{95} and ε_{99} decrease more markedly with height than ε_{med} in SDC. The differences in the gradient of ε with height between model and observations is more plainly seen for ε_{95} than for ε_{med}. In ODC, ε_{95} increases with height by an order of magnitude, whereas in SDC, ε_{95} decreases by an order of magnitude.

The differences in ε_{95} and ε_{99} between model and observations are very similar for shower clouds (Figure 5.7d). Values of ε_{95} and ε_{99} in SSC are again one and two orders of magnitude larger, respectively, than corresponding values in OSC. Values of ε_{95} and ε_{99} decrease with height in SSC, but at a slower rate (factor of two) when compared with SDC (factor of ten). However, this remains inconsistent with OSC, where both ε_{95} and ε_{99} are approximately constant with height.

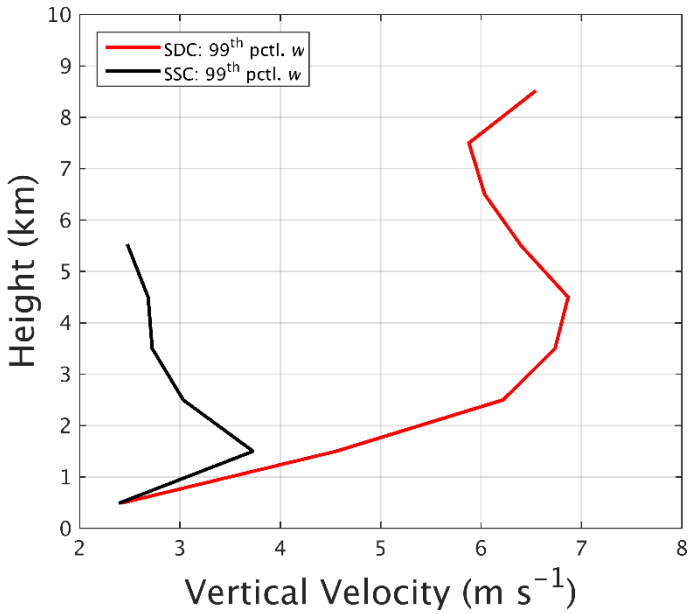

Figure 5.8: Comparison of the 99th percentile of vertical velocity through the simulated deep cloud (SDC – red line) and simulated shower cloud (SSC – black line).

It is not clear exactly why the vertical gradient of ε in simulated clouds is inconsistent with observations. However, in Section 4.2.3, the correlation between updraft ε and above-updraft ε in SCCCs was stronger in ODC, suggesting that deep updrafts were more effective at distributing strong turbulence towards the cloud top than the weaker updrafts in OSC. It is possible that the positive vertical gradient in ε in ODC results from the upward advection of turbulence in deep updrafts; a process that is not accounted for in the Smagorinsky-Lilly scheme. Instead, vertical gradients in ε will result solely from any vertical distribution in the strength of shear and buoyant production of TKE. Due to the strong TKE production associated with updrafts, vertical profiles of the 99th percentile of vertical velocity (w_{99}) in SDC and SSC are compared in Figure 5.8. Vertical profiles in both cloud types exhibit a decrease with height, primarily in the mid-upper levels of the cloud. This is consistent with the evaluation of updrafts performed for these cases by Nicol *et al*. (2015). In the case of SDC, the vertical profile of w_{99} has similar characteristics to that of ε_{99}; lowest near the surface, decreasing between 4 – 8 km, and increasing again near the cloud top.

Although it is not the aim of this chapter to identify exactly why the characteristics of ε differ in the MetUM, this does provide evidence that the absence of advection in the Smagorinsky-Lilly scheme can lead to significant differences in the vertical distribution of ε between observed and simulated clouds. In the future, this should be investigated for potential impacts on the evolution of convection within the MetUM, especially with regards to the impact of turbulent mixing in the upper levels of the cloud.

In this section, hundreds of vertical cross-sections through control simulation data have been analysed to directly compare the vertical distribution of ε in simulated and observed clouds. Typical values of ε are very similar between simulated and observed clouds, and between simulations, ranging from 0.01 – 0.03 $m^2\ s^{-3}$ in all cloud cases. However, the largest values of ε (ε_{95} and ε_{99}) in the control simulations are very large compared with observations. In both the shower and deep clouds, ε_{95} and ε_{99} are one and two orders of

magnitude larger, respectively, in the MetUM. In both of the control simulations, ε decreases with height. This is inconsistent with observations where ε is constant with height in shower cloud and increases with height in deep cloud. The rate of decrease with height of ε_{95} and ε_{99} was smaller in SSC (factor of 2) compared with SDC (factor of ten). The disparity between simulated and observed vertical gradients of ε was discussed in the context of the upward transport of turbulence via advection in observed updrafts. Future research should consider the impact of the advection of turbulence by updrafts, and the resulting effect on the evolution of convective clouds.

5.4 Evaluation of ε in simulated updrafts

Up until now, evaluation of the model has focused on the general intensity and distribution of ε. In Section 5.3, the general characteristics of ε were compared in simulated and observed clouds. This included a comparison of the appearance and spatial distribution of ε in individual cloud cases, the typical and large values of ε, and the distribution of ε with height in the cloud. Qualitatively, the characteristics of ε associated with simulated updrafts were found to differ significantly. Features of ε were smaller and more intense in the model and were more strongly co-located with gradients in vertical velocity w, than in observed clouds. By applying the same updraft detection methodology as applied to observed clouds (Section 4.4.1), the statistical relationships and probability distribution of ε in simulated updrafts of different strength can be evaluated through direct comparison with the updraft analysis presented for observations in Section 4.4.

For clarity of comparison, this section is structured identically to Section 4.4. Methods for model data sampling and updraft detection are summarised in Section 5.4.1, followed by the discussion and comparison of the statistics of updraft turbulence in simulated and observed clouds in Section 5.4.2. The broad characteristics of updrafts and associated

turbulence are compared between model and observations in Section 5.4.2.1, followed by a comparison of correlations between ε and updraft characteristics in Section 5.4.2.2. Finally, a comparison of the change in the probability distribution of ε within updrafts of different strength is presented in Section 5.4.2.3.

5.4.1 Detection of simulated updrafts

In Section 4.4, a flood-fill algorithm was applied to observations to detect coherent objects of w that exceeded a prescribed threshold. Updraft regions (or "updrafts") were then approximated by rectangular regions defined by the spatial scales of the detected object. The coordinates of detected updrafts were then superimposed on retrievals of ε to investigate the statistical properties of turbulence associated with convective updrafts. This methodology (detailed in Section 4.4.1) is now applied consistently to vertical cross-sections of w sampled from the control simulations.

For each of the three time-steps selected for analysis in the control simulations (see Section 5.2), vertical cross-sections were sampled throughout each domain at regular y-intervals of 3 km. In Section 4.4, the RHI dataset used for the analysis of updraft turbulence was comprised of statistically independent cloud observations. To ensure the application to model data is consistent with this, the y-interval of 3 km was selected to be large enough to minimise the over-sampling of individual updrafts, while remaining small enough to build a dataset of updrafts large enough to be suitable for statistical assessment. If the majority of simulated updrafts are less than 3 km wide (results in Section 5.4.2 reveal this corresponds to ~75% of updrafts in both cases), the majority of vertical cross-sections will contain statistically independent updrafts. Using this sampling method, 139 vertical cross-sections are considered for SDC, and 142 for SSC. These are suitably large datasets for statistical assessment when compared with the 33 RHIs analysed for OSC, and 44 RHIs for ODC, from which significant statistical relationships could be derived.

The threshold velocities ($w_{\min}$) that were applied to OSC (1 m s^{-1}) and ODC (1.5 m s^{-1}) are applied identically to detect updrafts in the vertical cross-sections of SSC and SDC. The flood-fill algorithm detects an updraft where at least 4 pixels of w are connected by their edges. Therefore, observed updrafts were filtered by width and depth thresholds to remove those that were small and insignificant. Depth thresholds were set to approximately one third of the cloud depth; 2 km in OSC and 3 km in ODC. Applying these thresholds to updrafts detected in model data resulted in 99% and 98% of updrafts being removed in SSC and SDC, respectively. This results from a key difference in the representation of updrafts between model and observations. Observed updrafts appear to more closely resemble "plumes" of large w that extend for a significant proportion of the cloud depth, e.g. in Figure 5.4a. However, simulated updrafts more closely resemble "thermals"; shallower pockets of large w, e.g. in Figure 5.4c. This characteristic difference means that applying the same depth thresholds would remove updrafts that are considered significant in the context of the model. To account for this, the depth threshold is relaxed to 1 km for model updrafts. The width threshold of 1.5 km is, however, applied consistently between model and observed updrafts.

Applying these filters leaves a dataset of 651 updrafts from SSC, and 386 updrafts from SDC. The coordinates of each of these are then overlaid onto corresponding fields of ε, where only $\varepsilon > \varepsilon_{\min}$ is considered for analysis. The analysis of observed updrafts (Section 4.4) has been reproduced to consider only $\varepsilon > \varepsilon_{\min}$ within each updraft to allow for a direct comparison to be made. Due to the generally high intensity of turbulence in observed updrafts, especially in deep clouds, thresholding ε has had little effect on the correlations between ε_{95} and updraft characteristics in Section 5.4.2.2.

5.4.2 Statistics of ε in simulated updrafts

The following three sections include statistical analyses of ε within the datasets of simulated updrafts described in Section 5.4.1. Direct comparisons are made with corresponding statistics for turbulence in observed updrafts to evaluate the generation of turbulence in model updrafts. This begins with a broad comparison of model updraft characteristics, and associated ε, with observations in Section 5.4.2.1. This is followed by a comparison of the strength of correlations between ε and updraft characteristics in Section 5.4.2.2, and a comparison of the probability distribution of ε in updrafts of different strength in Section 5.4.2.3.

5.4.2.1 Updraft characteristics and ε in model and observations

Data in all updrafts regions are combined for each cloud case to produce cumulative density functions (CDFs) of updraft ε, updraft velocity w, the magnitude of the horizontal gradient in updraft velocity $\left|\frac{dw}{dx}\right|$, and updraft area. These characteristics (the same as those compared for observations in Figure 4.11) are compared between SSC and OSC in Figure 5.9, and between SDC and ODC in Figure 5.10.

The CDFs of ε (Figure 5.9a and 5.10a) suggest turbulence is much stronger in simulated updrafts than those observed. This is consistent with the comparison of ε throughout all simulated and observed cloud, presented in terms of the vertical distribution of ε in Section 5.3. In Figure 5.9a, small values of ε (less than 0.01 $m^2\ s^{-3}$) comprise 45% of updraft values in OSC and 35% of values in SSC. This suggests that although a similar proportion of the spatial area within the updrafts is only weakly turbulent, weak turbulence is slightly more widespread in OSC updrafts. Significant differences then exist in the proportion of ε larger than 0.05 $m^2\ s^{-3}$, which is only 1% in OSC compared with 20% in SSC. This shows that the significant turbulence in SSC updrafts is considerably more intense than in observed

updrafts. The 95th and 99th percentiles of ε (ε_{95} and ε_{99}) in SSC updrafts (0.4 $m^2\ s^{-3}$ and 4 $m^2\ s^{-3}$) are approximately one and two orders of magnitude larger than the corresponding values in observed updrafts (0.03 $m^2\ s^{-3}$ and 0.04 $m^2\ s^{-3}$), respectively. This is consistent with the comparison of the vertical distribution of these percentiles in Section 5.3.2.

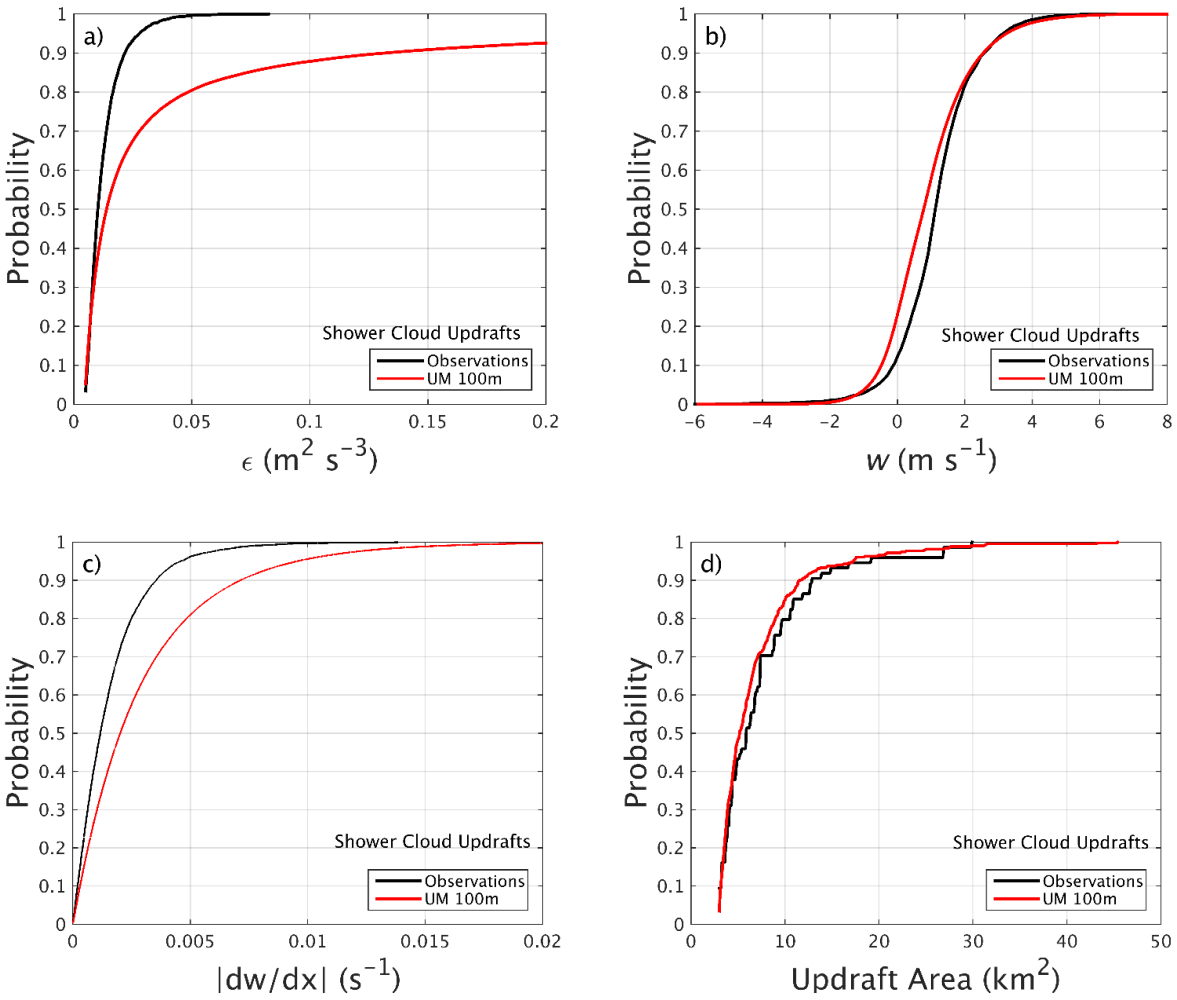

Figure 5.9: Comparison of the cumulative density functions (CDFs) of updraft characteristics in simulated and observed shower clouds; (a) ε; (b) vertical velocity, *w*; (c) magnitude of shear in *w*; (d) updraft area. CDFs include all values located within all detected updraft regions.

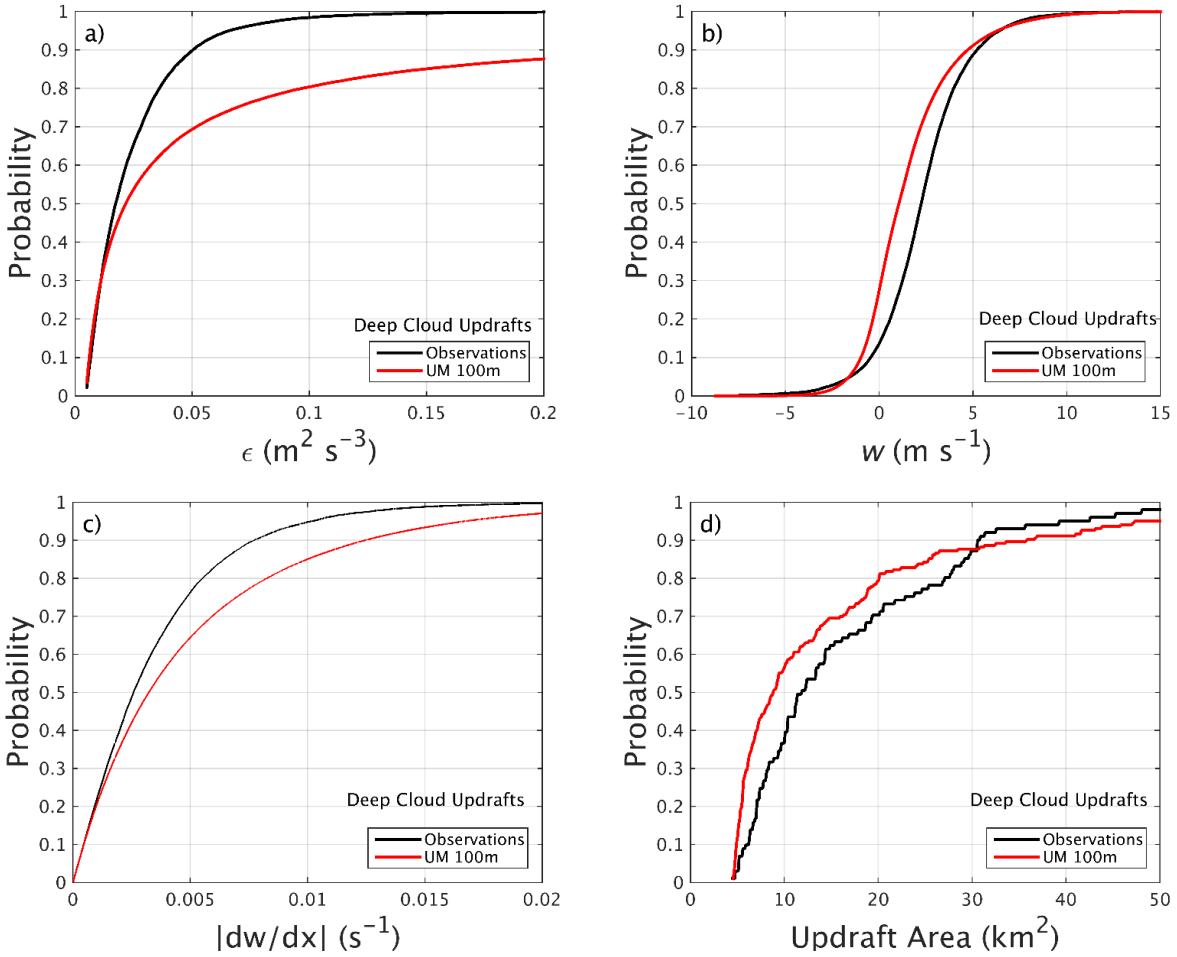

Figure 5.10: Comparison of the cumulative density functions (CDFs) of updraft characteristics in simulated and observed deep clouds; (a) ε; (b) vertical velocity, *w*; (c) magnitude of shear in *w*; (d) updraft area. CDFs include all values located within all detected updraft regions.

Similar comparisons can be made for deep clouds in Figure 5.10a. In both ODC and SDC, 25% of all values of ε are less than 0.01 $m^2\ s^{-3}$, suggesting the spatial extent of weak turbulence is the same in both cases, and more similar than for shower cloud updrafts. However, as for shower cloud updrafts, significant differences exist for larger values of ε. Only 2% of ε values in ODC updrafts are larger than 0.1 $m^2\ s^{-3}$ compared with 20% of values in SDC updrafts. Values of ε_{95} and ε_{99} in SDC updrafts (0.8 $m^2\ s^{-3}$ and 9 $m^2\ s^{-3}$) are approximately double those stated for SSC updrafts and are similarly one and two orders of magnitude larger than the corresponding values in ODC updrafts (0.07 $m^2\ s^{-3}$ and 0.1

$m^2\ s^{-3}$). The clear differences in the distribution of ε for both updraft cases are now discussed in the context of other updraft characteristics to identify the potential causes.

Figure 5.9b and Figure 5.10b show that the distribution of updraft strength is very similar between model and observations for both cloud cases. Generally, values of w are slightly larger in observed updrafts, however, this appears to result from a higher proportion of negative values in simulated updraft regions (21% for SSC; 26% for SDC) than in those observed (11% for OSC; 13% for ODC). This may result from thermal-type updrafts appearing more irregular in shape (a good example of this is shown in Figure 5.5c) than the plume-type updrafts found in observed clouds. If detected features of $w > w_{\min}$ are more irregular, the rectangular updraft regions defined by the spatial extremes of the feature are more likely to include values of $w < w_{\min}$. When considering only $w > 0$ (not shown), CDFs of w are almost identical for both cloud types. This is an important clarification to make when attempting to explain the marked difference in the CDFs of ε. Differences in updraft strength between model and observations would have impacted the distribution of ε. This was demonstrated in observations where CDFs of ε in updrafts changed significantly with w_{95} (Figure 4.13 and 4.14). By verifying the consistency in w between model and observations, characteristics aside from updraft strength must be responsible for the disparity in ε.

The CDFs in Figure 5.9d and Figure 5.10d compare updraft area between model and observations for shower and deep clouds, respectively. The depth and width thresholds impose a minimum area on observed updrafts of 3 km^2 for OSC, and 4.5 km^2 for ODC. Due to the lower depth threshold in the model, updraft area can be as low as 1.5 km^2. To ensure a fair comparison of probability in these figures, SSC updrafts with an area lower than 3 km^2, and SDC updrafts with an area lower than 4.5 km^2, have been removed. The resulting CDFs are very similar for shower clouds (Figure 5.9d). In deep clouds (Figure 5.10d), observed updrafts are generally larger, although not considerably, and the probability of

updrafts larger than 30 km^2 is marginally higher in SDC. Although there are small differences in the CDFs of updraft area, observed and simulated updrafts are broadly very similar in size. Again, this is important to demonstrate as significant positive correlations ($r = 0.3 - 0.4;\ p < 0.02$) were identified between ε and the dimensions of updrafts in Section 4.4. The similarity in updraft sizes suggest that any impacts on the CDFs of updraft ε are small.

The consistency in updraft size and strength between model and observations makes it very unlikely that these factors are responsible for the disparity in ε. However, this consistency does not apply to CDFs of $\left|\frac{dw}{dx}\right|$, displayed for shower and deep cloud in Figure 5.9c and Figure 5.10c, respectively. Shear was determined by differentiating model updraft w in the x-direction over every 100-m grid-point in each updraft.

A broader distribution of $\left|\frac{dw}{dx}\right|$ values exist in simulated updrafts for both cloud types, although the differences in the CDFs are not as pronounced as for ε. For shower updrafts in Figure 5.9c, only 4% of values in SSC updrafts exceed the largest observed shear of 0.014 s^{-1}, increasing only to 0.04 s^{-1}. The median, 95th and 99th percentiles of $\left|\frac{dw}{dx}\right|$ in SSC updrafts are approximately double those in OSC updrafts, indicating that shears are more generally a factor of two larger in SSC updrafts. There are smaller differences between the CDFs of shear for deep updrafts (Figure 5.10c), where only 0.7% of $\left|\frac{dw}{dx}\right|$ values in SDC updrafts exceed the largest in ODC updrafts of 0.03 s^{-1}. The median value of $\left|\frac{dw}{dx}\right|$ in SDC updrafts ($3.2 \times 10^{-3}\ s^{-1}$) is only 25% larger than in ODC updrafts ($2.6 \times 10^{-3}\ s^{-1}$), and the 95th and 99th percentiles of $\left|\frac{dw}{dx}\right|$ are only 65% larger in the model. This indicates that shear is larger in simulated updrafts, however, not to the degree of ε.

The method used to calculate shear is not entirely consistent with methods applied to observations. The resolution of w-retrievals resulted in shear being calculated over 500 m, compared with 100 m in model data. In Chapter 3, shear was generally higher when

calculated over smaller distances in radar observations, owing to high variability in the Doppler velocity from pulse to pulse. However, model fields of w are far smoother than radar retrievals of w (e.g. compare Figure 5.4a and 5.4c). As a result, the higher resolution of the model data is not expected to impact $\left|\frac{dw}{dx}\right|$. The most likely reason for $\left|\frac{dw}{dx}\right|$ to be larger in the model is illustrated in Figure 5.11, which includes the horizontal plane of w and ε at 2-km height for a limited area of the 1500 UTC domain of the deep cloud control simulation.

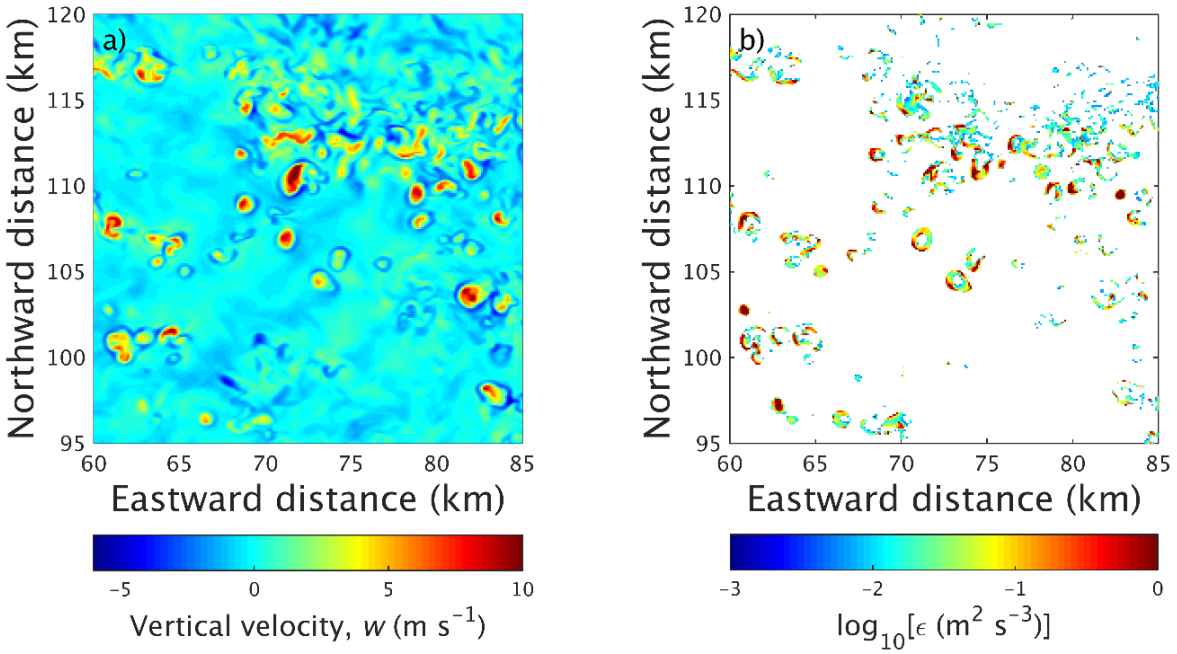

Figure 5.11: The horizontal plane of fields of w (a) and ε (b) at a height of 2 km in a limited domain area of the 1500 UTC deep cloud control simulation.

From this perspective, updrafts seen in Figure 5.11a are often closely encircled by compensating downdrafts. This results in strong velocity gradients around updraft edges that lead to ring-shaped features in ε shown in Figure 5.11b. Although updrafts and downdrafts have been seen in close proximity in some observed cases, compensating downdrafts are not always apparent (e.g. Figure 5.4a), and certainly not as consistently, or in such close proximity to updrafts, as those seen in the model. This provides a plausible explanation for the larger values of $\left|\frac{dw}{dx}\right|$ in simulated updraft regions, and possibly also the larger values of ε, which are clearly seen to be strongly associated with these gradients in Figure 5.11b.

However, caution is taken in drawing this conclusion at this point, as it remains to be demonstrated that the differences seen in shear magnitudes can be responsible for the substantial differences in ε. To investigate this further, the sensitivity of ε to the characteristics of model updrafts is assessed through correlation and compared with observations in Section 5.4.2.2.

5.4.2.2 Correlations of ε in model updrafts

By comparing correlations of ε within updrafts with observations, the sensitivity of model ε to the characteristics of individual updrafts is evaluated. For each updraft detected in the model, the 95th percentile of ε (ε_{95}) is recorded from values of $\varepsilon > 0.005$ m^2 s^{-3}. The 95th percentiles of updraft velocity (w_{95}) and magnitude of horizontal shear in w ($\left|\frac{dw}{dx}\right|_{95}$) are recorded, together with the updraft width and depth. Corresponding statistics from observed clouds are reproduced to consider only $\varepsilon > 0.005$ m^2 s^{-3} in each updraft. This has had very little effect on ε_{95} for each updraft, and therefore the scatter plots and correlations compared with the model in this section differ only slightly from those in Section 4.4.2.2.

Figure 5.12 and 5.13 display and compare correlations of ε_{95} with (a) w_{95}; (b) $\left|\frac{dw}{dx}\right|_{95}$; (c) updraft width; and (d) updraft depth, for shower and deep cloud, respectively. In both simulated cloud cases, there are no significant correlations ($p > 0.1$) between ε_{95} and any of the updraft characteristics considered. Qualitatively, the scatter plots for model updrafts appear quite similar to observations, with positive correlation evident especially when comparing ε_{95} with w_{95} and $\left|\frac{dw}{dx}\right|_{95}$. However, the lack of correlation (indicated by $-0.1 < r < 0.1$) has likely resulted from a broad range in ε_{95} in the model. In both models, values of ε_{95} span three orders of magnitude from $10^{-2} - 10$ m^2 s^{-3}, compared to only $10^{-2} - 10^{-1}$ m^2 s^{-3} typically found in observations. The data counts within individual updraft regions are small, especially when only considering $\varepsilon > 0.005$ m^2 s^{-3}.

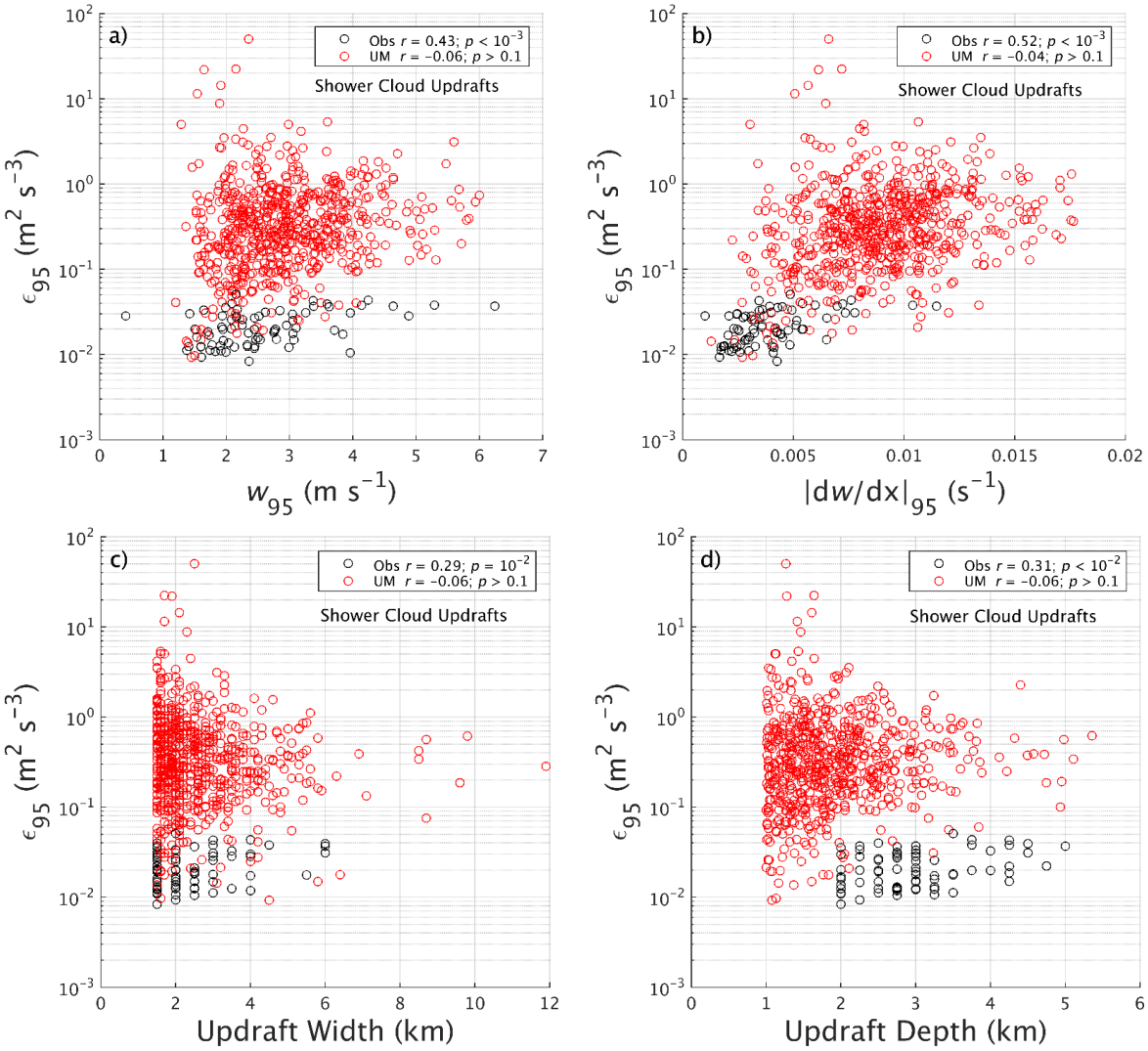

Figure 5.12: Scatter plots comparing correlations between the 95th percentile of ε in each simulated and observed shower updraft region, with (a) the 95th percentile of w; (b) 95th percentile of shear in w; (c) updraft width; (d) updraft depth. Each plotted point corresponds to one updraft region. Only $\varepsilon > 0.005$ m^2 s^{-3} is considered in all updrafts.

In model updraft regions, the median data count is 168 in SSC and 184 in SDC. Therefore, the 95th percentile is more likely to reflect the extremely large values of ε that have been identified in the MetUM. As illustrated in the SSC presented in Figure 5.4c, extreme values of ε (up to 110 m^2 s^{-3} in this example) can be found even within simulated clouds with weak updrafts. If the largest values of ε are not statistically related to cloud characteristics, this is likely to affect correlations of ε_{95} due to the small data samples within updraft regions.

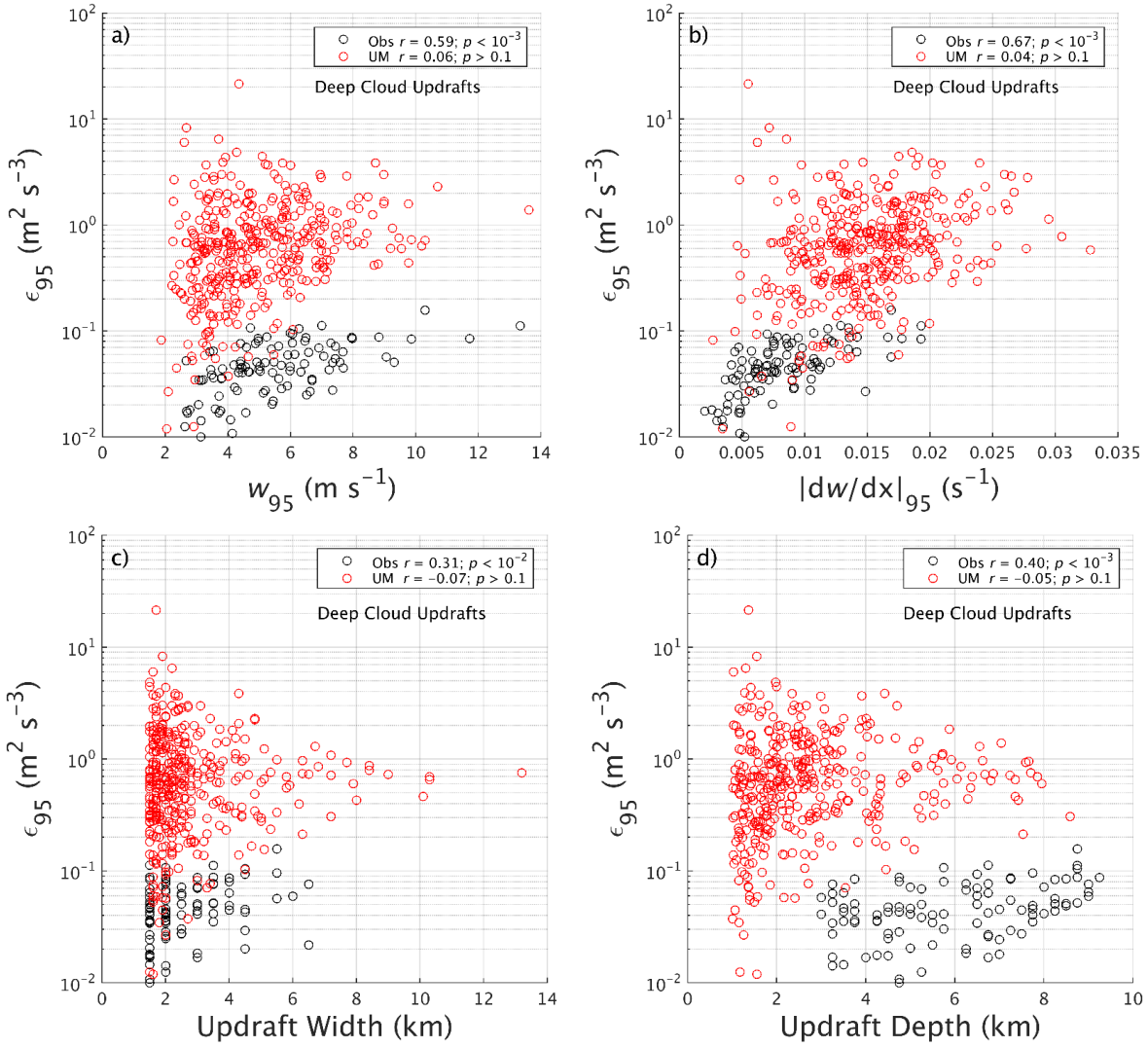

Figure 5.13: As for Figure 5.12 but for deep cloud updraft regions.

To improve the comparison of correlations between model and observations, two upper limits have been applied to ε_{95}, limiting the model updrafts that are considered for correlation. The first of these considers only model updrafts with $\varepsilon_{95} < 1\ \mathrm{m^2\ s^{-3}}$, which represents the largest ε that can be reliably observed by CAMRa. The second considers only model updrafts with ε_{95} less than the maximum ε_{95} in observed updrafts for both cloud cases ($0.05\ \mathrm{m^2\ s^{-3}}$ for OSC; $0.16\ \mathrm{m^2\ s^{-3}}$ for ODC). The resulting correlations are listed in Table 5.2, together with the number of model updraft regions involved in correlations after the thresholds to ε_{95} have been applied. When only $\varepsilon_{95} < 1\ \mathrm{m^2\ s^{-3}}$ is considered, updraft counts are reduced by 13% for SSC and 28% for SDC. Under this constraint, for both SSC and SDC

updrafts, statistically significant ($p < 0.05$) positive correlations are found between ε_{95} and w_{95}, and with $\left|\frac{dw}{dx}\right|_{95}$. Correlations between ε_{95} and the spatial dimensions of model updrafts are weaker than with w_{95} and $\left|\frac{dw}{dx}\right|_{95}$, but are significant except between ε_{95} and updraft width in SSC. Each correlation is stronger in SDC updrafts, although the largest r is only 0.36 between ε_{95} and w_{95}, indicating only weak positive correlation between $\varepsilon_{95} < 1$ m^2 s^{-3} and updraft characteristics in the model. When considering only updrafts with ε_{95} lower than the largest observed ε_{95} for both cases, updraft counts are reduced to only 35 for SSC, and 39 for SDC. Correlations between ε_{95} and updraft depth are insignificant in both SSC and SDC updrafts. There is a weak (significant) positive correlation between ε_{95} and updraft width for SDC ($r = 0.33$) that is very similar to that for ODC ($r = 0.31$). Correlations are improved with w_{95} and $\left|\frac{dw}{dx}\right|_{95}$ in both cloud cases, to as large as $r = 0.53$ between ε_{95} and $\left|\frac{dw}{dx}\right|_{95}$ for SSC updrafts.

	All ε_{95}		**$\varepsilon_{95} < 1$ m^2 s^{-3}**		**$\varepsilon_{95} < \max(\varepsilon_{95_{obs}})$**	
	SSC	**SDC**	**SSC**	**SDC**	**SSC**	**SDC**
Number of updrafts	639	383	557	274	35	39
$r(\varepsilon_{95}, w_{95})$	-0.06	0.06	**0.20**	**0.36**	**0.44**	**0.33**
$r\left(\varepsilon_{95}, \left\|\frac{dw}{dx}\right\|_{95}\right)$	-0.04	0.04	**0.27**	**0.29**	**0.53**	**0.34**
$r(\varepsilon_{95}, \mathbf{width})$	-0.06	-0.07	-0.02	**0.21**	-0.27	**0.33**
$r(\varepsilon_{95}, \mathbf{depth})$	-0.06	-0.05	**0.14**	**0.26**	0.15	0.30

Table 5.2: Correlation coefficients r, between ε_{95} and updraft characteristics for SSC and SDC updraft regions. Correlations are performed for: all updrafts, only updrafts with ε_{95} lower than the maximum ε reliably observable with CAMRa (1 m^2 s^{-3}), and updrafts with ε_{95} lower than the maximum observed ε_{95} (0.05 m^2 s^{-3} for OSC; 0.16 m^2 s^{-3} for ODC). Correlations with associated p-values lower than 0.05 are indicated in bold red.

Interestingly, correlations comparing ε_{95} with w_{95} and $\left|\frac{dw}{dx}\right|_{95}$ in shower clouds become almost identical in model and observations when considering only the range of ε_{95} observed. This is not true, however, for deep clouds, where correlations in simulated updrafts are approximately half those observed. Under this constraint to ε_{95}, correlations in SDC updrafts are now weaker than for those in SSC, indicating that correlations are sensitive to data sampling, and inconsistent with observations, where correlations were stronger in deep updrafts for all characteristics considered.

In summary, no significant correlations have been found between ε_{95} and the characteristics of model updrafts when considering the full range of ε_{95}. The far broader range of ε_{95} in model updrafts has made direct comparison with correlations in observed updrafts difficult to make. Correlations in model updrafts are improved when only considering $\varepsilon_{95} < 1\ \mathrm{m^2\ s^{-3}}$, with significant but weak positive correlations between ε_{95} and most updraft characteristics. The strongest correlations are found with w_{95} and $\left|\frac{dw}{dx}\right|_{95}$ in SDC updrafts. The strength of these correlations is improved again when only considering model updrafts with ε_{95} lower than the maximum ε_{95} in observed updrafts. In conclusion, significant correlations have been demonstrated for ε_{95} in model updrafts that are similar in strength to those observed. However, these remain generally weaker than in observed updrafts, indicating that ε_{95} is less sensitive to the selected updraft characteristics in the model. The variability of correlations with data sampling suggests these results may not reliable enough to compare critically with observations, but they are suitable to broadly compare the strength of relationships between ε and updraft characteristics.

5.4.2.3 Change in distribution of ε with model updraft strength

The correlation approach used in Section 5.4.2.2 was useful to assess the relationships between updraft characteristics and the largest values of ε. As for observations (Section

4.4.2.3), this analysis is extended to evaluate the change in the distribution of ε within model updrafts of different strength. Identical methods as those applied to observed updrafts are applied to model updrafts. Updraft regions are sorted into sets based on 2 m s^{-1} velocity intervals of w_{95}, e.g. all updraft regions with $0 < w_{95} < 2$ m s^{-1} are grouped together. All values of ε that exceed 0.005 m^2 s^{-3} within each updraft set are combined into a single dataset and presented in CDFs in Figure 5.14. These CDFs are produced for the intervals of w_{95} that were observed, allowing for a direct comparison. For consistency, the observed CDFs of ε have been reproduced to only consider $\varepsilon > 0.005$ m^2 s^{-3} in each updraft region, although this has had very little effect on their shape. Figure 5.14 contains the same information as the CDFs in Figure 5.9a and 5.10a, which include all ε in all updrafts, except in this case, CDFs are expressed as a function of w_{95}. Due to this similarity, this section will not include a discussion of the differences in the distribution of ε values between model and observed updrafts, as this was given in detail in Section 5.4.2.1. Instead, this section focuses on the sensitivity of CDFs of model ε to w_{95}, and comparing this with observations.

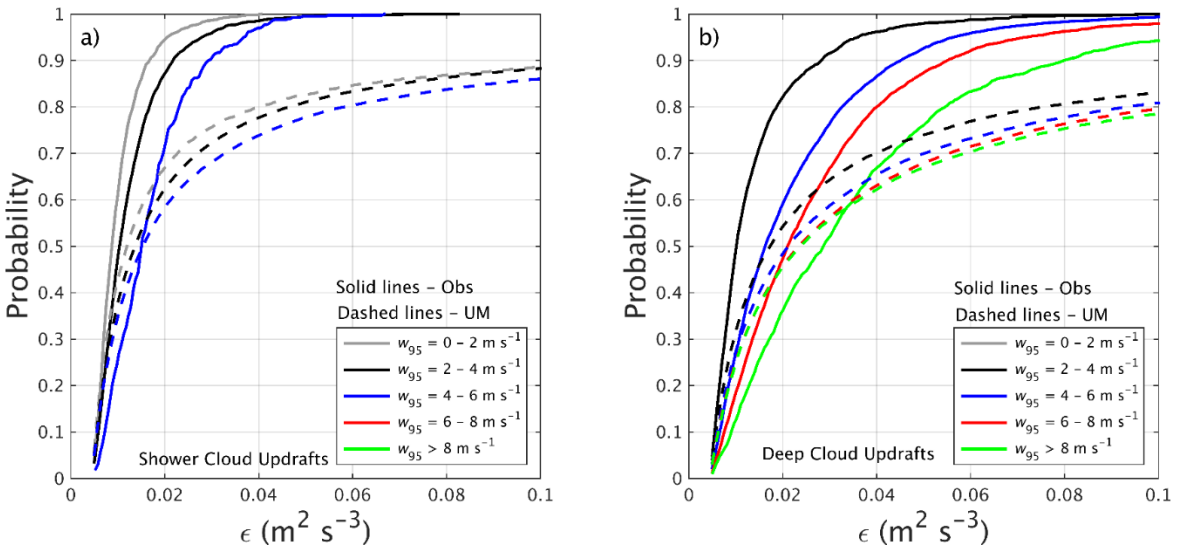

Figure 5.14: Comparison of the change in the cumulative density function (CDF) of ε in updraft regions with different 95th percentile values of w (w_{95}), between (a) simulated and observed shower updrafts, and (b) deep updrafts. Only $\varepsilon > 0.005$ m^2 s^{-3} is considered in all updrafts.

Figure 5.14a compares CDFs of ε in SSC updrafts for the three observed intervals of w_{95} in OSC updrafts; spanning 0 – 6 m s^{-1}. A trend towards a lower probability of small ε, and a higher probability of large ε is seen with model updraft strength. This is consistent with the trend in observed updrafts, although the differences between CDFs are smaller in the model. Importantly, the probability of large ε (more than 0.1 m^2 s^{-3}) appears to change very little with model updraft strength. For ε larger than 0.1 m^2 s^{-3} (not shown) the CDFs in Figure 5.14a gradually converge. These features are reflected in the comparison for deep cloud updrafts in Figure 5.14b. There is a more pronounced change in CDFs with w_{95} in ODC updrafts, than for OSC. However, CDFs in SDC updrafts remain similarly insensitive to updraft strength. The change in the probability of large values of ε is very small between model updrafts of $w_{95} = 2 - 4$ m s^{-1} and $w_{95} > 8$ m s^{-1}. Although this is true for ODC updrafts as well, the change in CDF for $\varepsilon < 0.1$ m^2 s^{-3} is far larger than for SDC updrafts, which remain very similar for all values of ε.

Presenting the distribution of ε as a function of updraft strength highlights potential reasons for the generally weaker correlations identified for model updrafts in Section 5.4.2.2. When considering model updrafts of all strength, there were no significant correlations with updraft characteristics. Constraints were applied to ε_{95} under the assumption that the large values of ε in the model were not correlated with updraft characteristics. The insensitivity of ε (including large values) to updraft strength shown in Figure 5.14 would suggest this assumption was correct, which likely explains why correlations are considerably weaker in the model. The improvement in the correlations when thresholding by lower ε_{95} would suggest smaller values of ε (those within the range observable by radar) are more sensitive to updraft characteristics than large values.

In Section 4.4.2.3, updrafts of similar strength observed in both clouds cases produced similar CDFs of ε, though with indications that turbulence was stronger in deep updrafts than in shower updrafts of the same strength, especially for the largest values of ε. By using only

snapshot vertical cross-sections through clouds, it appeared likely that the advection of turbulence within the cloud could easily lead to high ε being sampled from processes that were not directly observed. Interestingly, when comparing the CDFs of ε in similar strength updrafts between control simulations (Figure 5.15), ε is larger in deep updrafts. In fact, the distribution of ε in deep updrafts of $w_{95} = 2 - 4$ m s^{-1} is broader, albeit marginally, than the distribution of ε in stronger shower updrafts of $w_{95} = 4 - 6$ m s^{-1}. Because ε is determined only from local shear and buoyancy, the Smagorinsky-Lilly scheme does not account for the advection of turbulence. This would suggest that another process may be responsible (both in model and observations) that leads to broader distributions of ε in deep updrafts, than for shower updrafts of similar strength.

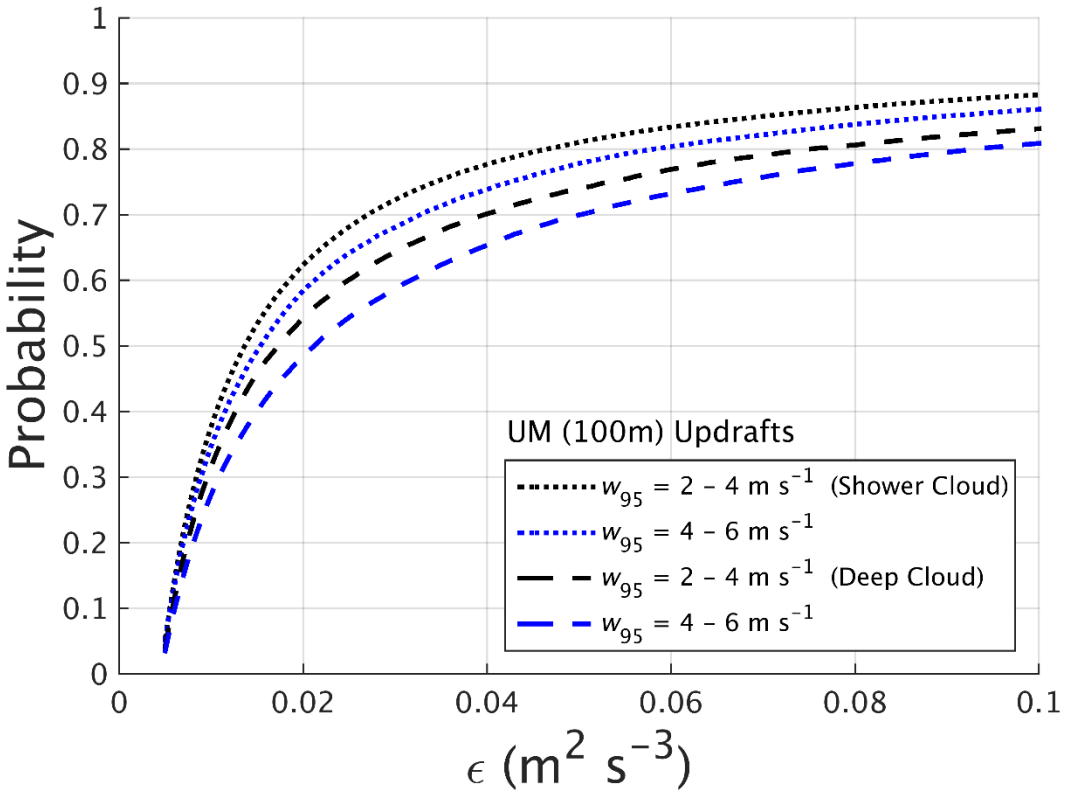

Figure 5.15: A comparison of the CDFs of ε in simulated updraft regions for the two intervals of w_{95} in Figure 5.14 for which simulated shower and deep updrafts were recorded. Simulated deep updrafts are more turbulent than shower updrafts of similar strength.

In summary, inspecting the change in the distribution of ε within updrafts of different strength has provided additional insight into the statistical relationships between ε and the characteristics of simulated updrafts. The CDFs of ε become broader with w_{95} as seen in observations, but the change between intervals of w_{95} is very small compared to observed updrafts. The probability of large ε (more than 0.1 $m^2\ s^{-3}$) is largely insensitive to w_{95}, providing an indication as to why there were no significant correlations between ε_{95} and w_{95} when considering the full range of ε_{95} in simulated updrafts, and why correlations improved when considering a restricted range of ε_{95}. This does, however, raise the question as to which processes are responsible for generating the large or extreme values of ε in the model, and why these are not necessarily statistically related to the characteristics of updrafts.

5.5 Spatial characteristics of ε in simulated clouds

As initially identified in Section 5.3, the appearance of dissipation features differs significantly between simulated and observed clouds. Features of ε in model clouds (e.g. see Figure 5.5d) appear smaller and more intense when compared to the more diffuse regions of generally weaker ε in observed clouds (e.g. see Figure 5.5b). To examine this difference quantitatively, the methods used to characterise the spatial scales of turbulent features in observed clouds in Section 4.5 are applied identically to vertical cross-sections of ε in control simulation data (Section 5.5.1). This is used to investigate the change in the spatial scales of ε features with intensity in the model and draw direct comparisons with observed features of similar intensity.

5.5.1 Detection of ε features in simulated clouds

Vertical cross-sections of ε in control simulation data are sampled throughout model domains with a y-interval of 3 km. This is performed for each of the three time-steps (1100,

1300 and 1500 UTC) for SSC and SDC. The 3-km spacing is chosen to be large enough to minimise the oversampling of features of ε. As in Section 5.4, where a 3-km spacing was selected to minimise the oversampling of updrafts, the resulting dataset is comprised of 142 vertical cross-sections through SSC and 139 through SDC.

To ensure consistency with observations collected using CAMRa, the thresholds z_{min} and Z_{min} are applied so that features of ε are sampled at least 150 m above the surface, and within cloud or precipitation that exceeds a reflectivity of 0 dBZ. It is unnecessary to apply the threshold $\varepsilon_{\mathrm{min}} = 0.005\ \mathrm{m^2\ s^{-3}}$ to this data, as the lowest threshold used to detect ε features ($\varepsilon_{\mathrm{thld}} = 0.01\ \mathrm{m^2\ s^{-3}}$) exceeds this value. The flood-fill algorithm used to detect spatially coherent features in ε in observed clouds is applied identically to model data (the algorithm and methodology is described in detail in Section 4.5.1). Features in model data are detected using values of $\varepsilon_{\mathrm{thld}}$ of 0.01, 0.03, 0.05, 0.1, 0.2, 0.5 and 1.0 $\mathrm{m^2\ s^{-3}}$. These thresholds overlap those applied to observed clouds allowing for a direct comparison, while accounting for higher values of ε found in the model up to the limit for reliable observation with CAMRa. Equations (4.1) and (4.2) are used to determine the median width W_{m}, and depth D_{m}, of ε features detected at each $\varepsilon_{\mathrm{thld}}$.

Two filters were applied to detected ε features in observations; a threshold minimum area of 0.1 $\mathrm{km^2}$ and a filter to remove features detected near the cloud top and base that are susceptible to biases in axial ratio (illustrated for observations in Figure 4.15). Both of these filters are applied identically to the model, where ε features are removed if detected within 1 km of cloud tops (5 – 6 km in SSC; 9 – 10 km in SDC) or detected within 1 km of the surface. Table 5.3 lists the data counts of features detected at each $\varepsilon_{\mathrm{thld}}$ for SDC and SSC, with the data counts before these filters were applied indicated in parentheses.

Simulated Deep Cloud		Simulated Shower Cloud	
ε_{thld} $(m^2\ s^{-3})$	Object counts (before filtering)	ε_{thld} $(m^2\ s^{-3})$	Object counts (before filtering)
0.01	3915 (10312)	0.01	1691 (9054)
0.03	2297 (6643)	0.03	642 (4890)
0.05	1590 (5207)	0.05	358 (3586)
0.1	905 (3480)	0.1	143 (2143)
0.2	408 (2177)	0.2	48 (1193)
0.5	114 (1081)	0.5	7 (499)
1.0	44 (559)	1.0	4 (224)

Table 5.3: Final object counts for each threshold of ε in SSCs and SDCs. Object counts before filtering by area and location are indicated in parentheses. Due to low data counts, objects detected in SSC at ε_{thld} of 0.5 $m^2\ s^{-3}$ and 1.0 $m^2\ s^{-3}$ are omitted from Figure 5.16.

5.5.2 Evaluation of the spatial characteristics of model ε

Consistent with methods used in Section 4.5.2, each dataset listed in Table 5.3 is split into three by terciles of area to compare the average and large features separately. Average features are those within the 33rd and 66th percentiles of area, and large features are those with an area larger than the 66th percentile. Ellipses with width W_m, and depth, D_m derived from each subset of features are used in Figure 5.16 to represent the median size and shape of features of ε detected at each ε_{thld}. Due to the low data counts for $\varepsilon_{thld} = 0.5\ m^2\ s^{-3}$ and $\varepsilon_{thld} = 1.0\ m^2\ s^{-3}$ in SSC (7 and 4 objects, respectively), ellipses are not plotted for these thresholds in Figure 5.16a and 5.16b.

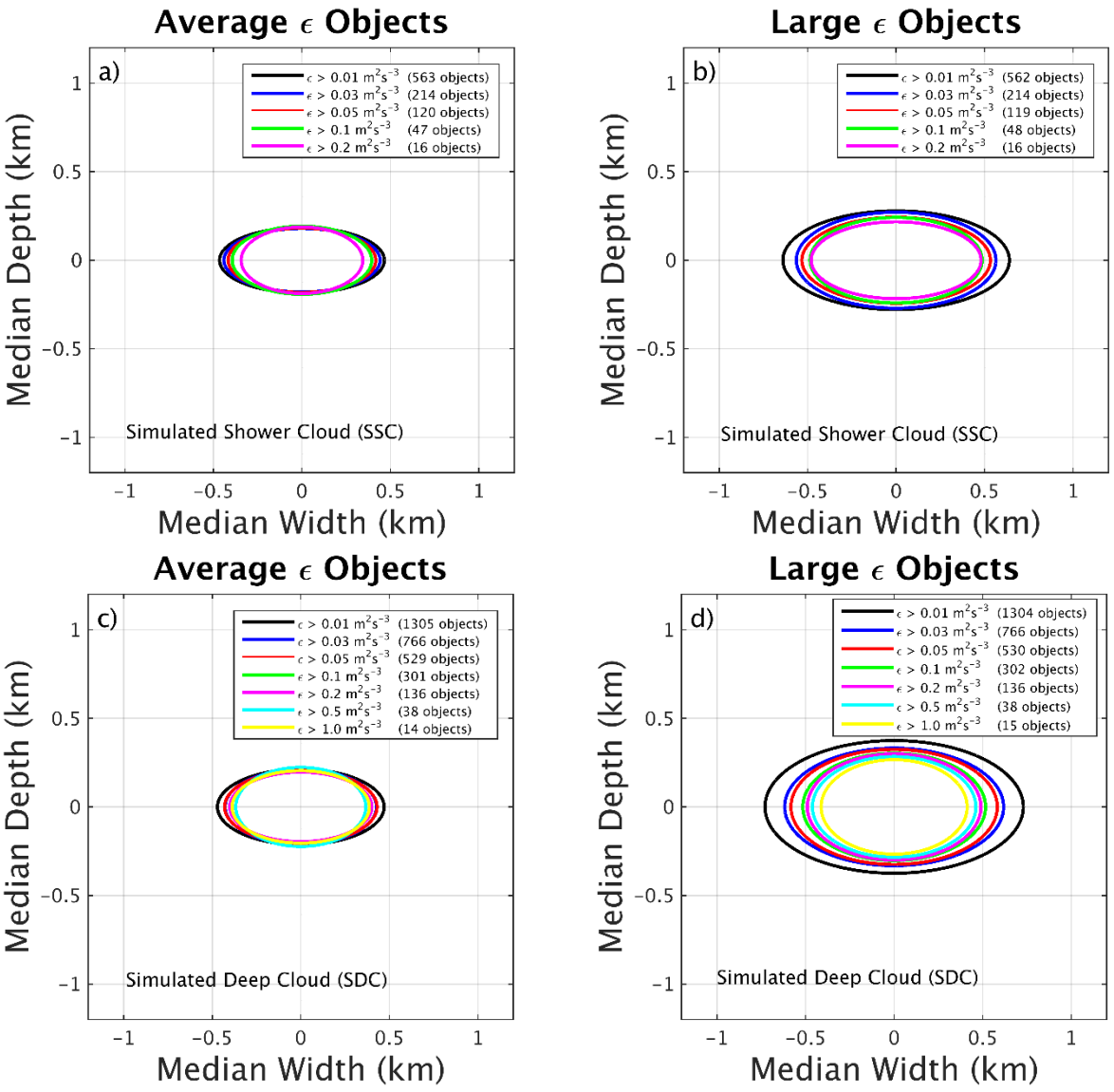

Figure 5.16: Median size of average and large ε objects in SSC ((a) and (b)), and SDC ((c) and (d)). Objects have been approximated by ellipses using methods identical to those applied to observed clouds in Section 4.5.

The shape and size of the average features of ε does not change significantly between SSC (Figure 5.16a) and SDC (Figure 5.16c), or with the intensity of $\varepsilon_{\text{thld}}$. Values of D_{m} vary between 0.35 – 0.40 km in SSC and between 0.40 – 0.45 km in SDC, with no clear trend with $\varepsilon_{\text{thld}}$. This suggests that the depth of average-sized ε features is insensitive to the intensity of dissipation and does not differ greatly in shower or deep clouds. Values of W_{m} decrease consistently with ε in both cases, but only slightly, falling from 0.94 – 0.78 km in SDC and from 0.93 – 0.69 km in SSC when ε increases from 0.01 – 0.2 $\text{m}^2\,\text{s}^{-3}$.

Consequently, for this range of ε, the ratio of width to depth (axial ratio, R_{m}) roughly decreases, but only from 2.5 to 2.

Comparison with observations (Figure 4.16a and 4.16c) suggests the average weak dissipation features ($\varepsilon > 0.01\ \mathrm{m^2\ s^{-3}}$) are approximately the same size and shape in the model. However, as ε increases, there is a clear transition to smaller features with much lower R_{m} (less than 1 for $\varepsilon > 0.05\ \mathrm{m^2\ s^{-3}}$) in observations. Although these trends are found in the model (features get smaller and R_{m} decreases), they are far less sensitive to changes in ε. This extends to the large features in the model (Figure 4.16b and 4.16d) which display similar insensitivity to ε in both cases, showing a small but consistent decrease in size and R_{m} with ε. The large weak dissipation features ($\varepsilon > 0.01\ \mathrm{m^2\ s^{-3}}$) are significantly smaller in simulated clouds, while intense dissipation features ($\varepsilon > 0.1\ \mathrm{m^2\ s^{-3}}$) are smaller in observed clouds. This characterises the broader distribution of ε found in the MetUM that has been identified in previous sections of this chapter. The larger spatial coverage of weak dissipation in observed clouds (and clearer changes in feature size with ε) may represent the effects of the advection and diffusion of large ε into broader regions of weaker dissipation; a process that is not accounted for in the Smagorinsky-Lilly scheme.

In summary, the typical spatial scales of dissipation features have been identified in MetUM simulations. The insensitivity of the spatial characteristics of dissipation features to the intensity of ε in the model represents a key difference with observations. Dissipation in the model is characterised by small, intense regions of ε, compared to broad, more diffuse regions of ε in observed clouds. A clear difference between features in the model is the insensitivity of R_{m} to ε. It is not clear what guides the transition to lower R_{m} with turbulent intensity in observations. And although there is some evidence of this trend in both cloud cases in the model, the change with ε is far smaller than observed. Until further investigation is conducted in observed clouds to identify which cloud processes affect the shape of

dissipation features, it is difficult to know whether this represents a problem with the Smagorinsky-Lilly scheme.

5.6 Sensitivity of ε to model configuration

Sections 5.3 – 5.5 demonstrate that clear differences exist in the characteristics of ε between observed and simulated clouds. Although the full range of observed values of ε are also produced by the model, and median values are similar, ε can be two orders of magnitude larger ($\sim 100\ \mathrm{m^2\ s^{-3}}$) than can be observed reliably with radar ($\sim 1\ \mathrm{m^2\ s^{-3}}$). When performing correlations for ε in Section 5.4, results suggested that large values (more than $1\ \mathrm{m^2\ s^{-3}}$) are much less sensitive to the characteristics of updrafts than values smaller than $1\ \mathrm{m^2\ s^{-3}}$. It is possible that large values of ε are instead more sensitive to the configuration of the model. Therefore, this section aims to determine whether the disparity in ε between model and observations can be reduced by applying reasonable changes to the model grid-length Δx, and sub-grid scheme mixing length, λ_0, as well as more generally assessing their impact on ε.

5.6.1 Introduction and hypotheses

As described in Section 2.3.3, two control simulations were performed with $\Delta x = 100$ m (assumed to be most comparable with the resolution of CAMRa) and $C_s = 0.2$ (default value) for both case days. These are listed together with 6 additional simulations in Table 2.3 which were performed to produce 100-m and 55-m grid-length forecasts using both $C_s = 0.2$ and $C_s = 0.4$, for both case days, using the procedure shown in Figure 2.9. These simulations are used to test the sensitivity of ε in the control simulations to a reduction in Δx from 100 m to 55 m and doubling λ_0 with respect to Δx by increasing C_s from 0.2 to 0.4.

The mixing length λ_0, is prescribed for the Smagorinsky-Lilly scheme as the product of C_s and Δx in (2.22). The sensitivity of ε to λ_0 is tested by simply comparing ε in simulations at a given Δx when C_s is changed from 0.2 to 0.4. According to (2.26), ε increases with λ_{UM}^2, which would suggest that doubling λ_0 with respect to Δx would lead to an increase in ε by a factor of four where $\lambda_0 \sim \lambda_{\mathrm{UM}}$. However, doubling λ_0 will increase the degree of sub-grid mixing which acts to smooth velocity and precipitation fields (Hanley *et al*, 2015). This is likely to result in a decrease in shear around updrafts due to increased entrainment. Given that ε is dependent on a shear term in (2.26), it is difficult to know precisely the net effect on ε when increasing λ_0 prior to testing in Section 5.6.2.

The sensitivity of ε to Δx cannot be tested as directly as for λ_0. For example, comparing ε in a 100-m simulation with a 55-m simulation while $C_s = 0.2$ is not suitable as λ_0 will change from 20 m to 11 m. However, a comparison of ε in a simulation with $\Delta x = 100$ m and $C_s = 0.2$ ($\lambda_0 = 20$ m) with a simulation with $\Delta x = 55$ m and $C_s = 0.4$ ($\lambda_0 = 22$ m) can be considered a fair way to test sensitivity to Δx. Under the assumptions of Kolmogorov (1941), the downscale transfer rate of TKE in the Richardson cascade is constant within the inertial sub-range of eddy scales – where it is given by ε. In applying this concept to the model, if the inertial sub-range has an outer scale Λ_0, that is larger than scales resolved in a 100-m grid-length model, it is expected that the statistics of ε remain largely the same in simulations with $\Delta x = 100$ m and $\Delta x = 55$ m. Similar reasoning is used when sampling turbulence with a radar beam which has spatial dimensions that increase with range. For example, ε is sampled consistently with range when the largest dimension of the beam increases from 55 – 100 m as long as $\Lambda_0 > 100$ m. If λ_0 remains within the inertial sub-range and Δx is suitable to resolve an inertial sub-range, characteristics of ε are expected to remain consistent when λ_0 is changed in simulations with a fixed Δx.

5.6.2 Sensitivity to model grid-length and mixing length

A convenient way to assess the sensitivity of model ε to Δx and λ_0 is to compare the vertical distribution of median ($\varepsilon_{\mathrm{med}}$) and 95th percentile ($\varepsilon_{95}$) values in each of the four simulations for each case. This method is used primarily to directly compare percentiles of ε rather than the impact on the vertical distribution. The method used to determine vertical distributions of $\varepsilon_{\mathrm{med}}$ and ε_{95} for both cases is consistent with that described in Section 5.3.2.

Figure 5.17 and Figure 5.18 include comparisons for SDC and SSC, respectively, where plotted lines corresponding to $\Delta x = 100$ m and $C_s = 0.2$ (control simulations) are identical to those presented in Figure 5.7. When models are compared in terms of λ_0 (which include 11 m, 20 m, 22 m and 40 m), there is a consistent increase in $\varepsilon_{\mathrm{med}}$ and ε_{95} with λ_0. The smallest values are found in the 55-m model using $\lambda_0 = 11$ m. However, even in this case, ε_{95} remains approximately an order of magnitude larger than observed values. The change in ε_{95} with λ_0 is more pronounced than for $\varepsilon_{\mathrm{med}}$ in both cloud cases, indicating that large values of ε are more sensitive to λ_0 in the model. Changes to Δx and λ_0 appear to have very little effect on the vertical distribution of ε in both cases.

When $\Delta x = 100$ m, increasing C_s from 0.2 – 0.4 (λ_0 from 20 m to 40 m) results in larger $\varepsilon_{\mathrm{med}}$ in both cloud cases. As a mean throughout the vertical profile, $\varepsilon_{\mathrm{med}}$ is larger by 31% in SDC, whereas $\varepsilon_{\mathrm{med}}$ appears less sensitive to λ_0 in SSC, increasing by only 8%. Interestingly, when C_s is increased from 0.2 – 0.4 (λ_0 from 11 m to 22 m) in the 55-m models, the mean percentage increase in $\varepsilon_{\mathrm{med}}$ is very similar (32% in SDC and by 7% in SSC). This could suggest that the impact on ε when increasing λ_0 occurs independent of Δx, though further investigation would be required to draw this conclusion. As highlighted in Section 5.6.1, the sensitivity of ε to Δx is most directly assessed by comparing the 100-m model using $C_s = 0.2$ and the 55-m model using $C_s = 0.4$. As shown in Figure 5.17 and Figure 5.18, although values of $\varepsilon_{\mathrm{med}}$ in these models are broadly similar, they are consistently larger in the 55-m model ($\lambda_0 = 22$ m) than in the 100-m model ($\lambda_0 = 20$ m). Values of $\varepsilon_{\mathrm{med}}$

increase by 16% in SDC and by 3% in SSC. Given the clear indication in Figure 5.17 and Figure 5.18 that ε increases more generally with λ_0, this difference may result from the slightly larger λ_0 in the 55-m model, rather than Δx itself. The difference in λ_0 is only 2 m, however, the mean percentage increases are roughly half those found when increasing λ_0 by 11 m in the 55-m models. Although these results indicate that ε is consistent between 100-m and 55-m models when λ_0 is constant, further model experiments may be required using identical λ_0 to demonstrate this more rigorously.

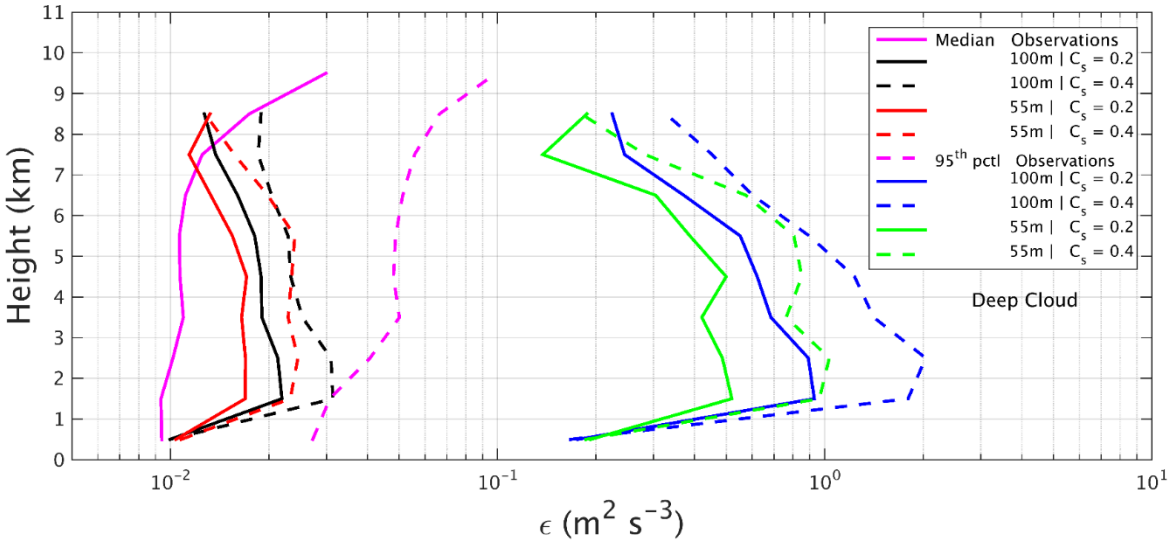

Figure 5.17: Sensitivity of the vertical distribution of median and 95th percentile values of ε to model grid-scale and mixing length constant C_s, in simulated deep cloud (SDC).

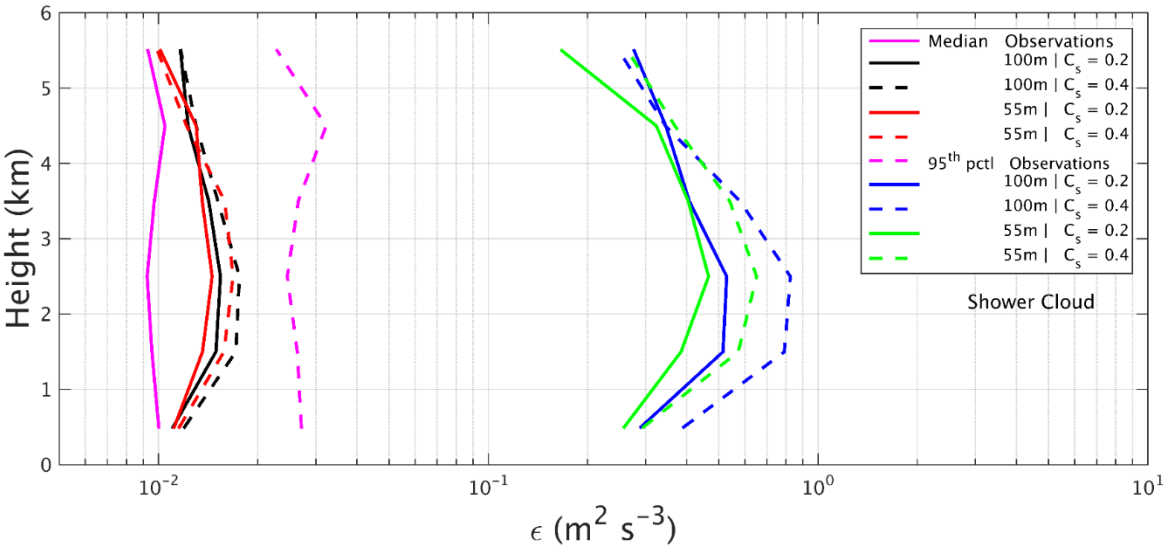

Figure 5.18: Sensitivity of the vertical distribution of median and 95th percentile values of ε to model grid-scale and mixing length constant C_s, in simulated shower cloud (SSC).

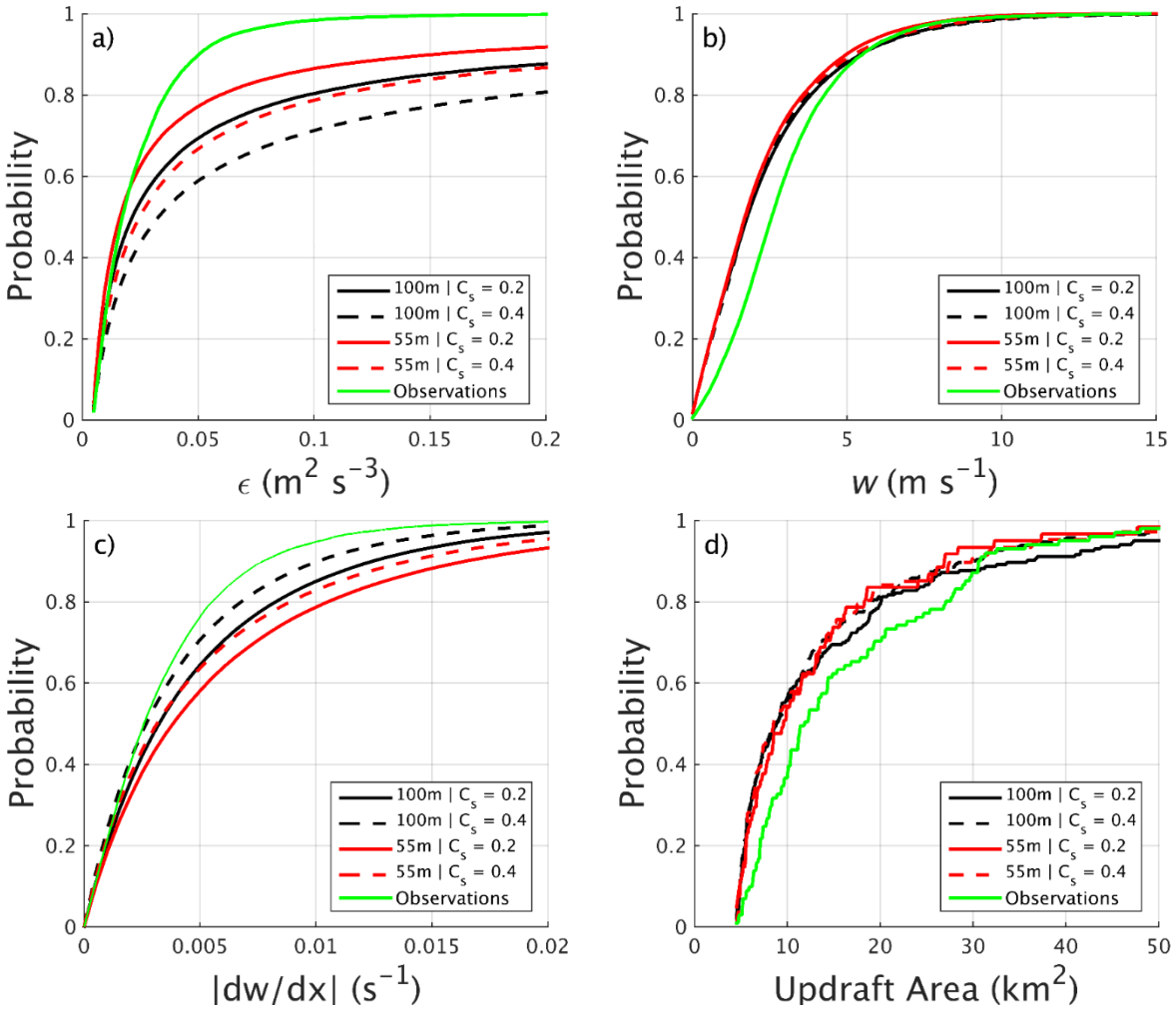

Figure 5.19: Sensitivity of cumulative density functions of updraft characteristics in simulated deep cloud (SDC) to model grid-scale and mixing length constant, C_s.

To provide a broader context for the impact of changing Δx and λ_0 on ε, sensitivity tests are now applied to characteristics of convective updrafts in SDC. To accomplish this, results displayed in Figure 5.10 have been reproduced for each of the sensitivity simulations and compared with observations; this is presented in Figure 5.19. Figure 5.19b and Figure 5.19d suggest that updraft velocity and updraft area remain consistent in each simulation. As suggested in Section 5.6.1, increasing λ_0 acts to smooth out velocity gradients around updrafts through increased entrainment, reducing $\left|\frac{dw}{dx}\right|$. CDFs of ε and $\left|\frac{dw}{dx}\right|$ are very similar in the 100-m model with $\lambda_0 = 20$ m and the 55-m model with $\lambda_0 = 22$ m, providing further evidence that ε is largely insensitive to Δx. When $\Delta x = 100$ m, doubling λ_0 from 20 m to

40 m produces a CDF of weaker $\left|\frac{dw}{dx}\right|$ values that is closer to the observed distribution; however, this simulation also produces the largest ε. Referring to (2.26), this result suggests that doubling λ_0 reduces the shear in the resolved flow (which, in isolation, will reduce ε), but this effect is small compared with the factor-of-four increase in ε due to the increased mixing when λ_0 is doubled.

In summary, ε becomes consistently larger with λ_0 across the four simulations for SDC, with $\varepsilon_{\mathrm{med}}$ increasing by 31% when λ_0 is doubled from 20 m to 40 m in the 100-m model. When this test is applied to SSC, values of ε appear less sensitive to changes in λ_0, with only an 8% increase in $\varepsilon_{\mathrm{med}}$. Values of ε_{95} are more sensitive to changes to λ_0 than $\varepsilon_{\mathrm{med}}$, though even at the smallest λ_0, ε_{95} remains an order of magnitude larger than observed values. Results suggest that models with different Δx but with similar λ_0 produce similar values of ε. This indicates that ε is insensitive to changes in model grid-length when $\Delta x \leq 100$ m, providing evidence that grid-lengths of 100 m and 55m were sufficient to resolve the inertial sub-range of turbulence. This improves the reliability of comparisons with inertial sub-range turbulence sampled with CAMRa. The size and strength of convective updrafts remains consistent when changing Δx and λ_0. When doubling λ_0, the reduction in ε due to weaker shear is small compared to the factor-of-four increase in ε from increased mixing. Models using grid-lengths of 55-m and $C_s = 0.2$ produce values of ε that are closest to observations but still remain much larger (values of model ε_{95} are larger by an order of magnitude). Perhaps of most importance is that reasonable changes to model and sub-grid scheme configuration can reduce ε, but not sufficiently to agree with observed values for these cases.

5.7 Summary and conclusions

Simulations have been performed in the MetUM with 100-m grid-length and a C_s of 0.2 (control) for the shower and deep cloud cases, for which radar observations were examined in detail in Chapter 4. Values of ε have been determined from diagnostic outputs from the Smagorinsky-Lilly sub-grid scheme in the MetUM (see Section 2.3.2) to compare with ε retrieved with CAMRa. In Chapter 4, analysis of radar-retrieved ε was performed using methods specifically designed to enable consistent application to model data. Before these methods were applied to model data, suitable thresholds and constraints were established in Section 5.2 to guide the sampling of model data to account for the characteristic differences with radar data. Vertical cross-sections of model data (comparable with RHIs with CAMRa) were sampled from 3-D domains at model time-steps that spanned the time period during which the majority of observations were collected. Numerical thresholds were applied to ε to account for a limit to the minimum ε observable with CAMRa, and to radar reflectivity to ensure ε was sampled only from model clouds with a reflectivity that would be detected by CAMRa. This was a key step to ensure a fair comparison between model and observations was possible.

The evaluation of ε in the MetUM commenced with a detailed comparison of individual observed and simulated cloud cases in Section 5.3. Consistent with observed clouds, values of ε were larger in the SDC than in the SSC, a large proportion of simulated clouds were only weakly turbulent, and high ε was spatially correlated with regions of vertical motion. Large ε in the model was often found in small, localised regions strongly co-located with regions of shear around updrafts. Although this was also evidenced in the observed cases, regions of large ε were much weaker and more diffuse. The largest values of ε in the simulated clouds far exceeded those in the observed clouds, but also exceed the largest ε that can be reliably observed with CAMRa by up to two orders of magnitude. A detailed

comparison of individual cloud cases was not sufficient to draw strong conclusions in the evaluation of model ε. Instead, results were used as guidance to explain the findings of the more general statistics-based approach to analysis used in later sections of the chapter.

The first statistical approach compared the vertical distribution of ε in simulated clouds (defined by model total radar reflectivity) with observations in Section 5.3.2. Median values of ε were very similar between simulated and observed clouds, ranging from 0.01 – 0.03 $m^2\ s^{-3}$ in all cases. However, the 95th and 99th percentiles of model ε were respectively one and two orders of magnitude larger than observed values for both cloud cases. The intensity of ε decreases with height in the model, in contrast to observations where ε remains constant with height in shower clouds and increases with height in deep clouds. Although the reason for this difference is unclear, the vertical transport of turbulence in deep updrafts is thought to play a role in generating a positive vertical gradient in ε with height; a process of advection that is not accounted for in the Smagorinsky-Lilly scheme. To determine whether this presents a significant problem for the model, further research is required in observed clouds to investigate the impact of the advection of turbulence by updrafts on cloud evolution.

The statistics of ε in simulated updraft regions were evaluated using observations (from Section 4.4) in Section 5.4. For positive vertical velocity, the distribution of updraft speed was very similar between model and observations for both cloud cases. Simulated updraft regions were also broadly similar in size. Despite these similarities, the 95th and 99th percentiles of ε in simulated updraft regions were respectively one and two orders of magnitude larger than those in observed updrafts; this is consistent with the comparison of the vertical distribution of these percentiles in model clouds in Section 5.3.2. There was a broader distribution of shear (given by $\left|\frac{dw}{dx}\right|$) in model updrafts. For the shower case, 95th percentile values were twice as large in the model, while values were 65% larger in the model

for the deep case. It is not clear whether stronger shear alone can account for the significantly larger ε in the model.

To evaluate the strength of relationships between the 95th percentile of model ε in updrafts (given by ε_{95}) to updraft characteristics, correlations were performed and compared directly with observations in Section 5.4.2.2. When considering the full range of ε_{95} in model updrafts, no significant correlations were identified with updraft strength, size or shear. When considering only ε_{95} in the range that can be reliably observed with radar (less than 1 $m^2\ s^{-3}$), significant weak positive correlations were found with updraft characteristics. The strength of these correlations improved further when considering only the range of ε_{95} that was observed in each case, becoming similar in strength to those observed, albeit slightly weaker in most cases. The variability of correlation strength to data sampling suggests a limit to how critically comparisons can be made with observations. However, results suggest that although the largest values of ε in model updrafts can far exceed those observed, they do not have significant correlation with updraft characteristics. Further evidence of this was presented in Section 5.4.2.3, where the probability of ε larger than 0.1 $m^2\ s^{-3}$ was largely insensitive to updraft strength in the model. Consistent with observations, the cumulative density functions (CDFs) of ε in model updrafts became broader with updraft strength but were much less sensitive to velocity changes than CDFs in observed updrafts.

The typical spatial scales of coherent features in ε were identified and compared with observations in Section 5.5. These scales were largely insensitive to the intensity of ε and remained similar in shower and deep clouds; a key difference with observations. Generally, weak ε features are smaller in the model and intense ε features are larger and more numerous. Results suggest that model turbulence is characterised by small, intense regions of ε, consistent with the qualitative inspection of individual cloud cases in Section 5.3. Further investigation is required to identify whether the size and shape of ε features is related to

cloud processes in observations. Until this happens, it is difficult to know whether the differing spatial characteristics of ε impacts cloud evolution in the model.

The sensitivity of model ε to grid-length Δx, and sub-grid scheme mixing length, λ_0 was presented in Section 5.6. Although the size and strength of updrafts remains consistent as Δx and λ_0 is changed, values of ε become consistently larger as λ_0 is increased. In 100-m models, doubling λ_0 led to an increase in median values of ε by 31% and 8% in SDC and SSC, respectively. When $C_s = 0.2$ was used in the 55-m model (which leads to the smallest considered λ_0 of 11 m), values of ε_{95} are most similar to observations but still remain approximately one order of magnitude larger. The similarity of ε in 55-m and 100-m models with similar λ_0 suggests ε is insensitive to Δx when $\Delta x < 100$ m, likely indicating that $\Delta x \leq 100$ m was sufficient to resolve an inertial sub-range for these simulations. When λ_0 is increased, the reduction in ε due to weaker shear is small compared to the factor-of-four increase in ε due to increased mixing (see (2.26)). Most importantly, no reasonable changes to model and sub-grid scheme configuration has reduced ε sufficiently to agree with observations.

Chapter 6

Summary and future work

6.1 Overview

The effects of turbulence in convective clouds are profound and wide-ranging; but remain poorly understood in observations and in numerical weather prediction (NWP) models. In convection-permitting models (CPMs), schemes to parametrise the sub-grid effects of turbulence are often taken from large-eddy simulation (LES) models; which use mixing-length-based TKE closure schemes. The suitability of such schemes for use in CPMs is not well understood. More specifically, it is not often clear that the assumptions required for these schemes to perform as intended are valid for CPMs. This is especially true when forecasting with grid-lengths larger than 100 m. The associated uncertainty is reflected in the widely-reported sensitivity of simulations of convective clouds to the configuration of turbulence schemes. To evaluate the parametrisation of sub-grid turbulence in CPMs, diagnostics from the schemes must be evaluated using comparable observations. However, a suitable observational dataset for this application has, until now, not been available.

Some high-resolution Doppler radars are capable of reliably sampling velocity variances from with the inertial sub-range of turbulence across large swathes of atmosphere. This method has clear benefits over in situ methods (such as aircraft) which can only collect time-series measurements from single points in space. Although the theoretical approach to retrieving turbulence from capable radars is well established, the development of a comprehensive retrieval method which can be applied consistently across many cloud cases, under a wide range of conditions, has not yet been presented. Such an approach is necessary to investigate statistics of turbulence to a level of detail that is sufficient for the evaluation of numerical models.

To address these points:

1. A comprehensive turbulence retrieval method to estimate the eddy dissipation rate ε, was presented in Chapter 3, with a focus on applications to data collected with the Chilbolton Advanced Meteorological Radar (CAMRa).
2. Using retrievals of ε performed for many cloud scans on two contrasting case days, a statistical assessment of relationships between ε and cloud characteristics was conducted in Chapter 4.
3. Observed statistical relationships were used to evaluate ε from the Smagorinsky-Lille sub-grid turbulence parametrisation in the Met Office Unified Model (MetUM) in Chapter 5. Simulations of the corresponding case days were performed and methods used to analyse observations were applied consistently to model data to produce comparable statistics.

In the following sections, the results, limitations and potential avenues for future work associated with these three chapters are summarised.

6.2 Turbulence retrieval with radar

6.2.1 Summary

In Section 2.1.2, the specifications of CAMRa and the scanning strategy used in data collection were discussed to demonstrate the suitability of CAMRa to turbulence retrieval. Specifically, CAMRa is of suitably high resolution that the width of the beam remains below estimates of the inertial sub-range outer-scale Λ_0, for the distances clouds were observed (30 – 150 km). In this sense, the Doppler velocity variance σ_v^2, measured by CAMRa includes variances from inertial sub-range eddies, allowing for the estimation of ε.

In Chapter 3, σ_v^2 measured by CAMRa was partitioned into a sum of variances from various contributing mechanisms (3.1), including that from turbulence which can be

converted to ε. By either calculating variance contributions or demonstrating their negligibility based on a threshold value of $0.5\ \mathrm{m^2\ s^{-2}}$, the contribution from turbulence was inferred from σ_v^2. To enable this process to be performed consistently for each σ_v^2 observation in a given scan (and across many separate scans), a detailed examination of each variance contributor under the range of observed conditions was required. The maximum sum of realistic variances from neglected contributors implied a positive bias in ε of 15% (when $\sigma_\mathrm{t}^2 = 5\ \mathrm{m^2\ s^{-2}}$) which decreased as σ_t^2 becomes larger.

In the context of CAMRa and the observations collected, velocity variance from antenna rotation and beam broadening (σ_α^2 and σ_B^2) were found to be negligible. Moreover, σ_α^2 and σ_B^2 remain negligible for any Doppler radar capable of sampling within the inertial sub-range for turbulence retrieval, except in the case of extreme rotation speeds (close to one revolution per second). Contributions from the oscillation, break-up and coalescence of hydrometeors were not calculated, but were neglected based on the chosen threshold using guidance from Zrnic and Doviak (1989).

The contribution from a distribution of hydrometeor fall-speeds within the sample volume (σ_TV^2) was analysed in detail owing to the range of elevations and potential hydrometeor types within the observational dataset. By deriving new hydrometeor-specific Doppler variance equations as a function of elevation angle, the negligibility of σ_TV^2 was assessed across the range of observed conditions. Variances from ice aggregates (accounting for observations above the melting layer) were negligible in all observed conditions and even if sampling vertically. Variances from rain (assumed only below the melting layer) were negligible when observed at elevation lower than 13.9°. Variances from hail were larger than for rain but remain negligible when observed at elevations lower than 11.5°. Results indicated that σ_TV^2 can be neglected if close-range, high-elevation scanning is avoided; as was true for observations collected with CAMRa.

Variance contributions from radial velocity shear σ_s^2, on scales larger than the sample volume have been removed from σ_v^2. This was achieved by fitting a velocity surface to Doppler velocity data (as is often applied in past studies). Using this method, linear radial and elevation shears were calculated over a fixed scale (Λ_s) of 900 m for each sample volume. These shears were used in variance equations that have been derived in Section 3.4.1 following uncertainty noted in the literature. Although Λ_s was selected to reflect the estimate of Λ_0, resulting values of ε (derived from σ_t^2 after shear removal) were found to be largely insensitive to Λ_s. This indicated that it is of primary importance that the largest scale of the sample volume is smaller than Λ_0. New equations were presented to account for shear in the azimuthal dimension of the radar beam in RHI scans by identifying statistical relationships with shear along the beam using PPI data. These relationships (mean and median values of azimuthal shear as a function of radial shear) were used to estimate the variance from a contributor to Doppler variance that cannot be measured directly in RHIs and is often overlooked, allowing the 3-D shear-induced Doppler variance to be estimated in 2-D radar scans.

The retrieval method summarised here has been developed to consider each term in (3.1) under a wide range of conditions, allowing reliable estimates of ε to be collected consistently throughout a large dataset of radar observations. The considerations of each term in (3.1) are suitably general to provide a retrieval method that can be applied simply to future observations with CAMRa. It also provides a reliable framework for turbulence retrieval with other Doppler-capable radars that are able to sample within the inertial sub-range.

6.2.2 Limitations and future work

Although it is highly probable that the resolution of CAMRa is sufficiently high to sample velocity variance from inertial sub-range turbulence, no steps have been taken to verify this assumption directly. The method presented in Chapter 3 included the assumption that Λ_0

was 900 m throughout each observed cloud over both case days. However, as noted by Sinclair (1974), the value of Λ_0 can vary spatially within individual clouds. The effects of this variability on the retrieval appears to be small, as indicated by the insensitivity of ε to Λ_s. Regardless of this, turbulent eddies closer than Λ_0 from the surface and from the cloud top would remain unlikely to be isotropic due to the suppression of the vertical dimension of eddies at the boundaries. This suggests that estimates of ε in these cloud regions may be unreliable.

It is not practical to make many estimates of Λ_0 for each cloud case over a dataset as large as that used for this application. However, using the spatial spectra approach (see Section 1.4.3) it is possible to make estimates of Λ_0 from Doppler velocity data (e.g. Brewster and Zrnic, 1986) in individual clouds. A sample of Doppler velocities from a scanned cloud could be used to estimate Λ_0 for each cloud case, allowing Λ_s to be determined on a case-to-case basis. Turbulence retrieval for the statistics-based evaluation of numerical models is unlikely to require precise measurements of Λ_0; however, uncertainty can be mitigated by retrieving ε only in cloud regions where turbulence is most likely to be isotropic (e.g. Kollias *et al.*, 2001). Measurements of turbulence near cloud edges have not been possible in this application as they are commonly areas with low signal-to-noise ratios which degrades the reliability of Doppler variance. Owing to the importance of turbulent entrainment processes in modulating the in-cloud environment, future research should investigate methods to improve the retrieval of ε near cloud edges.

Further research is required to investigate the variance contribution from the break-up and coalescence of rain drops and the rotation of hailstones, σ_{H}^2. Owing to the nature of these processes, a contribution from σ_{H}^2 is likely to be present in any sample volume that includes hydrometeors. Values of σ_{H}^2 are also unlikely to be dependent on radar viewing angle, suggesting that such variances cannot be avoided through changes to radar specifications of scanning strategy. The value of σ_{H}^2 was assumed to be similar to σ_{o}^2 and neglected in this

application without further investigation. Zrnic and Doviak (1989) suggest that the contributions from σ_{H}^2 should be accounted for when attempting to retrieve ε from Doppler variance. However, the significance of σ_{H}^2 remains poorly understood and more fundamental research into the small-scale processes associated with falling hydrometeors may be required.

6.2.3 An improved scanning strategy for turbulence retrieval

The accuracy of retrieved ε is likely to depend more on the degree to which variance contributors are justifiably neglected (σ_{TV}^2, σ_{α}^2, σ_{B}^2, σ_{o}^2 and σ_{H}^2) than the accuracy in which terms are calculated and removed directly (σ_s^2). This suggests that improvements to the retrieval of ε are made primarily through changes to scanning strategy and radar specifications to ensure that neglected terms remain as small as possible, while also improving the ability to calculate σ_s^2 directly.

The radar specifications and scanning strategy applied to collect the DYMECS data were not selected with turbulence retrieval as a priority. The data has been more than sufficient to retrieve turbulence from the collected data fields and perform analysis of in-cloud turbulence from RHI vertical cross-sections. However, in deriving and applying the turbulence retrieval method (see Chapter 3), the findings have been used to suggest improvements to future strategy and specifications in order to simplify the retrieval process, improve data collection, and to produce more accurate retrievals. The improvements summarised in this section have been applied to collect new observations of convective clouds with CAMRa on three days between July and September 2017. The improvements can be divided into two classes of recommendations. The first is comprised of radar specification and scanning constraints that both simplify the retrieval process and improve the retrieval accuracy (not limited to CAMRa). The second involves more preferential changes to scanning strategy to improve

the efficiency and quality of data collection for individual storm cases – these are described relative to DYMECS data collection and summarised first below.

During DYMECS, volume scans were obtained by performing PPI scans at progressively higher elevations following RHI sets. In this thesis, data from PPI scans are used to derive statistical relationships between radial velocity shear in the azimuthal and radial dimensions. This has allowed for the estimation of the velocity variance due to shear in the azimuthal direction in RHI scans, which do not provide the means for its direct measurement (Section 3.4). The derived relationships can now be used without the requirement for new PPI observations, allowing the prioritisation of RHI scanning when collecting observations. In practise, this allows more vertical cross-sections to be collected for each storm case, and more rapid sampling of many different storms when required. In the DYMECS observations, multiple RHIs were performed along lines of fixed azimuth through rainfall maxima. These scans provided no information regarding the horizontal changes in turbulent structures within the cloud. To investigate this, sequential RHIs are performed separated by small azimuthal increments to collect vertical profiles horizontally across a targeted storm. This strategy can be used to reconstruct 3D volumes of cloud for target storms. Where possible, the azimuthal spacing is set close to the beam-width of the radar (0.25°), which would avoid the need to interpolate between RHIs. Depending on the size and range of the target storm, the spacing was relaxed to 0.5° or 1° to avoid needing to perform tens of RHIs to cover the horizontal extent of the cloud.

The retrieval of turbulence can be further improved through changes to radar variables and scanning constraints. The radial pulse length of CAMRa is 75 m, however, this was averaged to 300 m in the DYMECS data. This has restricted the velocity surface fit scale to multiples of 300 m when removing velocity variance contributions due to shear (See Section 3.4.2). Although ε is shown to be largely insensitive to this scale in Section 3.4.2, the extra precision should be utilised, especially in cases where the largest scale of the inertial sub-range of turbulence can be measured. From thorough investigation into velocity variance

contributions from hydrometeor fall-speed distributions (Section 3.3), scanning methods can be constrained so that the contribution is small enough to be ignored. This is ensured completely when scanning through ice aggregates, and by limiting the elevation of RHIs to 11.5° when scanning through rainfall or hail. Under the assumption that rain and hail only exist below 3 km (with negligible contribution from ice aggregates above this level), observations can be collected at any elevation for storms located further than 15 km from the radar.

As outlined in Section 2.1.2, reliable observations of the spectrum width σ_v, can only be made between 0.6 and 6 m s^{-1}, owing to the Nyquist velocity of the radar. However, in the DYMECS scans, there appears to be a lower limit to the observable values of σ_v of ~ 0.9 m s^{-1}. Subsequent tests with CAMRa (Chris Westbrook, pers. comm.) have revealed that the minimum detectable σ_v is related to the number of pulse-pairs used while scanning. Using a higher number of pulse-pairs allows the collection of more signal returns per ray, at the cost of scanning speed. During DYMECS, 32 pulse-pairs were used to enable fast (2° s^{-1}) scanning in PPI mode; therefore, the time saved in omitting PPI scans can be used to scan with more pulses per ray in RHI mode. Figure 6.1 shows a comparison of σ_v observed by RHIs through cloud and precipitation on 17 May 2017, using 32 pulse-pairs (left) and 128 pulse-pairs (right). When using 32 pulse pairs, the lowest observed values of σ_v are again ~ 0.9 m s^{-1}. When scanning through the same cloud with 128 pulse pairs, values fall as low as ~ 0.6 m s^{-1}. When collecting new observations with 128 pulse-pairs, observations of σ_v can be made much closer to the lower limit imposed by the Nyquist velocity of CAMRa.

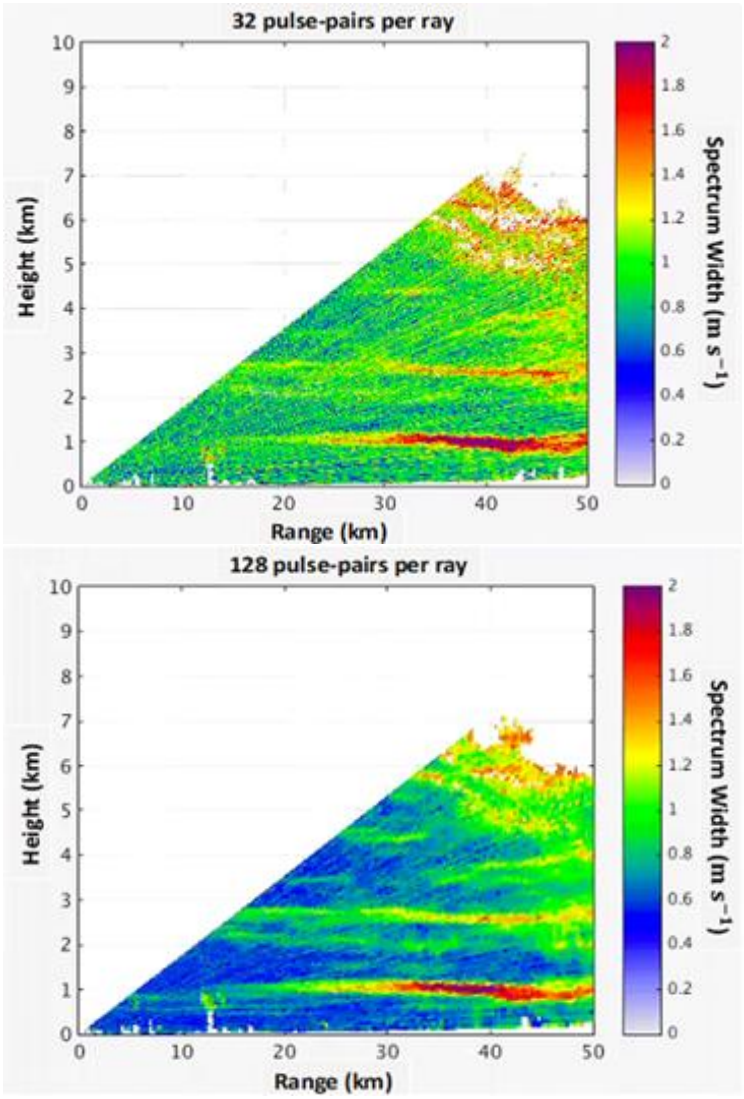

Figure 6.1: Comparison of Doppler spectrum width from RHIs performed on 17 May 2017 with 32 (top panel) and 128 (bottom panel) pulse-pairs (Chris Westbrook, pers. comm.).

6.3 Statistics of ε in observed clouds

6.3.1 Summary

The method developed in Chapter 3 to retrieve ε from the Doppler spectrum variance was applied to a subset of RHI observations collected with CAMRa for two case studies; shallow 'shower' clouds and more vigorous 'deep' clouds. By analysing fields of ε together with retrievals of vertical velocity *w*, performed previously for each cloud case, a detailed statistical analysis was conducted in Chapter 4 to determine relationships between ε and

cloud characteristics. The comparisons and methods used were carefully selected to be replicable with model data, ensuring a reliable evaluation of the model was possible.

Values of ε ranged from $10^{-3} - 10^{-1}$ m^2 s^{-3} in shower clouds and from $10^{-3} - 1$ m^2 s^{-3} in deep clouds. When comparing individual cloud cases, mean values of ε in the deep cloud (0.04 m^2 s^{-3}) were twice as large as those in the shower cloud and the maximum value of ε (0.61 m^2 s^{-3}) was a factor of six larger in the deep cloud. In both cases, turbulence was spatially correlated with the main updraft and, in the deep case, strong turbulence appeared more widely distributed in the upper regions of the cloud. These suggestions were investigated further by comparing the vertical distribution of various percentiles of ε calculated from all sampled clouds on both days. Median values of ε were similar (~ 0.01 m^2 s^{-3}) and remained approximately constant with height in both cloud types. The 95th percentile of ε increased consistently with height in deep clouds (from 0.01 – 0.1 m^2 s^{-3} from cloud base to cloud top) though remained approximately constant with height (~ 0.01 m^2 s^{-3}) in shower clouds. The range of observed ε values were consistent with those reported in clouds with similar updraft speeds in previous studies. Results suggested that a large proportion of the cloud area was only weakly turbulent in both cloud types, while the stronger updrafts in the deep clouds led to a positive vertical gradient in ε.

Statistical relationships between ε and cloud characteristics were sought through correlation techniques in 25 examples of single-cell convective clouds (SCCCs) identified (qualitatively) in the shower and deep cloud datasets. The mean magnitudes and 95th percentiles of w were found to be most strongly correlated with ε, while no significant correlations were found between ε and the spatial dimensions of the cloud or updraft. By splitting SCCCs into different regions, the largest ε was found within and above the main updraft; providing further evidence for the strong association between ε and updrafts, and the positive vertical gradient in ε identified earlier in this application and suggested in previous studies. Turbulence in cloud regions containing the main downdraft was 17% lower

than the cloud average, suggesting downdrafts are significantly less important in generating strong turbulence than updrafts.

Owing to the inadequacy of the results of the SCCC analysis for reliable model evaluation and the importance of updrafts in the intensity and spatial distribution of ε, a more focused investigation into ε in regions of convective updrafts was then performed. An automated updraft detection algorithm was used to record the spatial co-ordinates of updraft regions throughout the RHI datasets. These co-ordinates were overlaid onto fields of ε for statistical analysis. Strong positive correlations were found for the 95th percentile of ε (ε_{95}) with w_{95} and $\left|\frac{dw}{dx}\right|_{95}$ (consistent with suggestions from previous studies of individual clouds), while much weaker positive correlations existed with updraft dimensions. Combining data from both case days improved the strength of correlations, suggesting that consistent relationships may exist between ε and updraft characteristics that are independent of the day of observation. Cumulative density functions (CDFs) of ε were presented as a function of w_{95} indicating a consistent trend (for both cases) towards a lower probability of small ε and higher probability of large ε when w_{95} increases. In both cases, changes to the CDFs of ε became more pronounced as w_{95} became larger, indicating a non-linear relationship between the updraft velocity and the intensity of turbulence (as suggested by comparing previous studies in Table 1.1). CDFs of ε remained similar between shower and deep clouds for some intervals of w_{95}, further suggesting that ε could be expressed as a function of cloud characteristics independent of the day of observation.

Automated detection techniques were applied to fields of ε to characterise the spatial scales of dissipation features. Coherent features of weak turbulence ($\varepsilon > 0.01$ m^2 s^{-3}) had similar spatial scales in both shower and deep clouds (2.25 km wide and 1 km deep). As turbulence became more intense the median size of dissipation features decreased in both cases but, for given thresholds of ε, remained larger (and most notably deeper) in deep clouds.

The results of Chapter 4 have provided quantitative evidence for many of the characteristics of ε identified in previous studies in individual clouds, together with methods to identify new features of ε. These include:

- Quantifying the degree to which turbulent intensity increases with height in convective clouds and how this is affected by the updraft strength.
- Characterising the relationships between ε and cloud and updraft features using correlations and probability distributions. Such results provide the necessary quantitative detail required to evaluate numerical models beyond the limited (and often qualitative) identification of themes presented in previous studies.
- Characterising the spatial scales of coherent dissipation features in clouds with different updraft strength. The change in the feature shape and size has been demonstrated as a function of turbulent intensity.

6.3.2 Limitations and future work

A potential limitation of the research presented in Chapter 4 is associated with the assumption that values of w (from Nicol *et al*. (2015)) remain reliable for each cloud case. The single-Doppler method used by Nicol *et al*. (2015) requires numerous assumptions (see Section 2.2.3) to derive w from estimates of horizontal convergence using Doppler velocities collected only along the line-of-sight. In cases where convergence is not isotropic in the horizontal plane (i.e. convergence estimated along the line-of-sight cannot be used to estimate convergence perpendicular to the beam axis) w retrievals may become unreliable. There are likely to be cases where the assumption of isotropic convergence is not valid, which may affect statistical relationships between w and ε. However, any impact should be lower when comparing statistics of w and ε in individual clouds (as in Chapter 4) than if comparing point-for-point values. Future work could involve using the w-retrieval approach presented by Hogan *et al.* (2008) which involves tracking features in Doppler velocity in

consecutive RHI scans aligned with the mean wind as perhaps a more reliable method to estimate w in this data. Future data collection using dual-Doppler radar could be used to improve retrievals of w by estimating horizontal convergence from the Doppler velocity field sampled from two azimuths simultaneously.

A key limitation surrounds the use of RHI data alone in attempting to derive the statistics of in-cloud turbulence, i.e. one vertical cross-section through cloud observed at one instance. Reliably comparing ε with cloud features that are observed simultaneously at one instance requires two assumptions: (1) that the cascade of TKE to dissipation scales occurs on timescales that are small compared to the evolution the cloud environment; and (2) that the effects of eddy advection are small. Evidence of these effects was found by Istok and Doviak (1986) when attempting to explain ε in the context of cloud characteristics in an observed supercell thunderstorm. The effects of the advection of turbulence and the time-scales to dissipation will impact the degree to which ε can be reliably related to cloud processes observed simultaneously. The strength and significance of observed correlations would suggest that these effects have been small in this application; a likely benefit of the statistical approach taken, which avoids point-for-point comparisons of ε with other cloud variables. However, single RHI data alone is likely to be insufficient if a comprehensive explanation of ε in relation to cloud processes is desired.

Future research into the role of turbulence in convective clouds using radar observations can benefit from improvements to scanning strategy for data collection. These should include co-ordinated observations of clouds using multiple high-resolution Doppler radars capable of sampling inertial sub-range turbulence. By doing this, clouds can be observed from more than one direction simultaneously allowing the reconstruction of 3-D cloud structure. Repeatedly scanning target clouds over time-scales sufficient to capture the evolution of the cloud will allow ε to be analysed more specifically in the context of 3-D cloud processes. This may reveal the time-scales of turbulence in clouds from production to dissipation scales,

and the effects of advection on the spatial distribution of ε. Where possible, observations should be extended to clouds with much weaker and much stronger updrafts than those considered in this application to better examine how ε scales with updraft strength. Such an approach would allow for a more detailed evaluation of numerical models by testing results against turbulence in 3-D model cloud structures. Future projects (with or without CAMRa) should use the turbulence retrieval method designed in Chapter 3 and use improvements to scanning strategy and radar specification suggested in Section 6.2.3 to improve the quality of data collection.

Future research could also be aimed at identifying which cloud characteristics determine the size and shape of dissipation features. Of particular interest would be to investigate whether the spatial coverage of dissipation provides a better characterisation of cloud processes such as updrafts than the turbulent intensity alone.

6.4 Evaluation of ε in the MetUM

6.4.1 Summary

Diagnostic outputs from the Smagorinsky-Lilly sub-grid turbulence scheme have been used to derive ε in 100-m grid-scale MetUM (control) simulations of the shower and deep cloud cases. Constraints and thresholds were applied to model data to ensure a fair comparison with observations. Reliable evaluation of the model was performed by conducting a statistical analysis of ε in model clouds using methods that were consistent with those used in observations.

Vertical cross-sections of individual clouds of similar size and updraft strength were identified in observations and model simulations and compared for both cases. Many similarities with observations were present in the simulated clouds: (1) Values of ε were larger in the simulated deep cloud (SDC), than in the simulated shower cloud (SSC); (2) in

both model cloud cases, a large proportion of the cloud area was only weakly turbulent; (3) high ε was spatially correlated with regions of vertical (upward) motion in both model clouds. However, key differences included: (1) the largest values of ε in the model clouds far exceeded (by up to two orders of magnitude) values that were present in the observed cases and values that could be reliably sampled with CAMRa; (2) high ε was found in smaller, more intense regions that were much more strongly co-located with shear around updrafts than for the observed cases, where high ε was weaker and more diffuse.

When comparing the vertical distribution of ε in model clouds with observations, median values of ε were very similar, ranging from 0.01 – 0.03 $m^2\ s^{-3}$ in all cases. However, the 95th and 99th percentiles of ε were one and two orders of magnitude, respectively, larger in the model in both cloud cases. The intensity of model ε decreased with height, contrasting with the positive vertical gradient in observed deep cloud and consistency with height in observed shower cloud. In Chapter 4, stronger updrafts were thought to be more effective in transporting intense turbulence towards the upper regions of observed clouds; a process of advection that is not accounted for by the Smagorinsky-Lilly scheme and may explain the differing vertical profiles of ε.

Updraft velocities and sizes were well simulated by the model for both cloud cases. Despite this, the 95th and 99th percentiles of ε in model updraft regions were again one and two orders of magnitude larger than observed values. The horizontal gradients in updraft velocity were significantly stronger in the model; twice as large in SSC and 65% larger in SDC. Although the increased shear will result in larger values of ε from the Smagorinsky-Lilly scheme, it is not clear whether stronger shear alone can account for the significant differences in large ε found in the model. No significant correlations were initially found in model updrafts between ε_{95} and the updraft strength, size or shear. Including only values of ε_{95} that corresponded to the range of values that were observed resulted in significant positive correlations with updraft characteristics that were of similar strength (albeit slightly

weaker) to those observed. This suggested that the extreme values of ε_{95} found in the model were not significantly correlated with cloud characteristics. Consistent with observations, CDFs of ε became broader with model updraft strength, though distributions were much less sensitive to velocity changes in the model.

The spatial scales of coherent ε features in the model were found to be largely insensitive to the intensity of ε and remained very similar in both cloud cases. These were key differences with observations, where the spatial scales of dissipation features decreased with turbulent intensity and, for a given threshold of ε, were generally smaller in the shower case. Without further investigation into how the spatial scales of ε are related to observed cloud processes, it is not clear whether the differing characteristics of ε in the model affect the evolution of clouds.

Simulations were performed to test the sensitivity of ε to the model grid-length Δx, and sub-grid scheme mixing length, λ_0. Although the size and strength of updrafts did not change significantly with changes to Δx and λ_0, values of ε became consistently larger as λ_0 was increased. When Δx was 100 m, doubling λ_0 from 20 m to 40 m increased median ε by 31% in SDC and by 8% in SSC. The simulation using the smallest λ_0 of 11 m (55 m model using C_s of 0.2) produced the smallest median values of ε; however, ε_{95} remained an order of magnitude larger than observed values. When using very similar values of λ_0 in 55-m and 100-m models, the statistics of ε were approximately the same, suggesting that 100 m was within the inertial sub-range for these simulations. Doubling λ_0 acted to smooth velocity fields and reduce shear through increased mixing. According to (2.26), weaker shear (in isolation) will reduce ε. However, the effect is small compared to the factor-of-four increase in ε through the increased mixing, suggesting that ε is more sensitive to changes to λ_0. Of key importance was that no reasonable changes to λ_0 or Δx reduced values of ε sufficiently to agree with observations.

6.4.2 Limitations and future work

Although a fair comparison with observations has been attempted through careful consideration of thresholds and constraints to model data sampling, the quality of the comparison could be improved. During DYMECS, the targeting algorithm used to direct CAMRa prioritised scanning through the centre of mature, precipitating clouds. The sampling of model data involved taking vertical profiles (as they are comparable with RHIs) at regular intervals throughout the domain, rather than targeting the centre of precipitating model clouds. The impact on the comparison with observations is not clear; however, while performing an RHI to scan through the centre of a target cloud, non-target clouds in the line-of-sight were frequently sampled. This suggests that a large proportion of observed clouds were sampled with no directional preference, as is true in model data sampling. To improve the comparison with observations, model clouds could be targeted using an algorithm similar to that used in DYMECS and compared with the data associated only with target clouds in each RHI.

The primary aim of Chapter 5 was to identify *how* the characteristics of ε differed with observed values in the MetUM. Given the significant differences identified in model ε, future work should be focused on addressing the reasons as to *why* such differences exist. Of key importance is that the MetUM simulations are resolving an inertial sub-range for the Smagorinsky-Lilly scheme to perform correctly. Future research should focus on testing the assumption that models resolve an inertial sub-range though direct computation of velocity spectra (e.g. Bryan *et al.* 2003). Results presented in Chapter 5 indicated that ε was largely insensitive to changes to model grid-length when the mixing length was constant. As ε is scale-independent in the inertial sub-range, this result has been taken to suggest that both the 55-m and 100-m models have indeed resolved an inertial sub-range. If this is true (or an inertial sub-range is demonstrated using more direct methods), future research requires investigation into additional reasons for why values of ε remain so much larger in the model.

For a clear comparison, observations of ε have been used to evaluate MetUM simulations of the observed cases only. However, the observations also provide more general guidelines for the values of ε and relationships with cloud characteristics that are typical in clouds. As such, these observations can be compared with ε from any turbulence parametrisation given that ε can be derived. It would be particularly interesting to compare observed ε with values produced by the Smagorinsky-Lilly scheme when used in an LES model. Such an investigation would allow for a more critical evaluation of the Smagorinsky-Lilly scheme in the modelling environment for which is was designed, which would provide a better platform to judge how its performance changes when adopted for use in a CPM.

References

Adlerman EJ, Droegemeier KK. 2002. The sensitivity of numerically simulated cyclic mesocyclogenesis to variations in model physical and computational parameters. *Mon. Wea. Rev.* **130**: 2671–2691.

Anderson NF, Grainger CA, Stith JL. 2005. Characteristics of strong updrafts in precipitation systems over the central tropical Pacific Ocean and in the Amazon. *J. Appl. Meteorol.* **44**: 731-738.

Atlas D, Srivastava RC, Sekhon RS. 1973. Doppler radar characteristics of precipitation at vertical incidence. *Rev. Geophys. Space Phys*. **2**: 1-35.

Atlas D, Srivastava RC, Sloss PW. 1969. Wind shear and reflectivity gradient effects on Doppler radar spectra: II. *J. Appl. Meteorol.* **8**: 384-388.

Atlas D, Ulbrich CW. 1977. Path- and area-integrated rainfall measurement by microwave attenuation in the 1-3 cm band. *J. Appl. Meteorol.* **16**: 1322–1331.

Battan LJ. 1975. Doppler radar observations of a hailstorm. *J. Appl. Meteorol.* **14**: 98-108.

Battan LJ, Theiss JB. 1973. Wind gradients and variance of Doppler spectra in showers viewed horizontally. *J. Appl. Meteor.* **12**: 688-693.

Benmoshe N, Khain AP. 2014. The effects of turbulence on the microphysics of mixed-phase deep convective clouds investigated with a 2-D cloud model with spectral bin microphysics. *J. Geophys. Res. Atmos.* **119**: 207–221.

Benmoshe N, Pinsky M, Pokrovsky A, Khain A. 2012. Turbulent effects on the microphysics and initiation of warm rain in deep convective clouds: 2-D simulations by a spectral mixed-phase microphysics cloud model. *J. Geophys. Res*. **117**: D06220.

Best MJ, Pryor M, Clark DB, Rooney GG, Essery RLH, Menard CB, Edwards JM, Hendry MA, Porson A, Gedney N, Mercado LM, Sitch S, Blyth E, Boucher O, Cox PM, Grimmond CSB, Harding RJ. 2011. The Joint UK Land Environment Simulator (JULES), model description – part 1: energy and water fluxes. *Geoscientific Model Development.* **4**: 677–699.

Blyth AM. 1993. Entrainment in cumulus clouds. *J. Appl. Meteorol.* **32**: 626-641.

Blyth AM, Cooper AC, Jensen JB. 1988. A study of the source of entrained air in Montana Cumuli. *J. Atmos. Sci.* **45**: 3944-3964.

Blyth AM, Latham J. 1990. Airborne studies of the altitudinal variability of the microphysical structure of small, ice-free, Montana cumulus clouds. *Quart. J. Roy. Meteor. Soc.* **116**: 1405-1423.

Bouniol D, Illingworth AJ, Hogan RJ. 2003. Deriving turbulent kinetic energy dissipation rate within clouds using ground based 94 GHz radar. Preprints, 31st Conf. on Radar Meteorology, Seattle, WA, Amer. Meteor. Soc. 192-196.

Brewster KA, Zrnic DS. 1986. Comparison of eddy dissipation rates from spatial spectra of Doppler velocities and Doppler spectrum widths. *J. Atmos. Oceanic Technol*. **3**: 440-552.

Bryan GH, Wyngaard JC, Fritsch JM. 2003. Resolution requirements for the simulation of deep moist convection. *Mon. Wea. Rev.* **131**: 2394-2416.

Canuto VM, Cheng Y. 1997. Determination of the Smagorinsky–Lilly constant c_s. *Phys. Fluids*. **9**: 1368-1378.

Chapman D, Browning KA. 2001. Measurements of dissipation rate in frontal zones. *Q. J.*

R. Meteorol. Soc. **127**: 1939-1959.

Charney JG, Phillips NA. 1953. Numerical integration of the quasi-geostrophic equations for barotropic and simple baroclinic flows. *J. Meteor.* **10**: 71-99.

Cheng L, English M. 1982. A relationship between hailstone concentration and size. *J. Atmos. Sci.* **40**: 204-213.

Chonacky N, Deuel RW. 1988. Atmospheric optical turbulence profiling by stellar scintillometers: an instrument evaluation experiment. *Appl. Opt.* **27**: 2214-2221.

Clark P, Roberts N, Lean H, Ballard SP, Charlton-Perez C. 2016. Convection-permitting models: a step-change in rainfall forecasting. *Meteorol. Appl.* **23**: 165-181.

Cox GP. 1988. Modelling precipitation in frontal rainbands. *Q. J. R. Meteorol. Soc.* **114**: 115–127.

Davies T, Cullen MJP, Malcolm AJ, Mawson MH, Staniforth A, White AA, Wood N. 2005. A new dynamical core for the Met Office's global and regional modelling of the atmosphere. *Q. J. R. Meteorol. Soc.* **131**: 1759-1782.

Depue TK, Kennedy PC, Rutledge SA. 2007. Performance of the hail differential reflectivity (H_{DR}) polarimetric radar hail indicator. *J. Appl. Meteorol. Climatol.* **46**: 1290-1301.

Devenish BJ, Bartello P, Brenguier J-L, Collins LR, Grabowski WW, IJzermans RHA, Malinowski SP, Reeks MW, Vassilicos JC, Wang L-P, Warhaft Z. 2012. Droplet growth in warm turbulent clouds. *Q. J. R. Meteorol. Soc.* **138**: 1401 – 1429.

Donaldson RJ, Wexler R. 1969. Flight hazards in thunderstorms determined by Doppler velocity variance. *J. Appl. Meteor.* **8**: 128-133.

Doviak RJ, Zrnic DS. 1984. Doppler radar and weather observations. *Academic Press.*

Droegemeier KK, Bassett G, Xue M. 1994. Very high-resolution, uniform-grid simulations of deep convection on a massively parallel computer: Implications for small-scale predictability. *Preprints, 10th Conf. on Numerical Weather Prediction*, Portland, OR, Amer. Meteor. Soc. 376–379.

Droegemeier KK, Richardson YP, Bassett GM, Marroquin A. 1997. Three-dimensional numerical simulations of turbulence generated in the near-environment of deep convective storms. *Pre-prints, Seventh Conf. on Aviation, Range, and Aerospace Meteorology*, Long Beach, CA, Amer. Meteor. Soc. 169–174.

Edwards J, Slingo A. 1996. Studies with a flexible new radiation code. Part I: Choosing a configuration for a large-scale model. *Q. J. R. Meteorol. Soc.* **122**: 689–719.

Falkovich G, Fouxon A, Stepanov MG. 2002. Acceleration of rain initiation by cloud turbulence. *Nature*. **419**: 151-154.

Federal Aviation Administration. 2012. Aeronautical information manual (AIM). FAA Doc., 762 pp. [Available online at http://www.faa.gov/air_traffic/publications/ ATpubs/AIM/aim.pdf.]

Foote GB, Fankhauser JC. 1973. Airflow and moisture budget beneath a northeast Colorado hailstorm. *J. Appl. Meteor.* **12**: 1330-1353.

Frisch AS, Clifford SF. 1974. A Study of Convection Capped by a Stable Layer Using Doppler Radar and Acoustic Echo Sounders. *J. Atmos. Sci.* **31**: 1622–1628.

Frisch AS, Strauch RG. 1976. Doppler radar measurements of turbulent kinetic energy dissipation rates in a northeastern Colorado convective storm. *J. Appl. Meteor.* **15**: 1012-1017.

Goddard JWF, Eastment J, Thurai M. 1994. The Chilbolton Advanced Meteorological Radar: A tool for multidisciplinary atmospheric research. *Electronics and Communication Engineering Journal*, **6**: 77–86.

Gossard EE. 1990. Radar research on the atmospheric boundary layer, in Ed. Atlas D. Radar in meteorology. 477-527pp.

Gossard EE, Strauch RG. 1983. Radar observations of clear air and clouds. Elsevier, New York. 280 pp.

Grandia KL, Marwitz JD. 1975. Observational investigations of entrainment within the weak echo region. *Mon. Wea. Rev.* **103**: 227-234.

Gregory D, Rowntree P. 1990. A mass flux convection scheme with representation of cloud ensemble characteristics and stability dependent closure. *Mon. Wea. Rev.* **118**: 1483–1506.

Grover SN, Pruppacher HR. 1985. The effect of vertical turbulent fluctuations in the atmosphere on the collection of aerosol particles by cloud drops. *J. Atmos. Sci.* **42**: 2305-2318.

Gunn KLS, Marshall RS. 1958. The distribution of size of aggregate snowflakes. *J. Meteorol. Soc.* **80**: 522-545.

Hanley KE, Plant RS, Stein THM, Hogan RJ, Nicol JC, Lean HW, Halliwell CE, Clark PA. 2015. Mixing length controls on high resolution simulations of convective storms. *Q. J. R. Meteorol. Soc*. **141**: 272-284.

Haralick RM, Shapiro LG. 2002. Computer and robot vision (volume I). Addison Wesley Longman.

Harrison RG, Hogan RJ. 2006. In situ atmospheric turbulence measurement using the terrestrial magnetic field-A compass for a radiosonde. *J. Atmos. Oceanic. Technol.* **23**: 517-523.

Harrison DL, Norman K, Pierce C, Gaussiat N. 2011. Radar products for hydrological applications in the UK. *Proceedings of the Institution of Civil Engineers*. **165**: 89–103.

Heus T, van Dijk G, Jonker HJJ, van den Akker HEA. 2008. Mixing in shallow cumulus studied by Lagrangian particle tracking. *J. Atmos. Sci.* **65**: 2581-2597.

Hogan RJ, Illingworth AJ, Halladay K. 2008. Estimating mass and momentum fluxes in a line of cumulonimbus using a single high-resolution Doppler radar. *Q. J. R. Meteorol. Soc.* **134**: 1127-1141.

Holman JP. 2002. Heat Transfer. McGraw-Hill. p. 207.

Istok MJ, Doviak RJ. 1986. Analysis of the relation between Doppler spectral width and thunderstorm turbulence. *J. Atmos. Sci.* **43**: 2199-2214.

Keeler JR, Passarelli RE. 1990. Signal processing for atmospheric radars. *Radar in Meteorology*. DOI 10.1007/978-1-935704-15-7_21. 199-229.

Khain AP, Pinsky MB. 1995. Drops' inertia and its contribution to turbulent coalescence in convective clouds: Part 1. Drops' fall in the flow with random horizontal velocity. *J. Atmos. Sci.* **52**: 196-206.

Khvorostyanov VI, Curry JA. 1999. Toward the theory of stochastic condensation in clouds. Part I: A general kinetic equation. *J. Atmos. Sci.* **56**: 3985 – 3996.

Klemp JB, Wilhelmson RB. 1978. The simulation of three-dimensional convective storm dynamics. *J. Atmos. Sci.* **35**: 1070–1096.

Knupp KR, Cotton WR. 1982. An intense, quasi-steady thunderstorm over mountainous terrain, part III: Doppler radar observations of the turbulent structure. *J. Atoms. Sci.* **39**:

359-368.

Kollias P, Albrecht BA. Lhermitte R. Savtchenko A. 2001. Radar observations of updrafts, downdrafts, and turbulence in fair weather cumuli. *J. Atmos. Sci*. **58**: 1750-1766.

Kolmogorov AN. 1941. Dissipation of energy in the locally isotropic turbulence. *Dokl. Akad. Nauk. SSSR*, **32**: 16-18.

Labitt, M. 1981. Co-ordinated radar and aircraft observations of turbulence. Project Rep. ATC 108, MIT, Lincoln Lab, 39 pp.

Lean HW, Clark PA, Dixon M, Roberts NM, Fitch A, Forbes R, Halliwell C. 2008. Characteristics of high-resolution versions of the Met Office Unified Model for forecasting convection over the United Kingdom. *Mon. Wea. Rev.* **136**: 3408-3424.

Lee JT, Thomas K. 1989. Turbulence spectral widths view angle independence as observed by Doppler radar. Technical Report, DOT/FAA/SA-89-2. 47 pp.

Lhermitte RM. 1963. Motions of scatterers and the variance of the mean intensity of weather radar signals. SRRC-RR-63-57. Sperry-Rand Res. Cent., Sudbury, Massachusetts.

Lilly DK. 1967. The representation of small-scale turbulence in numerical simulation experiments. *Proc. IBM Scientific Symp. on Environmental Sciences*, Yorktown Heights, NY, IBM DP Division, 195–210.

Lock AP, Brown AR, Bush MR, Martin GM, Smith RNB. 2000. A new boundary layer mixing scheme. Part I: Scheme description and single-column model tests. *Mon. Wea. Rev*. **128**: 3187–3199.

MacCready PB Jr. 1962. Turbulence measurements by sailplane. *J. Geophys. Res.* **67**: 1041-1050.

MacPherson JI, Isaac GA. 1977. Turbulent characteristics of some Canadian cumulus clouds. *J. Atmos. Meteor.* **16**: 81-90.

Marshall JS, Palmer WM. 1948. The distribution of raindrops with size. *J. Meteorol.* **5**: 165-166.

Martini E, Freni A, Cuccoli F, Facheris L. 2017. Derivation of clear-air turbulence parameters from high-resolution radiosonde data. *J. Atmos. Oceanic Technol.* **34**: 277-293.

Martner BE, Battan LJ. 1976. Calculations of Doppler radar velocity spectrum parameters for a mixture of rain and hail. *J. Appl. Meteorol.* **15**: 491-498.

Mason PJ. 1994. Large-eddy simulation: A critical review of the technique. *Q. J. R. Meteorol. Soc.* **120**: 1-26.

Mason PJ, Brown AR. 1999. On subgrid models and filter operations in large eddy simulations. *J. Atmos. Sci.* **56**: 2101–2114.

Mason PJ, Callen NS. 1986. On the magnitude of the subgrid-scale eddy coefficient in large-eddy simulations of turbulent channel flow. *J. Fluid Mech.* **162**: 439-462.

Meehl GA, Zwiers F, Evans J, Knutson T, Mearns L, Whetton P. 2000. Trends in extreme weather and climate events: Issues related to modelling extremes in projections of future climate change. *Bull. Amer. Meteor. Soc.* **81**: 427-436.

Meishner P, Baumann R, Holler H, Jank T. 2001. Eddy dissipation rates in thunderstorms estimated by Doppler radar in relation to aircraft in-situ measurements. *J. Atmos. Oceanic. Technol*. **18**: 1609-1627.

Meyer W, Jank T. 1989. Dopplerspektren aus inkoharenter Ruckstreuung, Prinzip und Anwendungsbeispiele. Rep. DLR-FB 89-48, 58 pp. [English translation: Rep. ESA-TT-1197.]

Nastrom GD, Rao PB, Sivakumar V. 2004. Measurements of atmospheric turbulence with the dual-beam width method using the MST radar at Gadanki, India. *Ann. Geophys.* **22**: 3291-3297.

Nathanson FE. 1969. Radar design principles. McGraw-Hill, New York.

Neter J, Wasserman W. 1974. Applied linear statistical models. 842pp.

Nicol JC, Hogan RJ, Stein THM, Hanley KE, Clark PA, Halliwell CE, Lean HW, Plant RS. 2015. Convective updraft evaluation in high-resolution NWP simulations using single-Doppler measurements. *Q. J. R. Meteorol. Soc.* **141**: 3177-3189.

Oguchi T. 1983. Electromagnetic wave propagation and scattering in rain and other hydrometeors. *Proc. IEEE*. **71**: 1029-1078.

Panchev S. 1971. Random functions and turbulence. Pergamon Press. 444 pp.

Petch JC, Brown AR, Gray MEB. 2002. The impact of horizontal resolution on the simulations of convective development over land. *Q. J. R. Meteor. Soc.* **128**: 2031–2044.

Petch JC, Gray MEB. 2001. Sensitivity studies using a cloud-resolving model simulation of the tropical west Pacific. *Q. J. R. Meteorol. Soc.* **127**: 2287-2306.

Pinksy MB, Khain AP. 2002. Effects of in-cloud nucleation and turbulence on droplet spectrum formation in cumulus clouds. *Q. J. R. Meteorol. Soc.* **128**: 501-533.

Pinsky MB, Khain AP, Levin Z. 1999. The role of the inertia of cloud drops in the evolution of the spectra during drop growth by diffusion. *Q. J. R. Meteorol. Soc.* **125**: 553 – 581.

Potter MC, Wiggert DC, Ramadan BH. 2012. Mechanics of fluids (Fourth edition. ed.). p. 105. ISBN 978-0-495-66773-5.

Pruppacher HR, Klett JD. 1978. Microphysics of clouds and precipitation. D. Reidel Publishers, Dordrecht, 714pp.

Reynolds O. 1883. An experimental investigation of the circumstances which determine whether the motion of water in parallel channels shall be direct or sinuous and of the law of resistance in parallel channels. *Philos. Trans. R. Soc.* **174**: 935-982.

Rhyne RH, Steiner R. 1964. Power spectral measurements of atmospheric turbulence in severe storms and cumulus clouds. NASA Tech. Note. NASA TD D-2469, 1-48.

Sand WR. 1976. Observations in hailstorms using the T-28 aircraft system. *J. Appl. Meteor.* **15**: 641-650.

Sharman RD, Cornman LB, Meymaris G, Pearson J. 2014. Description and derived climatologies of automated in situ eddy-dissipation-rate reports of atmospheric turbulence. *J. Appl. Meteor. Climatol.* **53**: 1416-1432.

Shaw RA. 2003. Particle-turbulence interactions in atmospheric clouds. *Annu. Rev. Fluid Mech.* **35**: 183-227.

Shaw RA, Reade WC, Collins LR, Verlinde J. 1998. Preferential concentration of cloud droplets by turbulence: effects on the early evolution of cumulus cloud droplet spectra. J. Atmos. Sci. 55: 1965 – 1976.

Sidin RSR, IJzermans RHA, Reeks MW. 2009. A Lagrangian approach to droplet condensation in atmospheric clouds. *Phys. Fluids.* **21**: 106603, DOI: 10.1063/1.3244646.

Sinclair PC. 1974. Severe storm turbulent energy structure. *Conf. Aerosp. Aeronaut. Meteorol.* 6th, 1974, El Paso, Texas. (Unpublished manuscript).

Skamarock WC. 2004. Evaluating mesoscale NWP models using kinetic energy spectra. *Mon. Wea. Rev.* **132**: 3019-3032.

Smagorinsky J. 1963. General circulation experiments with the primitive equations. I: The basic experiment. *Mon. Wea. Rev.* **91**: 99–164.

Srivastava RC, Atlas D. 1974. Effect of finite radar pulse volume on turbulence measurements. *J. Appl. Meteorol.* **13**: 472-480.

Stein THM, Hogan RJ, Clark PA, Halliwell CE, Hanley KE, Lean HW, Nicol JC, Plant RS. 2015. The DYMECS Project: A statistical approach for the evaluation of convective storms in high-resolution NWP models. *Bull. Amer. Meteor. Soc.* **96**: 939-951.

Stein THM, Hogan RJ, Hanley KE, Nicol JC, Lean HW, Plant RS, Clark PA, Halliwell CE. 2014. The three-dimensional morphology of simulated and observed convective storms over southern England. *Mon. Wea. Rev.* **142**: 3264-3283.

Stommel H. 1947. Entrainment of air into a cumulus cloud. *J. Meteor.* **4**: 91-94.

Takemi T, Rotunno R. 2003. The effects of subgrid model mixing and numerical filtering in simulations of mesoscale cloud systems. *Mon. Weather Rev.* **131**: 2085-2101.

Tang Y, Lean HW, Bornemann J. 2013. The benefits of the Met Office variable resolution NWP model for forecasting convection. *Meteorol. Appl.* **20**: 417-426.

Ulbrich CW. 1974. Analysis of Doppler radar spectra of hail. *J. Appl. Meteorol.* **13**: 387-396.

Ulbrich CW. 1977. Doppler radar relationships for hail at vertical incidence. *J. Appl. Meteorol.* **16**: 1349-1359.

Verrelle A, Ricard D, Lac C. 2014: Sensitivity of high-resolution idealized simulations of thunderstorms to horizontal resolution and turbulence parametrization. *Q. J. R. Meteorol. Soc.* **141**: 433-448.

Vohl O, Mitra SK, Wurzler SC, Pruppacher HR. 1999. A wind tunnel study of the effects of turbulence on the growth of cloud droplets by collision and coalescence. *J. Atmos. Sci.* **56**: 4088-4099.

Waldvogel A, Schmidt W, Federer B. 1978. The kinetic energy of hailfalls. Part I: Hailstone spectra. *J. Appl. Meteorol.* **17**: 515-520.

Warner J. 1955. The water content of cumiliform cloud. *Tellus*. **7**: 449-457.

Weisman ML, Davis C, Wang W, Manning KW, Klemp JB. 2008. Experiences with 0-36 hr explicit convective forecasts with the WRF-ARW model. *Weather. Forecast.* **23**: 407-437.

Weisman ML, Skamarock WC, Klemp JB. 1997. The resolution dependence of explicitly modelled convective systems. *Mon. Wea. Rev.* **125**: 527–548.

Wilson DR, Ballard SP. 1999. A microphysically based precipitation scheme for the UK Meteorological Office Unified Model. *Q. J. R. Meteorol. Soc.* **125**: 1607–1636.

Zrnic DS, Doviak RJ, 1989. Effect of drop oscillations on spectral moments and differential reflectivity measurements. *J. Atmos. Oceanic Technol*. **6**: 532-536.